Lawrence Berkeley National Laboratory
Recent Work

Title
The Alpha-Induced Thick-Target Gamma-Ray Yield from Light Elements

Permalink
https://escholarship.org/uc/item/2r85f378

Author
Heaton, R.K.

Publication Date
1994-10-14

eScholarship.org Powered by the California Digital Library
University of California

LBL-36651
UC-413

Lawrence Berkeley Laboratory
UNIVERSITY OF CALIFORNIA

The α-Induced Thick-Target γ-Ray Yield from Light Elements

R.K. Heaton
(Ph.D. Thesis)

October 1994

U. C. Lawrence Berkeley Laboratory
Library, Berkeley

FOR REFERENCE

Not to be taken from this room

NUCLEAR SCIENCE DIVISION

REFERENCE COPY
Does Not
Circulate
Bldg. 50 Library.
LBL-36651
Copy 1

Prepared for the U.S. Department of Energy under Contract Number DE-AC03-76SF00098

DISCLAIMER

This document was prepared as an account of work sponsored by the United States Government. While this document is believed to contain correct information, neither the United States Government nor any agency thereof, nor the Regents of the University of California, nor any of their employees, makes any warranty, express or implied, or assumes any legal responsibility for the accuracy, completeness, or usefulness of any information, apparatus, product, or process disclosed, or represents that its use would not infringe privately owned rights. Reference herein to any specific commercial product, process, or service by its trade name, trademark, manufacturer, or otherwise, does not necessarily constitute or imply its endorsement, recommendation, or favoring by the United States Government or any agency thereof, or the Regents of the University of California. The views and opinions of authors expressed herein do not necessarily state or reflect those of the United States Government or any agency thereof or the Regents of the University of California.

LBL-36651
UC-413

The α-Induced Thick-Target γ-Ray Yield from Light Elements

R.K. Heaton
Ph.D. Thesis

Department of Physics
Queen's University
Kingston, Ontario, Canada

and

Nuclear Science Division
Lawrence Berkeley Laboratory
University of California
Berkeley, California 94720

October 1994

This work was supported by the the Natural Sciences and Engineering Research Council of Canada (NSERC), through the U.S. Department of Energy under Contract No. DE-AC03-76SF00098.

Abstract

The α-induced thick-target γ-ray yield from light elements has been measured in the energy range between 5.6 MeV $\leq E_\alpha \leq$ 10 MeV. The γ-ray yield for $E_\gamma >$ 2.1 MeV from thick targets of beryllium, boron nitride, sodium fluoride, magnesium, aluminum and silicon were measured using the α-particle beam from the Lawrence Berkeley Laboratories 88″cyclotron. The elemental yields from this experiment were used to construct the α-induced direct production γ-ray spectrum from materials in the SNO detector, a large volume ultra-low background neutrino detector located in the Creighton mine near Sudbury, Canada. This background source was found to be an order of magnitude lower than predicted by previous calculations. These measurements are in good agreement with detailed theoretical calculations of this spectrum based on a statistical nuclear model of the reaction, with the gross high energy spectrum structure being reproduced to within a factor of two. A detailed comparison of the experimentally and theoretically deduced excitation population distribution of several residual nuclei indicate the same level of agreement within experimental uncertainties.

Statement of Originality

The experimental measurements reported in this work were performed at Lawrence Berkeley Laboratories in collaboration with Dr. Eric Norman, Dr. Kevin Lesko, Dr. Bhaskar Sur of that institution, and with Dr. Henry Lee and Dr. Barry Robertson of Queen's University. The analysis, calculations and conclusions presented in this thesis are the original work of the author unless explicitly indicated in the text.

Acknowledgements

Many people have aided me in this research and help me maintain my sanity. I would like to thank my supervisor, Barry Robertson, for his guidance and patience in this research. Henry Lee has provided invaluable help in many forms and on many occasions, for which I am greatly in his debt. I would also like to acknowledge a debt of gratitude to H-B Mak, who has help me with several matters during my supervisor's absence. I would like to thank Rick Norman, Kevin Lesko, Bhaskar Sur and all the people at Lawrence Berkeley Laboratories who participated in our experiment. I am grateful to Ian Towner for supplying us with the Oxford DWBA computer code. I would also like to thank my fellow graduate students for stimulating conversations and the occasional gripe session. In particular I must thank Lorne, André, Chris, Victor, Jeff, Luc and Rob K., all of whom at one time or another were forced into sharing office space with me. And finally, I would like to thank Fawn, my wonderful wife, who has put up with me throughout this work. Thank you all.

Contents

List of Figures

List of Tables

Glossary

Glossary of Terms and Acronyms

FWHM: full width at half maximum of a peak.

HPGe: hyper-pure germanium.

MCA: multi-channel analyser.

SCA: single channel analyser.

background region: the channel region in a spectrum to either side of a peak used to calculate the background area beneath a peak. Preceded by "lower" and "upper" to indicate the section of the background from the energy region below and above a peak, respectively.

detector #1: detector positioned at the forward beam angle, 30.9° from the target–beam line coördinate system

detector #2: detector positioned at the backward beam angle, 109.9° from the target–beam line coördinate system

direct level population: the thick-target population per α-particle of a level in a residual nucleus induced by an (α, x) reaction. This is calculated by subtracting the population of the level by γ-ray cascade decay of higher energy levels.

direct production γ-rays: Gamma-rays resulting from the decay of residual nuclei from (α, x) reactions, and in particular excluding γ-rays resulting from neutron capture

escape order: a number used to identify peaks associated with a single γ-ray transition. "0" indicates a full energy peak, "1" indicates a first escape peak and "2" indicates a second escape peak.

level population: the thick-target population per α-particle of a level in a residual nucleus as deduced from the observed yield for different decay branches.

peak region: the channel region in a spectrum used to calculate the area and centroid of a γ-ray peak. The area of the peak is calculated by subtracting the interpolated background area beneath the peak from the total area of the peak region.

population distribution: the total level population per α-particle in a 1 MeV wide energy interval (bin) for a residual nucleus.

reduced spectrum: spectrum from which some first and second escape peaks have been subtracted

resolved levels: an energy level in a nucleus whose level population is known.

resolved transition: a transition whose yield is calculable.

transition: the de-excitation of a nucleus, and subsequent production of a γ-ray, from one level of definite energy to another level of definite energy.

unresolved transition: a transition whose yield is known only in combination with other transition yields.

Glossary of Symbols

a: the level density parameter for a nucleus

a_i: the fitted coefficients from a linear regression

$b \pm \delta b$: the background area and uncertainty. When indexed, refers to the background area for one channel.

c_i: the gross channel counts, without any escape subtraction.

$c_{ijk} \pm \delta c_{ijk}$: the intensity and uncertainty of an escape of order j from channel k in full energy peak i.

e: the charge of an electron, 1.602×10^{-19}C

$f_{ws}(x)$: the Woods-Saxon potential function

$g(x)$: composite Gaussian function. Subscripted to indicate individual Gaussian fits making up the composite

j: the total angular momentum quantum number of an incident particle

$j_l(x), \eta_l(x)$: the spherical Bessel and Neumann functions of order l

k: the wave number of an incident particle

l: the orbital angular momentum quantum number of an incident particle

m_α: the mass of an α-particle.

m_i:	the net positive counts in a channel above background
n:	the index reserved for the detector number (1 or 2).
n_{ch}:	the number of channels in the background regions of a fit.
n_d:	the number of beam dump (scalar) counts.
n_{eff}:	the effective number of counts used in the centroid calculation
q:	the charge state of the α-particle beam, in units of e.
s:	the intrinsic spin quantum number of an incident particle
s_i:	the energy dispersion of a spectrum i
t_i:	the channel offset for a spectrum i
u_{lj}:	the radial logarithmic wave function
v:	the velocity of an incident particle
w:	weight used in linear regression fits, usually defined as one over the square of the uncertainty
x:	the channel number of a fit. Subscripted when involved in a summation.
$\bar{x} \pm \delta\bar{x}$:	the channel centroid and uncertainty of a peak
Δx:	the amount of shift of a centroid
δy_i:	the total uncertainty in the channel counts. May differ from the statistical value due to escape peak subtractions.

δz_i: the additional uncertainty introduced into a channel due to escape peak subtraction.

$A \pm \delta A$: the net area and uncertainty of a peak

δA_{bkgd}: the background area uncertainty due to the selection of a particular background form, reflecting changes in the area reported from different background shapes

$A_{\text{pulser } n}$: the net pulser peak area for spectrum n.

$B_i \pm \delta B_i$: the branching ratio of a transition i. Subscript may appear as $i \rightarrow j$ to indicate the branching ratio of the decay of level i to a level j.

C_i: counts per α-particle in a detector peak, normalized to 4π emission.

E_α: the kinetic energy of an α-particle.

E_γ: the energy of a γ-ray emitted in a rest frame.

E': the Doppler shifted energy of a γ-ray. Subscripted with *max* to indicate maximum possible energy shift.

ΔE_{max}: the maximum change in energy due to a Doppler shift.

E_x: the transition energy between the constant temperature and increasing temperature level density form

E_R: the total reaction energy available for the excitation of a residual nucleus

$F_l(x)$, $G_l(x)$: the regular and irregular Coulomb functions of order l

H_{fi}: the interaction Hamiltonian from a state i to a state f

J_o: the ground state spin of the target nucleus

J: the spin of the compound nucleus

J_1: the spin of the residual nucleus

L_i: the live time fraction for the detector i spectrum

N: the number of particles on target

N_{free}: the number of degrees of freedom for a fit

P_{abs}: the probability of a nucleus absorbing a particle

P_i: the Legendre polynomial of order i

$\overline{P_i(\cos\theta_n)}$: the intensity of the i Legendre polynomial averaged over the area of detector n

Q: the energy released by a reaction

S_{fi}: the scattering matrix element for a particle from an initial state i to a final state f

$S(lj)$: the elastic (diagonal) scattering matrix element for a particle with orbital angular momentum l and total angular momentum j

$\boldsymbol{S}$: the scattering matrix operator

$\mathcal{S}$: the variance of the channel centroid distribution

T: the level density temperature for an excited nucleus

$T_i(x)$: the Chebyshev polynomial of order i.

U: the pairing energy corrected (back-shifted) excitation energy of a nucleus used in the calculation of the level density

$U_i \pm \delta U_i^{(stat)} \pm \delta U_i^{(sys)}$: the level population per α-particle for a level i and associated statistical and systematic uncertainties, based on the yield Y

V: the nuclear potential

V_c, r_c: the magnitude of the Coulomb part of the nuclear potential and the nucleon radius defining the potential shape

V_R, r_R, a_R: the magnitude of the real part of the nuclear potential and the nucleon radius and diffusivity defining the potential shape

V_{so}, r_{so}, a_{so}: the magnitude of the real spin-orbit part of the nuclear potential and the nucleon radius and diffusivity defining the potential shape

V_t, W_{st}: the isospin dependence parameters of the real and surface imaginary part of the nuclear potential, used to extrapolate phenomenological potentials to unstable nuclei

V_e, W_{se0}, W_{sew}: the energy dependence parameters of the real and surface imaginary part of the nuclear potential, used to extrapolate phenomenological potentials to different energies

W_{Iv}, r_{Iv}, a_{Iv}: the magnitude of the volume imaginary part of the nuclear potential and the nucleon radius and diffusivity defining the potential shape

W_{Is}, r_{Is}, a_{Is}: the magnitude of the surface imaginary part of the nuclear potential and the nucleon radius and diffusivity defining the potential shape

$W_{b:JjJ_1}$: the decay probability of a compound nucleus with spin J by the emission of a particle b with total angular momentum j and a residual nucleus with spin J_1

$W_i \pm \delta W_i^{(stat)} \pm \delta W_i^{(sys)}$: The direct level population of a level i and associated uncertainties, determined by subtracting the γ-ray cascade contribution from the level population U_i.

$\overline{E}_x \pm \delta \overline{E}_x$: The mean excitation energy and statistical uncertainty for a residual nucleus

$Y_{lm}(\Omega)$: the spherical harmonic function for orbital angular momentum l and magnetic substate projection m

Y_i: the yield per α-particle from a transition i. Subscripted with "*peak*" to indicate the total yield from peaks consisting of multiple transitions.

$\delta Y_i^{(stat)}$: the statistical uncertainty in the yield. Contains the uncertainty in the peak areas, the uncertainty in the efficiency and the statistical uncertainty in the live time.

$\delta Y_i^{(sys)}$: the systematic uncertainty in the yield. Contains any uncertainties that affect all yield determinations, including systematic live time and beam normalization effects.

α: functional coefficient derivative matrix used in linear regression fits

β: the ratio of a velocity to the speed of light

ϵ: the kinetic energy of an emitted particle in the centre-of-mass system

ε: the error matrix of a fit, $\varepsilon \equiv \alpha^{-1}$

κ: multiplicative term in uncertainty calculation used to account for a $\hat{\chi}^2 > 1$

ϕ: the angle subtended by a detector, measured in from the centre (symmetry axis) of the detector crystal

ψ: the wave function of a particle interacting with a nuclear potential

σ: the level density spin cut-off parameter

σ_l: the reaction or absorption cross section for an orbital angular momentum l. May contain additional subscripts and superscripts to refer to particular angular momentum and reaction channels.

$\rho(E, J)$: the level density of nucleus at excitation energy E and level spin J

θ: the angle in the plane defined by the beam path and the detector positions, as measured from the target origin.

χ^2: the measure of the goodness of fit of a linear regression, usually defined as the ratio of the root mean square sum of derivative coefficients to the root mean square sum of the data point uncertainties

$\hat{\chi}^2$: the reduced χ^2, defined as the χ^2 divided by the number of degrees of freedom for the fit

χ_s: the intrinsic spin part of a wave function

Ω: the angular coördinates

Chapter 1

Introduction

In recent years there has been a growing interest in experiments to test the predictions of Grand Unified Theories (GUTs) and extensions of electro-weak theories. These experiments, including proton decay, double beta decay and neutrino astrophysics investigations, typically involve measurements with low event rates and hence require large detector volumes. In many cases events in these detectors can be mimicked or overwhelmed by background effects, and particularly by high energy γ-rays. This study is an investigation of the high energy γ-ray component of the background and, in particular, the high energy γ-ray background above 5 MeV in the Sudbury Neutrino Observatory (SNO).

The SNO detector is a large volume ultra-low background Čerenkov detector designed to observe neutrinos from the Sun and other possible astrophysical sources. The detector consists of 1000 tonnes of heavy water (D_2O) contained in a spherical acrylic vessel 12 m in diameter surrounded by a 7300 tonne light water shield. The detector is located in a barrel shaped cavity within norite, the host rock, 2 km below ground level in the Creighton mine near Sudbury. Neutrinos are detected from their reactions in D_2O and are observed by an array of 9450 photomultiplier tubes fitted with aluminum light concentrators (reflectors). The photomultiplier tube array is arranged in an inward facing concentric geodesic shell, approximately 17 m in diameter and 2.5 m away from the acrylic vessel to provide a 60% surface area coverage of the D_2O [Wa92, Ro93]. The neutrino reactions,

$$d + \nu_e = p + p + e^- \tag{1.1}$$

$$e^- + \nu_x = e^- + \nu_x \tag{1.2}$$

produce relativistic electrons which emit Čerenkov light seen by the photomultiplier tube array. The decay of ^{8}B in the sun is the primary source of neutrinos detected by SNO, and produces a spectrum containing neutrinos up to 14 MeV, with a spectrum peak close to 6 MeV in energy [Ba89]. The major interaction in SNO, given by equation (1.1), produces electrons with an energy 1.442 MeV less than the reacting neutrino energy. These reactions are responsible for the majority of the neutrino events, occurring at an anticipated rate of 10 events per day above an electron threshold of 5 MeV in the D_2O, assuming a ^{8}B neutrino flux one third of that predicted by the standard solar model, and in accordance with flux measurements reported from other solar neutrino experiments [Ew87, Ba89]. Another neutrino reaction,

$$d + \nu_x = n + p + \nu_x \tag{1.3}$$

with a reaction threshold of 2.225 MeV also produces a signal through the detection of the neutron in the D_2O [Ew92].

Extensive effort has gone into understanding and reducing the backgrounds which could mask or mimic these reactions in the SNO detector. A large component of these backgrounds consists of high energy γ-rays created through nuclear reactions and decays, or as is the case for neutrons, through radiative capture, which then produce high energy electrons through Compton scattering. Background sources can be broadly separated into two categories: external backgrounds and intrinsic backgrounds. External backgrounds are controlled by shielding the detector, while intrinsic backgrounds, arising from the radioactive contamination of the detector components, can only be reduced through the careful selection of materials.

The primary external background component arises from cosmic rays and is reduced by the shielding provided by the rock overburden. The muon flux, the most penetrating component of the cosmic ray background, is attenuated to the point where it produces an estimated 1.5 spallation events per day in the detector. The neutron-rich spallation products in turn produce β-particles with energies up to 10 MeV. These events can be distinguished from neutrino events through the timing characteristics of this two-step process [Ew87]. Neutrons and γ-rays from the cavity host rock and backfill concrete are another external source of background which is reduced by the light water shield surrounding the detector.

The uranium and thorium contamination of the detector components is the primary source of intrinsic backgrounds. These elements and their decay daughters produce neutrons and γ-rays from spontaneous fission and α-induced reactions. Several other studies have determined the effect of neutron sources in and around the

SNO detector [He88, Sk94]. The γ-ray component of the background has not been as fully explored, and is the focus of this study. In particular, we are concerned with the production of γ-rays above 5 MeV which would interfere with the portion of the solar neutrino spectrum investigated by SNO. In a background study of the Baksan low background laboratory, Pomansky [Po86] presented yield estimates for the sources of these high energy γ-rays. The primary intrinsic γ-ray background came from (α, n) followed by (n, γ) reactions in the rock, with a surprisingly substantial contribution attributed to $(\alpha, p\gamma)$ and $(\alpha, n\gamma)$ reactions. This secondary γ-ray background source had not been considered significant and had not been investigated in previous background studies.

The α-induced γ-ray background is more important in the SNO detector than in the Baksan laboratory due to the light water shield and the boro-silicate glass of the photomultiplier tubes. In the presence of a good neutron moderator and a strong neutron absorber such as boron, neutron capture reactions produce few high energy γ-rays, and production through $(\alpha, p\gamma)$ and $(\alpha, n\gamma)$ reactions can come to dominate the intrinsic γ-ray background from a material. This is the case for the radioactive contamination in the photomultiplier array, where α-induced γ-rays are the largest single component above an energy of 5 MeV. The γ-ray background contribution from the photomultiplier tube array is comparable with that of the surrounding rock, with each accounting for approximately half of the γ-rays above 5 MeV entering the D_2O [Sk91]. This α-induced γ-ray background source has not previously been the subject of a detailed experimental study, and its characterization is the primary goal of this study.

1.1 Components of the γ-Ray Background

The γ-ray background is primarily caused by the radioactive decay of ^{40}K and the ^{238}U and ^{232}Th chains, and subsequent decay particle induced reactions. Below 3 MeV, the background is dominated by γ-rays accompanying the radioactive α-, β-, and fission decay of these isotopes [Gl71, So73]. Above 4 MeV, the γ-ray background is dominated by neutron capture γ-rays, both from fission and (α, n) reactions, with significant contributions from the $(\alpha, n\gamma)$ and $(\alpha, p\gamma)$ reactions. The contribution of these α-induced reactions to the γ-ray background not only depends on the concentration with which ^{238}U, ^{232}Th and their decay daughters are present, but also on the composition of the materials which contain these contaminants.

The compositional dependence of the high energy γ-ray background is a result of the generation of these neutrons and γ-rays primarily through secondary (α, n) and (α, p) reactions. The probability of the emitted α-particle causing a reaction in neighbouring nuclei depends primarily on the probability of the α-particle penetrating the Coulomb barrier and reaching the nuclear surface. The α-particles in the ^{232}Th and ^{238}U chains have energies less than 8.8 MeV and so Coulomb barrier considerations suggests that elements with atomic numbers greater than 17 (Cℓ) are unlikely to undergo α-induced reactions. Since the light elements are present in many components of the detector, such as in shielding concretes and photomultiplier tube glasses, an investigation of this source of background must focus on the yields associated with these light elements.

The generation of neutrons and their subsequent capture producing γ-rays is well understood [He89, He90, Sk91, Sk94], and is known to depend on a number of additional factors, including the details of geometry and the presence of neutron absorbing elements. These high energy γ-ray are generated by the capture of neutrons on heavy nuclei such as iron, which produce γ-rays with energies up to 10 MeV [Lo81]. For rock, neutron capture γ-rays account for 70% of the background above 5 MeV [Po86]. In components of the SNO photomultiplier array, this background source is reduced substantially through non-radiative neutron capture on boron, and the $(\alpha, p\gamma)$ and $(\alpha, n\gamma)$ play a more significant role in the high energy background [Sk91].

Among the light elements, only a few possess reaction Q-values allowing highly energetic excited states in the residual nucleus. The reactions and elements likely to produce high energy γ-rays are the (α, n) reaction on ^{9}Be, ^{10}B, ^{11}B, ^{19}F, ^{23}Na, ^{25}Mg, ^{26}Mg and ^{29}Si, and the (α, p) reaction on ^{10}B, ^{11}B, ^{23}Na, ^{27}Aℓ, and ^{28}Si [Gl78, Wa88]. Each of these isotopes is found in and around low background experiments, with Aℓ, Mg and Si commonly found in bulk rock and construction materials, B, Na and Si in glasses, Be in photomultiplier tube components, and F in some plastics.

1.2 Studies of the $(\alpha, n\gamma)$ and $(\alpha, p\gamma)$ Reactions

The $(\alpha, n\gamma)$ and $(\alpha, p\gamma)$ reactions have not previously been the subject of an experimental investigation of their absolute yield. Virtually all knowledge to date on this background is derived from information provided by Pomansky based on the theoretical work of Glotov [Gl78, Po86]. Glotov used total neutron production yields published in the literature and a statistical model of the reaction mechanism to estimate the γ-ray yield from both reactions. One purpose of our study is to check these estimates and establish the accuracy of such theoretical γ-ray spectra.

Although no catalogue of the high energy γ-ray yield from the $(\alpha, n\gamma)$ and $(\alpha, p\gamma)$ reactions in light elements is available in the literature, some studies have established the thick-target yield, or an energy survey of cross sections, for some transitions of interest. Many of these studies have focussed on extracting nuclear data and nuclear structure information from experiments, such as lifetime measurements, branching ratios and level spin assignments. In some of these studies, the neutron or proton emitted in the reaction was detected and associated with the excitation of a particular level in the residual nucleus. In these studies, only the highest energy particles were detected, corresponding to the ground state and first few excited states in the residual nucleus, which frequently fall below our energy of interest.

A notable exception to this situation is found in a number of detailed studies of the ^{9}Be(α, n) reaction which produces a 4439 keV γ-ray from a population of the first excited state in ^{12}C. The extensive investigations of this reaction arose from interest in determining the extent to which the direct or compound nucleus reaction mechanisms contributed to neutron production [Kj62a, Kj62b, Se63]. The studies by Kjellman *et al* used thin targets of Be to investigate the angular correlation between the neutron and γ-ray. Neutron energies were measured using a time-of-flight technique with a plastic scintillator, while γ-rays were detected using a NaI(Tℓ) scintillator. From their measurements and those of other groups, they concluded that the direct reaction dominated the production of all neutron groups, with some small contribution from the compound reaction mechanism. In addition, they also provided several measurements of the total cross section between $E_\alpha = 10$ and 14 MeV.

Seaborn *et al* surveyed the γ-ray distribution from the ^{9}Be(α, n) reaction for α-particle energies between 3 and 10 MeV using a NaI(Tℓ) spectrometer, but reported only differential cross section measurements. Total cross sections measurements at four α-particle energies spanning a range between 7 and 10 MeV were obtained by Verbinski *et al* [Ve68] using a proton recoil liquid scintillator and pulse shape discrimination to reject γ-ray signals. Measurements at twelve angles were used in the determination of the total cross sections for three well resolved neutron groups corresponding to population of the first three levels in ^{12}C.

Perhaps the most comprehensive determination of the ^{9}Be(α, n) reaction cross section, and consequently of the cross section for populating the 4439 keV level in ^{12}C, was performed by Geiger and Van der Zwan [Va70, Ge75, Ge76]. Their studies were aimed at providing detailed cross section information for determining the neutron yield and spectrum from standard radioactive (α, n) sources as well as investigating the importance of compound nuclear processes in the reaction. Their measurements were performed using a stilbene crystal scintillator supplemented by some measurements using an organic scintillator similar to that used by Verbinski *et al.* They measured the ^{9}Be(α, n) cross sections for populating the first three levels in ^{12}C by measuring the 0° differential cross section in 0.1 MeV intervals between 1.5 and 7.8 MeV, and constructing the integrated cross section from interpolations of their own and other groups measurements of the neutron angular distribution.

Similar angular studies for both isotopes of boron have also been reported in the literature, but at energies below those of interest in this study. Gallman, Hibou and Fintz [Ga69] used a Ge(Li) detector to measure the relative intensity of γ-rays up to 4 MeV from the ^{10}B(α, p) reaction at α-particle energies between 1 and 3.5 MeV in order to study the level structure of ^{14}N. Wilson [Wi75] extended these measurements up to 8 MeV, studying both the (α, p) and (α, n) reactions using a movable silicon surface barrier detector for protons and using a high pressure gas scintillation cell filled with ^{3}He for neutrons. Wilson investigated the angular distribution of the highest energy neutron group, populating the ground state of ^{13}N, and as well the four highest energy proton groups, populating states in ^{13}C up to 4 MeV. Total cross sections were not reported in a refereed publication. Cseh *et al* [Cs83] also investigated the level structure of ^{14}N with 2.5 to 3.1 MeV α-particles through the ^{10}B(α, p) reaction by measuring the resulting γ-ray distribution with a Ge(Li) detector. Again, no total cross sections for the excited states in ^{13}C were reported.

A similar situation is also seen in the literature covering α-particle reactions with ^{11}B. The ^{11}B(α, p) reaction was studied by both Dayras, Switkowski and Tombrello [Da76] and Hou *et al* [Ho78] at energies between 1.43 and 2.94 MeV, and 4.4 and 6.7 MeV, respectively. Both studies used silicon surface barrier detectors to measure the angular distribution of protons populating the ground state of ^{14}C. The ^{11}B(α, γ_0) giant dipole resonance reaction has also been studied by several groups using NaI(Tℓ) spectrometers to map out the angular distribution. Del Bianco, Kundau and Kim [De77] measured only the 90° differential cross section for E_α between 5.74 and 17.8 MeV, while Degré *et al* determined the total cross section for the 16.5 MeV γ-ray between α-particle energies of 6.8 to 9.5 MeV from angular distribution measurements.

The low energy γ-ray yield from other light elements of concern in background assessments has been measured by several groups. Lappealainen, Anttila and Räisänen measured thick-target γ-ray yields resulting from 2.4 MeV α-particles on Li, Be, B, C, N, O, F, Na, Mg, Aℓ, and Si targets at a 55° angle to the beam using a Ge(Li) detector [La83]. Their measurements, intended for use in elemental analysis, studied only a few γ-rays up to a maximum energy of 4.6 MeV. A more extensive survey of γ-ray yields was performed by Seamster *et al* [Se84], and Dyer *et al* [Dy85] who measured α-particle induced reaction cross sections on light element isotopes of ^{20}Ne, ^{24}Mg, ^{27}Aℓ, ^{28}Si, ^{12}C, ^{14}N and ^{16}O. These cross sections, intended for use in γ-ray astronomy, were measured from α-particle energies near threshold up to 26 or 27 MeV. In these two studies, the total cross section was determined by simultaneously measuring the yield at 30.6° and 109.9° using two Ge(Li) detectors. Only the first two even terms in the Legendre polynomial expansion of the differential cross section contributed to counts in the detectors for the γ-ray multipolarities studied. The authors of these two studies measured the cross section for producing the strongest γ-rays, typically with energies up to 2 MeV.

Norman *et al* [No86] also measured γ-ray cross sections intended for use in astronomical studies from α-particles reacting with ^{19}F and ^{23}Na. In this investigation, the cross sections for several γ-rays with energies below 2 MeV were measured at 90° for α-particle energies from 4.5 to 26 MeV. Conversion of the 90° differential cross section into a total cross section relied on an interpolation of angular measurements taken at intervals over the α-particle energies.

In our study, we have measured the α-particle induced γ-ray yield for γ-rays above 2 MeV from thick targets containing Be, B, F, Na, Mg, Aℓ and Si at energies encompassing the major α-particle energies associated with the uranium and thorium decay chains. Our experimental methods are similar to those employed by Seamster [Se84] and Dyer [Dy85]. The details of our experimental measurements are presented in chapter 2, and conversion of our measurements into thick-target γ-ray yields is detailed in chapter 3. The results of these measurements are presented in chapter 5 in two forms: the first set of tables lists the thick-target yields in a form appropriate for calculations of the γ-ray backgrounds; the second set lists the γ-ray yields from individual transitions which we have used to test our theoretical nuclear reaction models.

In chapter 4, we outline theoretical calculations based on the statistical model of nuclear reactions which we used to predict the measured γ-ray spectrum. We have investigated different sources for the theoretical cross sections and decay probabilities used by this model. In addition, we have explored several simplifying approximations frequently employed in these calculations, and have assessed their effects on the calculations. In this part of our study, our goal is to determine the applicability of these calculations to light elements and the accuracy to which these calculations can predict the high energy γ-ray background.

The direct-production γ-ray background spectrum (ie excluding (n,γ) reactions) from α-particles for a number of materials in the SNO detector was constructed using the first set of tables in chapter 5 and is presented in chapter 6. Theoretical predictions for these materials are also presented and compared, and the differences in the measurement-based and theoretical spectrum are discussed. These differences are further explored using the second set of tables in chapter 5 to examine the induced population density of the residual nucleus. An understanding of these differences is important in assessing the limitations of this reaction model which has been the primary method of obtaining γ-ray spectra prior to this study, and which may be used to assess the contributions from additional elements not covered by our experimental investigation.

Chapter 2

The Experiment

Measurements of the high energy γ-ray yields were performed using the facilities at the Berkeley 88″ cyclotron. Since the primary purpose of this study was to determine the high energy γ-ray yield, self-supporting thick targets of Aℓ, Be, BN, NaF, Mg and Si were used in the measurements. Each target, except for Si, was exposed to α-particles with energies of 10.0, 8.8, 7.7, 7.0, 6.3 and 5.6 MeV. Only one measurement using 10 MeV α-particles was performed on the Si target, the weakest γ-ray source. The physical arrangement of the beam line and detector components is shown in figure 2.1.

The emitted γ-rays were detected in two HPGe detectors, denoted as detectors #1 and #2, located at 30.6° and 109.9° with respect to the incident beam direction and approximately 19 cm and 15 cm from the target, respectively. The low energy γ-ray counting rate was reduced by placing 0.95 cm lead shields directly in front of each detector. The signals from the forward angle detector were processed by an Ortec 572 amplifier, while the backward angle detector used a Canberra 2021 amplifier. In the initial 10 MeV α-particle runs, the unipolar output of each amplifier was input directly

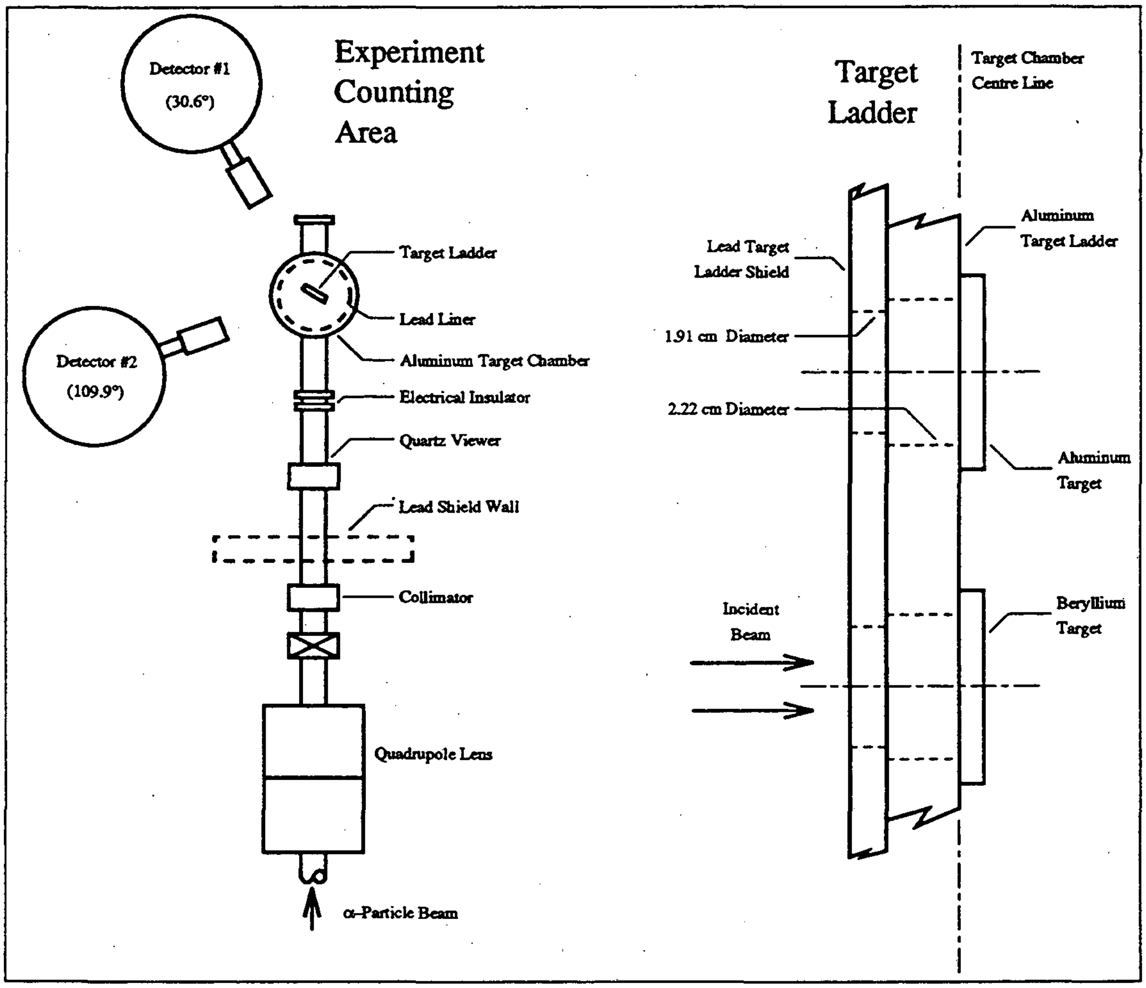

Figure 2.1: The experiment target and counting area for the γ-ray measurements. The target holder shown was positioned at a 30° angle with respect to the beam direction.

into an Ortec PC/MCA system. In subsequent α-particle runs, a low energy cutoff was implement by triggering an Ortec 442 linear gate and stretcher with an Ortec 551 timing SCA. The SCA generated a gating pulse whenever the bipolar amplifier signal exceeded an adjustable lower energy threshold. On receiving a gating signal, the linear gate and stretcher passed the delayed unipolar amplifier signal through to the MCA. This low energy cutoff is illustrated in figure 2.2. The linear gate and stretcher unit also functioned as pile-up reduction circuit by rejecting pulses occurring after the detection of a signal peak prior to the signal on the linear input dropping below the discriminator level.

The targets were attached to a 0.32 cm thick aluminum target ladder with a 2.22 cm diameter target hole. A 0.16 cm thick lead shield with corresponding 1.91 cm diameter holes protected the aluminum holder from the α-particle beam. The target ladder was rotated 30° clockwise from the beam direction to minimize the interference of the target ladder shield with γ-rays produced in the target. The current on target was measured by a beam current integrator which generated one dump count for each 1 nC of charge on target. Beam dumps were accumulated in Ortec 871 and 875 counters. Beam current leakage and secondary electron effects were minimized by collecting the beam current from the combined target ladder and target chamber. The target chamber was electrically isolated from the rest of the beam line as shown in figure 2.1. Beam currents were adjusted to maintain the detector dead times to between 15 and 25% as reported by the MCA units. All targets except for Be were exposed to currents ranging from 4 to 100 nA, while the more active Be target was

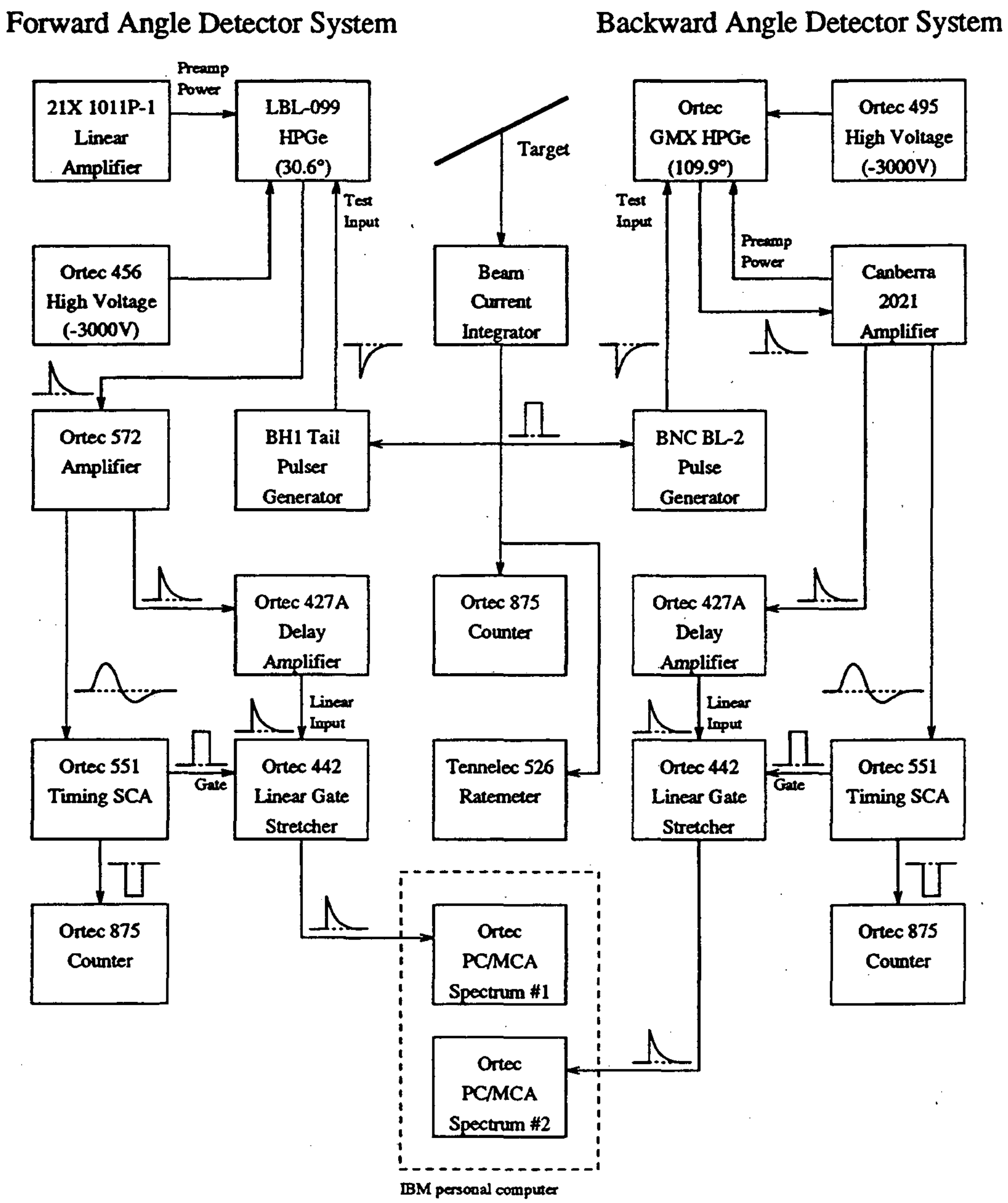

Figure 2.2: Detector counting system for the 8.8 through 5.6 MeV α-particle runs. The signal type for each component is indicated by the pictogram adjacent to the signal lines. The 10 MeV α-particle runs were recorded without the low-energy γ-ray suppression provided by the linear gate stretchers and timing SCA's. In this case, the unipolar output of the primary amplifiers (the Ortec 572 and Canberra 2021) were connected directly to the PC/MCA.

exposed to lower currents typically between 1 and 20 nA. Beam position and diameter were monitored using the quartz phosphor on the target ladder which could be viewed remotely through a camera. The beam spot diameter was estimated to be between 0.3 cm and 0.6 cm on the phosphor in each run.

Pile-up and dead time were monitored by placing a pulser signal on the test input of each detector preamp. Two pulse generators provided the pulser signals and were externally triggered by the beam current integrator. The pulser voltage was adjusted to place the pulser peak in the high energy (> 10 MeV) region of each spectrum, except during the 10 MeV runs in the forward angle detector when it was placed in the low energy portion of the spectrum. The pulser peak live time monitor was tested by taking spectra of calibration sources while a battery provided current for the beam current integrator circuit.

The absolute efficiency of the detector system was measured by a combination of sources placed in the target ladder. Spectra from calibrated sources of ^{137}Cs, ^{60}Co, ^{22}Na and ^{54}Mn were recorded both before and after the target runs. In addition, spectra from an uncalibrated ^{56}Co source placed in the target position were used to determine the energy dependence of the detector efficiencies. These spectra were also recorded before and after the target runs. A ^{238}Pu-^{13}C γ-ray source was used after the target runs to obtain a high energy γ-ray calibration point. This source, as well as the ^{60}Co and ^{137}Cs sources were then used to determine the effective thickness of the lead shielding by recording spectra from each source with the lead shielding removed.

Chapter 3

Spectrum Analysis

The goal of our analysis was to convert the peak intensities observed by the detectors into absolute γ-ray yields from particular levels in the residual nuclei and so measure the excitation of the residual nuclei. The first stage of this analysis required that a peak area be defined; this is described in section 3.1. In some cases these peaks contained interference from higher energy γ-rays due to their associated escape peaks; the removal of this interference is described in section 3.3.2. Once a peak area had been found, the absolute efficiency and live time of each detector was used to convert the area into a yield per incident α-particle. The yields from each detector were then used to determine the angular distribution of the γ-ray yield as well as the 4π γ-ray yield.

The complete set of total yields into 4π were used to calculate the excitation distribution of a residual nucleus. The direct population of each level was calculated by subtracting the cascade feeding of higher level decays using published decay schemes. A mean excitation energy was then used to characterize the dependence of the residual nucleus on the α-particle energy. This procedure is described in section 3.4.

3.1 Peak Fitting and Area Determination

The α-particle kinematics coupled with the use of thick targets in this experiment and the energy dependence of the γ-ray cross sections resulted in the observed spectrum peaks following a complex shape which could not be reliably parameterized. Instead of fitting the peak shape, the area of the peak was determined from the difference between the total number of counts in a peak region and the interpolated background area in the peak region.

3.1.1 Background and Centroid Determination

The peak backgrounds in each detector were fit using a discontinuous (stepped) second order polynomial expansion which in its most general form can be written

$$f(x) = \begin{cases} a_0 + a_1(x-\bar{x}) + a_2(x-\bar{x})^2 & x < \bar{x} \\ a_0 + a_1(x-\bar{x}) + a_2(x-\bar{x})^2 + a_3 & x \geq \bar{x}, \end{cases} \tag{3.1}$$

where $\bar{x}$ is the peak centroid, and the a_i are the fitted coefficients. Different types of background were obtained by fixing some of the a_i coefficients to zero. A total of four different forms of background were used. The two continuous forms were obtained by using only the linear, a_0 and a_1, and quadratic terms, a_0, a_1 and a_2. Two additional background types were obtained by adding a step at the centroid by including the a_3 term. Each fit used three regions to determine the background. A central peak region was used to determine the centroid and the net peak area. Lower and upper background regions were used to determine the a_i parameters, and were chosen in the closest region on either side of the peak which was free of subsidiary peaks after neighbouring escape peaks had been subtracted. The peak region was chosen as the smallest region which encompassed the entire peak.

The background was fit to the spectrum using standard linear regression to obtain values for the a_i coefficients of equation (3.1) [Ly86, Be69b], by minimizing the χ^2 of the fit defined by

$$\chi^2 = \sum_k w_k \left(y_k - f(x_k)\right)^2, \tag{3.2}$$

where y_k is the number of counts in channel x_k, w_k is the datum weight based on the uncertainty of each point, and k sums over all the channels contained in the lower and upper background regions. Coefficients were obtained by solving the matrix equation,

$$\mathcal{B} = a\alpha. \tag{3.3}$$

The column matrix $\mathcal{B}$ was calculated according to

$$\mathcal{B}_i = \sum_k \frac{y_k}{w_k} \frac{\partial f(x_k)}{\partial a_i}. \tag{3.4}$$

The elements of the square matrix α are given by the products of the derivatives of equation (3.1),

$$\alpha_{ij} = \sum_k \frac{1}{w_k} \frac{\partial f(x_k)}{\partial a_i} \frac{\partial f(x_k)}{\partial a_j}. \tag{3.5}$$

The weight, w_k, for each channel was calculated from the counting uncertainty in each channel k according to the equation,

$$w_k = 1/\left(f(x_k) + \delta z_k^2\right) \tag{3.6}$$

where the statistical uncertainty, $\sqrt{f(x_i)}$, was taken from the parent distribution, (background function) and δz_k accounted for any additional uncertainty in the counts in channel k introduced by escape peak subtractions. It has been shown by Bevington [Be69b] that a least squares regression using weights derived from the data rather than the parent distribution systematically underestimates the area of the fitted region by an amount approximately equal to the χ^2 for the fit. The iterative procedure reduces this underestimate, and provides a better determination of the background area under the peak. However, since the weight of each point depends on the background fit, the weights used to calculate the background are changed by the fit. It was thus necessary the iterate the background calculation until the coefficients converged onto stationary values.

The peak centroid was calculated from the weighted average of net positive counts above the background, m_i, in the selected peak region. The calculation used the method of moments [Ly86] to calculate the centroid $\bar{x}$ according to the equation,

$$\bar{x} = \frac{\sum\limits_i x_i m_i}{\sum\limits_i m_i}. \tag{3.7}$$

The weight m_i was calculated as

$$m_i = \begin{cases} y_i - f(x_i) & y_i > f(x_i) \\ 0 & y_i \leq f(x_i) \end{cases} \tag{3.8}$$

where x_i, y_i, and $f(x_i)$ are channel, channel counts, and background function given by equation (3.1). The variance of the distribution, $\mathcal{S}^2$, is then given by the equation,

$$\mathcal{S}^2 = \frac{\sum m_i (x_i - \bar{x})^2}{\sum m_i} \cdot \frac{n_{\text{eff}}}{n_{\text{eff}} - 1}, \tag{3.9}$$

where the effective number of counts, n_{eff} [Ly86], depends on the uncertainty δm_i of each y_i,

$$n_{\text{eff}} = \frac{(\sum m_i)^2}{\sum \delta m_i^2}. \tag{3.10}$$

In the event that δm_i is purely statistical, then $\delta m_i^2 = m_i$, and n_{eff} reduces to the expected value of $\sum m_i$. In the calculation of the centroid, δm_i includes the subtracted background uncertainty δb_i and escape peak subtraction uncertainty δz_i,

$$\delta m_i^2 = c_i + \delta b_i^2 + \delta z_i^2 \tag{3.11}$$

The variance in the centroid, $\delta \bar{x}$, is then given by the expression,

$$\delta \bar{x}^2 = \frac{S^2}{n_{\text{eff}}} = \frac{\sum m_i (x_i - \bar{x})^2}{\sum m_i} \cdot \frac{1}{n_{\text{eff}} - 1}. \tag{3.12}$$

This variance is taken as the uncertainty in the centroid determination, and is used in the calculation of the peak area uncertainty.

The a_i coefficients of equation (3.1) are defined using the peak centroid as an origin. After each fit, a new value for the peak centroid was calculated using the fitted background shape, and the fit coefficients were adjusted to reflect the new position of the origin. Since a movement of the centroid changes the peak background subtraction, the centroid calculation was iterated after the fit parameters had been transformed into the new coordinate system. These calculations were iterated until the peak centroid converged to a stationary value. Since the peak centroid only serves to define an origin for the background fit, the fit regions and hence the fit itself are unaffected by the centroid shift. For a quadratic background fit of the form of equation (3.1), the transformation of the coefficients from a_i to a_i' for a shift of the centroid from $\bar{x}$ to $\bar{x}' = \bar{x} + \Delta x$ can be shown to follow the relations

$$a_0' = a_0 + a_1 \Delta x + a_2 (\Delta x)^2 \tag{3.13}$$

$$a_1' = a_1 + 2a_3 \Delta x \tag{3.14}$$

$$a_2' = a_2. \tag{3.15}$$

These relations were used to transform the fitted coefficients into the new reference frame defined by the new centroid. The step a_3 at the centroid of a fit is unaffected by the change of coordinate system as long as the centroid does not overlap the upper and lower background regions.

3.1.2 Area Calculations

The net area under a peak is defined as the sum of the gross counts in the peak region less the counts under the background in the region. The area underneath a background function $f(x)$, described by equation (3.1), between channels x_1 and x_2 is given by the integral

$$b(x_1 : x_2) = \int_{x_1-0.5}^{x_2+0.5} f(x)\,dx \tag{3.16}$$

$$= a_0\,(x_2 - x_1 + 1) + \frac{a_1}{2}\left((x_2+0.5)^2 - (x_1-0.5)^2\right) + \frac{a_2}{3}\left[(x_2+0.5)^3 - (x_1-0.5)^3\right] + a_4\,(x_2 + 0.5 - \bar{x}), \tag{3.17}$$

where the half channel shifts account for the fit being defined in the centre of the channel. The uncertainty in this background area, δb, is due to the uncertainty in the fit parameters and is calculated from the error matrix of the fit $\varepsilon \equiv \alpha^{-1}$ according to the equation,

$$\delta b^2 = \left((\delta\bar{x}\cdot a_3)^2 + \sum_{i,j} \frac{\partial b}{\partial a_i}\,\varepsilon_{ij}\,\frac{\partial b}{\partial a_j}\right)\cdot\kappa, \tag{3.18}$$

where κ is defined in terms of the reduced χ^2, $\hat{\chi}^2$, by

$$\kappa = \begin{cases} 1, & \hat{\chi}^2 \le 1 \\ \hat{\chi}^2, & \hat{\chi}^2 > 1 \end{cases} \tag{3.19}$$

and the reduced χ^2 is defined as

$$\hat{\chi}^2 = \frac{\chi^2}{N_{free}} \tag{3.20}$$

where $N_{free} = n_{ch} - N - 1$ is the number of degrees of freedom for the fit with n_{ch} channels (data points) and N parameters varied in the background fit. The summation term in equation (3.18) accounts for the standard uncertainty from the fit. The first term accounts for the uncertainty introduced into the peak background area from the uncertainty in the centroid position. This uncertainty must be accounted for separately as the centroid is not varied in the fit. The contribution to the uncertainty in the area from the centroid was estimated by considering the effect of shifting the centroid. When the centroid is shifted, the origin of the fit is redefined, but the fit itself is not changed. Thus, a displacement of the centroid only causes a change in the position at which the background step is calculated, giving a difference in the calculated area of the shift size times the step height. This centroid uncertainty is thus incorporated into the area by treating the centroid uncertainty as a centroid shift and adding in quadrature the resultant change in area to the standard fit uncertainty area. The factor of κ simply increases the calculated uncertainty when the reduced χ^2 is greater than 1.

The total peak area was calculated by subtracting the background area from the gross counts in the reduced (escape peak subtracted) spectrum. The uncertainty in the peak area, δA, is the quadrature sum of the gross and background area uncertainties,

$$\delta A^2 = \delta b^2 + \delta A_{bkgd}^2 + \sum_i \delta y_i^2, \tag{3.21}$$

where δy_i is defined in terms of the gross channel counts c_i and the statistical uncertainty due to an escape peak subtraction δz_i according to the equation,

$$\delta y_i^2 = c_i + \delta z_i. \tag{3.22}$$

The δA_{bkgd} term represents the uncertainty in the background area due to the type of background selected, and is calculated from the differences in the background areas as described below.

For each peak, four different types of the background defined by equation (3.1) were used to calculate the area. The simplest type of background fixed the coefficients a_2 and a_3 to zero. This form of background, referred to as the "linear" background, was typically used in the determination of relatively weak peak transitions. In these cases, the statistics of the spectra were usually insufficient to generate a reliable or believable step. The next order background fit type added the a_3 step term and is referred to as the "linear + step" background. This background type was used to fit most peaks. The step portion of the background parameterization was used to model the increase in the background expected in the energy region below a full-energy peak. A "quadratic" form of the background consisting of coefficients from a_0 to a_2 was used when a significant curvature was observed in the background regions of the peaks being fitted. This usually occurred when large background regions were used, or when a low intensity peak was observed in the vicinity of a high intensity peak. The most complicated form of background used all the terms in the equation (3.1), and is referred to as the "quadratic + step" background. This background was used under similar conditions as the simple quadratic shape, when a reasonable step size was obtained.

Once a background type was selected, the remaining fit types were used to estimate a systematic uncertainty for the fitted peak area. The systematic uncertainty was calculated from a weighted sum of the squares of the differences of the net peak areas according to the equations,

$$\delta A^2_{bkgd} = \frac{\sum\limits_{i,i\neq j} w_{ij}\left(A_i - A_j\right)^2}{\sum\limits_{i,i\neq j} w_{ij}} \tag{3.23}$$

$$w_{ij} = \frac{1}{\delta b_i^{\,2} + \delta b_j^{\,2}}, \tag{3.24}$$

where j indicates the adopted fit, i sums over all fit types, b_i is the net peak area for fit type i, and δb_i is the fit uncertainty in the net area. This estimate of the systematic uncertainty provides a measure of how well the peak area is known; however, in some instances, one or more of the background fits may be non-physical in the sense of producing too large a step or a negative net area in peak region. This occurs most often when a "linear" background has been selected for the peak, and in these cases may over-estimate the systematic uncertainty.

3.1.3 Composite Peak Fitting

In a number of cases, two different γ-rays had a significant overlap of peak areas in a spectrum. In these cases, an attempt was made to separate the peaks by fitting the net peak shape to a pair of Gaussians. To ensure consistency with other area determinations, the Gaussian fits were used only to determine the ratio of the two peak areas. The individual areas, and hence the yields, were calculated by multiplying the total area by the Gaussian area ratios.

The fit to the Gaussian was calculated within the background-subtracted peak region. The two Gaussians, each defined by three coefficients, a_0 through a_2 and a_3 through a_5, combine to give the peak shape described by the equation,

$$g(x) = a_2 \exp\left[-\frac{1}{2}\left(\frac{x-a_0}{a_1}\right)^2\right] + a_5 \exp\left[-\frac{1}{2}\left(\frac{x-a_3}{a_4}\right)^2\right]. \tag{3.25}$$

This peak shape was used to determine a non-linear least squares fit to the peaks. The ratio of the peak areas, A_0 and A_1, is given by the equations

$$A_0 = \frac{a_2 a_1}{a_2 a_1 + a_5 a_4} \tag{3.26}$$

and

$$A_1 = \frac{a_5 a_4}{a_2 a_1 + a_5 a_4}, \tag{3.27}$$

with an uncertainty given by the equation,

$$\delta A_i^2 = \kappa \sum_{j=2}^{3} \sum_{k=2}^{3} \frac{\partial A_i}{\partial a_{j+3i}} \varepsilon_{jk} \frac{\partial A_i}{\partial a_{k+3i}}, \tag{3.28}$$

where ε_{jk} is the appropriate error matrix element for the Gaussian fit, and κ is again given by equation (3.19), using the reduced χ^2 for the Gaussian fit. This uncertainty in the fit was added in quadrature to the statistical uncertainty in the peak area for each transition.

3.2 Detector System Properties

There are three important properties of the detector system that must be determined in order to accurately calculate the absolute γ-ray yield. These are the absolute full-energy peak energy efficiency, the relative first and second escape peak efficiencies, and the energy calibration. The absolute full-energy peak efficiency was used directly in the conversion from peak areas into γ-rays per α-particle. The first and second escape peak efficiencies were also used in some cases to calculate the γ-ray yield, and as well were needed to remove interfering escape peaks from regions of full-energy peaks. Finally, the energy calibration affected both the peak identification and the calculation of the peak yield, as well as the escape peak subtractions. The peak efficiencies were determined using a combination of calibrated sources and a Monte Carlo model of the detector system. This process is discussed in section 3.2.1. The energy calibration of each detector was determined by a series of successive approximations; this procedure is discussed in section 3.2.2.

3.2.1 Detector Efficiencies

The absolute full energy peak efficiency of each detector was determined using a combination of calibrated sources, uncalibrated sources and Monte Carlo calculations. We utilized a series of Monte Carlo calculations to characterize the functional form of the efficiencies of each detector between 500 keV and 10 MeV. These efficiencies were also used to supplement the high energy efficiency data where few γ-ray source measurements were made. In order to do this, the γ-ray sources were used to determine a scaling factor for the Monte Carlo results. The scale factor was primarily determined from the ^{56}Co source which provided energy calibrations up to 3.6 MeV and a calibrated ^{238}Pu-^{13}C source. The ^{56}Co source was calibrated using a number of low energy standard sources.

The relative escape peak efficiencies were measured in a similar manner. Both calibrated and uncalibrated sources were used to determine the ratio of the escape peak to the full energy peak areas. The use of area ratios eliminated the dependence of these efficiencies on the source strength, and also allowed the use of data from the target runs. The relative escape efficiency line shape was defined from a Monte Carlo model of the detectors, and was scaled to the source and run data.

The peak areas and uncertainties were determined by the methods described in section 3.1. The areas were directly converted into efficiency measurements using the know source strengths and relative γ-ray intensities. Multiple measurements of the detector efficiency e at a given γ-ray energy were combined into a reduced data set before a fit was calculated. The data were combined according to the equation [Ly86],

$$e = \sum_i e_i / \left(\delta e_i^{(stat)}\right)^2 \tag{3.29}$$

$$\frac{1}{\left(\delta e^{(stat)}\right)^2} = \sum_i \frac{1}{\delta e_i^{(stat)}} \tag{3.30}$$

$$\delta e^2 = \left(\delta e^{(stat)}\right)^2 + \left(\delta e^{(sys)}\right)^2 \tag{3.31}$$

where $\delta e^{(stat)}$ is the total statistical uncertainty in the efficiency, including the statistical uncertainty from the peak area and the uncertainty based on the background function selected for the peak, and $\delta e^{(sys)}$ is the systematic uncertainty in the efficiency due to the uncertainties in the calibrated source strength. In the case of relative escape efficiencies, this systematic uncertainty cancels, and so $\delta e^{(sys)}$ is treated as zero.

The low energy calibrated sources were used to obtain a polynomial fit of the efficiency between 500 and 1500 keV. The least-squares fit was based on an expansion using the Chebyshev polynomials in order to minimize the coupling between the different order coefficients. A fourth order fit to the calibrated data was used to determine the strength of the ^{56}Co source by scaling the low energy γ-ray efficiencies to the fitted line.

A scaling factor $a_\circ$ for any function $f(x)$ was calculated by minimizing the one-dimensional χ^2 defined by the equation,

$$\begin{aligned}
\chi^2 &= \sum_i w_i \left(a_\circ f(x_i) - y_i\right)^2 && (3.32)\\
&= a_\circ^2 \sum_i w_i f^2(x_i) - 2a_\circ \sum_i w_i y_i f(x_i) + \sum_i w_i y_i^2 && (3.33)
\end{aligned}$$

where the weight for each point, w_i, was calculated from the total area uncertainty added in quadrature, δA_i of equation (3.21), and the functional fit uncertainty from the error matrix ε according to the equation

$$\begin{aligned}
w_i &= \left[\delta A_i^2 + \left(\frac{y_i}{f(x_i)}\right)^2 \sum_{jk} \frac{\partial f(x_i)}{\partial a_j} \varepsilon_{jk} \frac{\partial f(x_i)}{\partial a_k}\right]^{-1}. && (3.34)\\
& && (3.35)
\end{aligned}$$

The minimization of the χ^2 with respect to $a_\circ$ yields a value for $a_\circ$ and its uncertainty, $\delta a_\circ$, given by

$$\begin{aligned}
a_\circ &= \frac{\sum_i w_i y_i f(x_i)}{\sum_i w_i f^2(x_i)} && (3.36)\\
\delta a_\circ^2 &= 2\kappa \left(\frac{\partial^2 \chi^2}{\partial a_\circ^2}\right)^{-1} && (3.37)\\
&= \kappa \left(\sum_i w_i f^2(x_i)\right)^{-1}, && (3.38)
\end{aligned}$$

where κ is defined as in equation (3.19) with the number of degrees of freedom, N_{free}, determined by the number of efficiency data points, n_e, by

$$N_{free} = n_e - 2. \tag{3.39}$$

In the calculation of w_i, the value $y_i/f(x_i)$ is used as a "local" scaling factor for the functional uncertainties, since the value of a_o is not known during the calculation of the sums.

The determination of the ^{56}Co source strength extended the efficiency measurements up to a γ-ray energy of 3.6 MeV, while the ^{238}Pu-^{13}C calibrated source provided a measurement at 6.13 MeV. These measurements alone did not provide a sufficiently accurate measurement of the efficiency over the entire energy range of interest, with uncertainties rapidly increasing above $E_\gamma = 7$ MeV.

The uncertainty in the high energy efficiency was reduced by supplementing the source measurements with Monte Carlo generated efficiencies, and so constraining the fits with the known γ-ray interaction cross sections. The physical dimensions and geometry used in the simulation are given in table 3.1 and figure 3.1; these dimensions and geometries were derived from x-ray measurements of the LBL detector, and from the Ortec technical drawings. An accurate measurement of the thickness of the lead shield in front of each detector was determined by γ-ray attenuation measurements using the ^{137}Cs, ^{60}Co and ^{238}Pu-^{13}C sources. These measurements provided a more accurate determination of the thickness by averaging over surface variations and irregularities in the shield. All other dimensions were determined from measurements taken at the experiment site.

Table 3.1: Detector Geometry for EGS4 Simulation .

Parameter	Detector #1 (cm)	Detector #2 (cm)
Source to Detector Face (L_T)	18.98	15.33
Outer Reaction Chamber Diameter (D_C)	15.26	15.26
Reaction Chamber Thickness (T_C)	0.3175	0.3175
Lead Chamber Liner Thickness (T_L)	0.1588	0.1588
Lead Attenuator width (W_S)	8.89	7.62
Lead Attenuator height	8.89	7.62
Lead Attenuator thickness (T_S)	1.025†	1.006†
Detector Canister Diameter (D_V)	6.99	6.95
Detector Canister Thickness (T_V)	0.15	0.127
Beryllium Window Thickness (T_W)	0.0051	0.05
Beryllium Window Diameter (D_W)	2.223	5.715
Thermal Barrier to Window Distance (L_B)	0.00178	0.0025
Thermal Barrier Thickness (T_B)	0.2	0.2
Germanium Crystal to Window Distance (L_{CF})	0.5	0.5
Germanium Crystal Diameter (D_{CO})	5.09	5.20
Germanium Crystal Length (L_C)	5.40	5.70
Germanium Crystal Core Diameter (D_{CI})	1.0	1.0
Germanium Crystal Core Depth (L_{CC})	4.57	4.95
Outer Surface Dead Layer Thickness (T_{CS})	3.0×10^{-5}	3.0×10^{-5}
Inner Core Dead Layer Thickness (T_{CC})	0.1	0.1

† Derived from experimental measurements of shielded and bare detector efficiencies

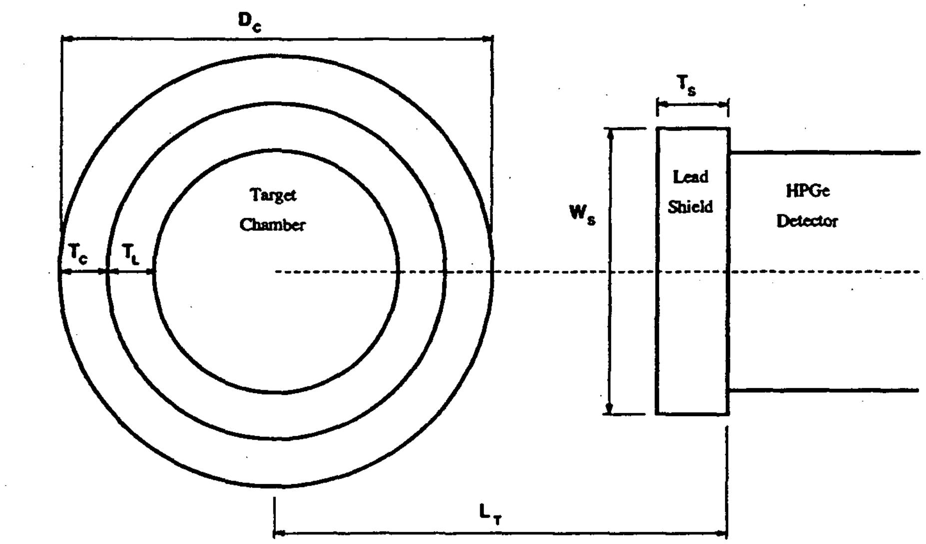

HPGe Detector:

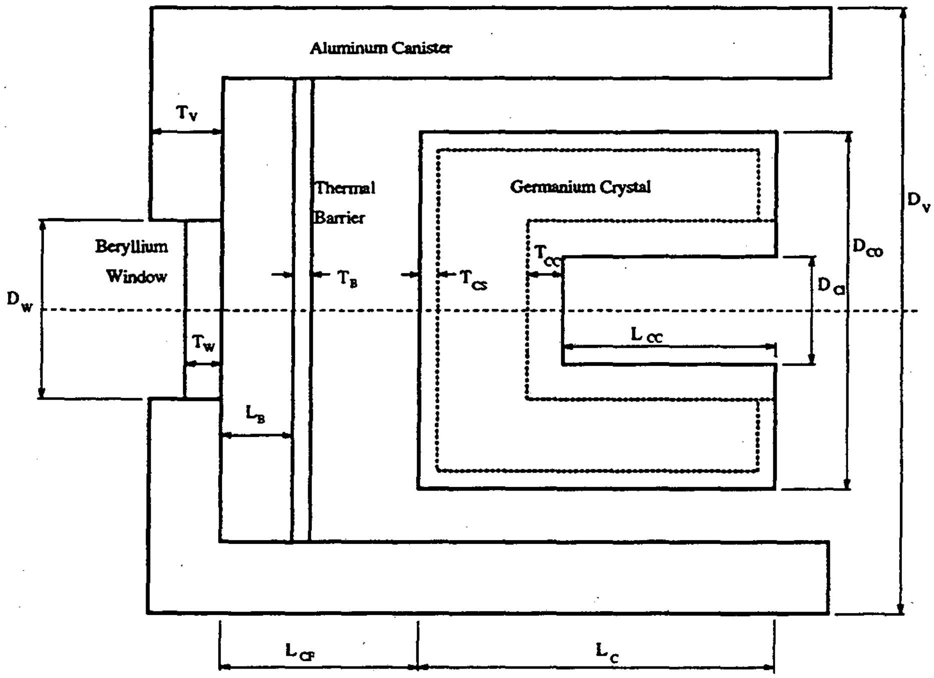

Figure 3.1: Geometry for EGS4 model of detector system. Dimensions for the detectors are given in Table 3.1.

The Monte Carlo data was combined with the source measurement data by first fitting the source data to a general equation for the absolute efficiency,

$$e_0 = \frac{\exp\left[\sum_{i=0}^{2} a_{i+2} T_i(E)\right]}{1 + \exp\left[\frac{E - a_0}{a_1}\right]} \tag{3.40}$$

where $T_i(E)$ is the appropriate Chebyshev polynomial. An equation of this form was found to provide a good fit to all the data over a range from 500 keV to 10 MeV. This fit of the experimental source measurements was used to determine a scaling factor for the Monte Carlo results according to equation (3.36). Source data above 2000 keV was used in this calculation, as uncertainties in modelling dead regions of the detector caused difficulties in obtaining the exact form of the efficiency maximum near 600 keV. The sensitivity of the scale factor to the 2000 keV cut was estimated by varying the cut between 1500 keV and 3000 keV. The calculated scale factor varied by approximately 5% for this range of cuts, and showed deviations of up to 15% from the measured 6130 keV calibration value. Based on this, an additional uncertainty of 15% was adopted for this scale factor, and applied to the Monte Carlo data above 4 MeV. This data was then combined with the source calibration data set and fit to equation (3.40). The coefficients obtained from the fit are given in table 3.2 and the resulting efficiency curve is shown in figure 3.2. The individual γ-ray efficiencies are indicated by the open circle, and the central curve indicates the fit results, while the 1σ range of the uncertainty using the fit error matrix is given by the lighter bracketing curves.

The Monte Carlo simulation was used to establish the form of the single and double escape relative efficiency curves in both detectors. The Monte Carlo results

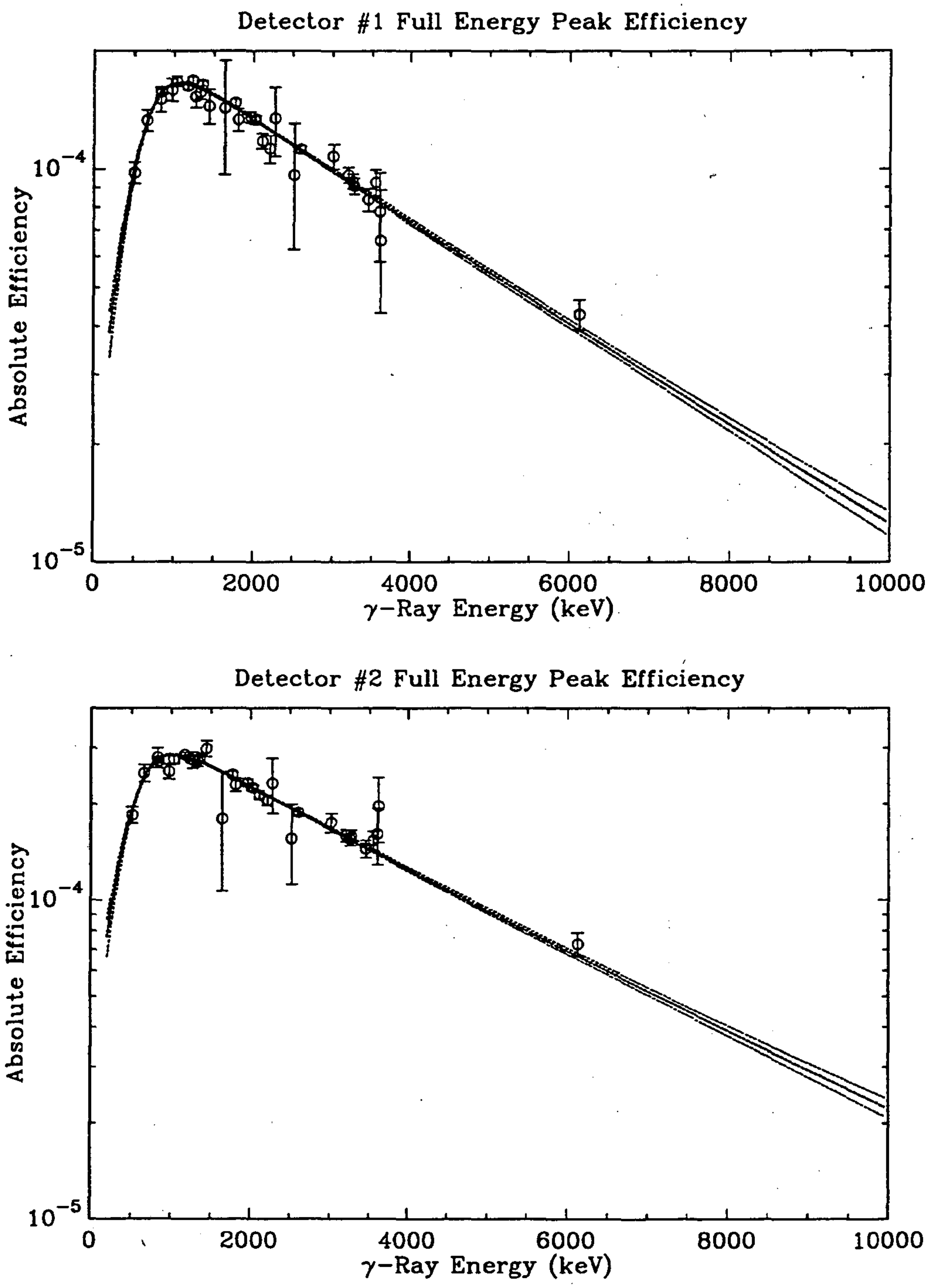

Figure 3.2: Absolute full energy peak efficiencies for detectors #1 and #2. The efficiency curves for both detectors were determined from a least-squares fit of calibration sources supplement with Monte Carlo results above 4 MeV.

Table 3.2: Absolute Full Energy Peak Efficiency

	Detector #1	Detector #2
$\hat{\chi}^2$	0.544	0.556
a_0	531 ± 13 keV	484 ± 13 keV
a_1	206 ± 16 keV	200 ± 17 keV
a_2	-8.316 ± 0.034	-7.780 ± 0.032
a_3	$(-3.03 \pm 0.21)10^{-4}$ keV^{-1}	$(-3.09 \pm 0.20)10^{-4}$ keV^{-1}
a_4	$(2.97 \pm 11.4)10^{-10}$ keV^{-2}	$(7.86 \pm 10.8)10^{-10}$ keV^{-2}

Table 3.3: First Escape Peak Efficiency

	Detector #1	Detector #2
Scale Factor	100.3±0.01%	100.4±0.8%
a_0 (keV)^0	0.082±0.027	0.11±0.02
a_1 (keV)^1	$(-1.75 \pm 0.33)10^{-4}$	$(-2.03 \pm 0.27)10^{-4}$
a_2 (keV)^2	$(4.91 \pm 0.69)10^{-8}$	$(5.39 \pm 0.56)10^{-8}$
a_3 (keV)^3	$(-2.13 \pm 0.57)10^{-12}$	$(-2.49 \pm 0.45)10^{-12}$
a_4 (keV)^4	$(3.24 \pm 1.54)10^{-17}$	$(3.99 \pm 1.22)10^{-17}$

above the pair creation threshold were fit to a fourth order polynomial as a function of the full energy peak energy, which was then scaled to the experimental data above 1200 keV using equation (3.36). Since only relative peak intensities were required in this calculation, data selected from the target runs were also used to extend the data into a higher energy region than was available through the use of standard sources alone. The Monte Carlo fit to the single escape efficiency in both detectors required no scaling within uncertainty, while the fit to the double escape efficiency was reduced by 2% to 3% in each detector. The resulting efficiency curves are shown in figures 3.3 and 3.4. The circles on this plot indicate calibration source data, while the squares indicate escape peaks taken from the target run data. The absolute efficiency for an escape peak of order k is easily calculated from a product of the absolute and relative

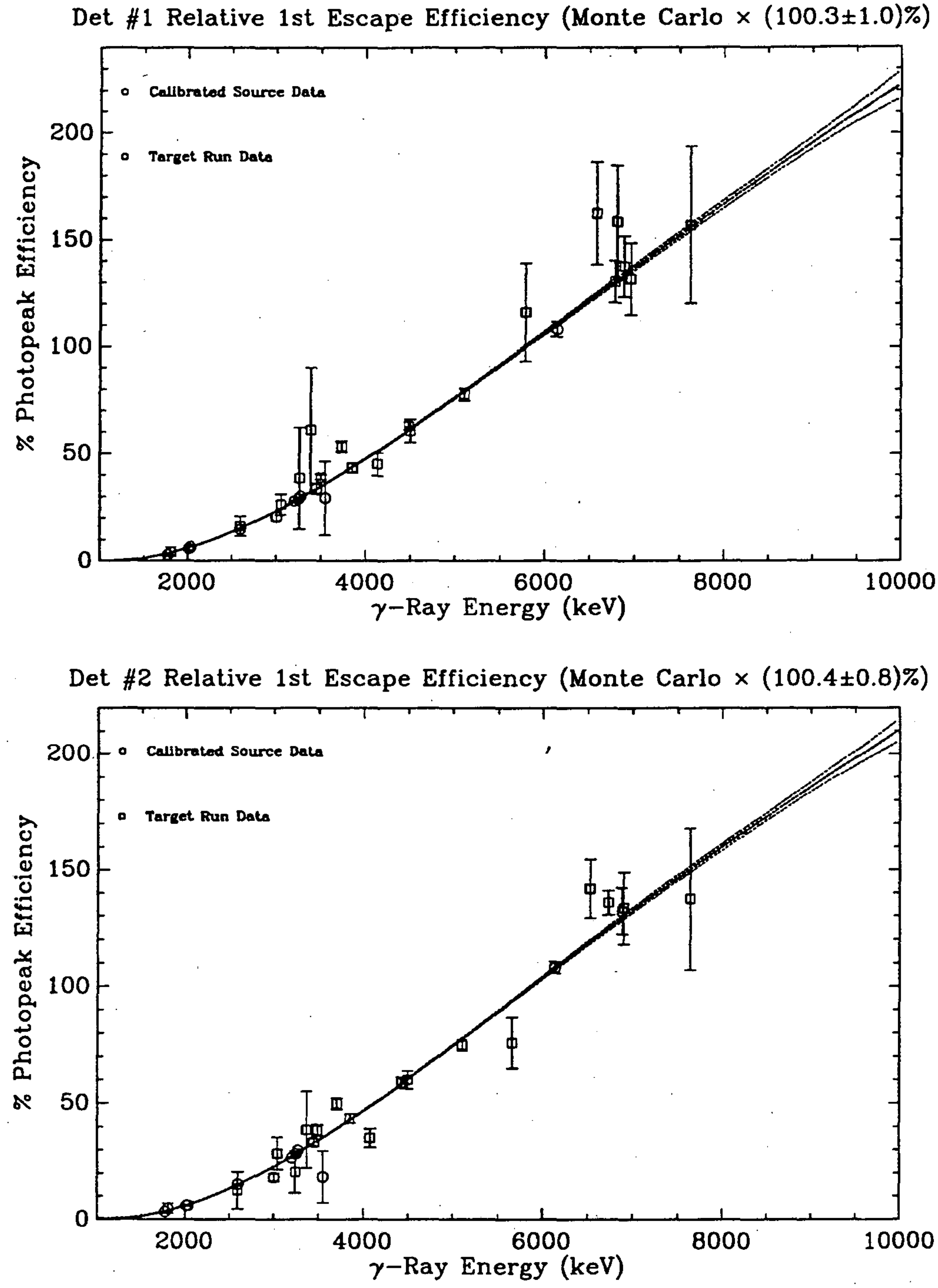

Figure 3.3: First Escape Peak Efficiencies. The curve shows the escape efficiencies and uncertainties for the two detectors as determined by the Monte Carlo simulation. The efficiencies have been scaled to match the first escape peak efficiencies determined by the calibration sources ("○") and by selected peaks from the target runs ("□").

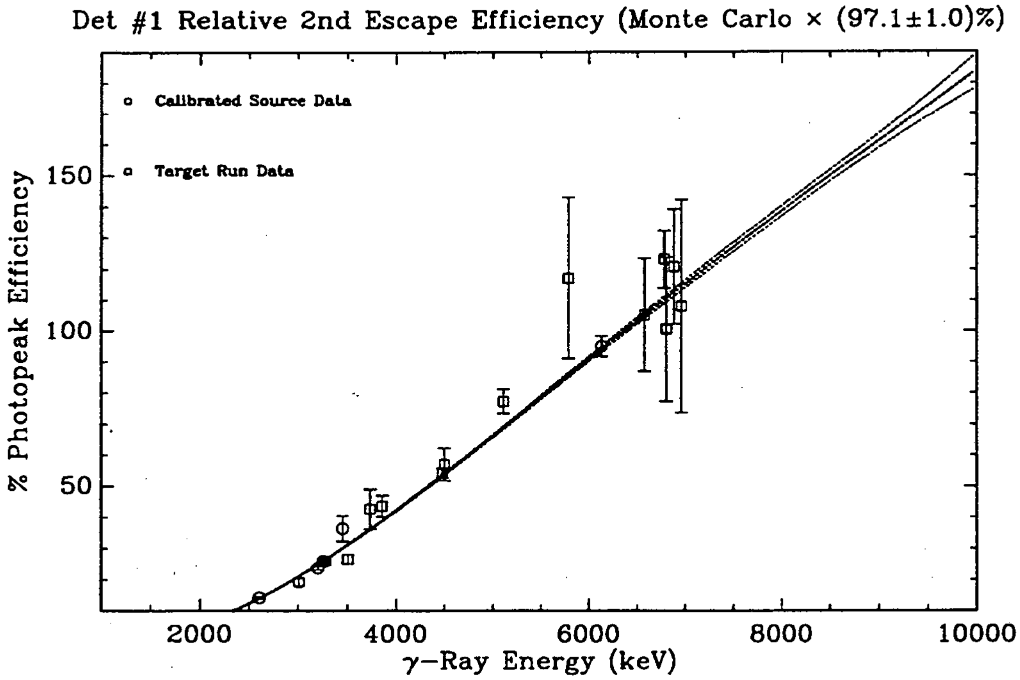

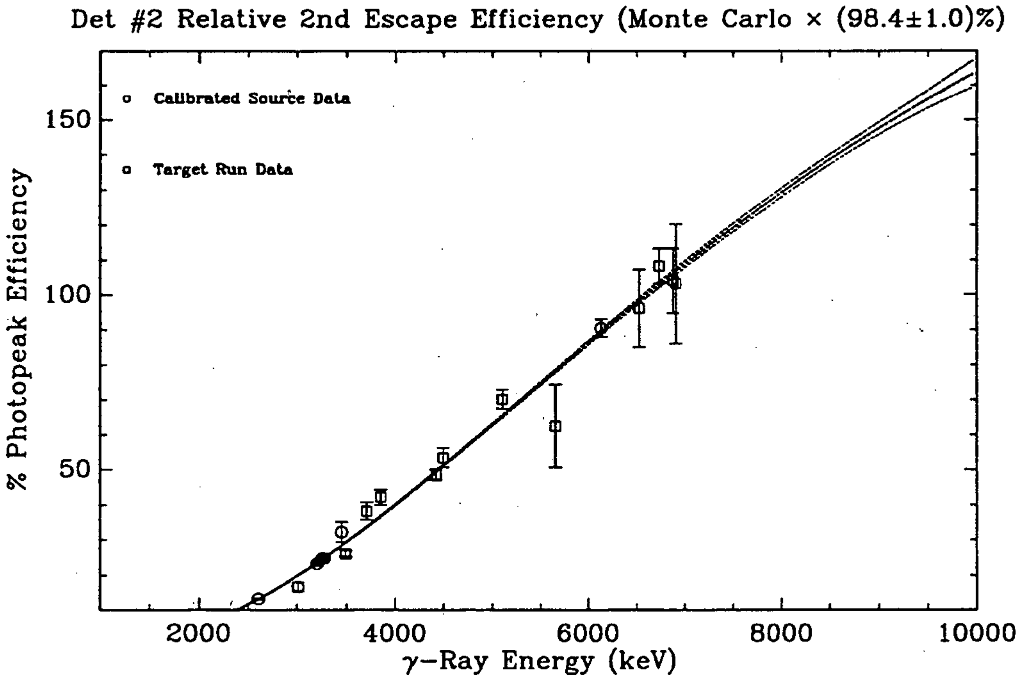

Figure 3.4: Second Escape Peak Efficiencies. The curve shows the escape efficiencies and uncertainties for the two detectors as determined by the Monte Carlo simulation. The efficiencies have been scaled to match the second escape peak efficiencies determined by the calibration sources ("○") and by selected peaks from the target runs ("□").

Table 3.4: Second Escape Peak Efficiency

	Detector #1	Detector #2
Scale Factor	97.1±1.0%	98.4±1.0%
a_0 (keV)^0	0.077 ± 0.024	0.081 ± 0.020
a_1 (keV)^1	$(-1.67 \pm 0.31)10^{-4}$	$(-1.64 \pm 0.25)10^{-4}$
a_2 (keV)^2	$(4.85 \pm 0.64)10^{-8}$	$(4.59 \pm 0.50)10^{-8}$
a_3 (keV)^3	$(-2.38 \pm 0.52)10^{-12}$	$(-2.17 \pm 0.41)10^{-12}$
a_4 (keV)^4	$(4.14 \pm 1.41)10^{-17}$	$(3.42 \pm 1.09)10^{-17}$

efficiency, $\hat{e_k}$ according to the relation

$$e_k(E_\gamma - k \cdot 511.03 \text{ keV}) = e_0(E_\gamma) \cdot \hat{e}_k(E_\gamma). \tag{3.41}$$

3.2.2 Spectrum Energy Recalibration

Gain shifts in the detector system over the course of the experiment necessitated a recalculation of the calibration of each spectrum. This entailed a two step process in which each step produced a more refined energy calibration for the spectra. The initial part of the procedure used the peak energy of positively identified transitions to determine the energy calibration. The centroids of the peaks were fit using linear regression to a straight line. This recalibration allowed the majority of the peaks to be positively identified. The next refinement to the calibration used cleanly identified peaks and escapes to determine the most accurate calibration. The details of this calculation are described below.

In the first step, a number of conditions were placed on the peaks used to recalibrate each spectrum. First, the peaks had to be uniquely identified, and the Doppler-shift of the peaks had to be known. This meant that peaks with a small Doppler shift had to be used, and also that the peak had to be well separated from adjacent peaks. Since thick targets were used in the experiment, peaks with a negligible Doppler shift could be identified by their narrow width, which was typically ~ 4 keV FWHM. In a number of cases, an insufficient number of narrow peaks were available in the detector #2 spectrum. For these spectra, Doppler shifted peaks were used in the recalibration. The energy of the Doppler shifted peak centroid was obtained by first calculating the energy of the corresponding peak in the recalibrated detector #1 spectrum, and expressing the peak energy as a percentage of the maximum Doppler for that detector angle and α-particle energy. The maximum Doppler shift, ΔE_{max}, is defined as the difference between the transition energy E_γ and the maximum Doppler shifted energy E'_{max}, $\Delta E_{max} = E'_{max} - E_\gamma$ and is given by the equations,

$$\begin{aligned} \Delta E_{max} &= E_\gamma \left(\frac{\sqrt{1-\beta_{max}^2}}{1-\beta_{max}\cos\theta} - 1 \right) && (3.42) \\ \beta &= \frac{v'_{max}}{c} = \frac{\sqrt{2E_\alpha m_\alpha}}{c(m_\alpha + M)}, && (3.43) \end{aligned}$$

where E_γ is the energy of the γ-ray transition, θ is the angle of the observing detector, and v'_{max} is the velocity of the compound nucleus after the absorption of an α-particle of energy E_α and mass m_α onto a target nucleus of mass M. It was assumed that the peak centroid in detector #2 experienced the same percentage of the maximum Doppler shift, and this energy was used to calculate the centroid energy of the γ-ray in the detector. As the Doppler shift energy range observed in detector #2 were significantly smaller than those in detector #1, the energies of the centroids in detector #2 could be accurately determined. These γ-ray energies were fit to a straight line as a function of channel number for each detector. Typically 6 to 12 peaks spread over 2 to 4 MeV were use in the first stage of the recalibration.

The calibration determined from the above procedure was then used to obtain better peak transition identifications and escape subtracted ("reduced") spectra. These reduced spectra were used to refine the energy calibration using positively identified escape peaks in the spectra. Typically 2 to 6 sets of transitions containing both full-energy peaks and escape peaks were identified above 4 MeV. Poorly known peaks were discarded from the calculation using a cut criterion based on the peak area uncertainty. Initially, any peak with an uncertainty exceeding 25% of the net area was removed from the calculation; however if a sufficient number of escape peaks could not be obtained, this cut criterion was relaxed to 40%. The calibration in each detector n, s_n, was calculated from a weighted average of the centroid separation according to the equations,

$$s_n = \frac{\sum_i \sum_{j=0}^{2} \sum_{k=j+1}^{2} w_{nijk} \left(\bar{x}_{nij} - \bar{x}_{nik} \right) \cdot 511.003 \, (j-k)}{\sum_i \sum_{j=0}^{2} \sum_{k=j+1}^{2} w_{nijk}} \tag{3.44}$$

$$w_{nijk} = \frac{1}{\delta \bar{x}_{nij}{}^2 + \delta \bar{x}_{nik}{}^2} \tag{3.45}$$

where i sums over the set of transitions used in the calculation, j and k sum over the escape order for each transition (full energy peak = 0, first escape = 1 and second escape = 2), and where $\bar{x}_{nij}$ and $\delta \bar{x}_{nij}$ are the centroid channel and uncertainty of the jth order escape peak for the ith transition in detector n. After a new slope had been obtained, a new escape peak subtracted spectrum was calculated for each detector, and the calculation was iterated until the dispersion s_n converged on a stationary value. This iteration was required because a change in the energy dispersion changes the calculated escape subtraction, and therefore the reduced spectra, enough to significantly affect the dispersion calculation. In some cases it was necessary to adjust the peak ranges between iterations to get a valid fitting range for the peaks used in the calibration.

The zero intercept of the energy calibration was then calculated by selecting uniquely identified peaks and selecting a value of the intercept so that the Doppler shift for each γ-ray was the same fraction of the full Doppler shift given by equation (3.42) for each detector. The zero intercept calculation begins by considering the mean observed Doppler shifted energy of a γ-ray, E', observed by a detector at an angle θ, which to first order is given by the equation,

$$E' = E_\gamma \frac{\sqrt{1-\beta^2}}{1-\beta\cos\theta} \tag{3.46}$$

$$\simeq \frac{E_\gamma}{1-\beta\cos\theta} \tag{3.47}$$

$$\simeq E_\gamma (1+\beta\cos\theta)\,. \tag{3.48}$$

The value of β in this equation is not treated as the maximum possible value, but instead is treated as a constant between 0 and β_{max} for the escape orders of each transition. Now, for two observations of the same γ-ray at angles θ_1 and θ_2,

$$E'_1 + E'_2 = 2E_\gamma + E_\gamma\beta(\cos\theta_1 + \cos\theta_2) \tag{3.49}$$

$$E'_1 - E'_2 = E_\gamma\beta(\cos\theta_1 - \cos\theta_2) \tag{3.50}$$

$$\tag{3.51}$$

which combined to eliminate the velocity dependency (β) gives,

$$2E_\gamma = E'_1 + E'_2 - \mu(E'_1 - E'_2) \tag{3.52}$$

$$= E_1'(1-\mu) + E_2(1+\mu), \tag{3.53}$$

where

$$\mu = \frac{\cos\theta_1 + \cos\theta_2}{\cos\theta_1 - \cos\theta_2}. \tag{3.54}$$

Calculating a linear regression over a number of transitions i with peak centroid energy $E_{\gamma i}$, the χ^2 is then defined as

$$\chi^2 = \sum_i \frac{(\Delta(2E_{\gamma i}))^2}{(\delta(2E_{\gamma i}))^2} \tag{3.55}$$

where

$$\begin{aligned}(\delta(2E_{\gamma i}))^2 &= [\delta E_{1i}'(1-\mu)]^2 + [\delta E_{2i}'(1+\mu)]^2, & (3.56)\\ \Delta 2E_{\gamma i} &= E_{1i}'(1-\mu) + E_{2i}(1+\mu) - 2E_{\gamma i}. & (3.57)\end{aligned}$$

Expressing the peak centroid energy for the transition i in terms of the spectrum calibration for detector n,

$$E_{ni}' = t_n + s_n\bar{x}_{ni}, \tag{3.58}$$

the χ^2 takes the form,

$$\begin{aligned}\chi^2 &= \sum_i \frac{1}{[(1-\mu)s_1\delta\bar{x}_{1i}]^2 + [(1+\mu)s_2\delta\bar{x}_{2i}]^2}\cdot[(1-\mu)t_1\\ &\quad + (1+\mu)t_2 + (1-\mu)s_1\bar{x}_{1i} + (1+\mu)s_2\bar{x}_{2i}]^2 & (3.59)\\ &= \sum_i w_i[\nu + (1-\mu)s_1\bar{x}_{1i} + (1+\mu)s_2\bar{x}_{2i}]^2 & (3.60)\end{aligned}$$

where,

$$\begin{aligned}w_i &= \frac{1}{[(1-\mu)s_1\delta\bar{x}_{1i}]^2 + [(1+\mu)s_2\delta\bar{x}_{2i}]^2} & (3.61)\\ \nu &= (1-\mu)t_1 + (1+\mu)t_2. & (3.62)\end{aligned}$$

Minimizing the χ^2 with respect to ν,

$$\frac{\partial \chi^2}{\partial \nu} = \sum_i w_i 2\left[\nu + (1-\mu)\, s_1 \bar{x}_{1i} + (1+\mu)\, s_2 \bar{x}_{2i} - 2E_{\gamma i}\right], \tag{3.63}$$

which when set to zero yields a value for ν of

$$\nu = \frac{2\sum_i w_i E_{\gamma i} - (1-\mu)\sum_i w_i s_1 \bar{x}_{1i} - (1+\mu)\sum_i w_i s_2 \bar{x}_{2i}}{\sum_i w_i}. \tag{3.64}$$

The spectrum offsets t_1 and t_2 are related to a calculated value of ν by equation (3.62). A maximum valid physical range was calculated by restricting t_1 and t_2 to values which placed the centroid of each peak, within uncertainty, between the maximum and minimum Doppler shift energy range. This typically determined the energy calibration to within 10 keV (approximately 2 channels in a 2k spectrum). A value for t_1 (and so t_2 through equation (3.62)) was selected which minimized the overall Doppler shift in both detectors. This step was repeated several times to ensure the convergence of the calibration.

3.3 Spectrum Analysis and Yield Calculation

3.3.1 Peak Selection

Once the energy calibration for each detector spectrum had been adjusted, a search for transitions was performed. This was done by marking out regions in the spectra corresponding to the maximum possible range permitted according to the Doppler shift of each kinematically allowed transition. A valid transition consisted of the presence of a peak in each spectrum in its kinematically allowed region. The paired peaks used the same type of background fit, and in cases of overlapping composite peaks, the peaks in both spectra were fit to double Gaussians. In many cases peaks within the spectra were consistent with more than one transition, and as a result were assigned multiple identifications.

The peak area was calculated according to the method discussed in section 3.1. The upper and lower background regions of the peak were chosen so that they were free of interference from other transitions. In some cases it was necessary to select background regions which bracketed more than one peak; in such instances, the same background was used to analyze each contained peak unless this created an unphysically large step in the peak background. In all cases, the peak region, used to determine the area, was selected to include as little of the background regions as possible.

3.3.2 Spectrum Reduction

In many instances, escape peaks from higher energy transitions interfered with the background and area calculations for full-energy peaks of lower energy transitions. This interference was accounted for by either separating the peaks through a fit to a composite curve as described in section 3.1.3, or by removing the escape peak through a subtraction process. The escape peak subtraction proceeded by first calculating the escape intensity of a given escape peak using the centroid of the full-energy peak. Then a channel subtraction value, c_{ijk}, was calculated from each channel in the full-energy peak range, and this subtraction was applied to the escape peak region. The contribution of a full-energy peak i to an escape of order j due to y_k counts in channel

x_k is denoted by c_{ijk} and is given by the equation,

$$c_{ijk} = \hat{e}_{ij}\left(y_k - f_i(x_k)\right) \tag{3.65}$$

$$\delta c_{ijk} = \hat{e}_{ij}\sqrt{\delta {y_k}^2 + (\delta f_i(x_k))^2} \tag{3.66}$$

where $\hat{e}_{ij}$ is the relative escape efficiency of the full energy peak centroid and $f_i(x_k)$ is the full-energy peak background in channel x_k as described by equation (3.1). The uncertainty $\delta f_i(x_k)$ was calculated according to equation (3.18) for integration over a single channel. In cases where the full-energy peak was part of a composite peak itself, the value y_k was reduced by the strength attributed to the partner Gaussian, and the uncertainty δy_k was increased according to the uncertainty in the partner Gaussian fit.

In general, the escape contribution calculated from one channel of the full energy peak corresponds to two channels in the escape peak. For a j order escape peak with the corresponding position x in the escape region $j \times 511$ keV below channel x_k bracketed by spectrum channels l and $l+1$, the reduced count y'_l and y'_{l+1} for the spectrum channels are given by the equations,

$$y'_l = y_l - c_{ijk}(l+1-x) \tag{3.67}$$

$$(\delta y'_l)^2 = \delta y_l^2 + \delta z_l^2 \tag{3.68}$$

$$= (\delta y_l)^2 + (l+1-x)\,(\delta c_{ijk})^2 + (l+1-x)\,(c_{ijk} \cdot \delta\hat{e}_{ij}/\hat{e}_{ij})^2 \tag{3.69}$$

$$y'_{l+1} = y_{l+1} - c_{ijk}(l-x) \tag{3.70}$$

$$\left(\delta y'_{l+1}\right)^2 = \delta y_{l+1}^2 + \delta z_{l+1}^2 \tag{3.71}$$

$$= (\delta y_{l+1})^2 + (l-x)\,(\delta c_{ijk})^2 + (l-x)\,(c_{ijk} \cdot \delta\hat{e}_{ij}/\hat{e}_{ij})^2, \tag{3.72}$$

where $\delta \hat{e}_{ij}$ is the uncertainty of the relative escape efficiency based on the error matrix of the fit, and δz is the additional uncertainty in the channel referred to in equation (3.22).

3.3.3 Sample Spectrum Fits

Examples of the different fits used in the area calculation fit are provided in figures 3.5 through 3.7. In each of these figures, both the transitions assigned to the peak and the subtracted escapes are listed above the spectrum plot. Each transition has been assigned a number which corresponds to a Doppler-shift range marker plotted beneath each spectrum. These Doppler-shift range markers show the kinematically allowed energy range of each γ-ray transition, corresponding to the maximum α-particle energy and the detector position. In detector #1 the Doppler-shift range covered an energy region typically 30 to 60 keV above the transition energy, while in detector #2 the range spanned a region approximately half this size below the transition energy. The recoil of the residual nucleus following the emission of a particle was not considered in calculating this range.

In each figure the unadjusted spectrum is shown by the dotted line, while the open circles and associated error bars indicate the escape-subtracted spectrum and uncertainty, respectively. The results of the background fit are shown by the thick continuous line beneath each peak. The regions involved in determining this background are indicated by the set of bracketed regions: square brackets ("[ ]") indicate range of the the upper and lower background regions, while the brace brackets ("{ }")

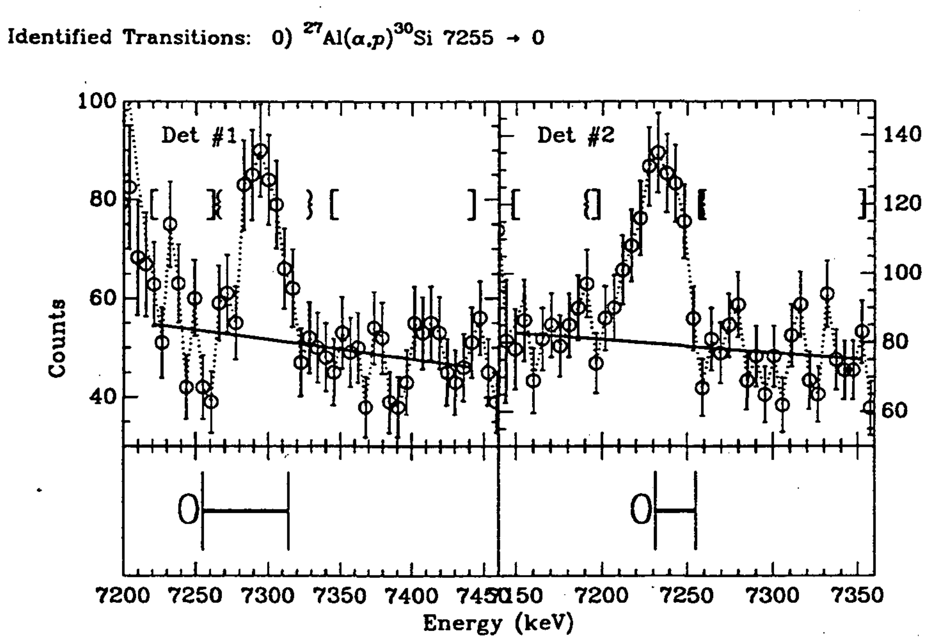

Figure 3.5: The 7255 keV peak from 10 MeV α-particles on Aℓ

indicate the peak area and centroid region. The lower part of each figure shows the Doppler-shift range of the identified transitions and subtracted escape peaks in the background regions. The Doppler-shift range of the identified peaks are indicated by a thick continuous line, while the regions of subtracted escape peaks use a thinner broken line.

The 7255 keV transition from the Aℓ target, shown in figure 3.5, illustrates the conditions under which a simple linear background was used in the area determination. The linear background was usually employed in regions of the spectrum which contained on the order of a few hundred counts per channel. In the case shown here, the backgrounds to either side of the peaks show a random fluctuation on the order of the statistical uncertainty which is also of the same order as the expected step in the background. This results in a step size which is highly dependent on the exact back-

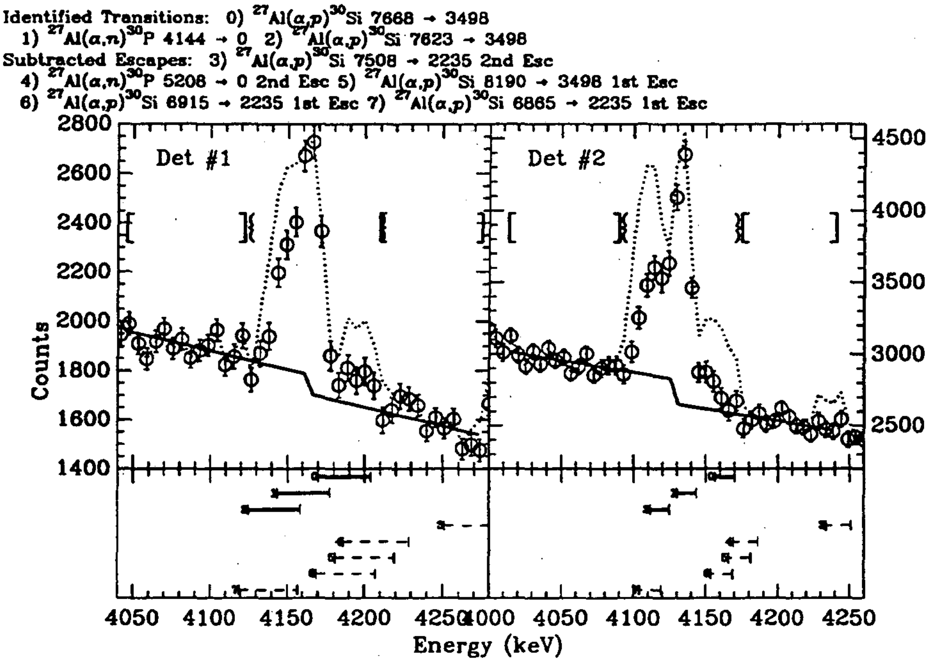

Figure 3.6: The 4140 keV peak from 10 MeV α-particles on the Aℓ

ground range used. In these cases, the step was considered to be a small background effect and the term describing it was dropped from the fit.

In regions of the spectra which contained a few thousand counts per channel, a linear + step background, shown in figure 3.6, was employed. In addition to the presence of the background step, this particular peak contained three individual γ-ray transitions as well as significant escape peak subtractions. Although the three transitions can be clearly seen in the spectrum for detector #2, the overlap of the Doppler shifted regions in detector #1 made it difficult to separate the individual transitions at the forward angle, and so a combined yield based on the total peak areas was calculated. The separation of the individual transition yields from a group such as this was accomplished through the use of published decay schemes as described in section 3.4.

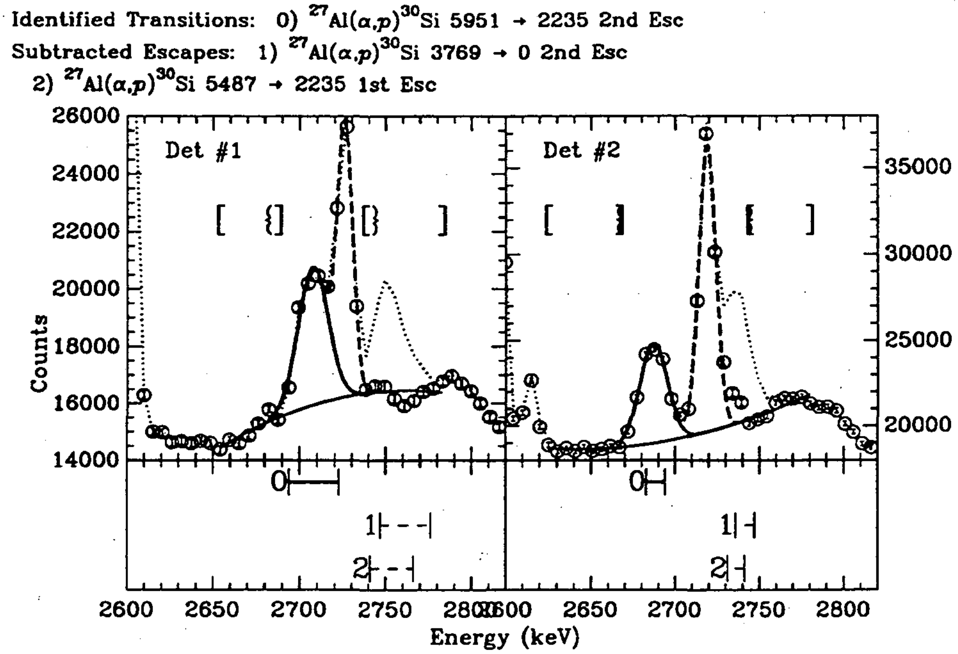

Figure 3.7: The second escape peak at 2720 keV from 10 MeV α-particles on Aℓ. The Doppler-shift range for the higher energy peak is not shown.

An example of a Gaussian shape separation of interfering peaks is shown in figure 3.7. In this case, the Gaussian fit for the identified transitions is shown by the thick solid line above the background line, while the thick broken line shows the sum of the two Gaussian functions. A non-stepped background was used for most sets of peaks separated by Gaussian fits, in order to avoid ambiguities in determining the step position and magnitude. Technically, a small step at the centroid of each Gaussian fit was expected, but insufficient information was available to determine these reliably. The area of each peak for such a separation was calculated from the ratio of the areas of the Gaussian fit in each case.

3.3.4 Yield Calculations

The peak area of each detector was converted into a yield for that detector. This yield can be expressed in terms of two components: an isotropic component which provides total γ-ray yield emitted into 4π, and an angular dependent component, which provides a measure of the angular distribution of the yield. These two components are characterized by an expansion of the distribution in terms of Legendre polynomials and fitting the yield in each detector to this expansion.

The yield in a given detector, $Y(\overline{\theta}_n)$, is given by the equation,

$$Y(\overline{\theta}_n) = \frac{A_n}{e_n \cdot N \cdot L_n}, \tag{3.73}$$

where e_n is the absolute energy efficiency for the peak in detector n of the appropriate escape order according to equation (3.41), N is the number of α-particles on target, and L_n is the live time and pile-up correction. The number of particles on target was calculated from the beam dump count n_d, which recorded one count per 10^{-9} Coulomb of beam on target. Thus, N is calculated according to the equation,

$$N = \frac{n_d \times 10^{-9}}{qe}, \tag{3.74}$$

where q is the charge state of the α-particle and $e = 1.602 \times 10^{-19}$ C is the charge of an electron. The dead time and pile-up correction were calculated from the counts in the pulser peaks of each spectrum. A pulser signal was injected into the test circuit of each detector preamp every time a dump count was produced, so the live time and pile-up corrections were simply given by the ratio of these two numbers,

$$L_n = \frac{A_{\text{pulser}\ n}}{n_d}. \tag{3.75}$$

Combining these expressions for N and L_n into equation (3.73), it then becomes,

$$Y(\overline{\theta}_n) = \frac{qeA_n \times 10^9}{e_{n,0}A_{\text{pulser}\ n}}, \tag{3.76}$$

where the dependence on the number of α-particles striking the target has been reduced to the effective number of α-particle counts contained in the pulser peak area. The uncertainty in $Y(\overline{\theta}_n)$ has been divided into two components: a "statistical" component that includes uncertainties in the relative detector efficiency and background shape, and a "systematic" component which includes uncertainties in the live time, beam condition and overall normalization. The statistical uncertainty in the detector yield, $\delta Y(\overline{\theta}_n)^{(stat)}$, was calculated from the relative uncertainties according to the equation

$$\left(\frac{\delta Y(\overline{\theta}_n)^{(stat)}}{Y(\overline{\theta}_n)}\right)^2 = \left(\frac{\delta A_n}{A_n}\right)^2 + \left(\frac{\delta A^{(stat)}_{\text{pulser}\ n}}{A_{\text{pulser}\ n}}\right)^2 + \left(\frac{\delta e_n}{e_n}\right)^2. \tag{3.77}$$

The systematic uncertainty in the detector yield, $\delta Y(\overline{\theta}_n)^{(sys)}$, is calculated by a similar equation

$$\left(\frac{\delta Y(\overline{\theta}_n)^{(sys)}}{Y(\overline{\theta}_n)}\right)^2 = \left(\frac{\delta A^{(sys)}_{\text{pulser}\ n}}{A_{\text{pulser}\ n}}\right)^2 + \left(\frac{\delta N}{N}\right)^2 + \left(\frac{\delta L^{(sys)}_n}{L_n}\right)^2, \tag{3.78}$$

where $\delta N/N$ is the fractional uncertainty in the number of α-particle on target and $\delta L^{(sys)}_n$ is any additional systematic uncertainty in the live time of the detectors.

The yield in each detector, $Y(\overline{\theta}_n)$, sampled the angular distribution of γ-rays. From symmetry considerations, it is known that only even order Legendre polynomial terms appear in this distribution. The detectors were positioned at angles where they would be most sensitive to the first two orders in the expansion, and would permit higher order terms to be neglected. The yield in each detector was then treated as containing an isotropic component, given by the magnitude of the zeroth order polynomial, and an angular dependent term determined by the magnitude of the second order polynomial. The total yield for a γ-ray transition is then given directly by the magnitude of the zeroth order polynomial. Expressing the detector area averaged intensity of the polynomial i over detector n as $\overline{P_i(\cos\theta_n)}$, the yield in each detector is expressed by the equations

$$\begin{aligned} Y(\overline{\theta}_1) &= a_0\overline{P_0(\cos\theta_1)} + a_2\overline{P_2(\cos\theta_1)} && (3.79) \\ Y(\overline{\theta}_2) &= a_0\overline{P_0(\cos\theta_2)} + a_2\overline{P_2(\cos\theta_2)}, && (3.80) \end{aligned}$$

where a_i is the coefficient of Legendre polynomial of order i. The average value of the Legendre polynomial subtended by a detector is roughly given by the value of the polynomial at the angle of the detector. In our calculations, we compensated for the effects of the finite detector geometry by approximating the contribution of each Legendre polynomial to the detector yield by the integral of the polynomial intensity over the area of each detector face. This calculation obtained values for the $\overline{P_2(\cos\theta_n)}$ to $\overline{P_0(\cos\theta_n)}$ ratio of 0.6081 and -0.3180 for $\theta_n = 30.6°$ and 109.9°, respectively.

Rearranging Equations (3.79) and (3.80) to solve for a_0 and a_2,

$$a_0 = \frac{1}{\overline{P_0(\cos\theta_1)}\,\overline{P_0(\cos\theta_2)}}\left[\frac{Y(\overline{\theta}_1)\overline{P_2(\cos\theta_2)} - Y(\overline{\theta}_2)\overline{P_2(\cos\theta_1)}}{\frac{\overline{P_2(\cos\theta_2)}}{\overline{P_0(\cos\theta_2)}} - \frac{\overline{P_2(\cos\theta_1)}}{\overline{P_0(\cos\theta_1)}}}\right] \tag{3.81}$$

$$a_2 = -\frac{1}{\overline{P_0(\cos\theta_1)}\,\overline{P_0(\cos\theta_2)}}\left[\frac{Y(\overline{\theta}_1)\overline{P_0(\cos\theta_2)} - Y(\overline{\theta}_2)\overline{P_0(\cos\theta_1)}}{\frac{\overline{P_2(\cos\theta_2)}}{\overline{P_0(\cos\theta_2)}} - \frac{\overline{P_2(\cos\theta_1)}}{\overline{P_0(\cos\theta_1)}}}\right] \tag{3.82}$$

Defining the constant ϵ as

$$\epsilon = \frac{1}{\overline{P_0(\cos\theta_1)}\,\overline{P_0(\cos\theta_2)}}\left[\frac{1}{\frac{\overline{P_2(\cos\theta_2)}}{\overline{P_0(\cos\theta_2)}} - \frac{\overline{P_2(\cos\theta_1)}}{\overline{P_0(\cos\theta_1)}}}\right], \tag{3.83}$$

Equations (3.81) and (3.82) become

$$\begin{aligned} a_0 &= \epsilon\left(\overline{P_2(\cos\theta_2)}Y(\overline{\theta}_1) - \overline{P_2(\cos\theta_1)}Y(\overline{\theta}_2)\right) && (3.84)\\ a_2 &= -\epsilon\left(\overline{P_0(\cos\theta_2)}Y(\overline{\theta}_1) - \overline{P_0(\cos\theta_1)}Y(\overline{\theta}_2)\right). && (3.85) \end{aligned}$$

The $\overline{P_i(\cos\theta_n)}$ are normalized to the zeroth order term in order to remove geometrical effects accounted for by calibration measurements. The zeroth order intensity terms are thus unity, and the equations for ϵ and a_2 reduce to the simple form of

$$\begin{aligned} \epsilon &= \frac{1}{\overline{P_2(\cos\theta_2)} - \overline{P_2(\cos\theta_1)}} && (3.86)\\ a_2 &= -\epsilon\left(Y(\overline{\theta}_1) - Y(\overline{\theta}_2)\right). && (3.87) \end{aligned}$$

The normalization of $Y(\overline{\theta}_n)$ causes the yield, Y, to be given directly by

$$Y = a_0, \tag{3.88}$$

and the ratio of the a_2 to the a_0 term provides a measure of the asymmetry of the angular distribution.

The uncertainty in the calculated yield was separated into two components, a "statistical" and "systematic" uncertainty, $\delta Y^{(stat)}$ and $\delta Y^{(sys)}$ respectively. These uncertainties were separated on the basis of how they propagate when yields were summed. The "statistical" uncertainties, which include statistical area uncertainty, the background shape uncertainty and the relative efficiency uncertainty, are added in quadrature. The "systematic" uncertainties, encompassing the live time uncertainty, the detector efficiency systematic uncertainty and the α-particle on target count uncertainty, are not reduced when yields are summed. Thus the yield for a number of transitions, $Y_{sum} = \sum_i Y_i$ had uncertainties

$$\left(\delta Y_{sum}^{(stat)}\right)^2 = \sum_i \left(\delta Y_i^{(stat)}\right)^2 \tag{3.89}$$

$$\delta Y_{sum}^{(sys)} = \sum_i \delta Y_i^{(sys)} \quad , \tag{3.90}$$

For an individual transition i, the statistical uncertainty was calculated from the uncertainties in the peak pair by assuming statistical uncertainties were uncorrelated, while systematic uncertainties were assumed to be fully correlated. Thus for statistical and systematic detector yield uncertainties as defined by equations (3.77) and (3.78),

$$\left(\delta Y_i^{(stat)}\right)^2 = \epsilon^2 \left[\left(\overline{P_2(\cos\theta_2)}\delta Y_i(\overline{\theta}_1)^{(stat)}\right)^2 + \left(\overline{P_2(\cos\theta_1)}\delta Y_i(\overline{\theta}_2)^{(stat)}\right)^2\right] \tag{3.91}$$

$$\delta Y_i^{(sys)} = \epsilon\left(\overline{P_2(\cos\theta_2)}\delta Y_i(\overline{\theta}_1)^{(sys)} - \overline{P_2(\cos\theta_1)}\delta Y_i(\overline{\theta}_2)^{(sys)}\right). \tag{3.92}$$

3.4 Transition Consistency and Level Excitation

Once all peak yields had been determined and transition identifications had been made, the reported yields were checked for identification consistency using the known decay schemes [Aj87, En90]. Only transitions from levels with a decay branch greater than 2% were identified. In the cases where peaks with multiple transition identifications existed, positive identifications and separation of the transitions were attempted by searching for different branches originating from the same level. When branching ratios and maximum possible yields indicated that a particular transition was expected to contribute less than 5% to a peak with multiple identifications, the particular transition identification was removed. The number of peaks with multiple identifications varied from target to target. Approximately 50% of the peaks below 5 MeV had two or more possible identifications in most targets. However, in the case of the NaF target, virtually every peak below 7 MeV contained at least two associated transitions, and could not be completely separated.

Yields from multiple transition peaks were separated into the individual transition yields through an iterative process. The procedure simultaneously determined the level population per α-particle for every residual nucleus from a target. Peak yields with unique transition identifications were used to determine the population of individual levels through the decay schemes reported in the literature. Peak yields with multiple identifications then had transitions from levels with known populations subtracted according to the branching ratios. This increased the number of level populations which could be determined. The calculation was iterated until no additional level population determinations were obtained for any residual nuclei.

The level population per α-particle U_l of a level l was calculated from the transition yield Y_i with a branching ratio B_i according to the equation

$$U_l = \frac{\sum_i w_i Y_i / B_i}{\sum_i w_i} \tag{3.93}$$

where i sums over the measured transition branches from a level. The weight w_i assigned to each determination of the level population was based on the total statistical uncertainty,

$$w_i = \left[Y_i^2 \left\{ \left(\frac{\delta B_i}{B_i} \right)^2 + \left(\frac{\delta Y_i^{(stat)}}{Y_i} \right)^2 \right\} \right]^{-1} \tag{3.94}$$

where $\delta Y_i^{(stat)}$ is the statistical uncertainty in the yield, and δB_i is the uncertainty in the branching ratio. The statistical uncertainty in the population, $\delta U_l^{(stat)}$ was given by

$$\delta U_l^{(stat)} = \frac{1}{\sqrt{\sum_i w_i}}. \tag{3.95}$$

The systematic uncertainty in the population, $\delta U_l^{(sys)}$, was calculated from the average systematic yield uncertainty as defined by equation (3.89),

$$\delta U_l^{(sys)} = U_l \cdot \frac{1}{n_l} \sum_i \frac{\delta Y_i}{Y_i}, \tag{3.96}$$

where n_l is the total number of determined transitions from level l.

The yield intensity for a particular transition Y_l with statistical and systematic uncertainties $\delta Y_l^{(stat)}$ and $\delta Y_l^{(sys)}$ contributing to a multiple transition peak was calculated from the level populations of the other transitions in the yield. The yield was then calculated from the total peak yield, Y_{peak}, according to the equations

$$\begin{aligned} Y_l &= Y_{peak} - \sum_{i,i \neq l} B_i U_i && (3.97) \\ \left(\delta Y_l^{(stat)} \right)^2 &= \left(\delta Y_{peak} \right)^2 + \sum_{i,i \neq l} \left(B_i U_i \right)^2 \times \left[\left(\frac{\delta B_i}{B_i} \right)^2 + \left(\frac{\delta U_i^{(stat)}}{U_i} \right)^2 \right] && (3.98) \\ \delta Y_l^{(sys)} &= Y_l \frac{\delta Y_{peak}^{(sys)}}{Y_{peak}} && (3.99) \end{aligned}$$

The interdependence of U_l and Y_l necessitated the iteration of the calculation until stationary values were obtained for each.

The direct population of a level in the residual nucleus, W_l, was calculated by subtracting the γ-ray cascade contribution from levels i decaying to level l by the equation

$$
\begin{aligned}
W_l &= U_l - \sum_i B_{i\to l} U_i && (3.100) \\
\left(\delta W_l^{(stat)}\right)^2 &= \left(\delta U_l^{(stat)}\right)^2 + \sum_i \left(B_{i\to l} U_i\right)^2 \left[\left(\frac{\delta U_i^{(stat)}}{U_i}\right)^2 \left(\frac{\delta B_{i\to l}}{B_{i\to l}}\right)^2\right] && (3.101) \\
\delta W_l^{(sys)} &= \delta U_l^{(sys)} + \sum_i B_{i\to l} \delta U_i^{(sys)}. && (3.102)
\end{aligned}
$$

This direct population of levels in the residual nucleus was used to calculate a population distribution by summing the populations into 1 MeV bins. This population distribution is directly comparable to the population distribution predictions of the statistical model calculations described in section 4.3. A mean excitation for a residual nucleus, $\overline{E}_x$ was also calculated from a weighted sum of level excitations,

$$
\begin{aligned}
\overline{E}_x &= \frac{\sum_l W_l E_l}{\sum_l W_l} && (3.103) \\
\left(\delta \overline{E}_x^{(stat)}\right)^2 &= \frac{\sum \left(\delta W_l^{(stat)}\right)^2 E_l^2 - 2\overline{E}_x \sum \left(\delta W_l^{stat}\right)^2 E_l + \overline{E}_x}{\left(\sum W_l\right)^2}. && (3.104)
\end{aligned}
$$

No systematic uncertainty was obtained for the mean excitation energy since systematic effects cancel in this calculation.

Chapter 4

The Statistical Model of Nuclear Reactions

4.1 Introduction

Statistical models of the nucleus have had some success in predicting average reaction properties such as the nuclear temperatures of compound nuclei and reaction cross sections. These calculations are typically performed on medium and heavy nuclei at high excitation energies where the level density of the nuclei can be treated as a continuous function of energy. In this study we are interested in extending this model to lower energies and lighter nuclei in order to determine its ability to predict the production rate and excitation of the residual nuclei. Our calculations are similar to that of Glotov [Gl78] who used a simple statistical model description of the particle emission process to estimate the excitation distribution of the residual nucleus. Glotov relied on experimental measurements of the (α, n) cross section for most of his calculations, and assumed that the (α, p) cross section was of the same order of magnitude, modified by energy phase space considerations and Coulomb barrier penetration probabilities. In these calculations Glotov used an exponential form for the level density of the residual nucleus, and neglected all spin and angular momentum effects.

In this study we are interested in extending the type of calculation used by Glotov to predict the γ-ray spectrum resulting from α-induced reactions. In extending his calculations, we investigated several cross section data sources, the effects of angular momentum, and the effects of discrete level densities on the calculations. We compared the predictions from each of these calculations with results from our experimental measurements.

The statistical model of nuclear reactions is based on the assumption that all reactions proceed through the formation of a compound nucleus which then undergoes decay through all energetically possible channels. The excitation of the compound nucleus is assumed to be sufficiently high that individual levels overlap and so the decay depends on statistical processes rather than the detailed configuration and structure of individual levels. The reaction cross sections calculation under these assumptions can be separated into two steps: the calculation of the probability for forming the compound nucleus, and the calculation of the branching ratios for the decay of the nucleus by the various channels. The first step is accomplished by calculating the absorption cross section for the incident particle based on the optical potential of the nucleus. The second step is accomplished by deducing the channel decay probability from the inverse absorption cross sections, which is calculated from the optical model absorption cross section and the density of nuclear states. These components are combined using the principle of detailed balance to obtain the total cross section for a particular reaction, and, through an extension of this principle, the average excitation energy of the residual nuclei. Calculations of this type are frequently used to determine cross sections for use in astrophysical models of energetic events such as supernovas, and agreement with experimental measurements of the total cross section to within a factor of two has typically been achieved for reactions on nuclei with masses down to $A = 27$ [Mo91, Mi70].

4.2 Absorption Cross Sections

Theoretical absorption cross sections are available from a number of different sources. Perhaps the most readily available source is that of Chatterjee, Murthy and Gupta [Ch81], who parameterized the optical model absorption calculations of other researchers [Ma63, Hu61, Au62] as a function of mass, atomic number and energy for neutrons, protons and α-particles. This parameterization, which reproduced the calculated cross sections to 10%, only provides values for the total absorption cross section for each of these nucleons, and so can only be used in calculations which ignore angular momentum coupling. Calculations using this data set are referred to in this study as "spin independent, parameterized".

More detailed calculations required the use of optical model codes to obtain more accurate absorption cross sections. Our own calculations used the Oxford computer code DSTWAV [Ha69] to obtain absorption cross sections from the scattering matrix calculated by this module. This distorted wave, Born approximation (DWBA) calculation and its relation to the S-matrix is presented in appendix A. The absorption cross sections from this calculation were used in two ways. First, calculations were were performed using total cross sections, ignoring all angular momentum couplings, in a calculation identical to that using the parameterized cross sections of Chatterjee. These calculations investigated the effect of using a parameterized interpolation of the cross section instead of a full calculation for the nuclei of interest. These calculations are referred to in this study as "spin independent".

In addition to these calculations, the cross sections derived from the DWBA calculation were used in properly coupled angular momentum calculations of the reaction rate, and through a comparison of these calculations the importance of angular momentum considerations in these calculations was assessed.

As well as investigating the various levels of complexity in using the optical model cross sections, we also investigated the different data sources for the optical potential used in optical model calculations of the absorption cross section. Two major sources are readily available in the literature. The first sources are global potentials, which apply to a range of nuclei and projectile energies. A major limitation in this study for many of these global potentials is that they have been derived from reaction cross sections for medium and heavy nuclei, and may not apply to the reactions and nuclei considered here. Another source of optical potential parameters is from phenomenological determinations from elastic scattering cross sections. These phenomenological determinations have usually been obtained using particle energies much higher than those of interest here, and as well may be inconsistent in the use of various parameters such as the mean nucleon radius. The cross sections from both these data sources, referred to as "global" and "phenomenological", respectively, have been used in the spin independent and angular momentum coupled calculations in order to evaluate which data set provides a better description of experimental results. Both the global and phenomenological optical potentials are described below.

4.2.1 The Optical Potential

The most common general form of the optical potential is expressed in terms of the Woods-Saxon potential, and can be written as [Pe76]

$$\begin{aligned} V(r,l,s,j) &= V_C(r) - V_R f_{ws}(R:r) - i\left[W_{Iv} f_{ws}(Iv:r) - 4W_{Is}\frac{d}{dx_{Is}} f_{ws}(Is:r)\right] \\ &\quad + V_{so}(\vec{s}\cdot\vec{l})\left(\frac{\hbar}{m_\pi c}\right)^2 \frac{1}{r}\frac{d}{dr} f_{ws}(so:r) \end{aligned} \tag{4.1}$$

where the subscripts "C", "R", "Iv", "Is" and "so" signify the Coulomb, real, imaginary volume, imaginary surface and spin-orbit components of the potential, respectively. $f_{ws}(i:r)$ is the Woods-Saxon function shape for a nucleus of A nucleons, parameterized by an average nucleon radius r_i and surface diffusiveness a_i of the form

$$f_{ws}(i:r) = \left(1 + e^{g_i(r)}\right)^{-1}, \text{ where } g_i(r) = \left(r - r_i A^{1/3}\right)/a_i. \tag{4.2}$$

The Coulomb potential V_C for an incident particle on a target nucleus with charges ze and Ze respectively is taken as that for a uniformly charged sphere,

$$V_c(r) = \begin{cases} \dfrac{zZe^2}{r}, & r \geq R_C \\ \dfrac{zZe^2}{2R_C}\left(3 - \dfrac{r^2}{R_C^2}\right), & r < R_C \end{cases} \tag{4.3}$$

where the charge radius of the nucleus is given in terms of the nucleon charge radius r_C, $R_C = r_C A^{1/3}$. The spin-orbit strength is defined in terms of the pion mass, m_π, which for historical reasons is always taken as $\left(\frac{\hbar}{m_\pi c}\right)^2 = 2.00 \text{ fm}^2$.

There are two terms in this potential responsible for the absorption of particles. These are the imaginary surface term and the imaginary volume term. In general low energy neutrons and protons have a short mean free path in nuclear matter, and the majority of the absorption occurs in the surface region of the nucleus. For the energies considered in this study, the imaginary potential can be treated as solely a surface function. For incident α-particles, the potential normally contains only the volume absorption term [Pe76].

A number of studies of have established global optical potential parameters for neutrons and protons. The two most recent studies by Becchetti and Greenlees [Be69a] and Varner, Clegg, McAbee and Thompson [Va87] indicate a dependence of the potential depths on both particle energy and nuclear isospin (the relative number of protons and neutrons). Both groups also restrict their parameterizations to nuclei with mass numbers of 40 and greater and to relatively high energies. These restrictions were adopted in order to avoid non-systematic nuclear structure effects in light nuclei, and to avoid significant compound nucleus contributions to elastic scattering in low energy nucleon scattering. These restrictions complicate the use of these global parameterizations for the studies conducted here, since we are interested in light nuclei with $A < 40$. In order to quantify our sensitivity to these problems, we performed two calculations using different sets of optical potential parameters. The first set of parameters was derived from the phenomenological potentials tabulated by Perey and Perey [Pe76] which were extrapolated to different energies and mass numbers, where necessary, according to the behaviour observed by Varner *et al* [Va87]. The phenomenological potential derived from experimental measurements is expected to contain the variations due to nuclear structure and shell effects that cause departures from the smooth dependence of the optical potential on atomic and mass numbers. The second set of potential parameters consisted of global parameterizations which have been developed and used by other researchers. In this set, the parameterization for the mass and energy region closest to that of interest in this study was used.

Only the potentials for neutrons and protons were treated as having an energy dependence. This energy dependence arises in part from the energy dependence of the nucleon-nucleon potential and in part from the presence of a non-local (ie velocity dependent) component to the nucleon-nucleus potential [Ho71].

The potentials based on the phenomenological potentials tabulated by Perey and Perey [Pe76] were obtained by extrapolating the phenomenological potentials, where necessary, to different mass numbers. This was usually required to obtain the decay cross sections for the compound nucleus. These derived potentials were then treated as having the same energy dependence as the global parameterizations.

The extrapolation started with the tabulated potential for a low energy nucleon incident on a nucleus with the same atomic number. The real and imaginary terms were then adjusted by

$$V_R(E_\circ) = V_{R0} \pm V_t \left[\frac{N-Z}{A} - \frac{N_0 - Z_0}{A_0}\right] \tag{4.4}$$

$$W_{Is}(E_\circ) = W_{Is0} \pm W_{st} \left[\frac{N-Z}{A} - \frac{N_0 - Z_0}{A_0}\right] \tag{4.5}$$

where the "0" subscript signifies the tabulated potential, and $E_\circ$ is the laboratory energy of the incident particle. The '+' in the '±' is used for protons, while the '−' in the '±' is used for neutrons. The magnitude of the isospin dependence given by Varner *et al* [Va87], $V_t = 13$ MeV and $W_{st} = 14$ MeV was used in the calculation.

Varner *et al* found that both proton and neutron potentials exhibited the same energy dependence. This energy dependence was incorporated to these potentials according to the equation

$$V_R(E) = V_R(E_\circ) + V_e(E - E_\circ) \tag{4.6}$$

$$W_{Is}(E) = W_{Is}(E_\circ)\left(\frac{1+\exp\{[E_\circ - E_c - W_{se0}]/W_{sew}\}}{1+\exp\{[E - E_c - W_{se0}]/W_{sew}\}}\right) \tag{4.7}$$

$$E_c = 6e^2 zZ/5R_c = 1.73zZ/R_c \text{ (MeV)} \tag{4.8}$$

The energy dependence is given by Varner *et al* [Va87] as $V_e = -0.30$ for energies in MeV, $W_{se0} = 29$ MeV and $W_{sew} = 23$ MeV. The form of the energy dependence of the imaginary potential was chosen by Varner *et al* to provide a smooth transition between the surface and volume form of the potential. The values of the potential parameters for neutrons, protons and α-particles are listed in table 4.1.

The second type of potential used in these calculations is a full global parameterization applicable in the low energy and medium mass range. As a result of the reaction

Table 4.1: Optical Potential Parameters from Perey and Perey [Pe76] for Absorption Cross Section Calculations

Target Nucleus	Particle and Energy (MeV)	Real Potential			Imaginary Potential†			Spin-Orbit Potential			Coulomb Radius r_C (fm)
		V_R (MeV)	r_R (fm)	a_R (fm)	V_I (MeV)	r_I (fm)	a_I (fm)	V_{so} (MeV)	r_{so} (fm)	a_{so} (fm)	
$^{27}\mathrm{A}\ell$	α, 8.7 MeV	77.0	2.5	0.31	22.0	2.5	0.31	—	—	—	2.5
^{30}Si	p, 17.13 MeV	52.39	1.17	0.65	3.85	1.33	0.6	6.51	0.94	0.6	1.2
^{30}P	n, 7.97 MeV	46.9	1.22	0.54	11.6	1.30	0.47	12.9	1.22	0.54	—
^{25}Mg	α, 22.1 MeV	51.2	1.694	0.585	11.13	1.694	0.585	—	—	—	1.65
$^{28}\mathrm{A}\ell$	p, 17 MeV	48.47	1.17	0.75	4.91	1.32	1.44	6.2	1.01	0.75	1.20
^{28}Si	n, 14.7 MeV	48.6	1.27	0.60	12.1	1.23	0.45	6.0	1.27	0.60	—
^{26}Mg	α, 15.7 MeV	80	1.61	0.52	13.5	1.61	0.52	—	—	—	1.5
$^{29}\mathrm{A}\ell$	p, 17 MeV	48.88	1.17	0.75	5.36	1.32	1.44	6.2	1.01	0.75	1.20
^{29}Si	n, 14.7 MeV	48.2	1.27	0.60	12.1	1.23	0.45	6.0	1.27	0.60	1.27
$^{27}\mathrm{A}\ell$	n, 4.0 MeV	49.1	1.20	0.62	7.99	1.20	0.48	8.0	1.26	0.48	—
^{31}P	p, 8.1 MeV	53.1	1.25	0.65	8.3	1.25	0.47	7.5	1.25	0.65	1.25
^{20}Ne	α, 16.8 MeV	56.90	1.73	0.584	5.18	1.73	0.464	—	—	—	1.73

† Absorbing potentials for neutrons (n) and protons (p) use a derivative Wood-Saxon surface form, while those for α-particles (α) use a volume Wood-Saxon form.

Q-values for the nuclei considered here, only the neutron, proton and α-particle potential were required in these calculations. In all these parameterizations, the laboratory frame energy of the incident particles is used, all energies and potential depths are in units of MeV, and all distances and diffusivities are in Fermis. For neutrons, a potential used in a study by Alexander *et al* [Al90] has been adopted:

$$\begin{aligned} V_R &= 49.72 - 0.3E - 17\left(\frac{N-Z}{A}\right) \text{ MeV}, \\ &\quad r_R = 1.256 \text{ fm},\ a_R = 0.626 \text{ fm} \qquad (4.9) \\ W_{Is} &= 5.22 + 0.4E - 10\left(\frac{N-Z}{A}\right) \text{ MeV}, \\ &\quad r_{Is} = 1.26 \text{ fm},\ a_{Is} = 0.0045E + 0.555 \text{ fm} \qquad (4.10) \end{aligned}$$

to which we have added the spin-orbit potential of Varner *et al* [Va87] with $V_{so} = 5.9$ MeV and $a_{so} = 0.65$ fm.

The global parameterization for low energy protons suggested by Perey and Perey [Pe76, Pe63] was used and has the form

$$\begin{aligned} V_R &= 53.3 - 0.55E + 27\left(\frac{N-Z}{A}\right) + 0.4\left(\frac{Z}{A^{1/3}}\right) \text{ MeV}, \\ &\quad r_R = 1.25 \text{ fm},\ a_R = 0.65 \text{ fm} \qquad (4.11) \\ W_{Is} &= 3A^{1/3} \text{ MeV},\ r_{Is} = 1.25 \text{ fm},\ a_{Is} = 0.47 \text{ fm} \qquad (4.12) \\ V_{so} &= 7.5 \text{ MeV},\ r_{so} = 1.25 \text{ fm},\ a_{so} = 0.47 \text{ fm} \qquad (4.13) \end{aligned}$$

It should be noted that both these potentials provide a reasonable description of the elastic scattering data for nuclei down to a mass number of ~30 [Pe76], and so are just within the mass range of the nuclei considered here. The proton potential used here was derived from data between 9 and 22 MeV, and as such represents an extrapolation of the potential into a region where it may not be valid.

Although many investigations have attempted to parameterize the optical potential for α-particles, consistent systematic potentials have not been found [Pe76]. The low energy behaviour has not been well established due to the predominance of Coulomb scattering in the region below 20 MeV [Mc66]. McFadden and Satchler [Mc66] have extensively investigated the optical potential at 24.7 MeV for elements ranging from oxygen to uranium, and were unable to find a reasonable mass parameterization of the potential. As well, there has been no well established energy dependence for an α-particle potential [Ma86], although there are reasons to expect an increase in the real potential in the energy region equal to the Coulomb barrier height due to the rapid rise of the imaginary potential. Given this, we have adopted the average values suggested by McFadden and Satchler for starting points in their search for fitting experimental angular distributions [Mc66] and have not introduced any energy dependence into these value. The global α-particle potential is then given by

$$V_R = 185 \text{ MeV}, \tag{4.14}$$

$$W_{I_v} = 25 \text{ MeV}, \tag{4.15}$$

$$r_R = r_{I_v} = r_c = 1.4 \text{ fm} \tag{4.16}$$

$$a_R = a_{I_v} = 0.52 \text{ fm} \tag{4.17}$$

for all nuclei considered here. Calculations using this potential might be expected to

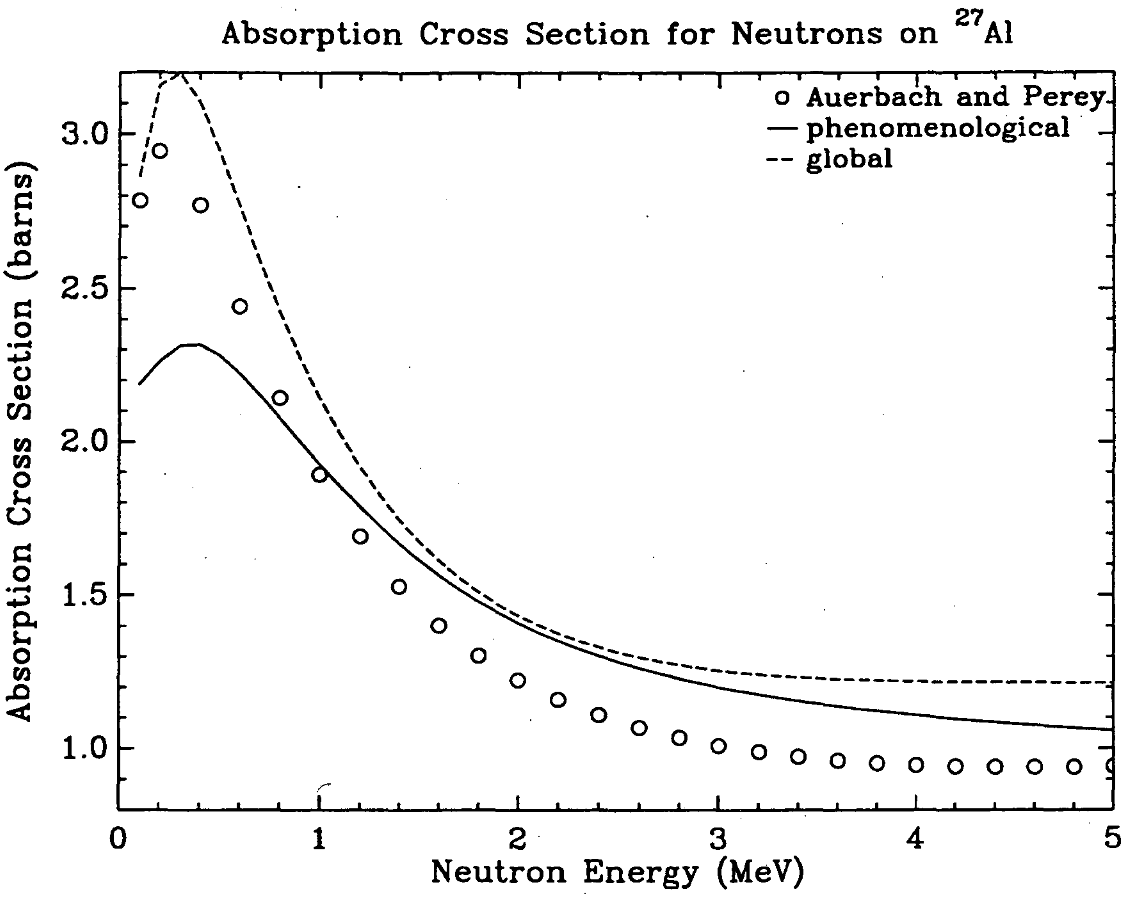

Figure 4.1: Neutron absorption cross section for $^{27}\mathrm{A}\ell$. The points (o) indicate the tabulated results of Auerbach and Perey [Au62], while the lines indicate the present calculation using the phenomenological potential (solid line) and global potential (dashed line).

show a large deviation from the experimental results as the scattering cross section of light nuclei similar to those studied here tend to be better fit by shallower potentials ($V_R \sim 50$ MeV) with a larger nucleon radius (~ 2 fm) [Mc66]; however, penetration of the Coulomb barrier is expected to dominate the absorption of α-particles at the energies considered here, and hence our calculations were not expected to depend heavily on the form of this nuclear potential.

Examples of absorption cross sections derived from these potentials are shown in

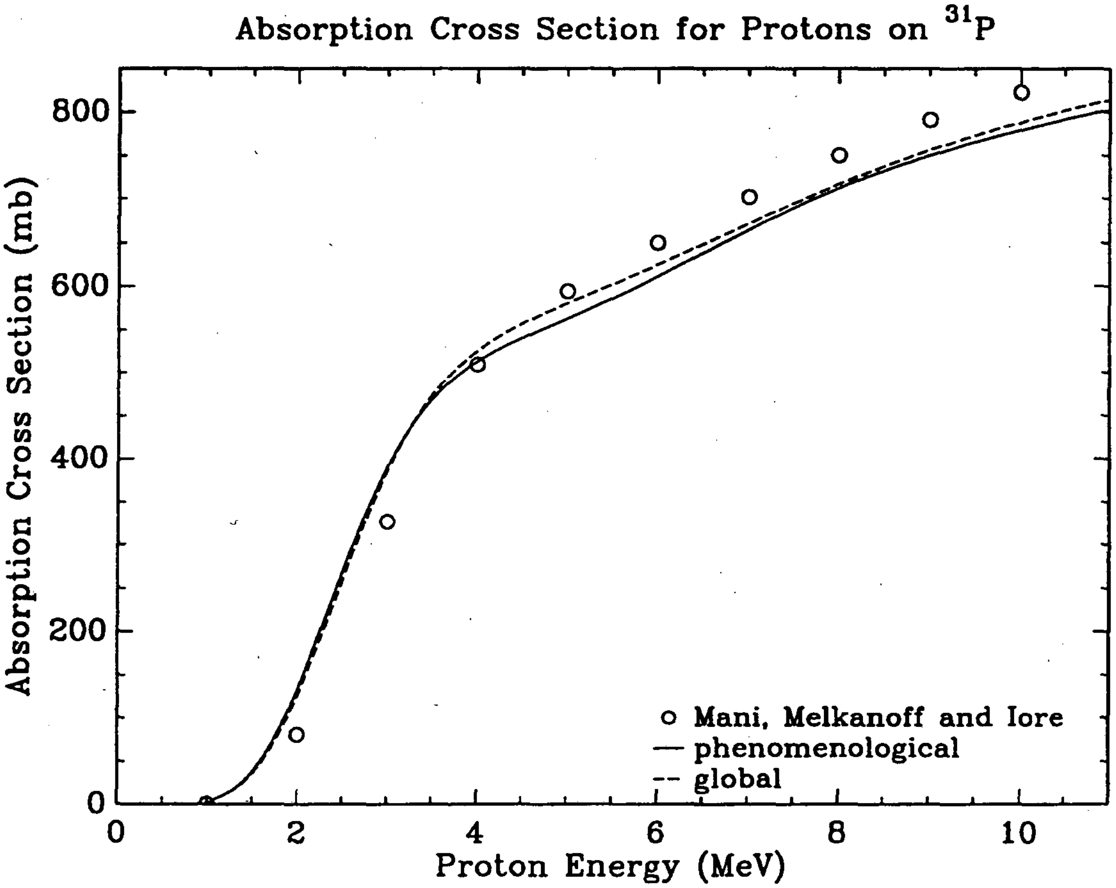

Figure 4.2: Proton absorption cross section for ^{31}P. The points (○) indicate the tabulated results of Mani *et al* [Ma63] while the lines indicate our present calculations using a phenomenological potential (solid line) and the global potential.

figures 4.1 through 4.3. Also shown in these figures are the absorption cross sections calculated by other groups. Previous calculations were typically performed for select stable target nuclei, and so similar nuclei in the mass region of interest of our study were chosen for this comparison. The different cross section calculations for neutrons and protons agree to within 20% over most of the particle energy range. Significant differences of up to 40% are seen in the neutron cross section below 0.8 MeV. The largest differences in the calculations are seen in the α-particle absorption cross sections, where disagreements on the order of 40% are observed between the different determinations.

4.2.2 Level Density

A large number of investigations have concentrated on the description of the nuclear level density. In recent years, efforts have focussed on deriving the level density structure under the assumption that the nucleons behave according to the generalized superfluid model as described by BCS theory [Be92, Ra90]. These theories derive a level density function which follows a constant nuclear temperature form at low excitation energies, and a Bethe form at higher energies [Ra90]. At excitation energies approaching 30 MeV, shell effects are expected to disappear; this has been accounted for by some researchers through an energy dependence in the level density parameter [Il92].

The nuclear level density used in the determination of the reaction cross sections was calculated according to the parameterization of Gilbert and Cameron [Gi65c],

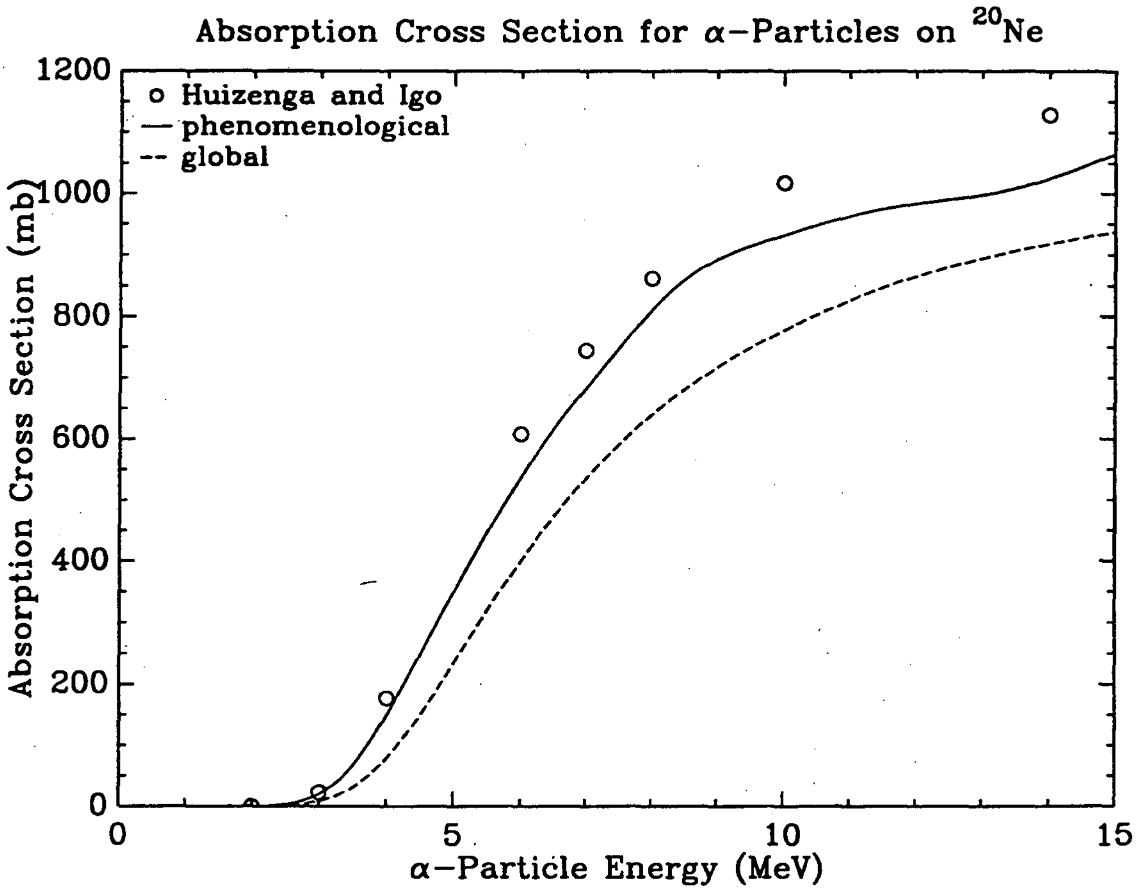

Figure 4.3: α-Particle absorption cross section for ^{20}Ne. The points (o) indicate the tabulated results of Huizenga and Igo [Hu61] while the lines indicate our calculations using the phenomenological potential (solid line) and global potential.

and in one case, the data of Von Egidy *et al* [Vo86]. This model of the level density is based on statistical thermodynamic descriptions of the excited nucleus as a non-interacting Fermi gas. In this parameterization, the level density behaviour is divided into two regions: a constant nuclear temperature region at low excitation energies, and an increasing nuclear temperature at higher energies which follows the standard exponential behaviour first derived by Bethe.

At low excitation energies E, the level density ρ follows the form

$$\rho(E) = \frac{\exp\left[(E - E_0)/T\right]}{T}, \tag{4.18}$$

where T is the nuclear temperature and E_0 is the energy associated with the ground state. At higher energies, the density of levels for all spin states is given by the equation

$$\rho(U) = \frac{\sqrt{\pi}}{12} \frac{\exp\left(2\sqrt{aU}\right)}{a^{1/4}U^{5/4}} \frac{1}{\sigma\sqrt{2\pi}} \tag{4.19}$$

where a is the level density parameter, U is the pairing corrected excitation energy, and σ is the spin cut-off parameter. The parameters for these equations were listed by Gilbert and Cameron for all nuclei of consequence here, as well as the transition energy E_x between the two density forms. The level spin dependence of the density function has also been discussed by various researchers. In all cases, the density of levels of both parities with a spin J has been described by the equation

$$\rho(E,J) = \frac{(2J+1)}{2\sigma^2} \exp\left[-\frac{(J+1/2)^2}{2\sigma^2}\right] \rho(E). \tag{4.20}$$

The integrated level density for the nuclei involved in the $^{27}\mathrm{A}\ell+\alpha$ reaction are shown in figures 4.4 and 4.5, along with the observed levels. The solid line shows the integral summed over the 6 lowest spin quantum numbers. In all cases the integrated level densities fall below the observed number of levels, primarily due to the non-statistical nature of the first few levels of the nucleus. The effects of these deviations from the statistical behaviour was explored by creating a modified level density which used the same form and values as the statistical level density, but whose functional form was modified over a small energy region. These modifications consisted of adding a constant to the density, and treating the density as a constant over particular regions. These modifications were independent of spin and distributed according to equation (4.20). The integrated modified levels densities are shown as a broken line in figures 4.4 and 4.5.

Von Egidy *et al* investigated whether the constant temperature or Bethe form of the level density provided a better parameterization of the low energy level density. They used both "complete" nuclear level schemes and s-wave neutron resonance spacings to obtain fits to both forms of the level density. For ^{30}Si, the level scheme up to 7.6 MeV was used, while for ^{31}P, the level scheme up to 6.0 MeV was used. Von Egidy *et al* concluded that at low excitation energies both the constant temperature and Bethe formulae provided equally good fits to the data [Vo88], with the fitted parameters ranging in agreement with those of Gilbert and Cameron [Vo86]. For the nuclei of consequence here only the ^{28}Aℓ level density of Von Egidy using the constant temperature form provided a significantly better agreement with the observed level scheme, and so in this case was used in preference to that of Gilbert and Cameron.

In summary, there is a solid theoretical justification for the use of the constant

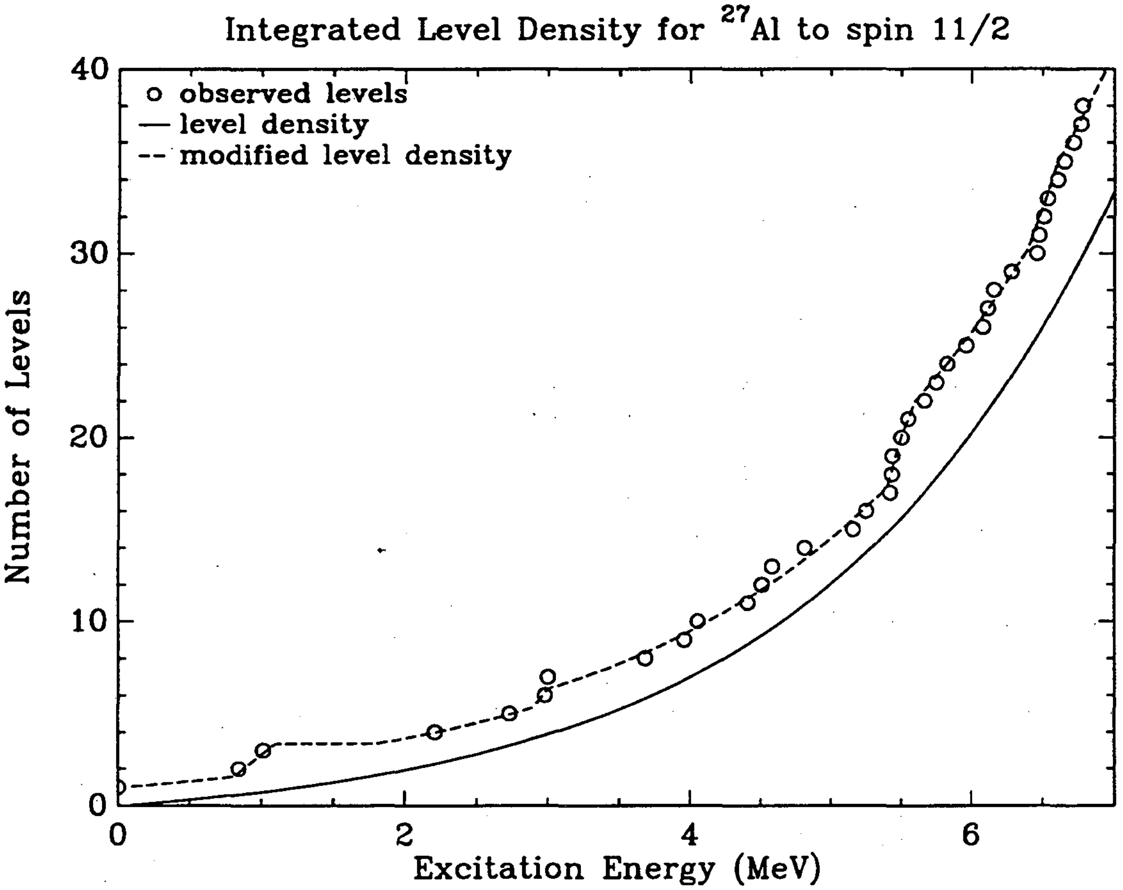

Figure 4.4: Integrated level density for ^{27}Aℓ. The solid line show the number of levels resulting from a numerical integration of the level density equation (4.20) summed over the 5 lowest spin quantum numbers. This integration follows the general trend of the observed levels, indicated by the open circles on the plot. A better agreement with the low energy levels is obtained using a modified level density, where the level density behaviour has been changed in particular energy regions.

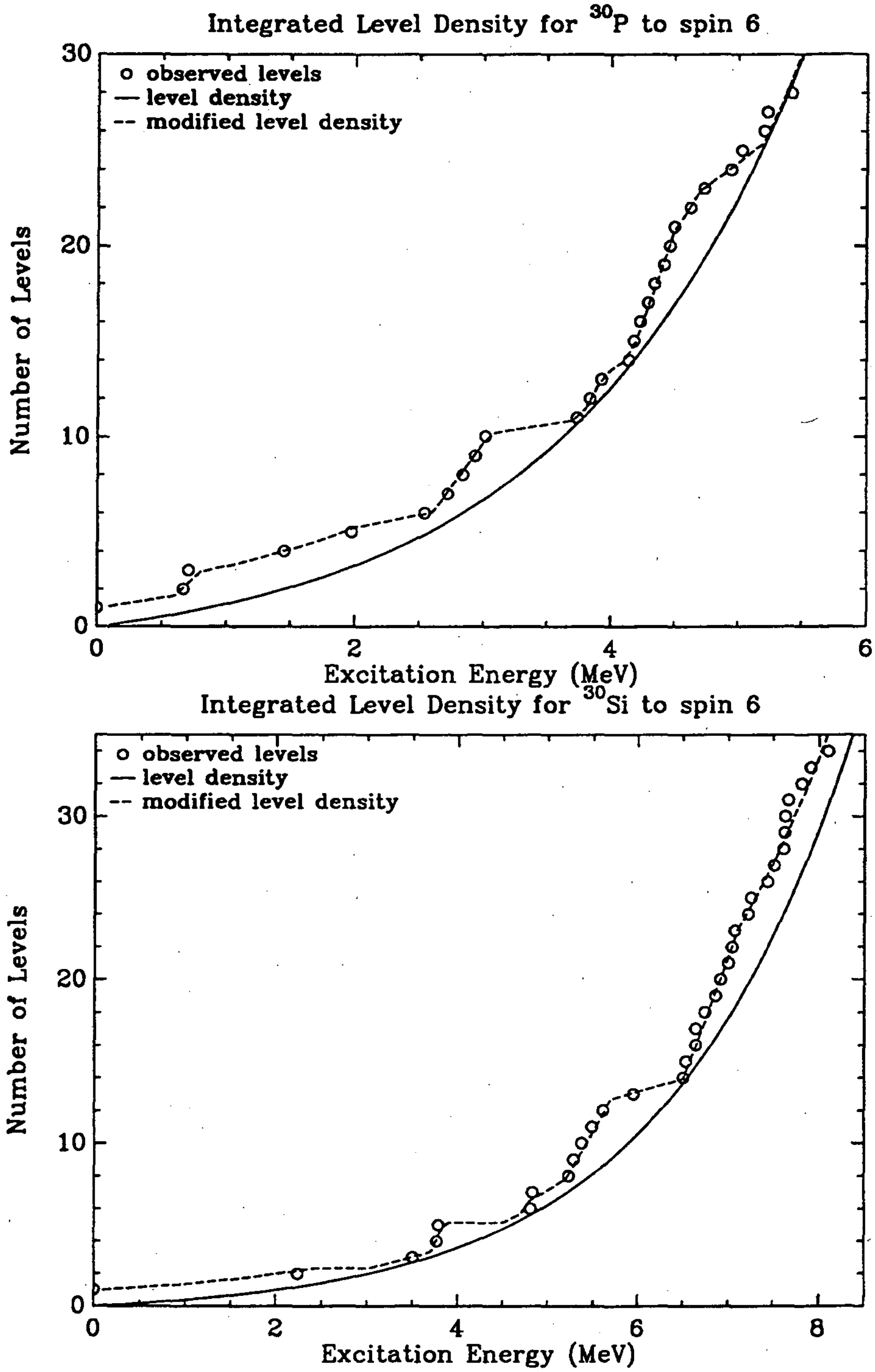

Figure 4.5: Integrated level density for ^{30}P and ^{30}Si. The solid and broken lines show the integrated level density under the same conditions as in figure 4.4. The circles indicate the position of the observed levels.

temperature level density formula at low energies and Fermi gas form at higher energies. The most comprehensive parameterization has been provided by the work of Gilbert and Cameron, and is used here unless significant disagreement with more recent level schemes was noted. More recent determinations of the level density have used similar parameterizations, and obtained values for the parameters that cover a range of agreement with Gilbert and Cameron's earlier work. For the nuclei of concern in our calculations, all parameterization provide essentially the same description of the level density, except in the one case, and are in agreement with the observed level structure.

4.3 Reaction Cross Section

The statistical reaction cross section for a reaction $A(a,b)B$ can be calculated according to the evaporation, or statistical, model of the reaction process through the optical cross sections for compound nucleus formation. Implicit in this calculation are the assumptions that the structure of the nuclei can be neglected and that the optical potential remains essentially unchanged by excitations of the target nucleus. The following is a summary of the theory based largely on the presentation of Roy and Nigam [Ro67], Marmier and Sheldon [Ma70] and Hodgson [Ho71].

In calculating the reaction cross section in the compound nucleus formalism, we require the probability for forming the compound nucleus, and the probability for the decay of the compound nucleus through each open channel. In addition to the cross section and decay probability factors, there is also a geometrical or statistical factor that arises from joining the angular momentum states of the particles involved. This factor is obtained by coupling angular momentum states of the reacting particles to a particular compound nucleus angular momentum and summing over the magnetic substates. Now, the cross section for forming a compound nucleus of a given spin J from an incident α-particle with a total angular momentum l on a target nucleus with spin $J_\circ$ which then decays through a particle b of total angular momentum j and residual nucleus with spin J_1 is defined in terms of the absorption cross section $\sigma_c(l) \equiv \sigma(lj)$ of equation (A.41) with $s = 0$ and $j = l$ and a branching probability $W_{b:JjJ_1}$ for the compound nucleus through the particular channel:

$$\begin{aligned}
\sigma_{l,J}^{(j,J_1)} &= \frac{1}{2J_\circ + 1} \sum_{\substack{m_\circ,\, M \\ m_j,\, m_1}} \sigma_c(l)\, |\langle l, 0, J_\circ m_\circ | JM \rangle|^2 \\
&\quad \times |\langle j, m_j, J_1, m_1 | JM \rangle|^2\, W_{b:JjJ_1} && (4.21) \\
&= \frac{\sigma_c(l) W_{b:JjJ_1}}{2J_\circ + 1} \sum_{m_\circ,\, M} |\langle l, 0, J_\circ m_\circ | JM \rangle|^2 \sum_{m_j,\, m_1} |\langle j, m_j, J_1, m_1 | JM \rangle|^2 && (4.22) \\
&= \frac{1}{2J_\circ + 1} \sigma_c(l) W_{b:JjJ_1} \sum_{m_\circ,\, M} |\langle l, 0, J_\circ m_\circ | JM \rangle|^2 && (4.23) \\
&= \frac{2J + 1}{(2J_\circ + 1)(2l + 1)} \sigma_c(l) W_{b:JjJ_1}. && (4.24)
\end{aligned}$$

where the $2J_\circ + 1$ term averages over the initial spin substates of the target nucleus and $W_{b:JjJ_1}$ is taken as the substate averaged probability. In general we are interested in the total cross section for forming a compound nucleus of a given spin J, and can sum over all channels for creating the compound nucleus without affecting the decay probability $W_{b:JjJ_1}$. The total cross section for creating the compound nucleus with spin J, σ_J, is then calculated through the sum

$$\sigma_J = \sum_{l=|J-J_\circ|}^{J+J_\circ} \frac{2J+1}{(2J_\circ+1)(2l+1)}\sigma_c(l) \tag{4.25}$$

In the calculations performed here we have combined the cross section for positive and negative parity states. This approximation is permitted only by the fact that our method for calculating the decay probability $W_{b:JjJ_1}$ does not distinguish between parity states in J. In more detailed calculations which distinguish between the different parities, this sum should be separated into even and odd values of l.

Having obtained the probability for forming the compound nucleus, it is next necessary to determine the probability for each decay channel. The probability of decay of the compound nucleus via different channels is related to the probability of the reverse reaction through the principle of detailed balance. For a compound nucleus C with excitation energy E_0 and spin J that can decay into the residual nucleus B with energy and spin E, J_1 and particle b with kinetic energy and total angular momentum ϵ, j, the transition probability $W_{b:JjJ_1}$ can be calculated from the compound nucleus formation cross section through the principle of detailed balance [Ma70, Ro67]. The transition probability W_{fi} from an initial state i to a final state f is given by perturbation theory as

$$W_{fi} = \frac{2\pi}{\hbar}\rho_f \left|H'_{fi}\right|^2 \tag{4.26}$$

$$= \sigma_{fi} v_i \tag{4.27}$$

where H'_{fi} is the matrix element for the transition from i to f, ρ_f is the density of final states per unit energy, σ_{fi} is the cross section for the process and v_i is the incident particle flux. The principle of detailed balance holds that the transition probability from i to f must be the same as from f to i so that

$$\left|H'_{if}\right| = \left|H'_{fi}\right| \tag{4.28}$$

and hence

$$\frac{W_{if}}{\rho_i} = \frac{W_{fi}}{\rho_f} = \frac{\sigma_{fi} v_i}{\rho_f}. \tag{4.29}$$

The cross section σ_{fi} is actually an average over initial states and a sum over final states which must be taken into account in calculating the magnetic substate averaged probability. The averaging over initial states is removed by multiplying the cross section by the $2s_i+1$ substates of the incident particle. The effect of the final substates sum is accounted for by the principle of semi-detailed balance, or reciprocity, which holds that

$$\sum_f W_{fi} = \sum_f W_{if} \tag{4.30}$$

so that the decay probability used in equation (4.24) is given by

$$W_{b:JjJ_l} = \frac{2s_b + 1}{2j + 1} v_b \sigma_{C \leftarrow bB} \frac{\rho_i}{\rho_f}, \tag{4.31}$$

where for clarity the angular momentum labels for the cross section have been absorbed into the particle labels C, b and B. In this case the term ρ_f is the density of states for the compound nucleus and ρ_i is the density of states for the particle b and residual nucleus B. The density of states for B is given by the level density equations (4.18) and (4.19) discussed previously, while the density of states for b is assumed to be that for a particle emitted into free space. ρ_i is simply the product of these two densities, integrated under the restriction of conserving the available energy

E^* and assuming a sufficiently massive residual nucleus so that momentum is always conserved:

$$\begin{aligned} v_b \rho_I dE &= v_b \rho_b(\epsilon)\, d\epsilon \rho_B(E)\, dE\, \delta(E^* - E - \epsilon) && (4.32) \\ &= \frac{p}{m_b} \frac{4\pi p^2 dp}{(2\pi\hbar)^3} \rho_b(E)\, dE\, \delta(E^* - E - \epsilon) && (4.33) \\ &= \frac{m_b \epsilon}{\pi^2 \hbar^3} \rho_b(E)\, dE && (4.34) \end{aligned}$$

where the momentum p has been expressed in terms of the particle energy ϵ and mass m_b. The transition probability is thus

$$W_{b:JjJ_1} = \frac{(2s_b + 1)}{2j + 1} \frac{m_b}{\pi^2 \hbar^3} \frac{\rho_B(E)}{\rho_C(E_0)} \epsilon \sigma_{C \leftarrow Bb}\, dE \qquad (4.35)$$

Combining this equation with that of the total cross section for forming the compound nucleus with a spin j, σ_J, as given in equation (4.25), the cross section for decay by emission of b is given by

$$\begin{aligned} \sigma_{Bb \leftarrow Aa} &= \sigma_J \frac{W_{Bb \leftarrow C}}{\sum W_{B'b' \leftarrow C}} && (4.36) \\ &= \sigma_J \frac{\int_0^{E_R} dE\, \frac{(2s_b+1)}{(2j+1)} m_b \epsilon \sigma_{C \leftarrow Bb} \rho_B(E)}{\sum \int_0^{E'_R} dE\, \frac{(2s_{b'}+1)}{(2j'+1)} m_{b'} \epsilon \sigma_{C \leftarrow B'b'} \rho_{B'}(E)} && (4.37) \end{aligned}$$

where we have normalized the total decay probability to unity and removed the dependence on the compound nucleus density of states by dividing over the sum of all possible decay channels of the compound nucleus with spin J. The integration occurs over the entire range of valid residual excitation energies between 0 and E_R, with $\epsilon = E_R - E$. We are also interested in determining the cross section into a residual nucleus excitation energy range between E_1 and E_2. This is easily found by substituting these values for the integration limits 0 and E_R in the numerator of equation (4.37), and summing over all spin contributions (l, J, j and J_1) to this energy range.

It should be noted that in this calculation we have neglected the compound nuclear elastic scattering component of the absorption cross section. In calculations such as this, this component is only a small portion of the total absorption cross section and so can usually be ignored. However, it is known that at low energies where there are only a few open reaction channels, the compound elastic cross section is a significant fraction of the absorption cross section. In these calculations, this increase in the low energy absorption cross section would cause an increased probability of a low particle energy/high residual nucleus excitation energy decay, and consequently, a larger than otherwise γ-ray background component near the maximum spectrum energy. In more elaborate calculations this cross section can be removed by solving a set of coupled differential equations which use a more elaborate coupled-channel potential. Such calculations are beyond the scope of this study.

4.3.1 Numerical Cross Section and Yield Calculations

The optical cross sections were calculated using the optical code of Hay and Perez [Ha69] and the optical potentials provided in sections 4.2.1. This programme solved equations (A.10) by numerical integration out to a radius where the nuclear potential was judged to be negligible, and the asymptotic form of the solution could be used. In the cases considered here, the integration proceeded out to one nuclear radius beyond the point where the nuclear potential fell below 0.5% of its maximum value, typically 15 fm for α-particles, and 10 fm for neutrons and protons. The required phase shifts and S-matrix elements were then obtained by matching the amplitude and logarithmic derivative of the radial wave function of the internal and asymptotic solutions.

These cross sections were used together with the level density formula to numerically evaluate the integrals in equation (4.37). The upper limit of each integration was calculated from the equation,

$$E_R = Q + E_{lab}\frac{M_t}{M_t + M_\alpha} \tag{4.38}$$

where the first term, Q, is the energy released by the reaction and the second term is the fraction of the incident particle kinetic energy, E_{lab}, available within the centre of mass system. In order to avoid unrealistically large neutron cross sections at energies near zero, the neutron cross section dependence was changed to

$$\sigma_n(\epsilon) = \sigma_n(\epsilon_{cut})\left(\frac{\epsilon_{cut}}{\epsilon}\right)^{1/2} \tag{4.39}$$

below a suitable cut-off energy ϵ_{cut}. The sensitivity of the calculation to E_{cut} was estimated by varying E_{cut} in the calculation between 0.1 and 1 MeV. Variations in the excitation energy cross section on the order of 5% were observed.

In addition, a large fraction of the α-particle absorption cross section occurs for high spin levels in the compound nucleus which are not experimentally observed. Such high spin levels primarily contribute to the elastic scattering of the α-particle. In order to remove this component of the cross section, the sum over J was restricted to the highest observed level spin near 8 MeV excitation in the compound nucleus; this restriction is equivalent to a restricting the sum over J to the first 5 or 6 lowest spins of the compound system. The effects of this restriction on the calculated $^{27}\mathrm{A}\ell(\alpha, n)$ and (α, p) cross sections are shown in figure 4.6, where our calculations using the

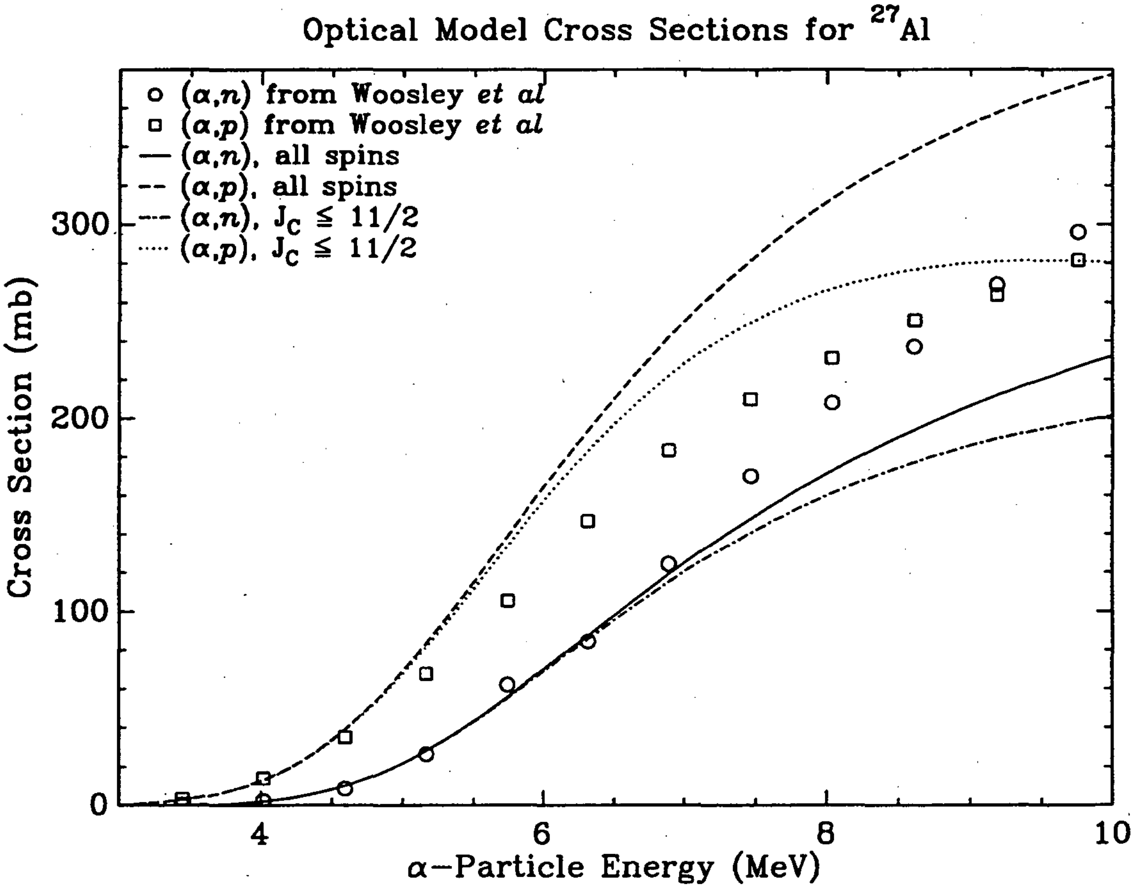

Figure 4.6: ^{27}Aℓ (α, n) and (α, p) cross sections. The lines show the results of a statistical calculation using the global potential under unrestricted compound nucleus spin and restricted $(J_C \leq 11/2)$ spin conditions. These cross sections are compared with Hauser-Feshbach calculations by Woosley *et al* [Wo76].

global potentials are also compared to a Hauser-Feshbach calculation by Woosley *et al* [Wo76]. We calculate somewhat different strengths for the neutron and proton channels than Woosley *et al*, with all cross sections agreeing to within 30%. The effect of restricting the compound nuclear spin to observed values is clearly seen from the 15 to 30% reduction in both channel cross sections at high α-particle energies.

In figure 4.7 the total thick-target neutron yield from the $^{27}\mathrm{A}\ell(\alpha,n)$ reaction using the calculated cross sections has been compared to reported experimental yields [We82, He90], and to the optical model Hauser-Feshbach calculations of Woosley *et al.* A number of different cross section calculations were used to generate our yields. In particular, we are interested in how the accuracy of these statistical model calculations is affected by a range of approximations. In the first level of approximation, the angular momentum coupling of the cross sections was ignored, except for a $2s+1$ factor term in the density of states for the incoming/out-going particle. Within this approximation, we have three different sets of cross sections: an interpolation of published optical cross sections by Chatterjee *et al* [Ch81], and the total cross section from optical calculations using the phenomenological and global potentials described in section 4.2.1. Each of these cross section sets is seen to over-estimate the total thick-target neutron yield by as much as a factor of three to five. The global potential cross section calculation provided the closest agreement with the neutron yields published in the literature. Introducing proper spin-coupling improved the overall agreement with published yields by close to 50% for both sets of optical potential cross sections, with approximately half the difference resulting from the restriction of

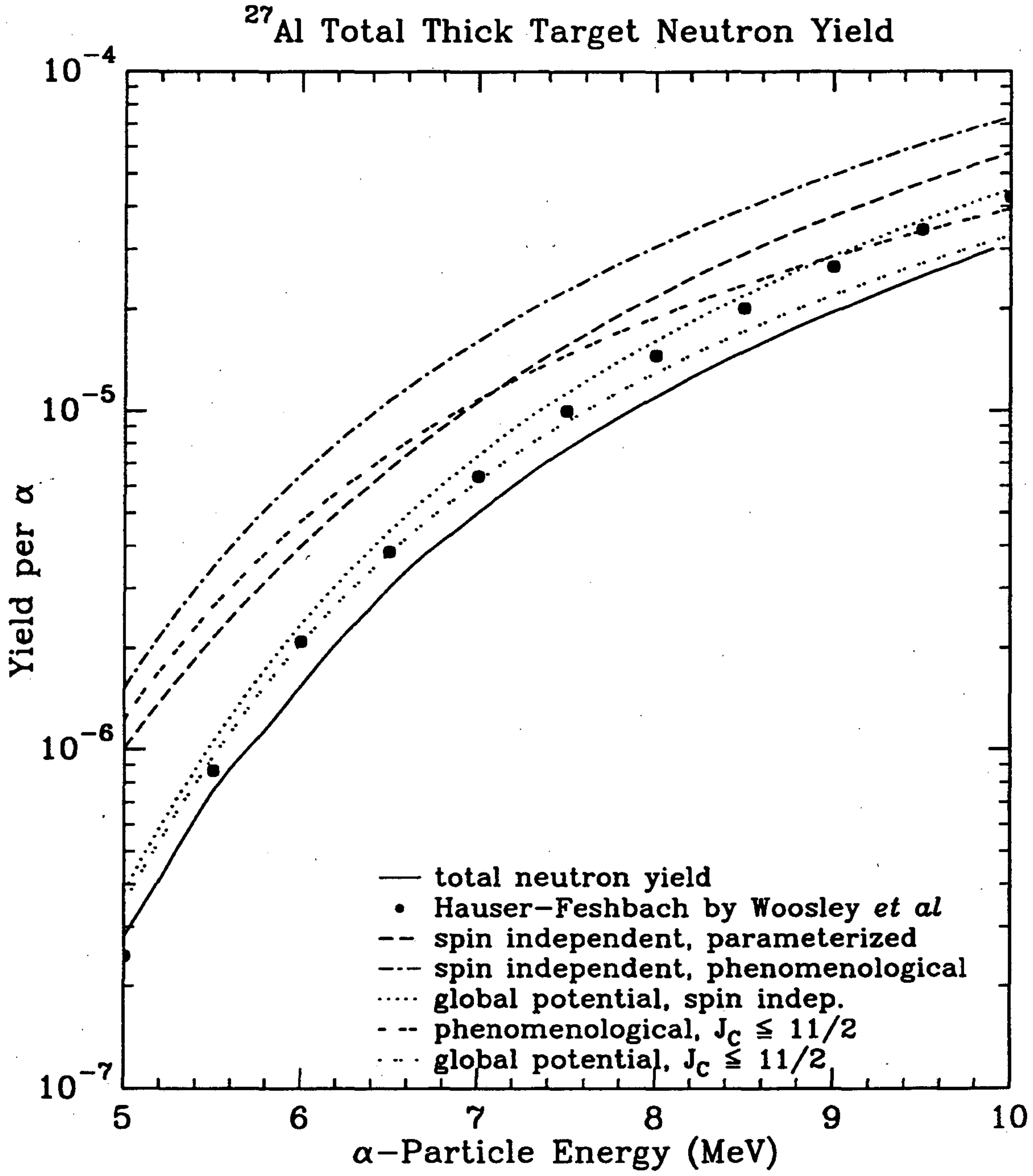

Figure 4.7: ^{27}Aℓ total thick-target neutron yield. The reported thick-target yields [We82, He90] are compared to statistical cross section calculations which have been integrated using the stopping powers of Ziegler *et al* [Zi85]. The yields labelled "spin independent" have been derived from cross section calculations which neglected spin coupling except for a $2s + 1$ factor in the density, while the last two lines considered full spin coupling in the cross section, restricted to a maximum compound nuclear spin of 11/2. The yield derived from the calculation of Woosley *et al* is also shown.

the compound nuclear spin to 11/2 or less. These results are similar to those from the Hauser-Feshbach calculations of Woosley *et al*, which differed primarily in the treatment of discrete levels. Both calculations reproduced the total neutron yield to within the same accuracy and obtained agreement with the reported experimental yield to within 50% over most of the energy range.

Chapter 5

Results

The $E_\alpha = 10$ MeV γ-ray spectrum from detector #2 for each target is presented in figures 5.1 through 5.12. Each figure shows the recorded spectrum with the identified transitions labelled at the peak centroid position. Multiple identifications of the same peak are indicated by successive level transitions following the reaction label, or by a brace bracket ("{") for identifications from different reactions. Escape peaks, when used in a yield calculation, are also indicated, and have a trailing identifier for first (1^{st}) and second (2^{nd}) escape peaks. The remainder of the peaks not labelled in each spectrum are escape peaks. In a number of cases escape peaks overlapped full energy peaks, and were removed prior to assigning an identification. The complexity of the γ-ray spectra vary from very simple for the beryllium target with 12 identified peaks, to that of the sodium fluoride and magnesium targets, with each containing over 100 identified transitions. The identification of these transitions was based on the reaction Q-values, given in table 5.1, and the published decay schemes and branching ratios [En90, En78, Aj87]. In addition to the target γ-ray transitions several neutron-induced background peaks were observed. In particular virtually all target spectra

Table 5.1: Q-Values for Target Reactions

Target	Reaction	Q-value (keV)	Target	Reaction	Q-value (keV)
Beryllium	$^{9}\mathrm{Be}\ (\alpha,n)^{12}\mathrm{C}$	5701	Magnesium	$^{24}\mathrm{Mg}\ (\alpha,p)^{27}\mathrm{A}\ell$	−1600
Boron Nitride	$^{10}\mathrm{B}\ (\alpha,n)^{13}\mathrm{N}$	1059		$^{25}\mathrm{Mg}\ (\alpha,n)^{28}\mathrm{Si}$	2654
	$^{10}\mathrm{B}\ (\alpha,p)^{13}\mathrm{N}$	4062		$^{25}\mathrm{Mg}\ (\alpha,p)^{28}\mathrm{A}\ell$	−1206
	$^{10}\mathrm{B}\ (\alpha,d)^{12}\mathrm{C}$	1340		$^{26}\mathrm{Mg}\ (\alpha,n)^{29}\mathrm{Si}$	35
	$^{11}\mathrm{B}\ (\alpha,n)^{14}\mathrm{N}$	158	Aluminum	$^{27}\mathrm{A}\ell\ (\alpha,n)^{30}\mathrm{P}$	−2643
	$^{11}\mathrm{B}\ (\alpha,n)^{14}\mathrm{C}$	784		$^{27}\mathrm{A}\ell\ (\alpha,p)^{30}\mathrm{Si}$	2372
	$^{14}\mathrm{N}\ (\alpha,p)^{17}\mathrm{O}$	−1192	Silicon	$^{28}\mathrm{Si}\ (\alpha,p)^{31}\mathrm{P}$	−1916
Sodium Fluoride	$^{19}\mathrm{F}\ (\alpha,n)^{22}\mathrm{Na}$	−1949		$^{29}\mathrm{Si}\ (\alpha,n)^{22}\mathrm{S}$	−1526
	$^{19}\mathrm{F}\ (\alpha,p)^{22}\mathrm{Ne}$	1676		$^{29}\mathrm{Si}\ (\alpha,p)^{32}\mathrm{P}$	−2454
	$^{23}\mathrm{Na}\ (\alpha,n)^{26}\mathrm{A}\ell$	−2968		$^{30}\mathrm{Si}\ (\alpha,n)^{33}\mathrm{S}$	−3493
	$^{23}\mathrm{Na}\ (\alpha,p)^{26}\mathrm{Mg}$	1818		$^{30}\mathrm{Si}\ (\alpha,p)^{33}\mathrm{P}$	−2960

contain a 7646/7631 keV doublet from thermal neutron capture on iron in the counting area and a 2614 keV γ-ray due to the inelastic scattering of fast neutrons on lead. Other general features of each target spectrum are discussed below.

5.1 γ-Ray Spectra

5.1.1 Be

The spectrum in figure 5.1 contains only the 4439 keV γ-ray transition from the first excited state of $^{12}\mathrm{C}$ created through the (α,n) reaction. The higher excited states of $^{12}\mathrm{C}$ are unbound to α-particle emission [Le78], and so produce negligible numbers of γ-rays, with the decay of the second excited state proceeding by γ-ray emission 1 in 2500 times [Aj80]. The remaining peaks result from neutrons interacting with materials around the target site. The strongest such peak in the spectrum results from the 2614 keV γ-ray from the $^{208}\mathrm{Pb}(n,n')$ reaction. The detector yield for this peak exhibited a large asymmetry with a yield in the forward detector typically twice

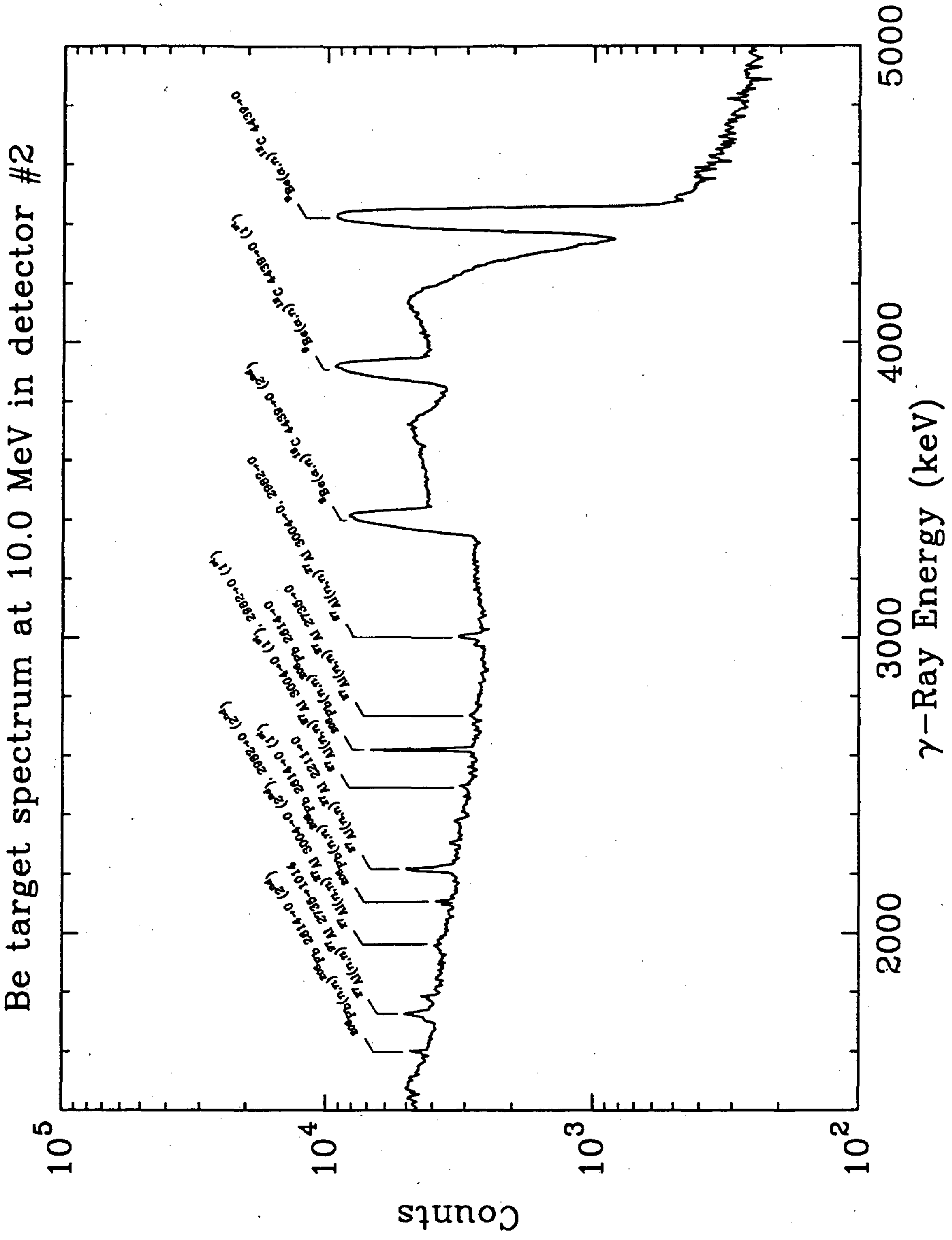

Figure 5.1: Beryllium target γ-ray spectrum in detector #2 from 10 MeV α-particles. All peaks used to calculate transition yields have been labelled. The remaining unlabelled peaks are comprised of escapes peaks. No γ-ray peaks above 4.6 MeV were observed.

that of detector #2, reflecting the known forward peaking of the neutron distribution and indicating that the lead shielding in front of each detector was the primary source of these γ-rays. The next strongest neutron induced reaction peak was the inelastic $^{27}\mathrm{A}\ell$ neutron scattering peak at 2211 keV. Aluminum in the target area included the positioning table for the detectors as well as the detector canister and cryostat. Because of the high yield of the 4439 keV γ-ray transition, only short runs with the Be target were performed, and a relatively small total number of neutrons were produced. Because of this, the neutron capture γ-rays from iron were not observed for this target.

5.1.2 BN

The principal γ-ray reactions observed in the BN target (figure 5.2) are the $^{10}\mathrm{B}(\alpha, p)$ and (α, d) reactions, the $^{11}\mathrm{B}(\alpha, n)$ and (α, p) reactions and the $^{14}\mathrm{N}(\alpha, p)$ reaction, in addition to inelastic scattering on target nuclei. The $^{14}\mathrm{N}$ nucleus was excited both by inelastic scattering and by the $^{11}\mathrm{B}(\alpha, n)$ reaction. The peaks resulting from the former reaction on the short-lived first, second and third excited states ($T_{1/2} < 0.9$ ps) should exhibit substantial peak broadening due to the additional Doppler shift from the scattered α-particle. The magnitude of such broadening should be comparable (approximately half, considering γ-ray energy, for a short-lived level near 2 MeV) with that of the $^{10}\mathrm{B}(\alpha, d)$ peak seen at 4440 keV in the spectrum. Since this broadening is not observed, inelastic scattering was not significant. This is supported by the results of Dyer *et al* [Dy85] who measured the inelastic scattering cross section on $^{14}\mathrm{N}$ between $E_\alpha = 7$ and 27 MeV. They reported observing significant excitations of only

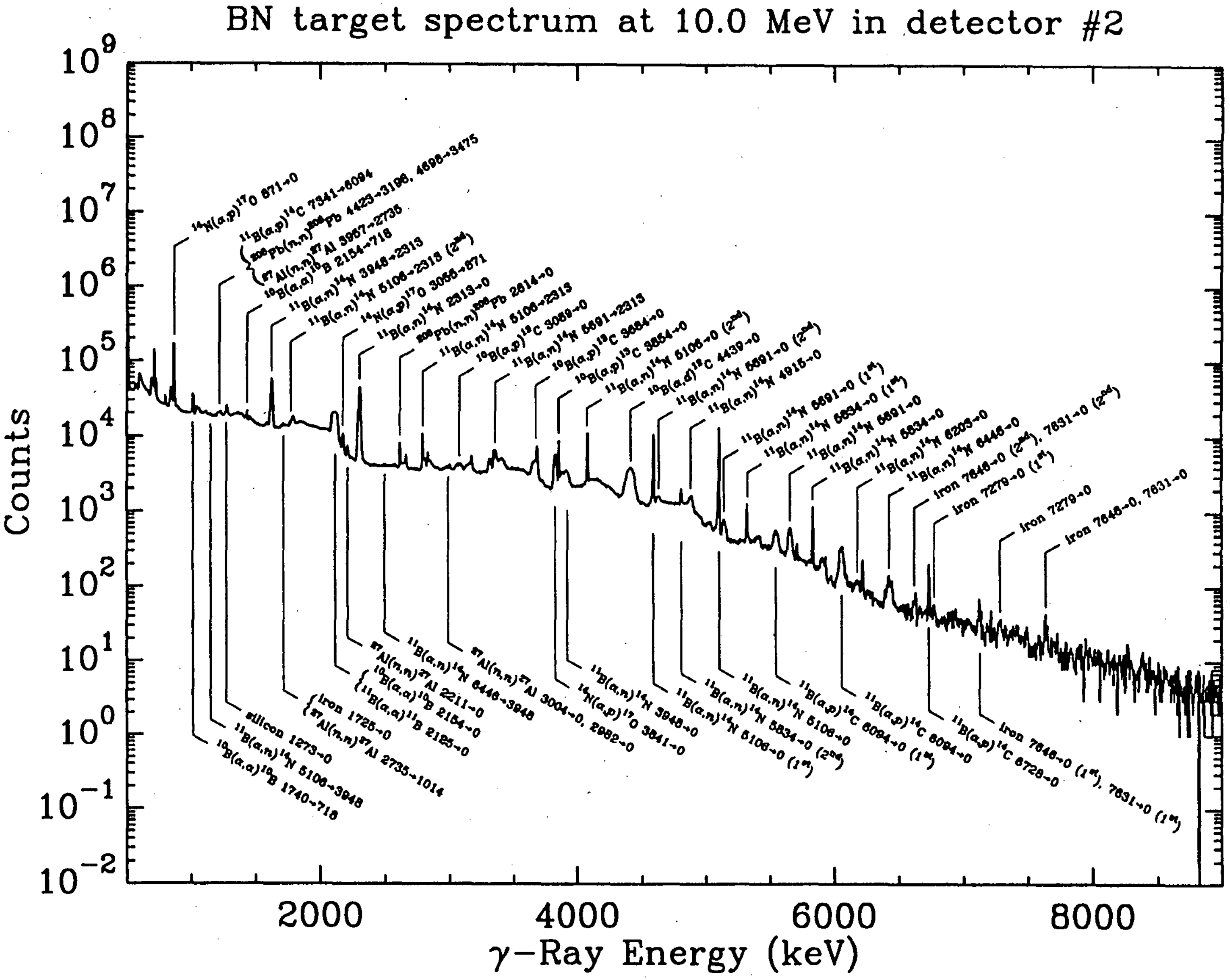

Figure 5.2: Boron nitride target γ-ray spectrum in detector #2 from 10 MeV α-particles. All peaks used to calculate transition yields have been labelled. The remaining unlabelled peaks are comprised of escapes peaks.

the second excited state of ^{14}N for E_α below 10 MeV which decayed through a cascade emission of a 1635 and 2313 keV γ-ray. From an integration of their reported cross sections, inelastic scattering was determined to be less than 15% of the (α, n) yield for this γ-ray at all energies.

Thermal neutron capture γ-rays from iron can be seen in the high energy region of the spectrum. The intensities of these peaks were affected by a number of factors including the neutron angular distribution and energy spectrum as well as the position of neutron thermalizing materials and neutron absorbers in the target area. The identification of this γ-ray is significant only for removing its interference and escape peaks from the spectrum.

5.1.3 NaF

The four observed reactions in the sodium fluoride target spectrum, (figures 5.3 through 5.5), consist of the (α, n) and (α, p) reactions on both ^{19}F and ^{23}Na. These reactions produced the most complicated γ-ray spectra of the targets studied here, and necessitated the subtraction of virtually all escape peaks. Reactions with the ^{19}F nucleus produced the most intense peaks, and in some cases obscured the less intense ^{23}Na reactions of a similar γ-ray energy. Peaks that contain significant contamination have been labelled with multiple identifications, and in some cases the individual intensity of these transitions could not be determined from the decay schemes.

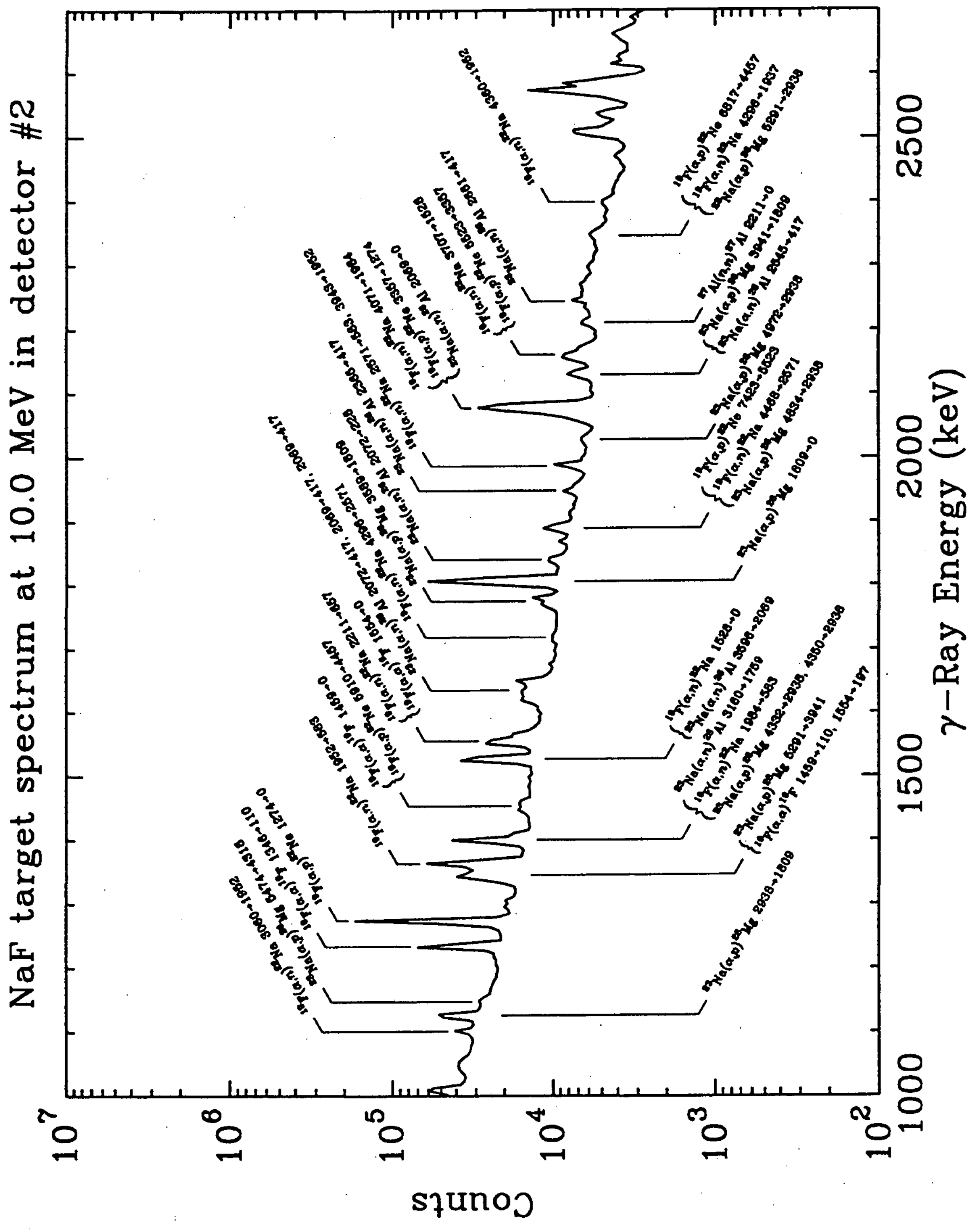

Figure 5.3: Sodium fluoride target γ-ray spectrum in detector #2 below 2.5 MeV from 10 MeV α-particles. All peaks used to calculate transition yields have been labelled. The remaining unlabelled peaks are comprised of escapes peaks.

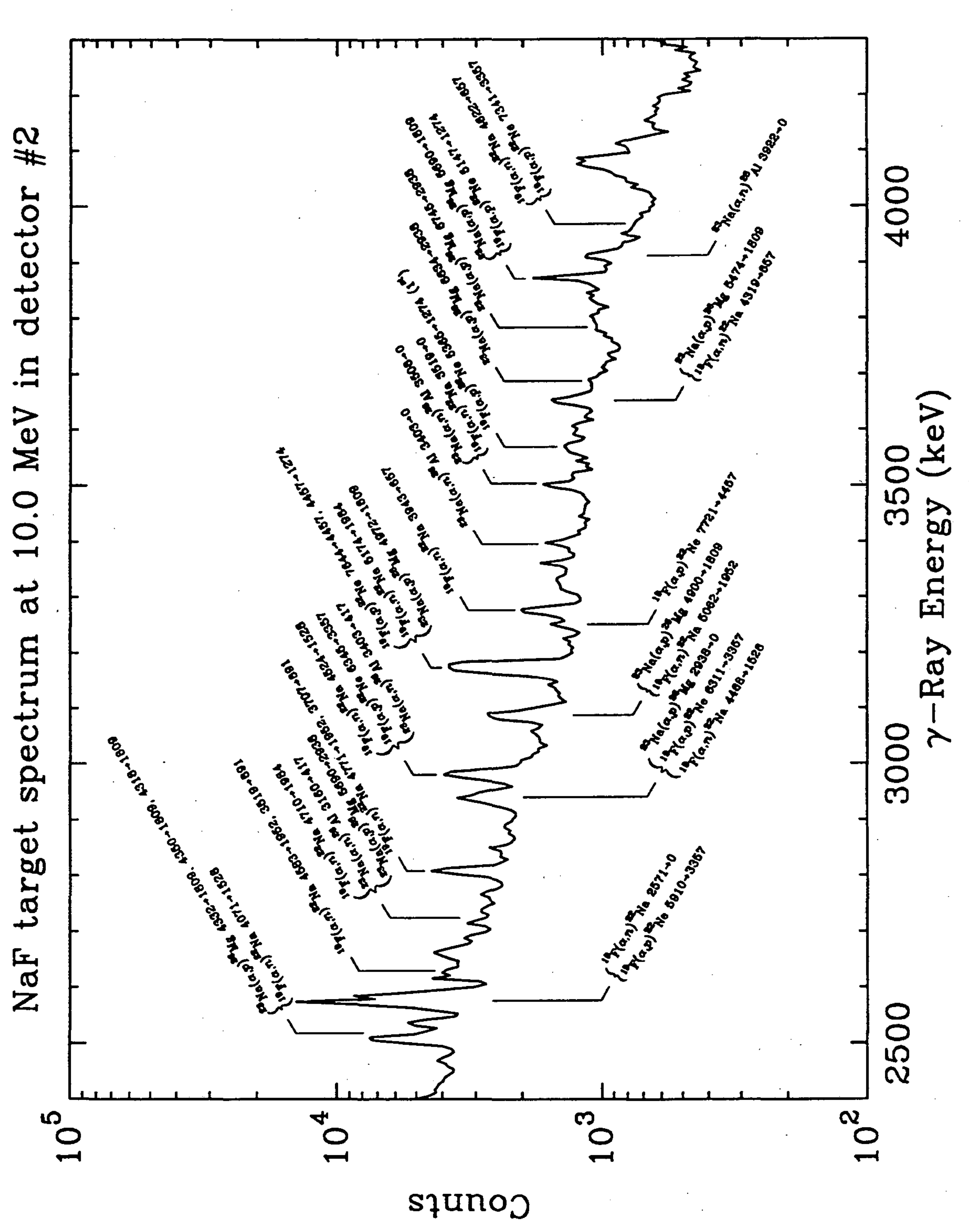

Figure 5.4: Sodium fluoride target γ-ray spectrum in detector #2 between 2.5 and 4 MeV from 10 MeV α-particles. All peaks used to calculate transition yields have been labelled. The remaining unlabelled peaks are comprised of escapes peaks.

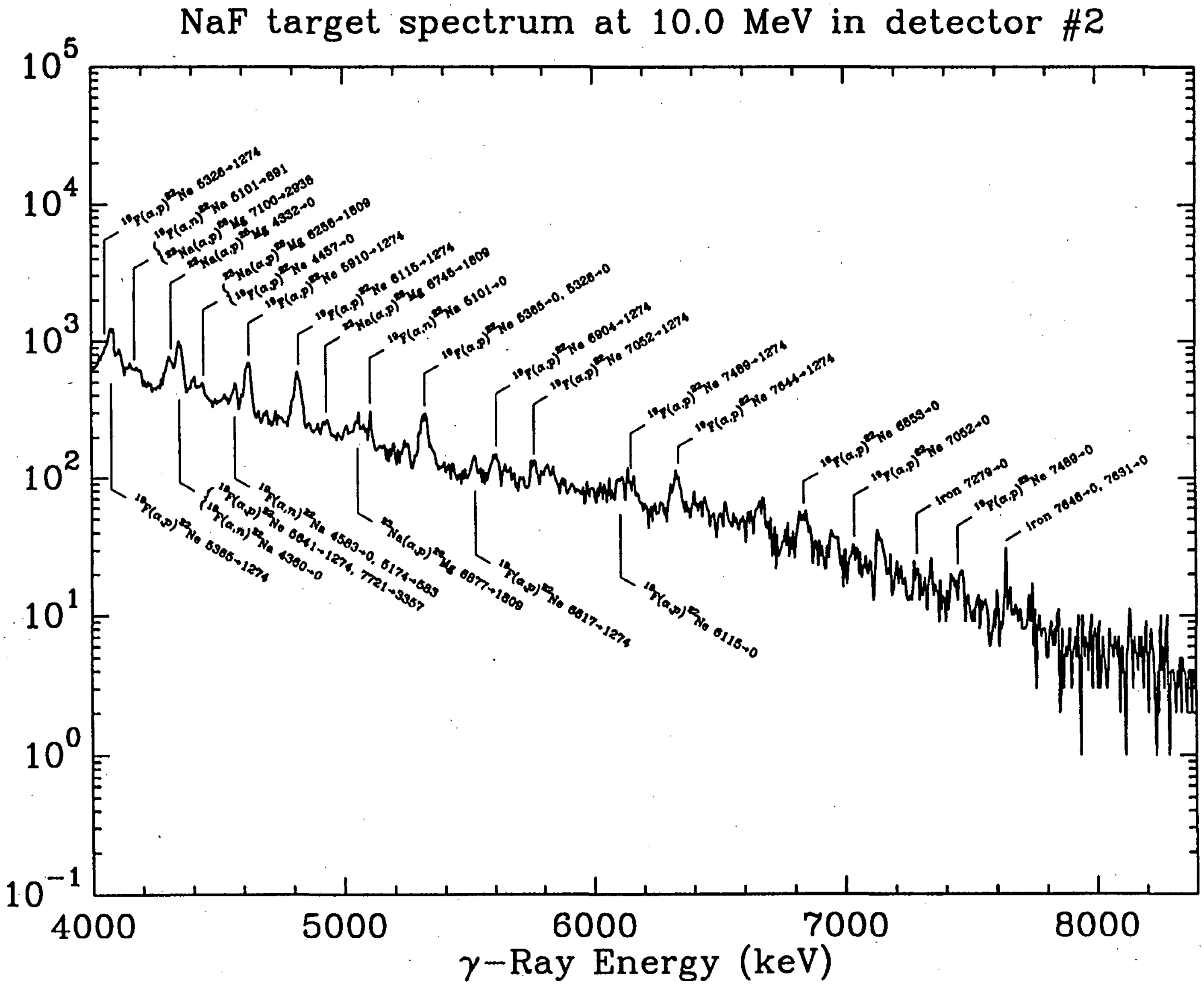

Figure 5.5: Sodium fluoride target γ-ray spectrum in detector #2 above 4 MeV from 10 MeV α-particles. All peaks used to calculate transition yields have been labelled. The remaining unlabelled peaks are comprised of escapes peaks.

5.1.4 Mg

The magnesium target spectrum, shown in figures 5.6 through 5.8, produced the most energetic γ-rays observed, with energies approaching 10 MeV. Five reactions contribute to the observed γ-ray spectrum: the (α, n) and (α, p) reactions on ^{25}Mg and ^{26}Mg and the (α, n) reaction on ^{24}Mg. The $^{25}\mathrm{Mg}(\alpha, n)$ reaction provided the dominant yield of high energy γ-rays for this target. The existence of the very highest energy γ-rays was indicated by the presence of the first and second escape peaks rather than the full energy peak, as escape peaks occurred at approximately twice the intensity of the full energy peak at these energies.

The pulser peak placed in the high energy part of each spectrum can be seen in figure 5.8. This peak occurs above 10 MeV in the spectra, and so is only shown when γ-rays approaching this energy were detected.

5.1.5 Aℓ

The aluminum target spectrum is shown in figures 5.9 and 5.10. Both the (α, n) and (α, p) reactions on ^{27}Aℓ contribute γ-rays to the spectrum, with the highest energy γ-rays resulting from the (α, p) reaction. At high α-particle energies the 7646/7631 keV iron doublet from thermal neutron capture doublet interfered with the 7623 keV γ-ray from the target.

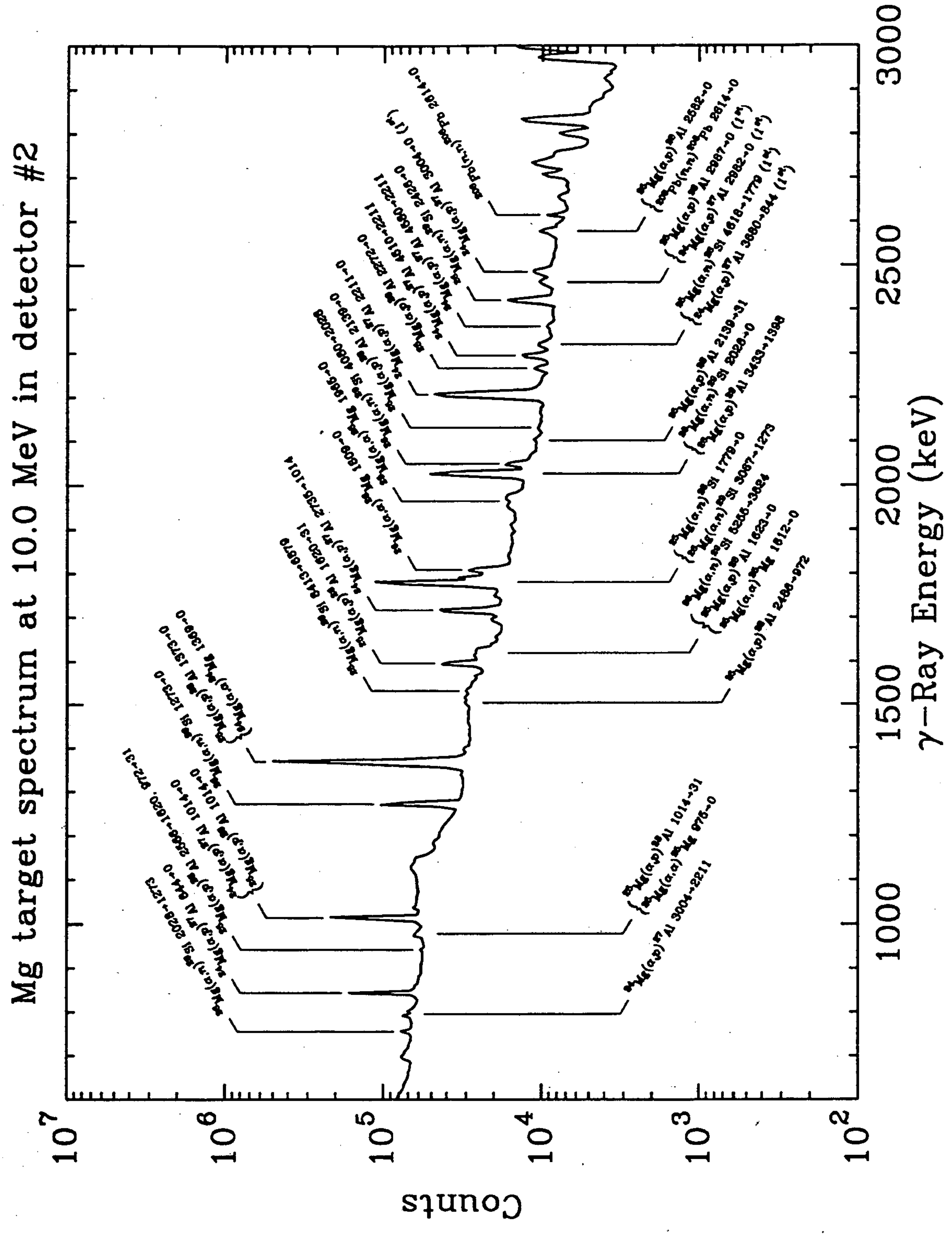

Figure 5.6: Magnesium target γ-ray spectrum in detector #2 below 2.65 MeV from 10 MeV α-particles. All peaks used to calculate transition yields have been labelled. The remaining unlabelled peaks are comprised of escapes peaks.

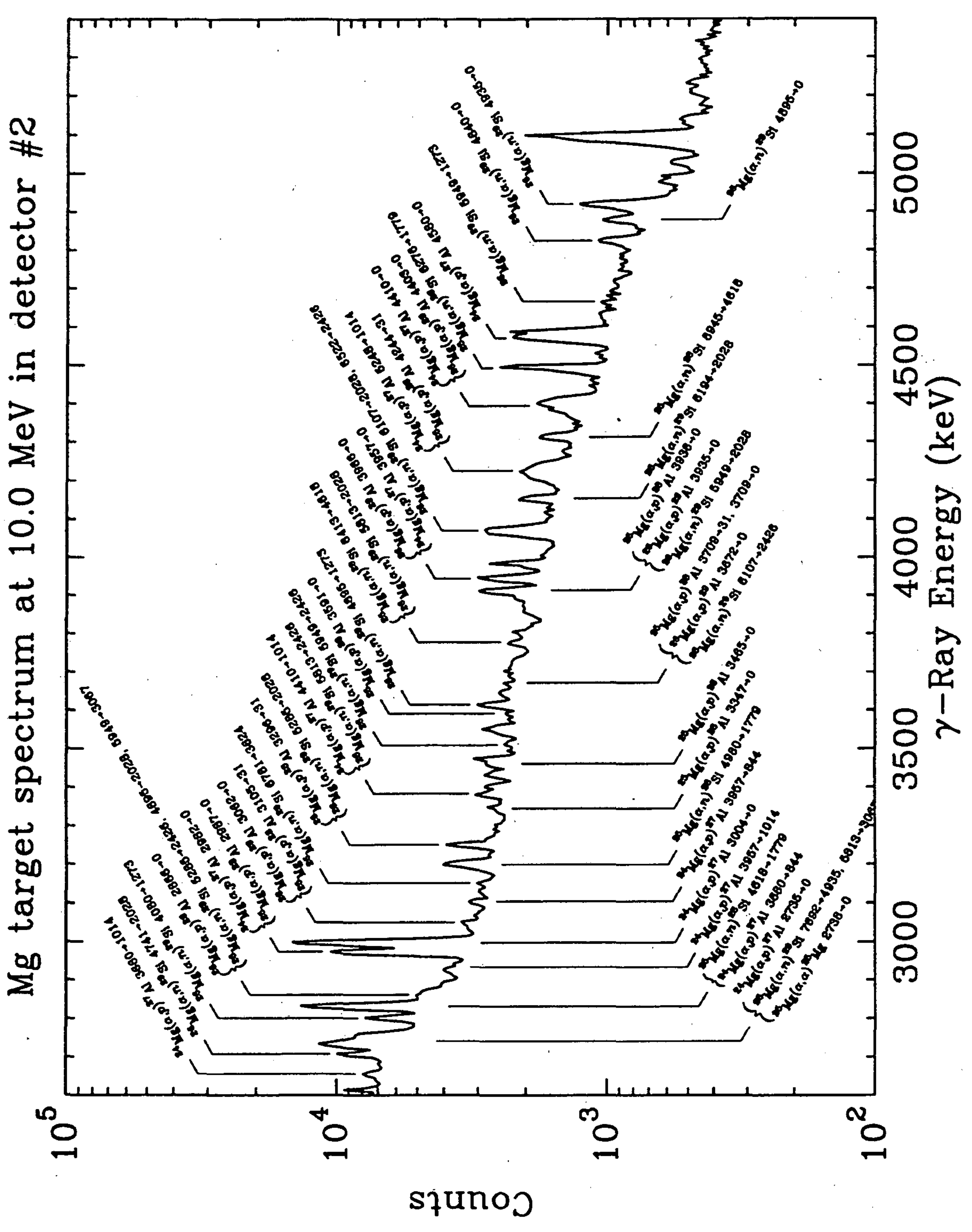

Figure 5.7: Magnesium target γ-ray spectrum in detector #2 between 2.65 and 5 MeV from 10 MeV α-particles. All peaks used to calculate transition yields have been labelled. The remaining unlabelled peaks are comprised of escapes peaks.

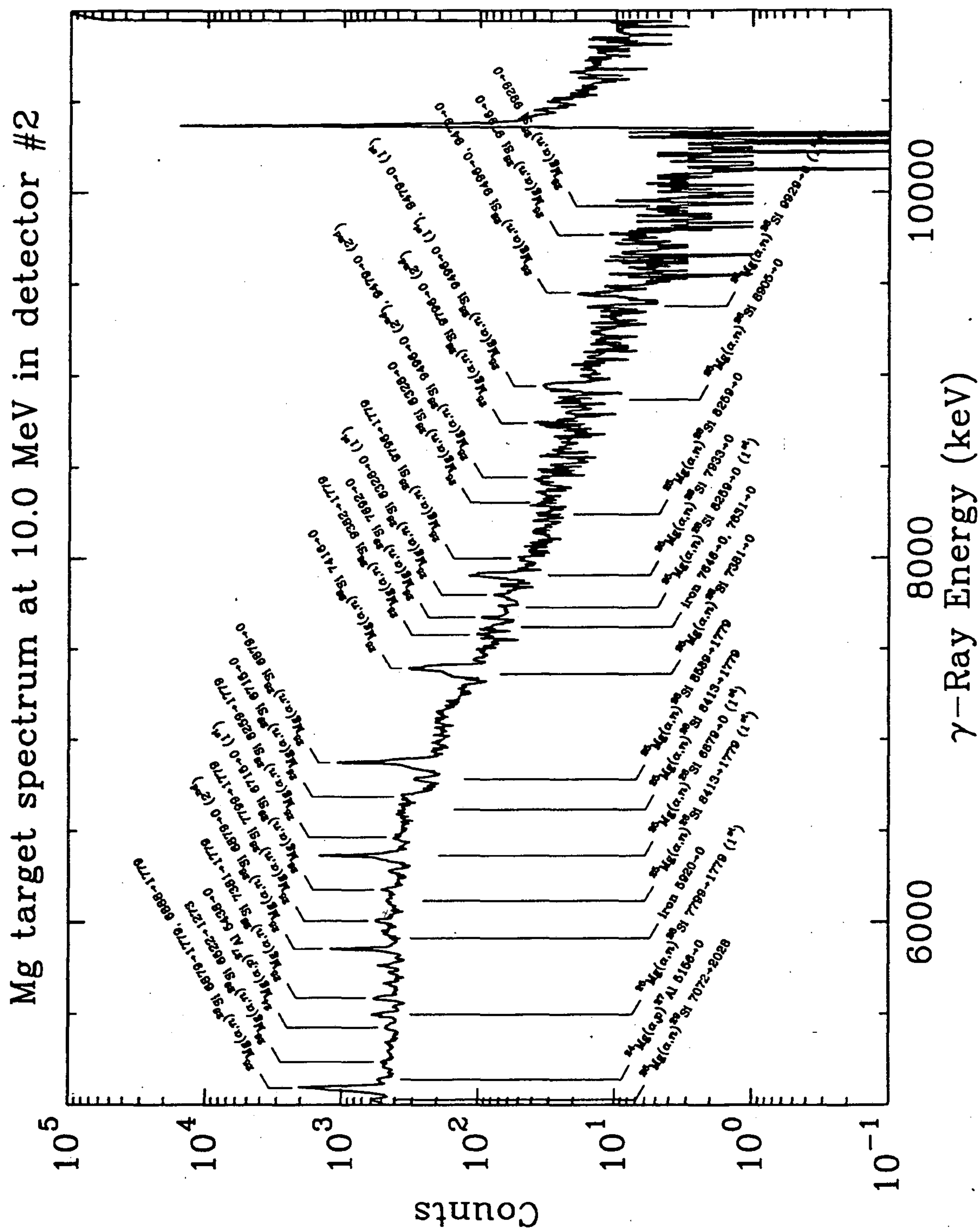

Figure 5.8: Magnesium target γ-ray spectrum in detector #2 above 5 MeV from 10 MeV α-particles. All peaks used to calculate transition yields have been labelled. The remaining unlabelled peaks are comprised of escapes peaks.

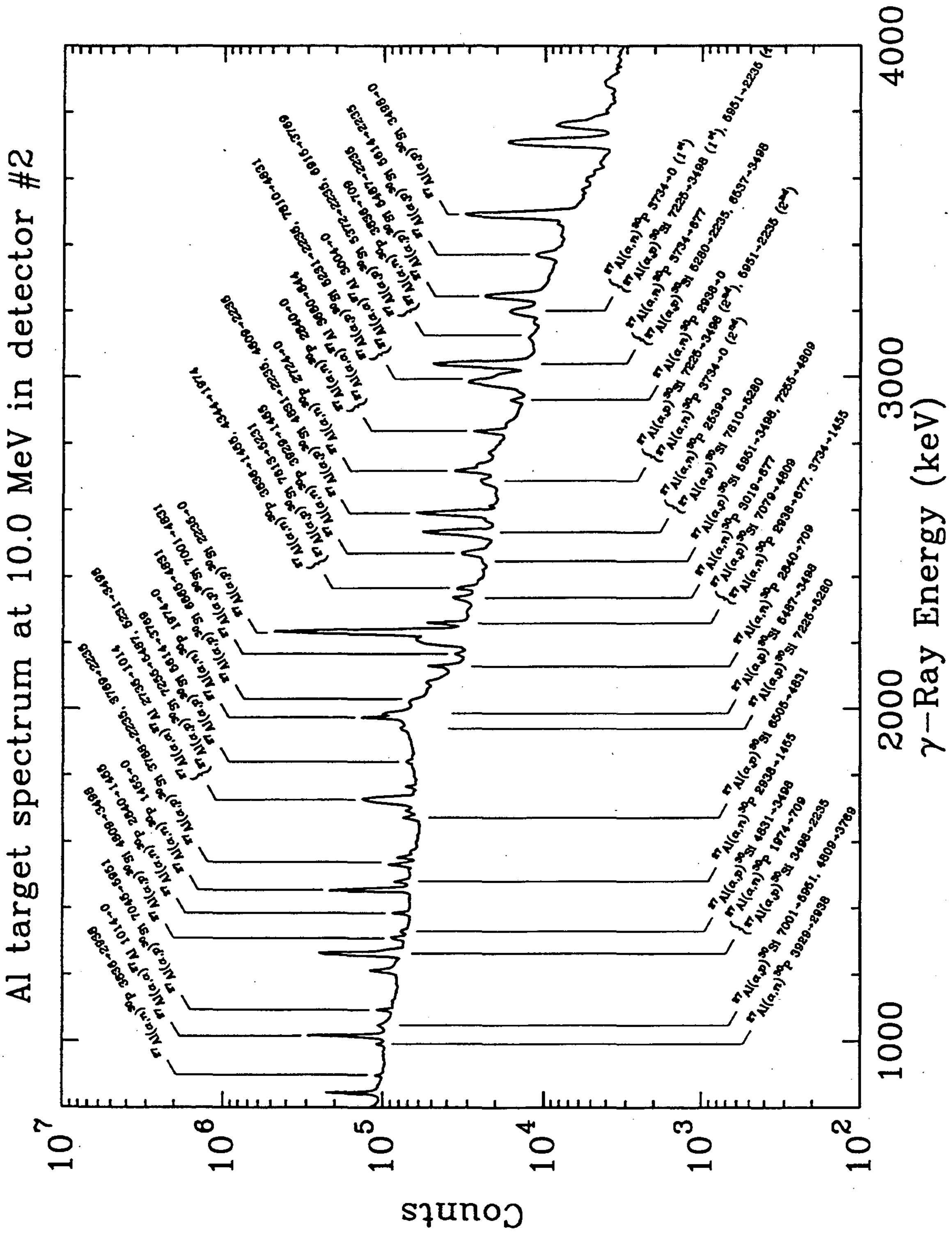

Figure 5.9: Aluminum target γ-ray spectrum in detector #2 below 3.5 MeV from 10 MeV α-particles. All peaks used to calculate transition yields have been labelled. The remaining unlabelled peaks are comprised of escapes peaks.

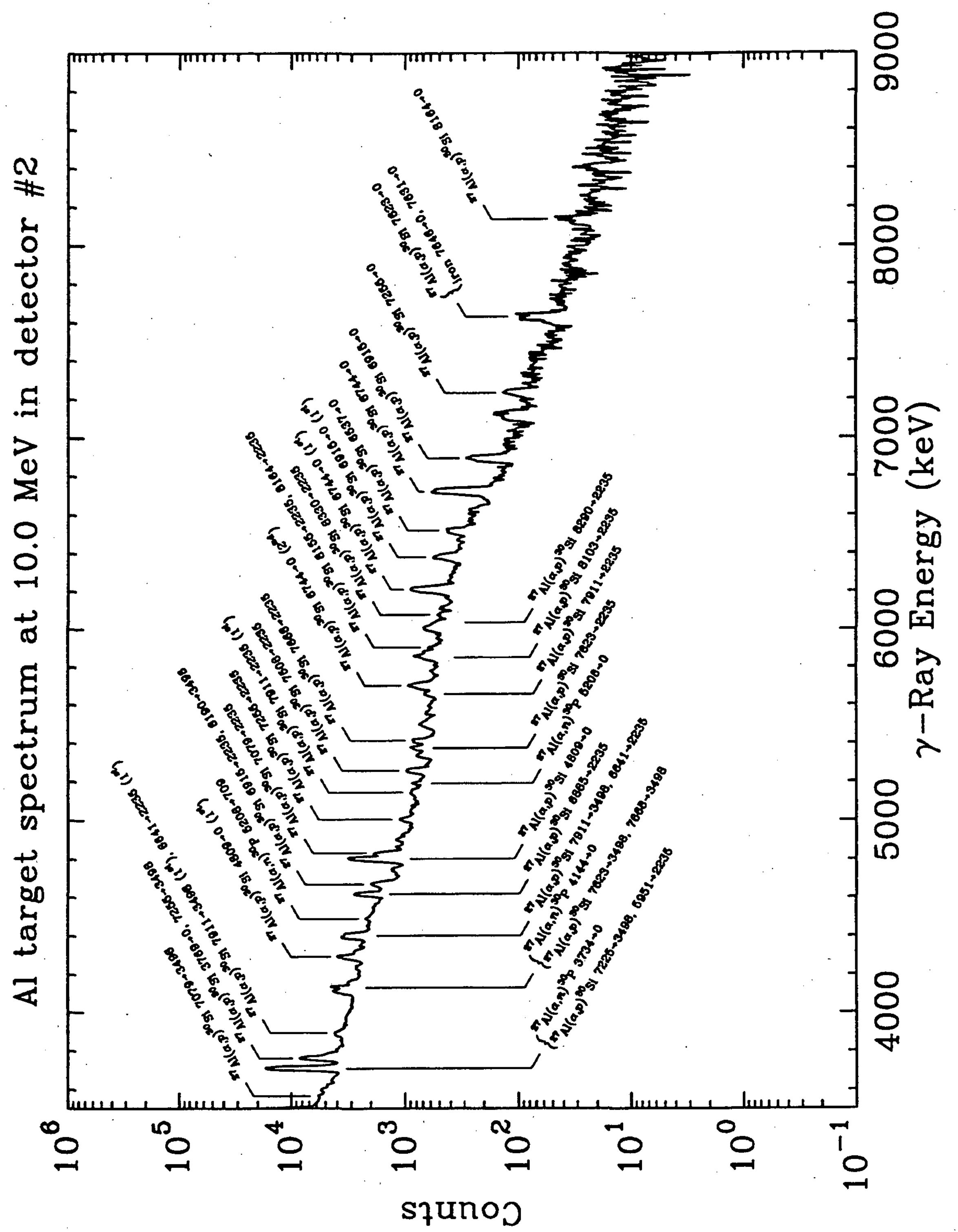

Figure 5.10: Aluminum target γ-ray spectrum in detector #2 above 3.5 MeV from 10 MeV α-particles. All peaks used to calculate transition yields have been labelled. The remaining unlabelled peaks are comprised of escapes peaks.

5.1.6 Si

Figures 5.11 and 5.12 show the silicon target γ-ray spectrum for 10 MeV α-particles in detector #2. This was the only α-particle energy at which this target was studied due to the relatively low activity and energy of the observed γ-rays. Reactions were seen from each of the ^{28}Si, ^{29}Si and ^{30}Si isotopes, although only the (α, p) reaction occurred in ^{28}Si, the most abundant isotope, while both the (α, n) and (α, p) reactions were observed from the other two isotopes.

5.2 Thick-Target Yields

Yields were determined from the area of the measured peaks in detectors #1 and #2 as described in section 3.3.4. The conversion of the peak areas into yields required knowledge of the absolute detection efficiency, the detector live times, and the number of α-particles on target. Each of these contributed to the systematic uncertainty of the measured yield. The detector efficiency contributed a γ-ray energy dependent uncertainty between 1% and 10%, in addition to a 3.5% uncertainty determined from stability measurements and target positioning considerations. The live time in each detector was determined for runs other than $E_\alpha = 10$ MeV to within 1% from the area of the pulser peak inserted into each spectrum; in some cases this uncertainty was increased in detector #1 by gain instabilities, and in detector #2 by a pile-up of γ-ray counts on the tail of the pulser. In these cases the live time uncertainty did not exceed 6% for either detector. In the 10 MeV runs, the live time was deduced from the counting rate in each detector, resulting in larger systematic uncertainties. The

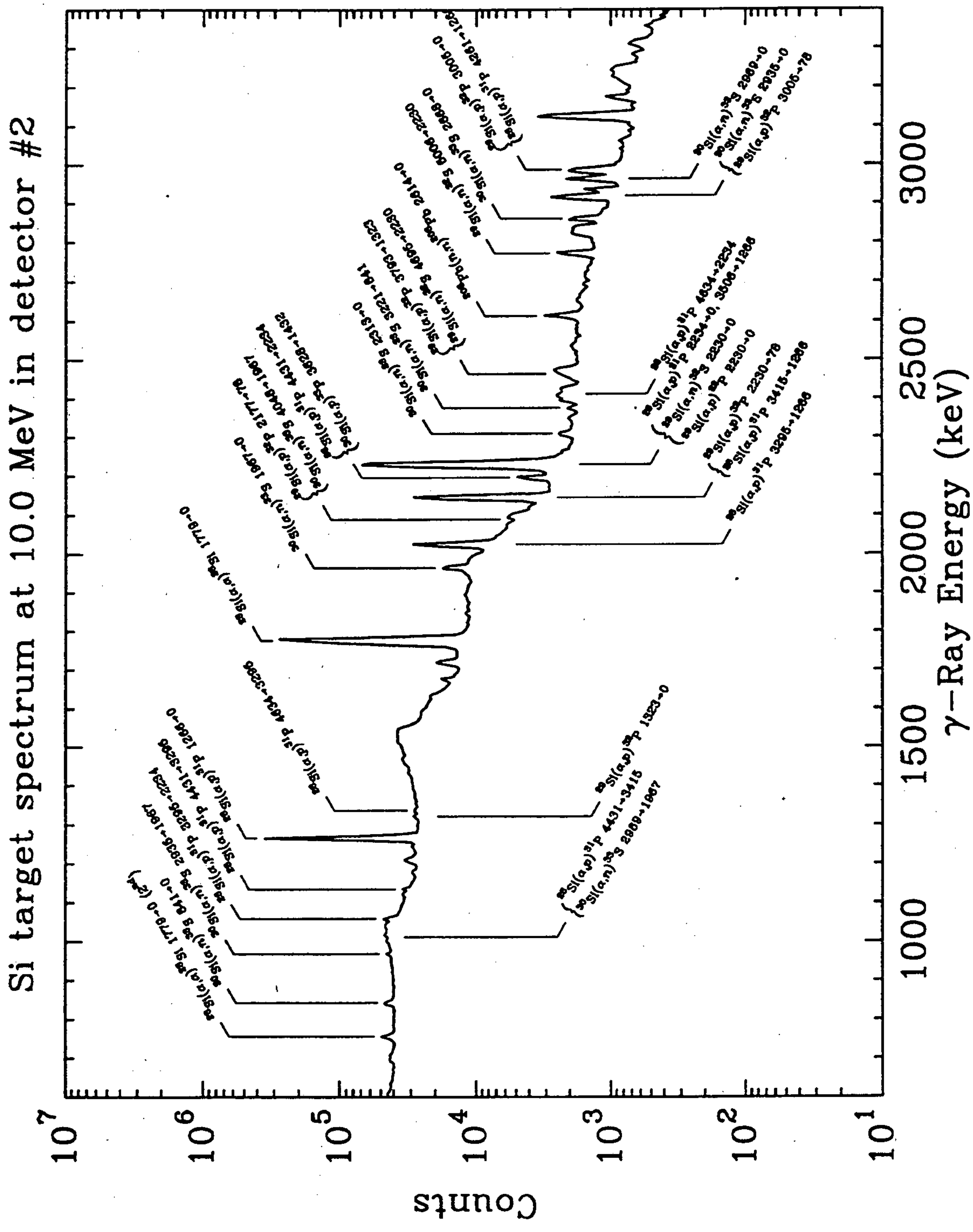

Figure 5.11: Silicon target γ-ray spectrum in detector #2 below 3.1 MeV from 10 MeV α-particles. All peaks used to calculate transition yields have been labelled. The remaining unlabelled peaks are comprised of escapes peaks.

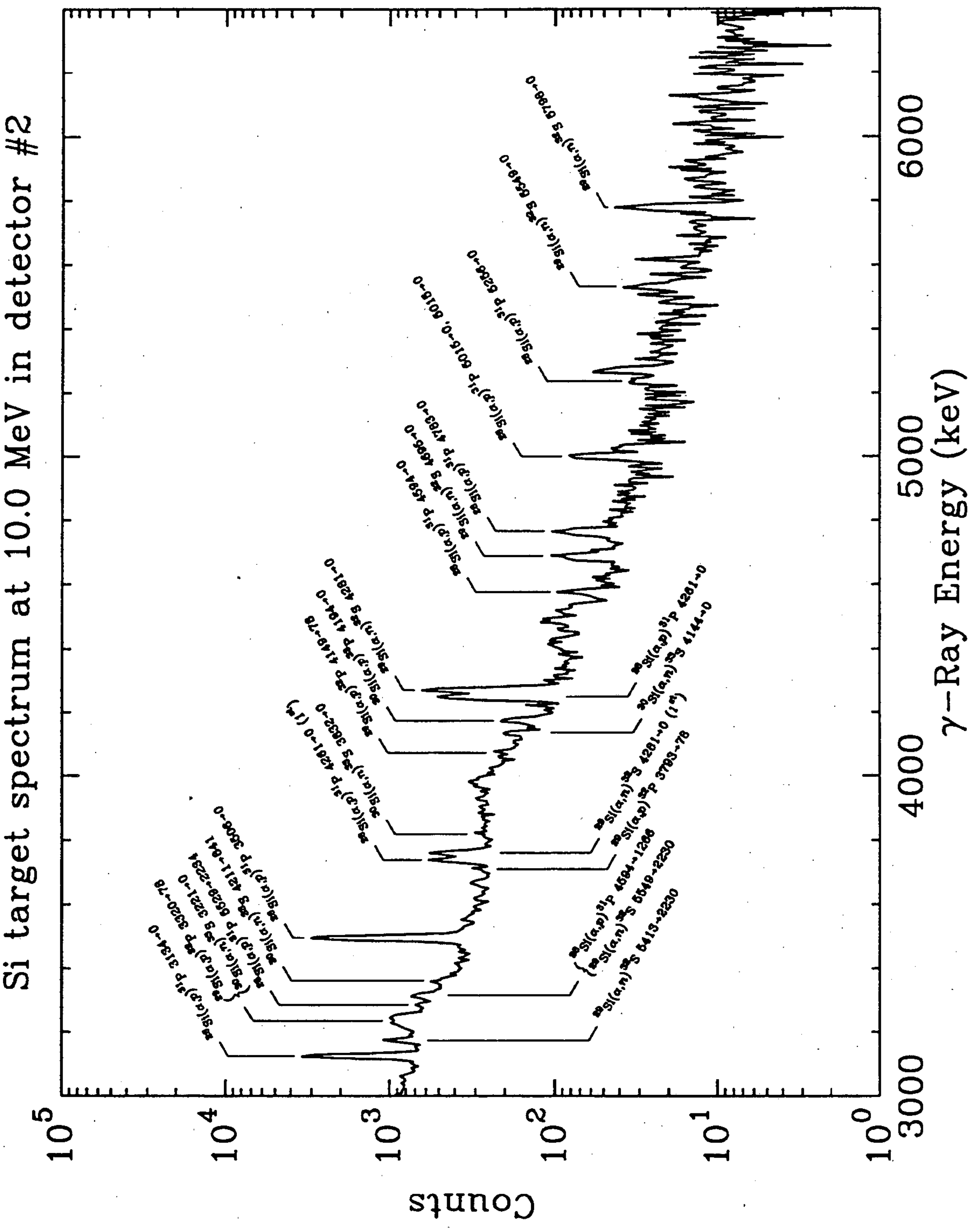

Figure 5.12: Silicon target γ-ray spectrum in detector #2 above 3.1 MeV from 10 MeV α-particles. All peaks used to calculate transition yields have been labelled. The remaining unlabelled peaks are comprised of escapes peaks.

uncertainty in the live time was taken as the difference between the rate-based live time and the pulser peak live time, which contributed an additional uncertainty of less than 10% in these live times, except for the Aℓ and Be targets, where an uncertainty of close to 20% was assessed for the forward detector. This live time calculation is detailed in appendix B.

The total number of particles on target was determined by the number of counts generated by the beam current integrator and accumulated in the scaler; since the pulser system was triggered by the same signal as the scaler, the area of the pulser peak directly determined the live-time corrected particles on target, and as such the beam count uncertainty was included in the determination of the live time uncertainty. The only case where an additional uncertainty was assessed for the number of particles on target was in the $E_\alpha = 8.8$ MeV runs, where a large beam halo was responsible for a loss of particles on the target ladder lead shielding. A $23 \pm 10\%$ beam loss was determined for the $E_\alpha = 8.8$ MeV runs. The determination of this factor is discussed below.

The beam halo in the $E_\alpha = 8.8$ MeV runs resulted from a degraded beam focus caused by using the cyclotron at the lower limit of its range in extracting He^{++} at 8.8 MeV. Both systematic changes in the yield behaviour and comparison of the measured yields to cross section data reported by other groups indicate that 20% to 30% of the beam was contained in the halo.

The size of the beam halo loss was deduced from a comparison of our thick target yields with those calculated from the cross section measurements of other groups.

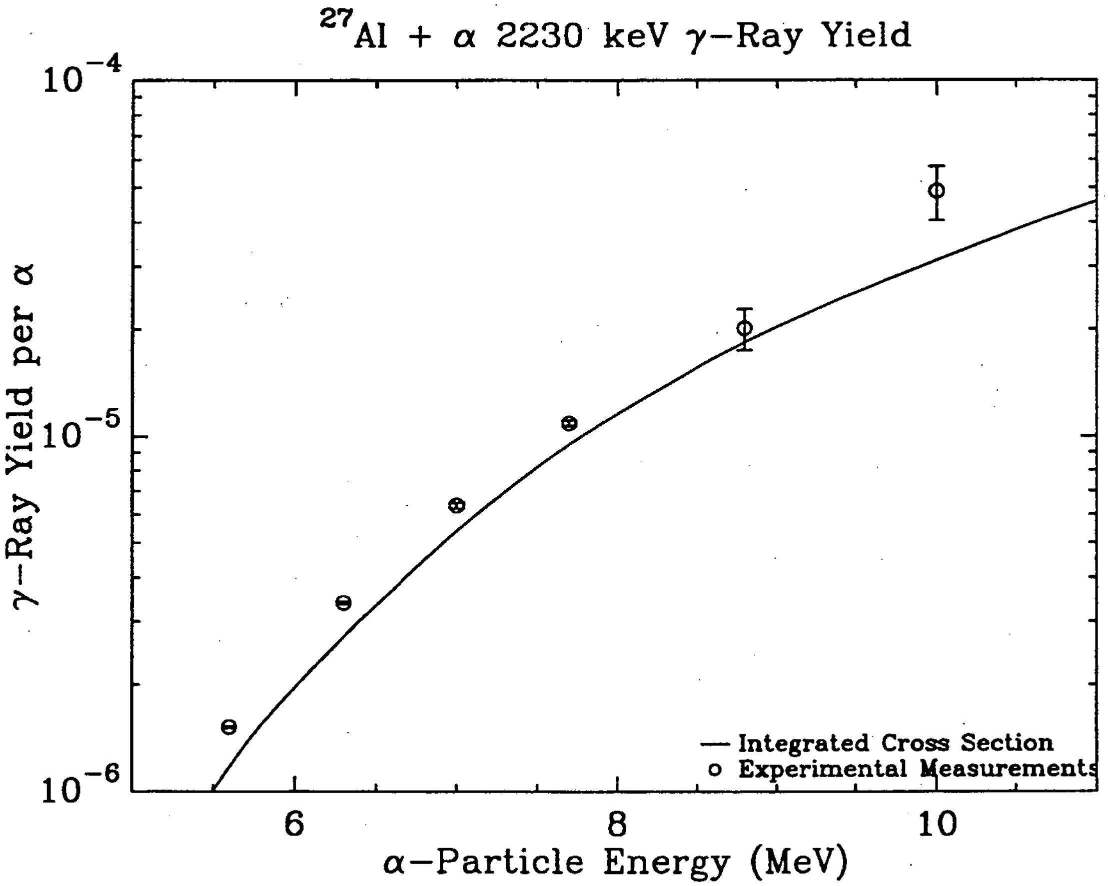

Figure 5.13: The 2230 keV yield from the $A\ell$ target. The points indicate the fully corrected yield measurements, while the solid line indicates the thick-target yield calculated from an integration of the cross sections of Seamster *et al.* Both data sets contain the yield from the 2235 keV and 2210 keV γ-rays resulting from the (α, p) and (α, α') reactions respectively. The large increase seen in the yield at 10 MeV is attributed to an increase in the 2210 keV (α, α') yield at this highest energy.

The cross sections for the 2230 keV and 2210 keV γ-rays from the $^{27}A\ell+\alpha$ and the $^{24}Mg(\alpha,p)$ reactions respectively have been measured by Seamster *et al* to an accuracy of 10% [Se84]. A comparison of our thick-target yields to those calculated from the cross sections reported by Seamster *et al* is shown in figures 5.13 and 5.14. At energies other than 8.8 MeV, our thick-target yields are approximately 13% higher than those based on the cross section measurements of Seamster. However, the unadjusted measured yields at $E_\alpha = 8.8$ MeV are significantly lower. Since no anomaly in either cross section was reported by Seamster *et al*, this behaviour was attributed to a large beam halo. A beam loss of 19% would increase the $A\ell$ target yield to the level of the measurements of Seamster *et al*, while a beam loss of 30% suggested by thick-target yields at other energies would increase the calculated yield to 16% above Seamster *et al.* Similarly, a beam loss of 24% would increase the yields from the Mg target to that of Seamster *et al*, while a beam loss of 30% would bring the yields to 11% above the cross section based yields.

A smaller beam halo loss is inferred from the Be target data. The 8.8 MeV data falls 12% below that of the cross section based yields and is consistent with the lower energy yields. The yields below 8 MeV were calculated from the cross section data of Geiger and Van der Zwan [Ge75, Ge76], who report a total uncertainty between 11 and 15%. The differential γ-ray cross section measurements of Seaborn *et al* [Se63] at 0° and 90° were used to obtain yields above 8 MeV. These cross sections agree within 30% with measurements at four energies by Verbinski *et al* [Ve68]. Consequently we have assessed the yield above 8 MeV with a larger uncertainty than that quoted by

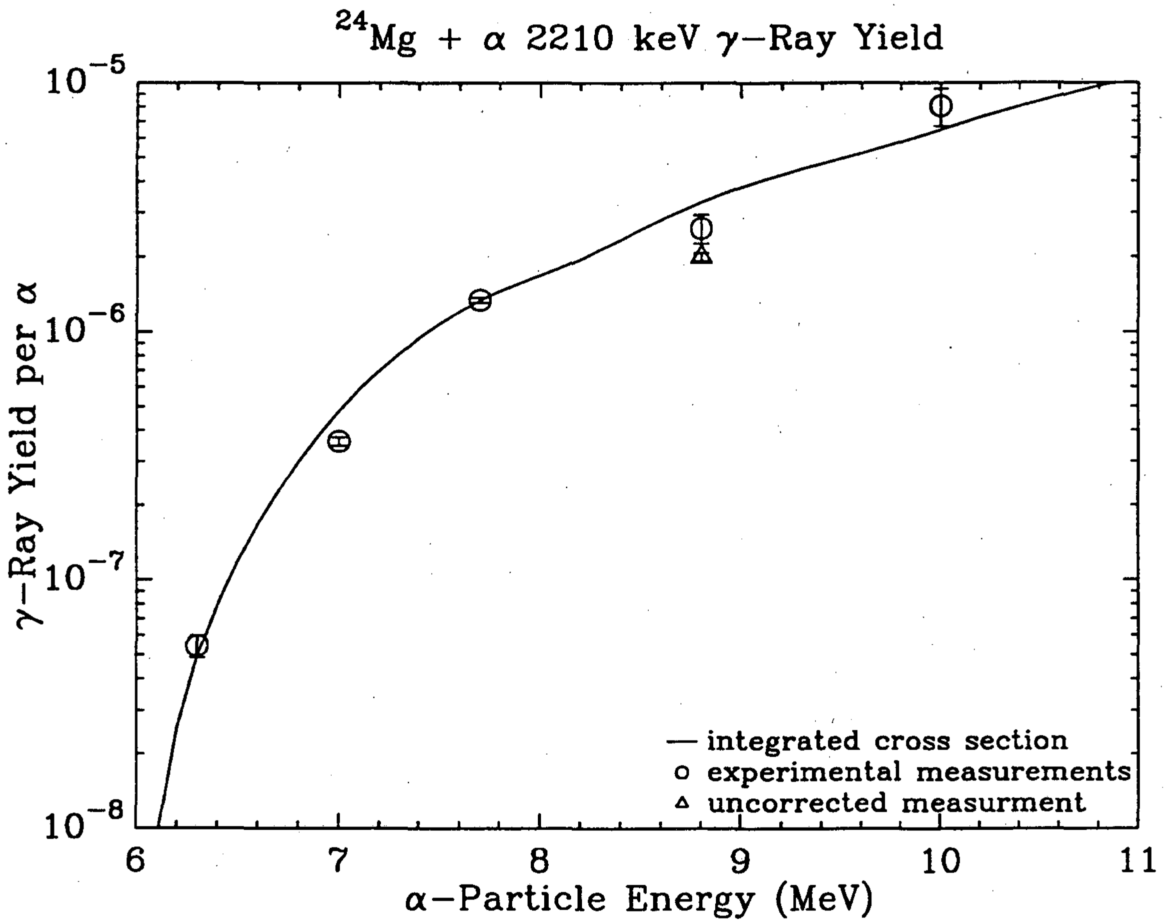

Figure 5.14: 2210 keV yield from the Mg target. The points indicate the fully corrected yield measurements, while the solid line indicates the thick-target yield calculated from an integration of the cross sections of Seamster *et al*[Se84].

Geiger and Van der Zwan, and so used these yields only as a guide in characterizing the beam halo loss.

As a result of these considerations, a beam loss of $(23 \pm 10)\%$ was attributed to all 8.8 MeV run data, resulting in a scaling of the yields by 1.30 ± 0.13.

The yields were calculated from the combined full energy and escape peak yields when available. The escape and full energy peak yields were found to be in agreement within statistical uncertainties in all cases. A representative number of the thick-target γ-ray yields are shown in figures 5.15 and 5.16. These yields correspond to single transition peaks from various reactions, and have been adjusted to provide yields from elemental targets. The thick-target yields in most cases follow a smooth function of energy. The yields for individual transitions change by as much as three orders of magnitude between 5.6 and 10 MeV α-particle energies. All thick-target yields follow the expected monotonic decrease with α-particle energy. In some instances, such as the $^{10}\mathrm{B}(\alpha, d)^{12}\mathrm{C}$ 4439 → 0 keV reaction in figure 5.15 and the $^{24}\mathrm{Mg}(\alpha, p)^{27}\mathrm{A}\ell$ 3004 → 0 keV reaction of figure 5.16, the effects of strong resonances cause a significant change in the yield behaviour.

The uncertainties in our calculated yields combine contributions from a number of different sources. In the highest α-particle energy runs, the most significant source of uncertainty resulted from the 10 MeV live time determinations and the 8.8 MeV beam halo adjustment. The 10 MeV live time determination introduced uncertainties ranging from as much as 15% for the Aℓ and Be targets to as little as 3% in the NaF target. At other energies, the detector live time contributed between 0.5% and

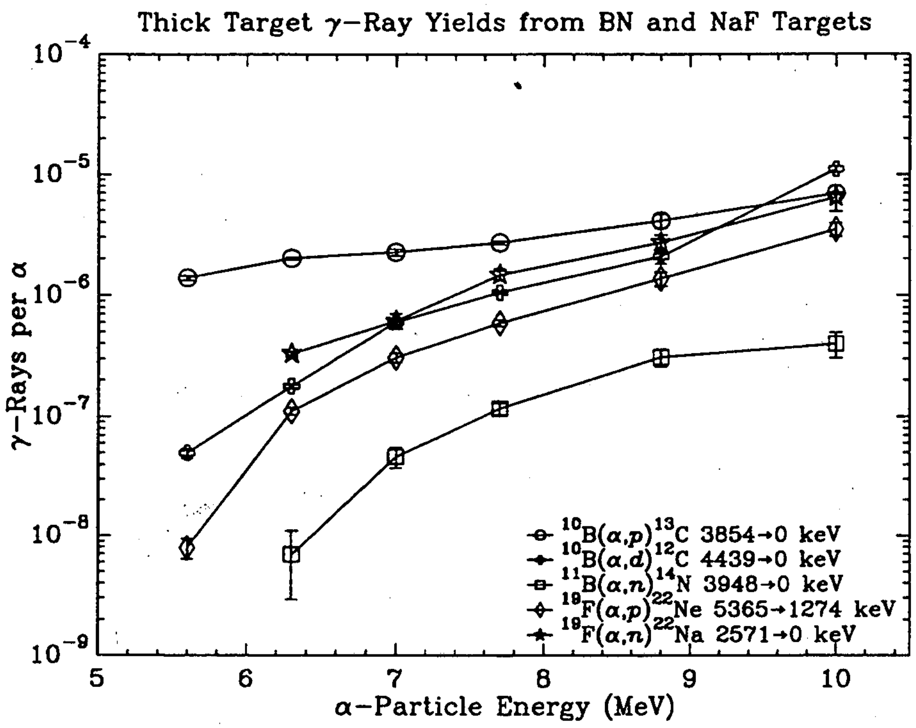

Figure 5.15: Selected yields from the BN and NaF targets. Only yields from peaks with unique identifications have been shown. The joining line between yields is provided as a visual aid only.

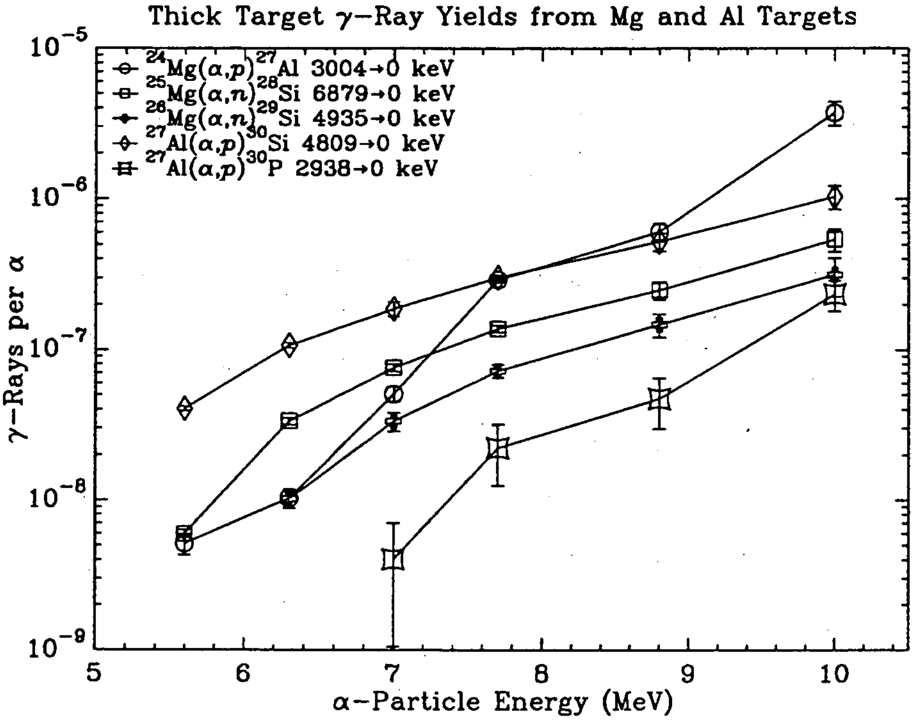

Figure 5.16: Selected yields from the Mg and $A\ell$ targets. Only the thick-target yields from peaks with unique identifications have been shown. The line joining measure yields is provided as a visual aid only.

2% to the yield uncertainty, and the detector efficiency uncertainties, discussed previously, played a more significant role with contributions as large as 11%. Statistical uncertainties in the peak area accounted for a contribution on the order of 10% to 15% for all but the weakest transitions. Uncertainties based on the selection of the background type were typically of the same order as the statistical uncertainties, with values ranging from 2% to 15% in most cases. In cases where branching ratios were required to separate individual transitions, the branching uncertainty typically added between 10% and 25% to the total uncertainty in the yield. Branching ratios were primarily used in the calculation of the NaF, Mg and Aℓ target yields.

Our yield measurements are presented below in two forms, reflecting the requirements of our studies. The first set of tables provides a basis from which γ-ray spectra for a composite material may be constructed for use in background calculations; such spectra are of importance in assessing the results obtained in rare-event experiments, and have been calculated for a number of materials in the SNO detector. The second set of tables reports the reaction based yield, and has been used in this study to quantify the excitation state of the residual nucleus, and so assess our statistical model calculations of nuclear reactions. Both these calculations are discussed in chapter 6.

5.2.1 High Energy γ-Ray Yields for Spectrum Calculations

Tables 5.2 through 5.8 provide a basis from which α-induced γ-ray spectra for composite materials can be calculated. The tables consist of the thick-target γ-ray yields for each element, summed into 1 MeV wide bins. These elements consist of common light elements with favourable Q-values for the production of high energy γ-rays. All α-particle energies investigated, except for 10 MeV, correspond to the range of primary α-particle energies encountered in the natural uranium and thorium decay chains. The 10 MeV measurement provided a limiting measurement for the highest possible yield. The yield for each element has been adjusted to reflect elementally pure targets with normal isotopic abundances. The yields measured from the composite BN and NaF targets were adjusted based on the ratio of the stopping powers of the individual elements in each target [He89]. For the BN target, this resulted in a multiplication of the observed boron yields by a factor of 2.30 and the nitrogen yields by a factor of 1.77. Similarly, for the NaF target, the fluorine yields were multiplied by 2.25 and the sodium by 1.80. Variations in the stopping power ratio calculation of 0.5% over the beam energies considered here were observed; this uncertainty has been neglected in these yield tables.

The uncertainties quoted in these tables contain both the statistical and systematic uncertainties discussed in the previous section. The statistical uncertainties were summed in quadrature, while the separate systematic uncertainties were simply added, and the total uncertainty in each bin determined from a quadrature sum of the individual statistical and systematic uncertainties for the bin. In this presentation of our data, no attempt has been made to separate γ-rays of a similar energy resulting from different reactions on the same element in the target, and so branching ratio uncertainties do not affect most binned yields. In some cases, yields from the composite BN and NaF targets had to be separated using decay schemes published in the literature

[En78, En90, Aj87], or estimated by other means. The treatment of the special cases directly affecting these tables is discussed briefly below; a more detailed discussion of individual transition yields adjustments is presented in section 5.2.2.

No yield table has been provided for the single α-particle energy investigation of the silicon target. The $E_\alpha = 10$ MeV summed yields for this target are $(1.84 \pm 0.07) \cdot 10^{-5}$ quanta MeV^{-1} per α for 2 to 3 MeV γ-rays, $(1.55 \pm 0.06) \cdot 10^{-6}$ quanta MeV^{-1} per α for 3 to 4 MeV, $(4.42 \pm 0.22) \cdot 10^{-7}$ quanta MeV^{-1} per α for 4 to 5 MeV and $(5.48 \pm 0.49) \cdot 10^{-8}$ quanta MeV^{-1} per α for 5 to 6 MeV γ-rays.

Only yields from the NaF target were significantly affected by ambiguous γ-ray transition identifications. In cases where a spectrum peak was associated with reactions from both target nuclei, published decay schemes were used to separate the yields where possible. In cases where only an estimate of a transition yield from a minor contributor to the total peak was available, a 100% uncertainty for that contributor was adopted. In most cases these estimated yields only accounted for a small fraction the yield attributed to a given energy bin. An exception to this is seen in the 2 to 3 MeV bin, where a large peak associated with both the ^{23}Na$(\alpha,n)^{26}$Aℓ 2069 $\rightarrow$ 0 keV and the ^{19}F$(\alpha,p)^{22}$Ne 3357 $\rightarrow$ 1274 keV yield accounts for about 70% of the yield from the target in this energy range. In this case, the yield was divided equally between the two reactions with a 100% uncertainty in both yields. This uncertainty dominates the total uncertainty for this energy range in both the fluorine and sodium yields.

For the BN target, it should be noted that a very high energy γ-ray resulting from the giant dipole resonance on ^{10}B has been reported [De77, De78]. This 17 MeV γ-ray, which is above the energy range investigated in this study, has an unusually large cross section, on the order of several microbarns, over the range α-particle energies studied here [De78]. Based on these cross sections, we estimate γ-ray yields from a boron target with normal isotopic abundance of 2.5×10^{-10} quanta per α at $E_\alpha =$ 8.8 MeV, 1.2×10^{-10} quanta per α at 7.7 MeV, and 6.9×10^{-12} quanta per α at 7.0 MeV, with an estimated uncertainty of 15%. Although this γ-ray occurs with a comparatively weak yield, its high energy and consequent low attenuation suggests it should be considered and added to any backgrounds calculated from the yields listed in table 5.3.

Table 5.2: 4439 keV γ-Ray Yield in Beryllium (γ-ray quanta MeV^{-1} per α)

γ-Ray Energy Range (MeV)	α-Particle Energy (MeV)					
	10 MeV	8.8 MeV	7.7 MeV	7.0 MeV	6.3 MeV	5.6 MeV
4 – 5	$(1.18 \pm 0.23) \cdot 10^{-4}$	$(1.03 \pm 0.14) \cdot 10^{-4}$	$(7.06 \pm 0.31) \cdot 10^{-5}$	$(6.38 \pm 0.25) \cdot 10^{-5}$	$(5.66 \pm 0.25) \cdot 10^{-5}$	$(4.06 \pm 0.16) \cdot 10^{-5}$

Table 5.3: Binned γ-Ray Yield in Boron (γ-ray quanta MeV^{-1} per α)

γ-Ray Energy Range (MeV)	α-Particle Energy (MeV)					
	10 MeV	8.8 MeV	7.7 MeV	7.0 MeV	6.3 MeV	5.6 MeV
2 – 3	$(5.17 \pm 0.23) \cdot 10^{-5}$	$(1.20 \pm 0.26) \cdot 10^{-5}$	$(8.49 \pm 0.35) \cdot 10^{-6}$	$(4.53 \pm 0.33) \cdot 10^{-6}$	$(1.96 \pm 0.08) \cdot 10^{-6}$	$(8.62 \pm 0.45) \cdot 10^{-7}$
3 – 4	$(1.37 \pm 0.06) \cdot 10^{-5}$	$(6.66 \pm 0.91) \cdot 10^{-6}$	$(4.08 \pm 0.17) \cdot 10^{-6}$	$(3.39 \pm 0.25) \cdot 10^{-6}$	$(2.99 \pm 0.76) \cdot 10^{-6}$	$(2.13 \pm 0.11) \cdot 10^{-6}$
4 – 5	$(1.25 \pm 0.07) \cdot 10^{-5}$	$(2.40 \pm 0.33) \cdot 10^{-6}$	$(1.16 \pm 0.05) \cdot 10^{-6}$	$(6.00 \pm 0.44) \cdot 10^{-7}$	$(1.77 \pm 0.09) \cdot 10^{-7}$	$(4.97 \pm 0.50) \cdot 10^{-8}$
5 – 6	$(1.10 \pm 0.04) \cdot 10^{-5}$	$(9.78 \pm 1.32) \cdot 10^{-7}$	$(2.00 \pm 0.09) \cdot 10^{-7}$	—	—	—
6 – 7	$(7.43 \pm 0.49) \cdot 10^{-7}$	—	—	—	—	—

Table 5.4: Binned γ-Ray Yield in Nitrogen (γ-ray quanta MeV^{-1} per α)

γ-Ray Energy Range (MeV)	α-Particle Energy (MeV)		
	10 MeV	8.8 MeV	7.7 MeV
2 – 3	$(2.09 \pm 0.38) \cdot 10^{-6}$	$(5.23 \pm 1.02) \cdot 10^{-7}$	$(2.42 \pm 0.18) \cdot 10^{-7}$
3 – 4	$(4.71 \pm 0.22) \cdot 10^{-6}$	$(1.35 \pm 0.36) \cdot 10^{-7}$	—

Table 5.5: Binned γ-Ray Yield in Fluorine (γ-ray quanta MeV^{-1} per α)

γ-Ray Energy Range (MeV)	α-Particle Energy (MeV)					
	10 MeV	8.8 MeV	7.7 MeV	7.0 MeV	6.3 MeV	5.6 MeV
2 – 3	$(7.58 \pm 2.08) \cdot 10^{-5}$	$(1.93 \pm 0.72) \cdot 10^{-5}$	$(9.30 \pm 3.35) \cdot 10^{-6}$	$(3.04 \pm 2.18) \cdot 10^{-6}$	$(1.51 \pm 1.14) \cdot 10^{-6}$	$(9.15 \pm 0.44) \cdot 10^{-7}$
3 – 4	$(1.72 \pm 0.19) \cdot 10^{-5}$	$(5.63 \pm 0.58) \cdot 10^{-6}$	$(3.21 \pm 0.13) \cdot 10^{-6}$	$(2.09 \pm 0.18) \cdot 10^{-6}$	$(8.73 \pm 0.41) \cdot 10^{-7}$	$(2.77 \pm 0.13) \cdot 10^{-7}$
4 – 5	$(1.37 \pm 0.15) \cdot 10^{-5}$	$(3.42 \pm 0.49) \cdot 10^{-6}$	$(1.39 \pm 0.09) \cdot 10^{-6}$	$(6.17 \pm 0.64) \cdot 10^{-7}$	$(1.78 \pm 0.14) \cdot 10^{-7}$	$(1.99 \pm 0.31) \cdot 10^{-8}$
5 – 6	$(2.62 \pm 0.34) \cdot 10^{-6}$	$(7.38 \pm 1.12) \cdot 10^{-7}$	$(2.59 \pm 0.23) \cdot 10^{-7}$	$(9.24 \pm 1.01) \cdot 10^{-8}$	$(3.54 \pm 0.39) \cdot 10^{-8}$	$(8.50 \pm 1.75) \cdot 10^{-9}$
6 – 7	$(1.63 \pm 0.27) \cdot 10^{-6}$	$(9.33 \pm 2.01) \cdot 10^{-8}$	—	—	—	—
7 – 8	$(2.81 \pm 0.94) \cdot 10^{-7}$	—	—	—	—	—

Table 5.6: Binned γ-Ray Yield in Sodium (γ-ray quanta MeV^{-1} per α)

γ-Ray Energy Range (MeV)	α-Particle Energy (MeV)					
	10 MeV	8.8 MeV	7.7 MeV	7.0 MeV	6.3 MeV	5.6 MeV
2 – 3	$(3.56 \pm 1.61) \cdot 10^{-5}$	$(1.26 \pm 0.57) \cdot 10^{-5}$	$(6.41 \pm 2.67) \cdot 10^{-6}$	$(4.47 \pm 1.77) \cdot 10^{-6}$	$(2.19 \pm 0.92) \cdot 10^{-6}$	$(5.15 \pm 0.26) \cdot 10^{-7}$
3 – 4	$(8.13 \pm 1.25) \cdot 10^{-6}$	$(2.22 \pm 0.43) \cdot 10^{-6}$	$(9.35 \pm 1.63) \cdot 10^{-7}$	$(5.51 \pm 0.61) \cdot 10^{-7}$	$(1.32 \pm 0.09) \cdot 10^{-7}$	$(3.23 \pm 0.32) \cdot 10^{-8}$
4 – 5	$(2.16 \pm 0.80) \cdot 10^{-6}$	$(2.37 \pm 0.96) \cdot 10^{-7}$	$(1.16 \pm 0.26) \cdot 10^{-7}$	$(7.51 \pm 1.11) \cdot 10^{-8}$	$(3.51 \pm 0.77) \cdot 10^{-8}$	$(8.49 \pm 2.47) \cdot 10^{-9}$
5 – 6	$(4.43 \pm 1.50) \cdot 10^{-7}$	$(8.27 \pm 2.07) \cdot 10^{-8}$	—	—	—	—

Table 5.7: Binned γ-Ray Yield in Magnesium (γ-ray quanta MeV^{-1} per α)

γ-Ray Energy Range (MeV)	α-Particle Energy (MeV)					
	10 MeV	8.8 MeV	7.7 MeV	7.0 MeV	6.3 MeV	5.6 MeV
2 – 3	$(2.88 \pm 0.49) \cdot 10^{-5}$	$(1.00 \pm 0.13) \cdot 10^{-5}$	$(5.06 \pm 0.20) \cdot 10^{-6}$	$(2.41 \pm 0.15) \cdot 10^{-6}$	$(1.18 \pm 0.06) \cdot 10^{-6}$	$(4.89 \pm 0.28) \cdot 10^{-7}$
3 – 4	$(6.73 \pm 1.19) \cdot 10^{-6}$	$(1.30 \pm 0.19) \cdot 10^{-6}$	$(5.87 \pm 0.28) \cdot 10^{-7}$	$(1.47 \pm 0.12) \cdot 10^{-7}$	$(5.40 \pm 0.36) \cdot 10^{-8}$	$(2.13 \pm 0.16) \cdot 10^{-8}$
4 – 5	$(3.24 \pm 0.57) \cdot 10^{-6}$	$(9.01 \pm 1.29) \cdot 10^{-7}$	$(4.00 \pm 0.21) \cdot 10^{-7}$	$(2.39 \pm 0.18) \cdot 10^{-7}$	$(1.11 \pm 0.07) \cdot 10^{-7}$	$(2.97 \pm 0.18) \cdot 10^{-8}$
5 – 6	$(1.33 \pm 0.23) \cdot 10^{-6}$	$(5.52 \pm 0.76) \cdot 10^{-7}$	$(2.93 \pm 0.12) \cdot 10^{-7}$	$(1.76 \pm 0.13) \cdot 10^{-7}$	$(8.89 \pm 0.53) \cdot 10^{-8}$	$(1.55 \pm 0.11) \cdot 10^{-8}$
6 – 7	$(1.19 \pm 0.20) \cdot 10^{-6}$	$(3.91 \pm 0.57) \cdot 10^{-7}$	$(1.66 \pm 0.12) \cdot 10^{-7}$	$(9.02 \pm 0.67) \cdot 10^{-8}$	$(3.36 \pm 0.22) \cdot 10^{-8}$	$(5.97 \pm 0.42) \cdot 10^{-9}$
7 – 8	$(6.14 \pm 1.57) \cdot 10^{-7}$	$(2.22 \pm 0.36) \cdot 10^{-7}$	$(1.09 \pm 0.09) \cdot 10^{-7}$	$(5.65 \pm 0.58) \cdot 10^{-8}$	$(1.60 \pm 0.13) \cdot 10^{-8}$	—
8 – 9	$(1.03 \pm 0.27) \cdot 10^{-7}$	$(1.89 \pm 0.42) \cdot 10^{-8}$	$(5.45 \pm 1.74) \cdot 10^{-9}$	$(1.82 \pm 0.91) \cdot 10^{-9}$	—	—
9 – 10	$(7.16 \pm 1.72) \cdot 10^{-8}$	—	—	—	—	—

Table 5.8: Binned γ-Ray Yield in Aluminum (γ-ray quanta MeV^{-1} per α)

γ-Ray Energy Range (MeV)	α-Particle Energy (MeV)					
	10 MeV	8.8 MeV	7.7 MeV	7.0 MeV	6.3 MeV	5.6 MeV
2 – 3	$(7.07 \pm 1.24) \cdot 10^{-5}$	$(2.62 \pm 0.36) \cdot 10^{-5}$	$(1.42 \pm 0.08) \cdot 10^{-5}$	$(7.54 \pm 0.66) \cdot 10^{-6}$	$(3.78 \pm 0.19) \cdot 10^{-6}$	$(1.68 \pm 0.08) \cdot 10^{-6}$
3 – 4	$(2.14 \pm 0.39) \cdot 10^{-5}$	$(9.53 \pm 1.33) \cdot 10^{-6}$	$(5.02 \pm 0.28) \cdot 10^{-6}$	$(2.57 \pm 0.23) \cdot 10^{-6}$	$(1.30 \pm 0.07) \cdot 10^{-6}$	$(4.57 \pm 1.64) \cdot 10^{-7}$
4 – 5	$(3.32 \pm 0.56) \cdot 10^{-6}$	$(9.27 \pm 1.27) \cdot 10^{-7}$	$(4.62 \pm 0.27) \cdot 10^{-7}$	$(2.11 \pm 0.24) \cdot 10^{-7}$	$(1.09 \pm 0.06) \cdot 10^{-7}$	$(4.07 \pm 0.21) \cdot 10^{-8}$
5 – 6	$(7.45 \pm 1.36) \cdot 10^{-7}$	$(6.44 \pm 1.53) \cdot 10^{-8}$	$(7.74 \pm 2.32) \cdot 10^{-9}$	—	—	—
6 – 7	$(7.76 \pm 1.40) \cdot 10^{-7}$	$(2.18 \pm 0.30) \cdot 10^{-7}$	$(9.21 \pm 0.56) \cdot 10^{-8}$	$(1.77 \pm 0.18) \cdot 10^{-8}$	—	—
7 – 8	$(8.74 \pm 1.92) \cdot 10^{-8}$	$(1.53 \pm 0.31) \cdot 10^{-8}$	$(4.55 \pm 1.17) \cdot 10^{-9}$	—	—	—
8 – 9	$(2.99 \pm 0.72) \cdot 10^{-8}$	—	—	—	—	—

5.2.2 Thick-Target γ-Ray Transition Yields

Tables 5.10 through 5.25 report the measured thick-target reaction yields per α-particle from each element for an elementally pure target. The conversion of the composite BN and NaF target yields into elemental yields have been previously discussed in section 5.2.1. Table 5.9 reports the yield from uniquely determined (α, α') reactions for all targets studied here. Each table reports reaction yields for targets with natural isotopic abundances; in cases where reaction yields from a single isotope are desired, these yields must be increased by a factor corresponding to the reciprocal of the isotopic abundance.

Only yields which could be assigned uniquely to a residual nucleus are reported. In cases where a peak was attributed to multiple transitions, the constituent yields were separated using decay schemes published in the literature [En78, En90, Aj87]. Only transitions expected to contribute at least 5% to the total peak yield are reported. Two methods were used to calculate the yield from multiple transition peaks. The primary method for separating the yields required subtracting other components based on their deduced level population and the published branching ratio for the transition. However, in some instances small yield components in a peak (<20% of total yield) resulted in uncertainties determined from subtraction exceeding the component yield. In these instances the weak yield and its uncertainty was obtained from the published branching ratio for the weak transition and the population of the level inferred by different transitions from the same level. In such cases, the total statistical uncertainty was calculated from the quadrature sum of the level population and the branching ratio uncertainty. A "‡" symbol next to the transition identification indicates the cases where this was done for all yields, and next to the yield entry indicates cases where this was required for the particular yield.

In a few cases, unambiguous transition identifications could not be obtained due to the presence of kinematically allowed but not otherwise observed transitions. In some instances, the excitation behaviour of the residual nucleus suggested only one major component to the transition. In these situations, the total yield was attributed to the major component and the uncertainty in the yield was increased by the estimated contamination of the yield for each energy run. The estimate of the contamination was obtained from the average population of neighbouring levels in the residual nucleus and the branching ratio for the decay. In most cases, these corrections affected the $E_\alpha = 10$ and 8.8 MeV yields, with estimated uncertainties ranging from 5 to 50%. Transitions marked with a "†" symbol indicated that an adjustment or contamination has significantly increased the uncertainty in the yield.

Several significant peaks in the BN, NaF, Mg and $A\ell$ targets could not be unambiguously identified, and so were excluded from these tables. The most important of these are discussed below.

The broad peak in the BN target spectrum near 2140 keV was attributed to inelastic scattering off both ^{10}B and ^{11}B. This peak was present at all measured energies, and had elemental yields ranging from 1.89×10^{-5} at $E_\alpha = 10$ MeV to 7.41×10^{-8} at $E_\alpha = 5.6$ MeV.

The NaF target peak at 3880 keV was attributed to both the ^{23}Na$(\alpha,n)^{26}$Mg 5690 → 1809 keV and ^{19}F$(\alpha,p)^{22}$Ne 5147 → 1274 keV transition. The target yield for this peak ranged from 1×10^{-6} γ-rays per α-particle at 10 MeV to 2×10^{-7} at 7 MeV. The 2130 keV peak in the NaF target also had an ambiguous transition identification. Both the ^{23}Na$(\alpha,n)^{26}$Aℓ 2545 → 417 keV and the ^{23}Na$(\alpha,p)^{26}$Mg 3941 → 1809 keV transitions could contribute to the yield to the same extent based on the excitation of the residual nuclei. This peak was observed at all measured α-particle energies.

In the Mg target, a peak at 3936 keV attributed to the ^{25}Mg$(\alpha,p)^{28}$Aℓ 3936 → 0 keV and ^{26}Mg$(\alpha,p)^{29}$Aℓ 3935 → 0 keV transitions was excluded from the tables. This peak was observed in the $E_\alpha = 10$ through 7.7 MeV runs. A peak at 3255 keV for this target attributed to the ^{25}Mg$(\alpha,p)^{28}$Aℓ 3296 → 31 keV and ^{26}Mg$(\alpha,n)^{29}$Si 5285 → 2028 keV transitions was observed at energies of 10 MeV through 7.0 MeV, and was also excluded. Due to the small number of excitations observed for the ^{25}Mg(α,p) reaction, these two exclusions may account for as much as half the γ-ray strength from the ^{28}Aℓ residual nucleus.

Special corrections were required for a number of yield determinations. In these cases additional calculations were performed in order to obtain an accurate measure of the γ-ray yield and to remove contamination from neutron-induced reactions. These calculations are detailed below for each target.

The production of neutrons by (α,n) reactions on the target nuclei gave rise to additional γ-ray peaks in the detector spectra. These γ-rays result from a variety of neutron interactions, the most important of which are neutron capture, inelastic neutron scattering on ^{208}Pb and (n, x) charged particle reactions in the detector crystals [Ch65]. In most cases these γ-rays produced small peaks, with more counts in the forward angle detector due to the forward angle emission bias of the neutron distribution. These peaks were identified and ignored unless significant interference with target γ-rays was suspected.

The 2614 keV γ-ray from neutron scattering on the lead shielding in the counting area produced a narrow peak in the spectra. The narrow width of the peak allowed the area of the peak to be determined in cases when the peak was superimposed on a target transition γ-ray.

The only neutron capture γ-ray with enough strength to cause significant interference with the measured areas was the 7631/7647 keV doublet from neutron capture on iron which occurs with a combined intensity of 52.64 γ-rays per 100 captures [Lo81]. The counting rate per α-particle in this peak was found to have an α-particle energy dependence which scaled linearly with the total thick-target neutron yield for each target, with a target-dependent scaling factor. When interference effects were noted, this linear behaviour was used to calculate a corrected peak area. The statistical uncertainty in the corrected peak area was increased by the the uncertainty in the area from the interpolated capture γ-ray rate, added in quadrature.

5.2.2.1 Be Target

No table has been provided for the single γ-ray transition observed from Be. The yield for the 4439 keV γ-ray from the ^{9}Be$(\alpha, n)^{12}$C reaction can be taken from the single entry in table 5.2. As there is only the one γ-ray emitted in the 1 MeV energy covered by this bin, the number of 4439 keV γ-rays per α-particle is the same as the binned value quoted.

5.2.2.2 BN Target

A table for the ^{11}B$(\alpha,p)^{14}$C yields has not been provided due to the small number of yields observed. Only two excitations were observed for this reaction, and both of these occurred only for $E_\alpha = 10$ MeV. At this α-particle energy, the 6728 → 0 keV yield was $(2.64 \pm 0.27) \cdot 10^{-7}$ per α-particle and the 6094 → 0 keV yield was $(1.07 \pm 0.06) \cdot 10^{-6}$ per α-particle.

Although the Q-value for the ^{10}B$(\alpha,n)^{13}$N reaction suggests a high excitation for the residual nucleus, no γ-rays from this reaction were seen, due to the dominance of proton decay from excited states of ^{13}N [Va73, Le78, Aj81].

The contamination of the 2313 keV level from the ^{11}B$(\alpha,n)^{14}$N reaction by inelastic scattering of the α-particles on ^{14}N was removed by determining the (α,α') contribution from an integration of the cross sections reported by Dyer *et al* [Dy85] with the stopping powers of Ziegler [Zi85]. These cross sections indicate an (α,α') thick-target yield for this γ-ray of 3.01×10^{-6} at $E_\alpha = 10$ MeV, 9.12×10^{-7} at $E_\alpha = 8.8$ MeV, and 1.06×10^{-7} at $E_\alpha = 7.7$ MeV. A 10% uncertainty in these yields was adopted based on the uncertainty reported by Dyer *et al.* These yields, weighted by the stopping power fraction of ^{14}N, were subtracted from the total yield to obtain the (α,n) yield for this transition. At 10 MeV, the (α,n) reaction accounted for less than

Table 5.9: Thick-Target γ-Ray Yields from the (α, α') Reaction (quanta per α)

Transition (energies in keV)	α-Particle Energy (MeV)					
	10.0	8.8	7.7	7.0	6.3	5.6
^{19}F 2780 → 197 †(2583)	$(2.48 \pm 0.14) \cdot 10^{-5}$	$(6.64 \pm 0.93) \cdot 10^{-6}$	$(3.58 \pm 0.22) \cdot 10^{-6}$	—	—	—
^{25}Mg 2738 → 0 (2738)	$(1.65 \pm 0.41) \cdot 10^{-6}$	—	—	—	—	—
^{27}Aℓ 3680 → 844 (2837)	$(6.18 \pm 2.31) \cdot 10^{-7}$	—	—	—	—	—

Table 5.10: Thick-Target γ-Ray Yields from the ^{10}B$(\alpha, p)^{13}$C Reaction in Boron (quanta per α)

Transition (energies in keV)	α-Particle Energy (MeV)					
	10.0	8.8	7.7	7.0	6.3	5.6
3854 → 0 (3854)	$(2.53 \pm 0.14) \cdot 10^{-6}$	$(1.49 \pm 0.21) \cdot 10^{-6}$	$(8.39 \pm 0.31) \cdot 10^{-7}$	$(7.36 \pm 0.54) \cdot 10^{-7}$	$(6.55 \pm 0.27) \cdot 10^{-7}$	$(5.15 \pm 0.25) \cdot 10^{-7}$
3684 → 0 (3684)	$(6.90 \pm 0.29) \cdot 10^{-6}$	$(4.12 \pm 0.57) \cdot 10^{-6}$	$(2.71 \pm 0.13) \cdot 10^{-6}$	$(2.26 \pm 0.16) \cdot 10^{-6}$	$(2.01 \pm 0.09) \cdot 10^{-6}$	$(1.39 \pm 0.07) \cdot 10^{-6}$
3089 → 0 (3089)	$(1.62 \pm 0.23) \cdot 10^{-6}$	$(6.67 \pm 0.97) \cdot 10^{-7}$	$(4.16 \pm 0.23) \cdot 10^{-7}$	$(3.54 \pm 0.39) \cdot 10^{-7}$	$(3.13 \pm 0.30) \cdot 10^{-7}$	$(2.23 \pm 0.13) \cdot 10^{-7}$

Table 5.11: Thick-Target γ-Ray Yields from the ^{10}B$(\alpha, d)^{12}$C Reaction in Boron (quanta per α)

Transition (energies in keV)	α-Particle Energy (MeV)					
	10.0	8.8	7.7	7.0	6.3	5.6
4439 → 0 (4439)	$(1.11 \pm 0.08) \cdot 10^{-5}$	$(2.09 \pm 0.29) \cdot 10^{-6}$	$(1.06 \pm 0.05) \cdot 10^{-6}$	$(6.00 \pm 0.44) \cdot 10^{-7}$	$(1.77 \pm 0.09) \cdot 10^{-7}$	$(4.97 \pm 0.49) \cdot 10^{-8}$

Table 5.12: Thick-Target γ-Ray Yields from the ^{11}B$(\alpha, n)^{14}$N Reaction in Boron (quanta per α)

Transition (energies in keV)	α-Particle Energy (MeV)					
	10.0	8.8	7.7	7.0	6.3	5.6
6446 → 0 (6446)	$(4.78 \pm 0.36) \cdot 10^{-7}$	—	—	—	—	—
6203 → 0 (6203)	$(1.31 \pm 0.36) \cdot 10^{-7}$	—	—	—	—	—
5834 → 0 (5834)	$(1.06 \pm 0.05) \cdot 10^{-6}$	—	—	—	—	—
5691 → 0 (5691)	$(9.64 \pm 0.63) \cdot 10^{-7}$	—	—	—	—	—
5106 → 0 (5106)	$(7.77 \pm 0.29) \cdot 10^{-6}$	$(9.43 \pm 1.26) \cdot 10^{-7}$	$(2.00 \pm 0.09) \cdot 10^{-7}$	—	—	—
4915 → 0 (4915)	$(1.43 \pm 0.12) \cdot 10^{-6}$	$(3.06 \pm 0.52) \cdot 10^{-7}$	$(9.54 \pm 1.00) \cdot 10^{-8}$	—	—	—
3948 → 0 (3948)	$(3.98 \pm 0.98) \cdot 10^{-7}$	$(3.08 \pm 0.52) \cdot 10^{-7}$	$(1.16 \pm 0.13) \cdot 10^{-7}$	$(4.62 \pm 0.91) \cdot 10^{-8}$	$(6.95 \pm 4.03) \cdot 10^{-9}$	—
5691 → 2313 (3378)	$(2.24 \pm 0.12) \cdot 10^{-6}$	—	—	—	—	—
5106 → 2313 (2793)	$(2.22 \pm 0.64) \cdot 10^{-6}$†	$(2.39 \pm 0.38) \cdot 10^{-7}$	$(4.69 \pm 0.80) \cdot 10^{-8}$	—	—	—
6446 → 3948 (2498)	$(9.22 \pm 3.55) \cdot 10^{-8}$	—	—	—	—	—
2313 → 0 (2313)	$(2.65 \pm 0.13) \cdot 10^{-5}$	$(9.51 \pm 1.41) \cdot 10^{-6}$	$(5.22 \pm 0.20) \cdot 10^{-6}$	$(2.85 \pm 0.21) \cdot 10^{-6}$	$(1.40 \pm 0.06) \cdot 10^{-6}$	$(7.89 \pm 0.41) \cdot 10^{-7}$

† yield contains additional uncertainty from adjustment or contamination
‡ yield determined from deduced level population

13% of the total yield, and at 7.7 MeV accounted for less than 3% of the yield.

5.2.2.3 NaF Target

The $^{19}\mathrm{F}(\alpha,p)^{22}\mathrm{Ne}$ 6115 → 1274 keV transition contained an unresolved contamination by the $^{23}\mathrm{Na}(\alpha,n)^{26}\mathrm{Mg}$ 4834 → 0 keV transition at $E_\alpha = 10$ and 8.8 MeV. From the intensity of these transitions determined at lower energies, it is known that the contribution of 4834 → 0 keV transition was no more than 20% of the total peak yield at 7.7 MeV. Thus, the total yield at 10 and 8.8 MeV has been attributed to the 6115 → 1274 keV transition, and an additional uncertainty of 20% has been added at each energy. No yield for the 4834 → 0 keV transition in the 10 and 8.8 MeV E_α runs has been assigned, while at the lower energies this transition was a significant component of the total peak yield, and so yields have been provided.

The $^{19}\mathrm{F}(\alpha,n)^{22}\mathrm{Na}$ 3519 → 0 keV yield was separated from the $^{23}\mathrm{Na}(\alpha,n)^{26}\mathrm{A}\ell$ 3508 → 0 keV yield through the dependence of the γ-ray peak shape on the lifetime of the level from which it decays. The 3519 keV level in $^{22}\mathrm{Na}$ has a lifetime of 0.6 ps, which is also the same order as the stopping time (0.5 ps [Al78]) for an ion in the target, while the 3508 keV level in $^{26}\mathrm{A}\ell$ has a much shorter lifetime of 0.02 fs. The combined peak appeared in the spectra as a sharp, fully Doppler-shifted peak from the 3508 keV level on top of an extended broad peak which covered the full range of Doppler shifts. This structure permitted their separation by estimating the areas of the sharp 3508 keV and 3519 keV peaks, and dividing the yield from these levels according to the determined ratio. An additional uncertainty of 20% was assessed for

Table 5.13: Thick-Target γ-Ray Yields from the $^{14}N(\alpha,p)^{17}O$ Reaction (quanta per α)

Transition (energies in keV)	α-Particle Energy (MeV)					
	10.0	8.8	7.7	7.0	6.3	5.6
3841 → 0 (3841)	$(4.71 \pm 0.22) \cdot 10^{-6}$	$(1.35 \pm 0.36) \cdot 10^{-7}$	—	—	—	—
3055 → 871 (2184)	$(2.09 \pm 0.38) \cdot 10^{-6}$	$(5.22 \pm 1.03) \cdot 10^{-7}$	$(2.42 \pm 0.18) \cdot 10^{-7}$	—	—	—

Table 5.14: Thick-Target γ-Ray Yields per α from the $^{19}F(\alpha,n)^{22}Na$ Reaction (quanta per α)

Transition (energies in keV)	α-Particle Energy (MeV)					
	10.0	8.8	7.7	7.0	6.3	5.6
5101 → 0 (5101)	$(1.63 \pm 0.79) \cdot 10^{-7}$	—	—	—	—	—
5174 → 583 (4591) 4583 → 0 (4583)	$(7.81 \pm 1.45) \cdot 10^{-7}$	—	—	—	—	—
4360 → 0‡ (4360)	$(2.54 \pm 0.68) \cdot 10^{-6}$	$(3.69 \pm 0.95) \cdot 10^{-8}$	$(1.10 \pm 0.40) \cdot 10^{-8}$	—	—	—
5101 → 891‡ (4210)	$(1.36 \pm 0.80) \cdot 10^{-7}$	—	—	—	—	—
4622 → 657‡ (3965)	$(6.10 \pm 3.18) \cdot 10^{-7}$	—	—	—	—	—
4319 → 657 (3662)	$(9.29 \pm 2.74) \cdot 10^{-7}$	—	—	—	—	—
3519 → 0 † (3519)	$(1.10 \pm 0.23) \cdot 10^{-6}$	$(1.85 \pm 0.10) \cdot 10^{-7}$	$(4.57 \pm 2.59) \cdot 10^{-8}$	—	—	—
3943 → 657 (3286)	$(2.03 \pm 0.26) \cdot 10^{-6}$	$(2.48 \pm 0.53) \cdot 10^{-7}$	—	—	—	—
4524 → 1528 † (2996)	$(5.42 \pm 2.10) \cdot 10^{-6}$	$(4.75 \pm 2.12) \cdot 10^{-7}$	—	—	—	—
3707 → 891 (2816) 4771 → 1952 (2819)	$(4.61 \pm 0.36) \cdot 10^{-6}$	$(3.56 \pm 0.68) \cdot 10^{-7}$	$(1.23 \pm 0.25) \cdot 10^{-7}$	—	—	—
4622 → 1952 (2670)	$(9.13 \pm 3.83) \cdot 10^{-7}$	—	—	—	—	—
4583 → 1952 †(2631)	$(6.03 \pm 6.32) \cdot 10^{-7}$	—	—	—	—	—
2571 → 0 † (2571)	$(6.43 \pm 2.01) \cdot 10^{-6}$	$(2.72 \pm 0.68) \cdot 10^{-6}$	$(1.48 \pm 0.34) \cdot 10^{-6}$	$(6.14 \pm 1.74) \cdot 10^{-7}$	$(3.29 \pm 0.80) \cdot 10^{-7}$	—
4360 → 1952 (2408)	$(1.08 \pm 0.21) \cdot 10^{-6}$	$(1.56 \pm 0.36) \cdot 10^{-7}$	$(4.66 \pm 1.50) \cdot 10^{-8}$	—	—	—
4296 → 1937 (2359)	$(1.34 \pm 0.67) \cdot 10^{-6}$	—	—	—	—	—
3707 → 1528‡ (2179)	$(6.98 \pm 5.32) \cdot 10^{-7}$	$(1.67 \pm 0.36) \cdot 10^{-7}$	$(5.80 \pm 1.30) \cdot 10^{-8}$	—	—	—

† yield contains additional uncertainty from adjustment or contamination
‡ yield determined from deduced level population

Table 5.15: Thick-Target γ-Ray Yields from the $^{19}F(\alpha,p)^{22}Ne$ Reaction (quanta per α)

Transition (energies in keV)		α-Particle Energy (MeV)					
		10.0	8.8	7.7	7.0	6.3	5.6
7489 → 0	(7489)	$(1.87 \pm 0.55) \cdot 10^{-7}$	—	—	—	—	—
7052 → 0	(7052)	$(9.43 \pm 7.93) \cdot 10^{-8}$	—	—	—	—	—
6853 → 0	(6853)	$(6.17 \pm 0.96) \cdot 10^{-7}$	—	—	—	—	—
6691 → 0	(6691)	$(3.94 \pm 1.27) \cdot 10^{-7}$	$(9.31 \pm 2.01) \cdot 10^{-8}$	—	—	—	—
7644 → 1274	(6369)	$(1.57 \pm 1.06) \cdot 10^{-7}$	—	—	—	—	—
7489 → 1274	(6214)	$(4.34 \pm 0.82) \cdot 10^{-7}$	—	—	—	—	—
6115 → 0	(6115)	$(4.61 \pm 1.41) \cdot 10^{-7}$	—	—	—	—	—
7052 → 1274	(5777)	$(4.79 \pm 0.81) \cdot 10^{-7}$	—	—	—	—	—
6904 → 1274	(5629)	$(1.64 \pm 0.83) \cdot 10^{-7}$	—	—	—	—	—
6817 → 1274	(5542)	$(3.40 \pm 1.25) \cdot 10^{-7}$	$(8.35 \pm 3.34) \cdot 10^{-8}$	—	—	—	—
5365 → 0	(5365)	$(3.87 \pm 4.19) \cdot 10^{-7}$	$(1.25 \pm 1.09) \cdot 10^{-7}$	$(5.17 \pm 4.61) \cdot 10^{-7}$	$(3.08 \pm 1.55) \cdot 10^{-8}$	$(1.20 \pm 1.21) \cdot 10^{-8}$‡	$(8.82 \pm 9.05) \cdot 10^{-10}$‡
5326 → 0	(5326)	$(1.61 \pm 0.44) \cdot 10^{-6}$	$(5.02 \pm 1.72) \cdot 10^{-7}$	$(1.93 \pm 0.70) \cdot 10^{-7}$	$(5.85 \pm 3.47) \cdot 10^{-8}$	$(2.34 \pm 1.26) \cdot 10^{-8}$	$(7.63 \pm 1.98) \cdot 10^{-9}$
6115 → 1274†	(4840)	$(1.87 \pm 0.41) \cdot 10^{-6}$	$(6.41 \pm 1.62) \cdot 10^{-7}$	$(1.50 \pm 0.19) \cdot 10^{-7}$	$(4.70 \pm 1.36) \cdot 10^{-8}$	$(1.27 \pm 0.67) \cdot 10^{-8}$	$(1.23 \pm 1.67) \cdot 10^{-8}$
5910 → 1274	(4635)	$(2.59 \pm 0.20) \cdot 10^{-6}$	$(6.64 \pm 1.04) \cdot 10^{-7}$	$(2.27 \pm 0.22) \cdot 10^{-7}$	$(5.83 \pm 0.90) \cdot 10^{-8}$	—	—
4457 → 0†	(4457)	$(3.82 \pm 2.68) \cdot 10^{-7}$	$(1.38 \pm 1.10) \cdot 10^{-7}$	$(7.42 \pm 1.18) \cdot 10^{-8}$	$(5.76 \pm 2.28) \cdot 10^{-8}$	$(1.62 \pm 0.36) \cdot 10^{-8}$	$(5.35 \pm 1.27) \cdot 10^{-9}$
5641 → 1274	(4367)	$(3.04 \pm 0.93) \cdot 10^{-6}$	$(8.80 \pm 1.43) \cdot 10^{-7}$	$(2.27 \pm 0.53) \cdot 10^{-7}$	$(1.18 \pm 0.22) \cdot 10^{-7}$	$(1.89 \pm 0.36) \cdot 10^{-8}$	$(2.21 \pm 1.18) \cdot 10^{-9}$
7721 → 3357‡	(4364)	$(2.59 \pm 0.64) \cdot 10^{-6}$	—	—	—	—	—
5365 → 1274	(4090)	$(3.49 \pm 0.45) \cdot 10^{-6}$	$(1.37 \pm 0.20) \cdot 10^{-6}$	$(5.92 \pm 0.42) \cdot 10^{-7}$	$(3.06 \pm 0.29) \cdot 10^{-7}$	$(1.10 \pm 0.08) \cdot 10^{-7}$	$(7.90 \pm 1.55) \cdot 10^{-9}$
5326 → 1274	(4052)	$(9.81 \pm 7.97) \cdot 10^{-7}$	$(2.68 \pm 0.53) \cdot 10^{-7}$	$(1.05 \pm 0.16) \cdot 10^{-7}$	$(3.06 \pm 0.59) \cdot 10^{-8}$	$(2.00 \pm 0.43) \cdot 10^{-8}$	$(3.22 \pm 0.80) \cdot 10^{-9}$
7341 → 3357	(3984)	$(4.59 \pm 4.97) \cdot 10^{-7}$	—	—	—	—	—
7721 → 4457	(3264)	$(5.85 \pm 1.06) \cdot 10^{-7}$	—	—	—	—	—
4457 → 1274 †	(3182)	$(1.00 \pm 0.12) \cdot 10^{-5}$	$(4.48 \pm 0.72) \cdot 10^{-6}$	$(2.68 \pm 0.10) \cdot 10^{-6}$	$(1.73 \pm 0.15) \cdot 10^{-6}$	$(8.73 \pm 0.41) \cdot 10^{-7}$	$(2.68 \pm 0.13) \cdot 10^{-7}$
6311 → 3357†	(2954)	$(3.67 \pm 1.23) \cdot 10^{-6}$	—	—	—	—	—
5910 → 3357‡	(2553)	$(1.85 \pm 0.94) \cdot 10^{-7}$	—	—	—	—	—
6817 → 4457‡	(2360)	$(2.17 \pm 0.83) \cdot 10^{-7}$	$(5.33 \pm 2.22) \cdot 10^{-8}$	—	—	—	—
5523 → 3357	(2166)	$(6.30 \pm 2.15) \cdot 10^{-6}$	$(1.62 \pm 0.24) \cdot 10^{-6}$	$(6.84 \pm 0.45) \cdot 10^{-7}$	$(2.65 \pm 0.37) \cdot 10^{-7}$	$(4.63 \pm 1.07) \cdot 10^{-8}$	—

Table 5.16: Thick-Target γ-Ray Yields from the $^{23}Na(\alpha,n)^{26}A\ell$ Reaction (quanta per α)

Transition (energies in keV)		α-Particle Energy (MeV)					
		10.0	8.8	7.7	7.0	6.3	5.6
3922 → 0	(3922)	$(8.42 \pm 1.25) \cdot 10^{-7}$	—	—	—	—	—
3508 → 0	(3508)	$(9.92 \pm 1.85) \cdot 10^{-7}$	$(1.16 \pm 0.26) \cdot 10^{-7}$	$(3.64 \pm 2.09) \cdot 10^{-8}$	—	—	—
3403 → 0	(3403)	$(6.59 \pm 1.30) \cdot 10^{-7}$	$(7.99 \pm 2.09) \cdot 10^{-8}$	—	—	—	—
3403 → 417‡	(2986)	$(1.02 \pm 0.20) \cdot 10^{-6}$	$(1.23 \pm 0.30) \cdot 10^{-7}$	—	—	—	—
2661 → 417	(2244)	$(8.37 \pm 1.25) \cdot 10^{-7}$	$(1.80 \pm 0.42) \cdot 10^{-7}$	—	—	—	—

† yield contains additional uncertainty from adjustment or contamination
‡ yield determined from deduced level population

these yields to account for the fluctuation of area ratios between detectors.

A similar procedure was followed in separating the yield of the ^{19}F$(\alpha,n)^{22}$Na 2571 → 0 keV transition from the ^{19}F(α,α') 2780 → 197 keV transition. The 2571 keV transition has a very long lifetime compared to the stopping time of the residual nucleus in the target, and so appeared as a sharp peak on the broad transition of the ^{19}F reaction. These peaks were separated by selecting a background for the 2571 keV peak on top of the (α,α') structure. Due to uncertainties in the position of the background level within the crowded spectrum of detector #1, a variation of 40 to 50% in the area of this peak was observed, which contributed an additional 20% uncertainty to the total yield determination. In addition to this subtraction, the area due to the ^{208}Pb 2614 keV peak was removed from detector #1 as described previously.

In the case of the yield from the ^{23}Na$(\alpha,p)^{26}$Mg 4834 keV level, both the transition to the ground state and to the first excited state at 1809 keV are very weak branches ($6\pm2\%$ and $4\pm1\%$ [En90] respectively). At high E_α these weak peaks were obscured by other γ-ray and escape peaks, and so are not reported in these cases.

In the $E_\alpha = 10$ MeV run, the ^{23}Na$(\alpha,p)^{26}$Mg 5715 → 2938 keV transition was obscured by the pulser peak inserted into the detector #1 spectrum. The area of the peak on top of the pulser was estimated by subtracting the area of the pulser peak determined from a background set on the broader γ-ray peak from the total peak area. This procedure resulted in a large statistical uncertainty of 85% for the γ-ray peak area.

Table 5.17: Thick-Target γ-Ray Yields from the ^{23}Na$(\alpha,p)^{26}$Mg Reaction (quanta per α)

Transition (energies in keV)	α-Particle Energy (MeV)					
	10.0	8.8	7.7	7.0	6.3	5.6
6877 → 1809 (5069)	$(4.41 \pm 1.50) \cdot 10^{-7}$	$(8.28 \pm 2.07) \cdot 10^{-8}$	—	—	—	—
6745 → 1809 (4936)	$(3.83 \pm 0.87) \cdot 10^{-7}$	$(3.87 \pm 3.13) \cdot 10^{-8}$	$(1.55 \pm 0.53) \cdot 10^{-8}$	—	—	—
4834 → 0 † (4834)	—	—	$(2.95 \pm 1.82) \cdot 10^{-8}$	$(2.23 \pm 1.30) \cdot 10^{-8}$	$(1.10 \pm 0.83) \cdot 10^{-8}$	$(1.19 \pm 1.76) \cdot 10^{-9}$
4332 → 0 (4332)	$(5.49 \pm 7.31) \cdot 10^{-7}$	$(1.05 \pm 0.30) \cdot 10^{-7}$	$(7.06 \pm 1.77) \cdot 10^{-8}$	$(5.27 \pm 1.01) \cdot 10^{-8}$	$(2.39 \pm 0.37) \cdot 10^{-8}$	$(6.57 \pm 1.73) \cdot 10^{-9}$
7100 → 2938 (4162)	$(9.59 \pm 1.70) \cdot 10^{-7}$	—	—	—	—	—
6745 → 2938 (3807)	$(4.46 \pm 1.16) \cdot 10^{-7}$	—	—	—	—	—
6634 → 2938 (3696)	$(4.81 \pm 1.68) \cdot 10^{-7}$	$(6.77 \pm 5.07) \cdot 10^{-8}$	—	—	—	—
5474 → 1809 (3665)	$(5.51 \pm 2.84) \cdot 10^{-7}$	$(2.83 \pm 0.59) \cdot 10^{-7}$	$(7.69 \pm 1.48) \cdot 10^{-8}$	$(6.28 \pm 1.01) \cdot 10^{-8}$	—	—
4900 → 1809† (3092)	$(3.87 \pm 1.94) \cdot 10^{-6}$	$(1.39 \pm 0.34) \cdot 10^{-6}$	$(7.02 \pm 0.38) \cdot 10^{-7}$	$(4.23 \pm 0.35) \cdot 10^{-7}$	$(1.24 \pm 0.09) \cdot 10^{-7}$	$(3.22 \pm 0.33) \cdot 10^{-8}$
4834 → 1809 † (3026)	—	—	—	$(1.94 \pm 1.22) \cdot 10^{-8}$	$(7.65 \pm 3.57) \cdot 10^{-9}$	—
2938 → 0 (2938)	$(5.17 \pm 0.74) \cdot 10^{-6}$	$(6.59 \pm 0.97) \cdot 10^{-7}$	$(3.80 \pm 0.38) \cdot 10^{-7}$	$(2.88 \pm 0.37) \cdot 10^{-7}$	$(1.98 \pm 0.13) \cdot 10^{-7}$	$(9.16 \pm 0.59) \cdot 10^{-8}$
5715 → 2938 † (2777)	$(2.57 \pm 1.75) \cdot 10^{-7}$	$(1.20 \pm 0.43) \cdot 10^{-7}$	$(6.95 \pm 2.75) \cdot 10^{-8}$	$(1.84 \pm 0.85) \cdot 10^{-8}$	—	—
5690 → 2938† (2751)	$(9.94 \pm 5.19) \cdot 10^{-7}$	$(1.33 \pm 0.41) \cdot 10^{-7}$	$(6.39 \pm 2.84) \cdot 10^{-8}$	$(2.18 \pm 1.42) \cdot 10^{-8}$	—	—
4350 → 1809 (2541) 4332 → 1809 (2524) 4318 → 1809 (2510)	$(1.15 \pm 0.07) \cdot 10^{-5}$	$(4.68 \pm 0.69) \cdot 10^{-6}$	$(2.57 \pm 0.25) \cdot 10^{-6}$	$(1.87 \pm 0.19) \cdot 10^{-6}$	$(8.73 \pm 0.47) \cdot 10^{-7}$	$(3.51 \pm 0.18) \cdot 10^{-7}$
5291 → 2938 (2352)	$(1.44 \pm 0.26) \cdot 10^{-6}$	$(3.49 \pm 0.60) \cdot 10^{-7}$	$(1.89 \pm 0.17) \cdot 10^{-7}$	$(1.34 \pm 0.36) \cdot 10^{-7}$	$(3.73 \pm 0.43) \cdot 10^{-8}$	$(5.26 \pm 1.88) \cdot 10^{-9}$

Table 5.18: Thick-Target γ-Ray Yields from the ^{24}Mg$(\alpha,p)^{27}$Aℓ Reaction in Magnesium (quanta per α)

Transition (energies in keV)	α-Particle Energy (MeV)					
	10.0	8.8	7.7	7.0	6.3	5.6
5438 → 0 (5438)	$(4.20 \pm 3.86) \cdot 10^{-8}$	—	—	—	—	—
5156 → 0 (5156)	$(5.20 \pm 1.83) \cdot 10^{-8}$	—	—	—	—	—
4580 → 0 (4580)	$(4.42 \pm 0.82) \cdot 10^{-7}$	—	—	—	—	—
4410 → 0 (4410)	$(8.16 \pm 5.42) \cdot 10^{-8}$	$(6.32 \pm 2.82) \cdot 10^{-8}$	—	—	—	—
3957 → 0 (3957)	$(5.06 \pm 0.87) \cdot 10^{-7}$	—	—	—	—	—
4410 → 1014‡ (3396)	$(4.92 \pm 3.26) \cdot 10^{-8}$	$(7.31 \pm 3.96) \cdot 10^{-9}$	—	—	—	—
3957 → 844 (3113)	$(4.33 \pm 1.53) \cdot 10^{-8}$	—	—	—	—	—
3004 → 0 (3004)	$(3.72 \pm 0.69) \cdot 10^{-6}$	$(6.09 \pm 0.86) \cdot 10^{-7}$	$(2.92 \pm 0.15) \cdot 10^{-7}$	$(5.07 \pm 0.62) \cdot 10^{-8}$	$(1.03 \pm 0.15) \cdot 10^{-8}$	$(5.14 \pm 0.83) \cdot 10^{-9}$
2982 → 0† (2982)	$(2.20 \pm 0.60) \cdot 10^{-6}$	$(5.81 \pm 1.18) \cdot 10^{-7}$	$(2.62 \pm 0.14) \cdot 10^{-7}$	$(1.98 \pm 0.26) \cdot 10^{-8}$	$(4.39 \pm 0.92) \cdot 10^{-9}$	$(2.10 \pm 0.50) \cdot 10^{-9}$
3957 → 1014 (2942)	$(5.68 \pm 2.72) \cdot 10^{-8}$	—	—	—	—	—
3680 → 844‡ (2837)	$(3.67 \pm 1.51) \cdot 10^{-7}$	$(5.66 \pm 2.07) \cdot 10^{-8}$	$(1.61 \pm 1.23) \cdot 10^{-8}$	—	—	—
2735 → 0 (2735)	$(1.03 \pm 0.47) \cdot 10^{-6}$	$(3.56 \pm 0.54) \cdot 10^{-7}$	$(1.20 \pm 0.11) \cdot 10^{-7}$	—	—	—
3680 → 1014 (2666)	$(2.27 \pm 0.52) \cdot 10^{-7}$	$(3.50 \pm 1.35) \cdot 10^{-8}$	$(9.94 \pm 8.25) \cdot 10^{-9}$	—	—	—
4580 → 2211 (2369)	$(1.12 \pm 0.48) \cdot 10^{-7}$	—	—	—	—	—
4510 → 2211 (2299)	$(8.07 \pm 1.62) \cdot 10^{-7}$	—	—	—	—	—
2211 → 0 (2211)	$(8.05 \pm 1.42) \cdot 10^{-6}$	$(2.60 \pm 0.35) \cdot 10^{-6}$	$(1.34 \pm 0.06) \cdot 10^{-6}$	$(3.61 \pm 0.27) \cdot 10^{-7}$	$(5.42 \pm 0.63) \cdot 10^{-8}$	$(1.47 \pm 0.46) \cdot 10^{-8}$

† yield contains additional uncertainty from adjustment or contamination
‡ yield determined from deduced level population

5.2.2.4 Mg Target

In a few cases, low yield transitions became obscured at high α-particle energies by stronger transitions and escape peaks. In all these cases, yields are reported only for the α-particle energies that they could be reliably obtained. Such a transition is seen in table 5.20 for the 2201 → 31 keV transition from the $^{26}\mathrm{A}\ell$ nucleus, which was obscured in the $E_\alpha = 10$ MeV run by the 2211 → 0 keV $^{27}\mathrm{A}\ell$ transition. The changing Doppler-shift and intensities of these transitions permitted a separation in lower energy runs.

A similar situation in the case of the $^{26}\mathrm{Mg}(\alpha,n)^{29}\mathrm{Si}$ 4840 → 1273 keV transition was observed, where a large escape peak subtraction at $E_\alpha = 10$ MeV prevented a determination of the peak area. Finally, the $^{26}\mathrm{Mg}(\alpha,p)^{29}\mathrm{A}\ell$ 3641 → 0 keV transition at $E_\alpha = 10$ MeV was not seen due to the low intensity of the decay falling below the level at which a yield could be calculated in this run.

5.2.2.5 Aℓ Target

The $^{27}\mathrm{A}\ell(\alpha,p)^{30}\mathrm{Si}$ 7623 → 0 keV transition was contaminated by γ-rays from neutron capture on iron; this contamination was removed as discussed previously. The contamination-correction yield for this transition agrees with the level population deduced from the observed transition to the 2235 keV level.

A similar calculation was performed to remove the broad peak observed in each detector between 2300 and 2360 keV and attributed to fast neutron reactions in the

Table 5.19: Thick-Target γ-Ray Yields from the $^{25}\mathrm{Mg}(\alpha,n)^{28}\mathrm{Si}$ Reaction in Magnesium (quanta per α)

Transition (energies in keV)	α-Particle Energy (MeV)					
	10.0	8.8	7.7	7.0	6.3	5.6
9929 → 0 (9929)	$(9.62 \pm 3.43) \cdot 10^{-9}$	—	—	—	—	—
9796 → 0 (9796)	$(1.83 \pm 0.92) \cdot 10^{-8}$	—	—	—	—	—
9496 → 0 (9496) 9479 → 0 (9479)	$(4.45 \pm 1.00) \cdot 10^{-8}$	—	—	—	—	—
8905 → 0 (8905)	$(3.28 \pm 1.21) \cdot 10^{-8}$	$(8.61 \pm 2.97) \cdot 10^{-9}$	—	—	—	—
8328 → 0 (8328)	$(3.36 \pm 1.48) \cdot 10^{-8}$	$(1.03 \pm 0.22) \cdot 10^{-8}$	$(5.45 \pm 1.73) \cdot 10^{-9}$	$(1.82 \pm 0.91) \cdot 10^{-9}$	—	—
8259 → 0 (8259)	$(2.10 \pm 0.92) \cdot 10^{-8}$	—	—	—	—	—
9796 → 1779 (8017)	$(1.59 \pm 0.88) \cdot 10^{-8}$	—	—	—	—	—
7933 → 0 (7933)	$(1.49 \pm 0.29) \cdot 10^{-7}$	$(5.90 \pm 0.94) \cdot 10^{-8}$	$(2.91 \pm 0.27) \cdot 10^{-8}$	$(1.16 \pm 0.18) \cdot 10^{-8}$	—	—
9382 → 1779 (7603)	$(5.53 \pm 3.62) \cdot 10^{-8}$	—	—	—	—	—
7416 → 0 (7416)	$(2.73 \pm 0.71) \cdot 10^{-7}$	$(1.19 \pm 0.22) \cdot 10^{-7}$	$(6.11 \pm 0.70) \cdot 10^{-8}$	$(3.68 \pm 0.47) \cdot 10^{-8}$	$(1.26 \pm 0.10) \cdot 10^{-8}$	—
7381 → 0 (7381)	$(1.10 \pm 0.99) \cdot 10^{-7}$	$(4.43 \pm 1.12) \cdot 10^{-8}$	$(1.83 \pm 0.29) \cdot 10^{-8}$	$(8.13 \pm 1.24) \cdot 10^{-9}$	$(3.38 \pm 0.62) \cdot 10^{-9}$	—
6879 → 0 (6879)	$(5.39 \pm 0.93) \cdot 10^{-7}$	$(2.49 \pm 0.36) \cdot 10^{-7}$	$(1.38 \pm 0.09) \cdot 10^{-7}$	$(7.58 \pm 0.51) \cdot 10^{-8}$	$(3.36 \pm 0.22) \cdot 10^{-8}$	$(5.97 \pm 0.42) \cdot 10^{-9}$
8589 → 1779 (6810)	$(9.06 \pm 2.15) \cdot 10^{-8}$	$(2.18 \pm 0.72) \cdot 10^{-8}$	$(6.00 \pm 3.54) \cdot 10^{-9}$	—	—	—
8413 → 1779 (6634)	$(1.51 \pm 0.31) \cdot 10^{-7}$	$(2.28 \pm 1.06) \cdot 10^{-8}$	—	—	—	—
8259 → 1779 (6480)	$(8.57 \pm 2.91) \cdot 10^{-8}$	$(3.17 \pm 0.71) \cdot 10^{-8}$	—	—	—	—
7799 → 1779 (6020)	$(1.74 \pm 0.36) \cdot 10^{-7}$	$(6.56 \pm 1.08) \cdot 10^{-8}$	$(2.28 \pm 0.60) \cdot 10^{-8}$	$(1.44 \pm 0.30) \cdot 10^{-8}$	—	—
7381 → 1779 (5602)	$(1.51 \pm 0.43) \cdot 10^{-7}$	$(6.26 \pm 1.08) \cdot 10^{-8}$	$(3.47 \pm 0.31) \cdot 10^{-8}$	$(2.21 \pm 0.22) \cdot 10^{-8}$	$(5.22 \pm 0.68) \cdot 10^{-9}$	—
6888 → 1779 (5109)	$(7.79 \pm 1.40) \cdot 10^{-7}$	$(3.92 \pm 0.55) \cdot 10^{-7}$	$(2.05 \pm 0.10) \cdot 10^{-7}$	$(1.24 \pm 0.09) \cdot 10^{-7}$	$(7.06 \pm 0.44) \cdot 10^{-8}$	$(1.32 \pm 0.09) \cdot 10^{-8}$
6879 → 1779 (5100)	$(2.10 \pm 0.61) \cdot 10^{-7}$	$(9.72 \pm 2.30) \cdot 10^{-7}$	$(5.37 \pm 0.75) \cdot 10^{-8}$	$(2.96 \pm 0.44) \cdot 10^{-8}$	$(1.31 \pm 0.22) \cdot 10^{-8}$	$(2.33 \pm 0.65) \cdot 10^{-9}$
6276 → 1779 (4497)	$(6.11 \pm 1.07) \cdot 10^{-7}$	$(3.88 \pm 0.54) \cdot 10^{-7}$	$(2.22 \pm 0.10) \cdot 10^{-7}$	$(1.56 \pm 0.11) \cdot 10^{-7}$	$(8.36 \pm 0.50) \cdot 10^{-8}$	$(2.97 \pm 0.18) \cdot 10^{-8}$
8945 → 4618 (4327)	$(1.16 \pm 0.24) \cdot 10^{-7}$	—	—	—	—	—
8413 → 4618‡ (3795)	$(1.89 \pm 0.41) \cdot 10^{-8}$	—	—	—	—	—
4980 → 1779 (3201)	$(4.22 \pm 0.76) \cdot 10^{-7}$	$(1.17 \pm 0.18) \cdot 10^{-7}$	$(6.44 \pm 0.38) \cdot 10^{-8}$	$(4.42 \pm 0.39) \cdot 10^{-8}$	$(3.41 \pm 0.22) \cdot 10^{-8}$	$(1.62 \pm 0.11) \cdot 10^{-8}$
4618 → 1779 (2839)	$(2.21 \pm 0.39) \cdot 10^{-6}$	$(1.20 \pm 0.17) \cdot 10^{-6}$	$(6.49 \pm 0.35) \cdot 10^{-7}$	$(4.58 \pm 0.31) \cdot 10^{-7}$	$(2.94 \pm 0.17) \cdot 10^{-7}$	$(1.43 \pm 0.08) \cdot 10^{-7}$
2272 → 0 (2272)	$(4.06 \pm 0.88) \cdot 10^{-7}$	$(1.29 \pm 0.20) \cdot 10^{-7}$	$(6.20 \pm 0.79) \cdot 10^{-8}$	$(3.10 \pm 0.46) \cdot 10^{-8}$	$(1.37 \pm 0.55) \cdot 10^{-8}$	—

Table 5.20: Thick-Target γ-Ray Yields from the $^{25}\mathrm{Mg}(\alpha,p)^{28}\mathrm{A}\ell$ Reaction in Magnesium (quanta per α)

Transition (energies in keV)	α-Particle Energy (MeV)					
	10.0	8.8	7.7	7.0	6.3	5.6
3591 → 0 (3591)	$(3.71 \pm 1.53) \cdot 10^{-8}$	$(2.07 \pm 2.31) \cdot 10^{-8}$	—	—	—	—
3465 → 0 (3465)	$(1.11 \pm 0.27) \cdot 10^{-7}$	—	—	—	—	—
3347 → 0 (3347)	$(1.11 \pm 0.26) \cdot 10^{-7}$	$(2.59 \pm 0.90) \cdot 10^{-8}$	$(1.62 \pm 0.43) \cdot 10^{-8}$	—	—	—
2272 → 0 (2272)	$(4.06 \pm 0.88) \cdot 10^{-7}$	$(1.29 \pm 0.20) \cdot 10^{-7}$	$(6.20 \pm 0.79) \cdot 10^{-8}$	$(3.10 \pm 0.46) \cdot 10^{-8}$	$(1.37 \pm 0.55) \cdot 10^{-8}$	—
2201 → 31 † (2171)	—	$(1.66 \pm 1.06) \cdot 10^{-8}$	$(2.46 \pm 2.15) \cdot 10^{-8}$	—	—	—
2139 → 0 (2139)	$(5.69 \pm 2.78) \cdot 10^{-8}$	$(3.66 \pm 1.23) \cdot 10^{-8}$	$(1.64 \pm 0.69) \cdot 10^{-8}$	$(9.63 \pm 3.99) \cdot 10^{-9}$	$(8.04 \pm 4.33) \cdot 10^{-9}$	—
2139 → 31 (2108)	$(1.69 \pm 0.78) \cdot 10^{-7}$	$(4.76 \pm 1.96) \cdot 10^{-8}$	$(1.81 \pm 0.40) \cdot 10^{-8}$	$(1.25 \pm 0.39) \cdot 10^{-8}$	$(6.28 \pm 3.68) \cdot 10^{-9}$	—

† yield contains additional uncertainty from adjustment or contamination

‡ yield determined from deduced level population

Table 5.21: Thick-Target γ-Ray Yields from the ^{26}Mg(α, n)^{29}Si Reaction in Magnesium (quanta per α)

Transition (energies in keV)	α-Particle Energy (MeV)					
	10.0	8.8	7.7	7.0	6.3	5.6
7692 → 0 (7692)	$(2.73 \pm 1.50) \cdot 10^{-8}$	—	—	—	—	—
6715 → 0 (6715)	$(1.50 \pm 0.36) \cdot 10^{-7}$	—	—	—	—	—
6522 → 1273 (5249)	$(3.52 \pm 1.30) \cdot 10^{-8}$	—	—	—	—	—
7072 → 2028 (5044)	$(6.19 \pm 2.74) \cdot 10^{-8}$	—	—	—	—	—
4935 → 0 (4935)	$(3.16 \pm 0.92) \cdot 10^{-7}$	$(1.47 \pm 0.27) \cdot 10^{-7}$	$(7.21 \pm 0.75) \cdot 10^{-8}$	$(3.34 \pm 0.48) \cdot 10^{-8}$	$(1.02 \pm 0.13) \cdot 10^{-8}$	—
4895 → 0 (4895)	$(1.54 \pm 0.46) \cdot 10^{-7}$	$(7.59 \pm 1.51) \cdot 10^{-8}$	$(4.52 \pm 0.84) \cdot 10^{-8}$	$(2.07 \pm 0.36) \cdot 10^{-8}$	$(1.17 \pm 0.13) \cdot 10^{-8}$	—
4840 → 0 (4840)	$(1.39 \pm 0.34) \cdot 10^{-7}$	$(1.21 \pm 0.19) \cdot 10^{-7}$	$(4.99 \pm 0.45) \cdot 10^{-8}$	$(2.94 \pm 0.27) \cdot 10^{-8}$	$(5.81 \pm 1.26) \cdot 10^{-9}$	—
5949 → 1273 (4676)	$(4.25 \pm 2.52) \cdot 10^{-8}$	$(1.64 \pm 0.99) \cdot 10^{-8}$	$(9.95 \pm 4.01) \cdot 10^{-9}$	—	—	—
6194 → 2028 (4166)	$(1.91 \pm 0.46) \cdot 10^{-7}$	$(3.97 \pm 1.07) \cdot 10^{-8}$	—	—	—	—
6522 → 2426‡ (4096)	$(2.69 \pm 1.01) \cdot 10^{-8}$	—	—	—	—	—
6107 → 2028 (4079)	$(1.39 \pm 0.37) \cdot 10^{-7}$	$(5.02 \pm 1.61) \cdot 10^{-8}$	—	—	—	—
5813 → 2028 (3785)	$(1.10 \pm 0.30) \cdot 10^{-7}$	$(3.15 \pm 0.77) \cdot 10^{-8}$	$(1.39 \pm 0.29) \cdot 10^{-8}$	—	—	—
6107 → 2426‡ (3681)	$(6.63 \pm 1.81) \cdot 10^{-8}$	$(2.84 \pm 1.65) \cdot 10^{-8}$	—	—	—	—
4895 → 1273 (3622)	$(2.49 \pm 0.45) \cdot 10^{-7}$	$(1.13 \pm 0.30) \cdot 10^{-7}$	$(5.63 \pm 0.33) \cdot 10^{-8}$	$(2.33 \pm 0.27) \cdot 10^{-8}$	$(9.59 \pm 0.87) \cdot 10^{-9}$	—
4840 → 1273† (3567)	—	$(2.26 \pm 0.86) \cdot 10^{-8}$	$(1.09 \pm 0.27) \cdot 10^{-8}$	$(6.73 \pm 2.49) \cdot 10^{-9}$	—	—
5949 → 2426 (3523)	$(5.14 \pm 4.06) \cdot 10^{-8}$	$(1.08 \pm 0.66) \cdot 10^{-8}$	$(9.47 \pm 4.50) \cdot 10^{-9}$	—	—	—
5813 → 2426 (3387)	$(1.19 \pm 0.45) \cdot 10^{-7}$	$(1.86 \pm 1.56) \cdot 10^{-8}$	$(1.22 \pm 0.39) \cdot 10^{-8}$	—	—	—
6781 → 3624 (3157)	$(6.74 \pm 1.81) \cdot 10^{-8}$	—	—	—	—	—
5949 → 3067 ‡ (2882)	$(5.05 \pm 2.59) \cdot 10^{-8}$	$(1.59 \pm 0.73) \cdot 10^{-8}$	$(1.15 \pm 0.37) \cdot 10^{-8}$	—	—	—
4895 → 2028 ‡ (2867)	$(8.84 \pm 1.92) \cdot 10^{-8}$	$(5.11 \pm 1.18) \cdot 10^{-8}$	$(2.00 \pm 0.26) \cdot 10^{-8}$	—	—	—
4080 → 1273 (2807)	$(7.61 \pm 1.56) \cdot 10^{-7}$	$(3.26 \pm 0.47) \cdot 10^{-7}$	$(1.49 \pm 0.15) \cdot 10^{-7}$	$(8.59 \pm 0.66) \cdot 10^{-8}$	$(3.54 \pm 0.32) \cdot 10^{-8}$	$(5.88 \pm 0.46) \cdot 10^{-9}$
5813 → 3067 (2746)	$(2.29 \pm 0.61) \cdot 10^{-7}$‡	$(7.25 \pm 3.20) \cdot 10^{-8}$	$(2.67 \pm 1.58) \cdot 10^{-8}$	—	—	—
4741 → 2028 (2713)	$(9.32 \pm 1.72) \cdot 10^{-7}$	$(2.69 \pm 0.39) \cdot 10^{-7}$	$(1.49 \pm 0.10) \cdot 10^{-7}$	$(6.94 \pm 0.62) \cdot 10^{-8}$	$(2.10 \pm 0.23) \cdot 10^{-8}$	—
2426 → 0 (2426)	$(1.30 \pm 0.21) \cdot 10^{-6}$	$(7.68 \pm 1.07) \cdot 10^{-7}$	$(4.56 \pm 0.26) \cdot 10^{-7}$	$(3.27 \pm 0.23) \cdot 10^{-7}$	$(2.28 \pm 0.13) \cdot 10^{-7}$	$(1.19 \pm 0.07) \cdot 10^{-7}$

Table 5.22: Thick-Target γ-Ray Yields from the ^{26}Mg(α, p)^{29}Aℓ Reaction in Magnesium (quanta per α)

Transition (energies in keV)	α-Particle Energy (MeV)					
	10.0	8.8	7.7	7.0	6.3	5.6
4403 → 0 (4403)	$(2.40 \pm 0.77) \cdot 10^{-7}$	—	—	—	—	—
3641 → 0 † (3641)	—	$(1.72 \pm 1.20) \cdot 10^{-8}$	—	—	—	—
2866 → 0† (2866)	$(2.16 \pm 1.43) \cdot 10^{-7}$	$(1.11 \pm 0.54) \cdot 10^{-7}$	$(4.52 \pm 2.13) \cdot 10^{-8}$†	$(1.17 \pm 2.71) \cdot 10^{-8}$	—	—

† yield contains additional uncertainty from adjustment or contamination
‡ yield determined from deduced level population

Table 5.23: Thick-Target γ-Ray Yields from the $^{27}\mathrm{A}\ell(\alpha, n)^{30}\mathrm{P}$ Reaction (quanta per α)

Transition (energies in keV)	α-Particle Energy (MeV)					
	10.0	8.8	7.7	7.0	6.3	5.6
5208 → 0 (5208)	$(4.33 \pm 1.44) \cdot 10^{-8}$	—	—	—	—	—
5208 → 709 (4499)	$(2.17 \pm 1.69) \cdot 10^{-8}$	—	—	—	—	—
4144 → 0 (4144)	$(4.01 \pm 0.92) \cdot 10^{-7}$	—	—	—	—	—
3734 → 0 (3734)	$(1.86 \pm 0.60) \cdot 10^{-6}$	—	—	—	—	—
3734 → 677 (3057)	$(1.37 \pm 0.85) \cdot 10^{-6}$	—	—	—	—	—
2938 → 0 (2938)	$(2.34 \pm 0.55) \cdot 10^{-7}$	$(4.72 \pm 1.75) \cdot 10^{-8}$	$(2.23 \pm 0.98) \cdot 10^{-8}$	$(4.04 \pm 2.98) \cdot 10^{-9}$	—	—
2840 → 0 (2840)	$(4.52 \pm 0.98) \cdot 10^{-7}$	$(1.33 \pm 0.39) \cdot 10^{-7}$	$(7.31 \pm 1.95) \cdot 10^{-8}$	—	—	—
2724 → 0 (2724)	$(1.73 \pm 0.34) \cdot 10^{-6}$	$(6.48 \pm 1.09) \cdot 10^{-7}$	$(2.84 \pm 0.20) \cdot 10^{-7}$	$(6.61 \pm 2.10) \cdot 10^{-8}$	—	—
2539 → 0† (2539)	$(4.04 \pm 0.85) \cdot 10^{-6}$	$(1.23 \pm 0.19) \cdot 10^{-6}$	$(6.79 \pm 0.72) \cdot 10^{-7}$	$(1.82 \pm 0.31) \cdot 10^{-7}$	—	—
3929 → 1455 (2474)	$(2.51 \pm 1.02) \cdot 10^{-7}$	—	—	—	—	—
3019 → 677 (2342)	$(8.73 \pm 1.88) \cdot 10^{-7}$	$(2.11 \pm 0.68) \cdot 10^{-7}$	$(9.61 \pm 2.15) \cdot 10^{-8}$	$(1.26 \pm 1.41) \cdot 10^{-8}$	—	—
3734 → 1455 (2279)	$(6.03 \pm 2.21) \cdot 10^{-7}$	—	—	—	—	—
2938 → 677 (2261)	$(5.51 \pm 2.57) \cdot 10^{-7}$	—	—	—	—	—
2840 → 709 (2131)	$(1.23 \pm 0.24) \cdot 10^{-6}$	$(3.85 \pm 1.22) \cdot 10^{-7}$ ‡	$(1.31 \pm 0.37) \cdot 10^{-7}$	$(4.55 \pm 1.73) \cdot 10^{-8}$	—	—

Table 5.24: Thick-Target γ-Ray Yields from the $^{27}\mathrm{A}\ell(\alpha, p)^{30}\mathrm{Si}$ Reaction (quanta per α)

Transition (energies in keV)	α-Particle Energy (MeV)					
	10.0	8.8	7.7	7.0	6.3	5.6
8164 → 0 (8164)	$(2.99 \pm 0.72) \cdot 10^{-8}$	—	—	—	—	—
7623 → 0 † (7623)	$(2.23 \pm 1.00) \cdot 10^{-8}$	$(3.74 \pm 1.54) \cdot 10^{-9}$	—	—	—	—
7255 → 0 (7255)	$(6.51 \pm 1.38) \cdot 10^{-8}$	$(1.15 \pm 0.24) \cdot 10^{-8}$	$(4.55 \pm 1.17) \cdot 10^{-9}$	—	—	—
6915 → 0 (6915)	$(1.85 \pm 0.35) \cdot 10^{-7}$	$(3.65 \pm 0.53) \cdot 10^{-8}$	$(1.43 \pm 0.14) \cdot 10^{-8}$	$(2.85 \pm 0.47) \cdot 10^{-9}$	—	—
6744 → 0 (6744)	$(3.64 \pm 0.64) \cdot 10^{-7}$	$(1.26 \pm 0.18) \cdot 10^{-7}$	$(5.20 \pm 0.31) \cdot 10^{-8}$	$(9.95 \pm 1.03) \cdot 10^{-9}$	—	—
6537 → 0 (6537)	$(1.35 \pm 0.25) \cdot 10^{-7}$	$(5.49 \pm 0.78) \cdot 10^{-8}$	$(2.41 \pm 0.17) \cdot 10^{-8}$	$(4.92 \pm 0.61) \cdot 10^{-9}$	—	—
8330 → 2235 (6095)	$(3.72 \pm 1.35) \cdot 10^{-8}$	—	—	—	—	—
8290 → 2235 (6055)	$(5.48 \pm 2.24) \cdot 10^{-8}$	—	—	—	—	—
8164 → 2235 (5929) 8155 → 2235 (5920)	$(4.25 \pm 1.34) \cdot 10^{-8}$	—	—	—	—	—
8103 → 2235 (5868)	$(8.85 \pm 2.73) \cdot 10^{-8}$	—	—	—	—	—
7911 → 2235 (5676)	$(6.98 \pm 1.58) \cdot 10^{-8}$	—	—	—	—	—
7668 → 2235 (5433)	$(1.50 \pm 0.30) \cdot 10^{-7}$	$(1.73 \pm 0.81) \cdot 10^{-8}$	—	—	—	—
7623 → 2235 (5388)	$(1.16 \pm 0.25) \cdot 10^{-7}$	$(1.83 \pm 0.89) \cdot 10^{-8}$	—	—	—	—
7508 → 2235 (5273)	$(1.59 \pm 0.30) \cdot 10^{-7}$	$(1.75 \pm 0.38) \cdot 10^{-8}$	$(5.13 \pm 1.30) \cdot 10^{-9}$	—	—	—

† yield contains additional uncertainty from adjustment or contamination

‡ yield determined from deduced level population

Table 5.24 (Continued): Thick-Target γ-Ray Yields per α from the $^{27}\mathrm{A}\ell(\alpha,p)^{30}\mathrm{Si}$ Reaction (quanta per α)

Transition (energies in keV)		α-Particle Energy (MeV)					
		10.0	8.8	7.7	7.0	6.3	5.6
7255 → 2235	(5020)	$(7.48 \pm 1.72) \cdot 10^{-8}$	$(1.14 \pm 0.45) \cdot 10^{-8}$	$(2.67 \pm 1.19) \cdot 10^{-9}$	—	—	—
7079 → 2235	(4844)	$(2.28 \pm 0.49) \cdot 10^{-7}$	$(5.76 \pm 1.41) \cdot 10^{-8}$	$(2.05 \pm 0.61) \cdot 10^{-8}$	—	—	—
4809 → 0	(4809)	$(1.03 \pm 0.18) \cdot 10^{-6}$	$(5.24 \pm 0.72) \cdot 10^{-7}$	$(3.03 \pm 0.16) \cdot 10^{-7}$	$(1.87 \pm 0.22) \cdot 10^{-7}$	$(1.07 \pm 0.05) \cdot 10^{-7}$	$(4.07 \pm 0.21) \cdot 10^{-8}$
8190 → 3498	(4692)	$(5.48 \pm 8.70) \cdot 10^{-8}$	—	—	—	—	—
6915 → 2235	(4680)	$(2.60 \pm 1.07) \cdot 10^{-7}$	$(4.92 \pm 1.48) \cdot 10^{-8}$	$(1.82 \pm 0.28) \cdot 10^{-8}$	$(3.59 \pm 1.31) \cdot 10^{-9}$	—	—
6865 → 2235	(4630)	$(4.54 \pm 0.97) \cdot 10^{-7}$	$(1.42 \pm 0.25) \cdot 10^{-7}$	$(4.43 \pm 0.59) \cdot 10^{-8}$	$(7.34 \pm 2.14) \cdot 10^{-9}$	—	—
7911 → 3498 ‡	(4413)	$(1.72 \pm 0.68) \cdot 10^{-8}$	—	—	—	—	—
6641 → 2235	(4406)	$(6.25 \pm 0.97) \cdot 10^{-7}$	$(1.54 \pm 0.21) \cdot 10^{-7}$	$(7.65 \pm 0.48) \cdot 10^{-8}$	$(1.32 \pm 0.15) \cdot 10^{-8}$	$(1.32 \pm 1.59) \cdot 10^{-9}$	—
7668 → 3498 ‡	(4170)	$(3.45 \pm 1.17) \cdot 10^{-8}$	—	—	—	—	—
7623 → 3498 ‡	(4125)	$(1.89 \pm 0.57) \cdot 10^{-8}$	—	—	—	—	—
3769 → 0	(3769)	$(1.17 \pm 0.20) \cdot 10^{-6}$	$(7.26 \pm 1.10) \cdot 10^{-7}$	$(4.00 \pm 0.33) \cdot 10^{-7}$	$(1.71 \pm 0.37) \cdot 10^{-7}$	$(1.11 \pm 0.09) \cdot 10^{-7}$	$(3.70 \pm 0.38) \cdot 10^{-8}$
7255 → 3498	(3757)	$(5.48 \pm 1.77) \cdot 10^{-7}$	—	—	—	—	—
5951 → 2235	(3716)	$(2.31 \pm 0.68) \cdot 10^{-6}$	$(1.50 \pm 0.23) \cdot 10^{-6}$	$(6.72 \pm 0.40) \cdot 10^{-7}$	$(2.23 \pm 0.20) \cdot 10^{-7}$	$(5.98 \pm 0.37) \cdot 10^{-8}$	$(6.57 \pm 1.26) \cdot 10^{-9}$
7079 → 3498	(3581)	$(1.69 \pm 0.55) \cdot 10^{-7}$	$(1.69 \pm 1.08) \cdot 10^{-8}$	—	—	—	—
3498 → 0	(3498)	$(6.07 \pm 1.06) \cdot 10^{-6}$	$(3.02 \pm 0.41) \cdot 10^{-6}$	$(1.67 \pm 0.09) \cdot 10^{-6}$	$(9.40 \pm 0.81) \cdot 10^{-7}$	$(5.52 \pm 0.28) \cdot 10^{-7}$	$(2.43 \pm 0.11) \cdot 10^{-7}$
5614 → 2235	(3379)	$(4.98 \pm 1.05) \cdot 10^{-7}$	$(2.69 \pm 0.60) \cdot 10^{-7}$	$(1.36 \pm 0.17) \cdot 10^{-7}$	$(6.22 \pm 1.39) \cdot 10^{-8}$	$(2.61 \pm 0.59) \cdot 10^{-8}$	$(5.64 \pm 2.86) \cdot 10^{-9}$
5487 → 2235	(3252)	$(2.33 \pm 0.42) \cdot 10^{-6}$	$(1.09 \pm 0.15) \cdot 10^{-6}$	$(5.69 \pm 0.44) \cdot 10^{-7}$	$(3.34 \pm 0.54) \cdot 10^{-7}$	$(1.41 \pm 0.11) \cdot 10^{-7}$	$(3.81 \pm 0.65) \cdot 10^{-8}$
6915 → 3769‡	(3146)	$(5.21 \pm 2.20) \cdot 10^{-8}$	$(1.01 \pm 0.41) \cdot 10^{-8}$	$(3.83 \pm 1.48) \cdot 10^{-9}$	$(7.73 \pm 3.16) \cdot 10^{-10}$	—	—
5372 → 2235	(3137)	$(1.08 \pm 0.44) \cdot 10^{-7}$	$(8.24 \pm 3.17) \cdot 10^{-8}$	$(3.41 \pm 0.85) \cdot 10^{-8}$	$(1.98 \pm 0.64) \cdot 10^{-8}$	$(1.07 \pm 0.47) \cdot 10^{-8}$	—
5280 → 2235	(3045)	$(4.94 \pm 1.00) \cdot 10^{-6}$	$(2.64 \pm 0.37) \cdot 10^{-6}$	$(1.40 \pm 0.10) \cdot 10^{-6}$	$(8.17 \pm 0.73) \cdot 10^{-7}$	$(4.02 \pm 0.22) \cdot 10^{-7}$	$(1.26 \pm 0.08) \cdot 10^{-7}$
6537 → 3498‡	(3039)	$(4.32 \pm 1.22) \cdot 10^{-6}$	$(1.77 \pm 0.91) \cdot 10^{-7}$	$(7.81 \pm 2.02) \cdot 10^{-8}$	—	—	—
5231 → 2235	(2996)	$(4.10 \pm 1.46) \cdot 10^{-6}$	$(7.38 \pm 2.57) \cdot 10^{-7}$	$(2.65 \pm 0.86) \cdot 10^{-7}$	$(6.42 \pm 1.63) \cdot 10^{-8}$	$(3.44 \pm 0.73) \cdot 10^{-8}$	$(1.12 \pm 0.87) \cdot 10^{-8}$
4831 → 2235	(2596)	$(5.37 \pm 0.96) \cdot 10^{-6}$	$(2.28 \pm 0.32) \cdot 10^{-6}$	$(1.46 \pm 0.12) \cdot 10^{-6}$	$(7.17 \pm 0.65) \cdot 10^{-7}$	$(3.15 \pm 0.20) \cdot 10^{-7}$	$(1.32 \pm 0.11) \cdot 10^{-7}$
4809 → 2235‡	(2574)	$(4.51 \pm 1.01) \cdot 10^{-7}$	$(2.23 \pm 0.46) \cdot 10^{-7}$	$(1.29 \pm 0.21) \cdot 10^{-7}$	$(7.94 \pm 1.47) \cdot 10^{-8}$	$(4.56 \pm 0.74) \cdot 10^{-8}$	$(1.73 \pm 0.29) \cdot 10^{-8}$
5951 → 3498 7255 → 4809	(2453) (2446)	$(1.84 \pm 0.74) \cdot 10^{-7}$	—	—	—	—	—
7079 → 4809‡	(2270)	$(1.90 \pm 0.32) \cdot 10^{-7}$	—	—	—	—	—
2235 → 0	(2235)	$(4.89 \pm 0.86) \cdot 10^{-5}$	$(2.02 \pm 0.28) \cdot 10^{-5}$	$(1.11 \pm 0.06) \cdot 10^{-5}$	$(6.37 \pm 0.56) \cdot 10^{-6}$	$(3.39 \pm 0.17) \cdot 10^{-6}$	$(1.52 \pm 0.07) \cdot 10^{-6}$
7001 → 4831	(2170)	$(3.56 \pm 0.75) \cdot 10^{-7}$	$(7.29 \pm 1.58) \cdot 10^{-8}$	$(2.15 \pm 0.82) \cdot 10^{-8}$	—	—	—

† yield contains additional uncertainty from adjustment or contamination
‡ yield determined from deduced level population

Table 5.25: 10 MeV Thick-Target γ-Ray Yields from the Si Target (quanta per α)

Transition	Yields	Transition	Yields
^{28}Si$(\alpha,p)^{31}$P:			
5256 → 0 (5256)	$(6.86 \pm 1.97) \cdot 10^{-9}$	5015.4 → 0 (5015) 5015.2 → 0 (5015)	$(2.29 \pm 0.26) \cdot 10^{-8}$
4783 → 0 (4783)	$(2.42 \pm 0.32) \cdot 10^{-8}$	4594 → 0 (4594)	$(1.45 \pm 0.67) \cdot 10^{-8}$
4261 → 0 (4261)	$(1.46 \pm 0.09) \cdot 10^{-7}$	3506 → 0 (3506)	$(7.48 \pm 0.28) \cdot 10^{-7}$
4594 → 1266 (3327)	$(2.92 \pm 0.72) \cdot 10^{-8}$	5529 → 2234 (3296)	$(1.81 \pm 0.64) \cdot 10^{-8}$
3134 → 0 (3134)	$(5.45 \pm 0.22) \cdot 10^{-7}$	4261 → 1266 (2995)	$(6.89 \pm 1.62) \cdot 10^{-8}$
4634 → 2234 (2400)	$(2.44 \pm 0.66) \cdot 10^{-7}$	3506 → 1266 ‡ (2240)	$(5.20 \pm 0.36) \cdot 10^{-7}$
2234 → 0 (2234)	$(1.04 \pm 0.21) \cdot 10^{-5}$	4431 → 2234 (2197)	$(1.69 \pm 0.21) \cdot 10^{-7}$
3415 → 1266 (2148)	$(3.34 \pm 0.69) \cdot 10^{-6}$		
^{29}Si$(\alpha,n)^{32}$S:			
5798 → 0 (5798)	$(1.41 \pm 0.22) \cdot 10^{-8}$	5549 → 0 (5549)	$(1.09 \pm 0.23) \cdot 10^{-8}$
4695 → 0 (4695)	$(2.88 \pm 0.39) \cdot 10^{-8}$	4281 → 0 (4281)	$(1.90 \pm 0.09) \cdot 10^{-7}$
5549 → 2230 (3319)	$(1.54 \pm 0.92) \cdot 10^{-8}$	5413 → 2230 (3183)	$(6.26 \pm 0.67) \cdot 10^{-8}$
5006 → 2230 (2776)	$(1.25 \pm 0.14) \cdot 10^{-7}$	4695 → 2230 (2465)	$(3.23 \pm 1.62) \cdot 10^{-8}$
^{29}Si$(\alpha,p)^{32}$P:			
4149 → 78 (4071)	$(7.02 \pm 4.83) \cdot 10^{-9}$	3793 → 78 (3715)	$(9.12 \pm 4.02) \cdot 10^{-9}$
3320 → 78 (3242)	$(7.78 \pm 1.73) \cdot 10^{-8}$	3005 → 0 (3005)	$(3.26 \pm 1.61) \cdot 10^{-8}$
3005 → 78 (2927)	$(1.82 \pm 0.40) \cdot 10^{-7}$	3793 → 1323 (2470)	$(1.24 \pm 1.39) \cdot 10^{-8}$
^{30}Si$(\alpha,n)^{33}$S:			
4144 → 0 (4144)	$(1.64 \pm 0.53) \cdot 10^{-8}$	3832 → 0 (3832)	$(1.12 \pm 0.42) \cdot 10^{-8}$
4211 → 841 (3370)	$(1.74 \pm 0.62) \cdot 10^{-8}$	3221 → 0‡ (3221)	$(1.78 \pm 0.76) \cdot 10^{-8}$
2969 → 0 (2969)	$(2.04 \pm 0.32) \cdot 10^{-7}$	2935 → 0 (2935)	$(1.13 \pm 0.48) \cdot 10^{-7}$
2868 → 0 (2868)	$(9.92 \pm 1.84) \cdot 10^{-8}$	3221 → 841 (2380)	$(3.11 \pm 1.39) \cdot 10^{-8}$
2313 → 0 (2313)	$(7.05 \pm 2.20) \cdot 10^{-8}$		
^{30}Si$(\alpha,p)^{33}$P:			
4194 → 0 (4194)	$(1.49 \pm 0.41) \cdot 10^{-8}$		

† yield contains additional uncertainty from adjustment or contamination
‡ yield determined from deduced level population

germanium crystals. The characteristics of neutron reaction peaks make them readily identifiable. These peaks were quite broad due to electron-hole production by the recoiling germanium nucleus [Ch65], and reflected the energy spectrum of the incident neutrons. Unlike the γ-ray peaks in the detectors, the neutron-induced peak centroids were independent of the angle of observation, and were broadened by the same amount. The work of Chasman *et al* [Ch65] suggests that other broad peaks may exist at 4400 keV, 5440 keV and 7520 keV; however the peaks at these energies were quite wide and were usually present as an extended background. In cases where the neutron-induced peak was sufficiently narrow that it could not be dealt with as a background, the area of the interfering peak was estimated from the height of the neutron peak extending beyond the narrow γ-ray peak. An additional statistical uncertainty based on the scaling of these deduced areas to the total neutron yield on the order of 20% was added to these yields.

Chapter 6

Discussion

6.1 Thick Target γ-Ray Yields

In most cases, the yields and decay scheme information from our measurements were sufficient to separate the individual transitions, but insufficient to improve the accuracy of the published branching ratio measurements. In addition, the low energy cut-off near 2 MeV in this experiment typically permitted only the detection of transitions to the ground and first few excited states, and so prevented the determination of complete decay sequences. The branching ratios determined here are in agreement with published values [En78, En90, Aj87] within statistical uncertainty, which usually amounted to between ±7 to 15% in the calculated branching ratio. The only exception to this behaviour was observed in the decay of the 4895 keV level in the ^{29}Si nucleus populated through the ^{26}Mg(α, p) reaction. The published branching ratios for the decay of this level indicate that the ground state transition occurs with a relative intensity of $18 \pm 2\%$ while the transition to the 1273 keV level occurs with an intensity of $55 \pm 3\%$, and hence these two transitions are expected to decay in a ratio of 1:3. Our measurements indicate a stronger ground state branch and a ratio between 1:2 to 1:1. Our statistical uncertainty in this ratio in different α-particle runs is typically around 20%, and in several α-particle runs we exclude the published decay scheme at the 1σ level of statistical uncertainty. This disagreement may be due to some unidentified contamination of the weak ground state transition.

6.2 α-Induced γ-Ray Yields from Materials

One of the primary aims of this study was to provide a method of generating reliable direct production α-induced γ-ray spectra for materials containing traces of the radioactive uranium and thorium chains. Such spectra, together with other calculations of the spontaneous fission and radiative neutron capture contributions, enable a characterization the γ-ray background from the radioactive content of these materials. In this section, we provide calculations of the direct production α-induced component of these spectra for a number of materials in the SNO detector, based on the γ-ray background tables presented in section 5.2.1. We compare these measurement-based spectra to theoretically calculated spectra, and explore the level of agreement obtained from using different data sources and different levels of complexity in these calculations.

Calculations of γ-ray spectra are frequently required for materials in and around low-background laboratories which contain the naturally occurring radioactive uranium and thorium decay chains. Both the uranium and thorium chains emit a number of α-particles with energies, listed in table 6.1, in the range covered by our measure-

Table 6.1: Equilibrium α-Particle Intensity from the ^{238}U and ^{232}Th Decay Chains

^{238}U			^{232}Th		
α-Emitter	Average α-Particle Energy (MeV)	α-Particle Intensity per decay ^{238}U	α-Emitter	Average α-Particle Energy (MeV)	α-Particle Intensity per decay ^{232}Th
^{238}U	4.19	1.0	^{232}Th	4.00	1.0
^{234}U	4.76	1.0	^{228}Th	5.40	1.0
^{230}Th	4.66	1.0	^{224}Ra	5.65	1.0
^{226}Ra	4.77	1.0	^{220}Rn	6.29	1.0
^{222}Rn	5.49	1.0	^{216}Po	6.78	1.0
^{218}Po	6.00	1.0	^{212}Bi	6.05	0.36
^{214}Po	7.69	1.0	^{212}Po	8.78	0.64
^{210}Po	5.31	1.0			

ments. These α-particle energies and intensities were used to calculate the γ-ray spectra from the ^{238}U and ^{232}Th chains in a number of materials using our results from section 5.2.1. Since the uncertainties quoted in these yield tables are largely dominated by systematic uncertainties, our calculations using these tables have combined and propagated the uncertainties linearly, rather than in quadrature.

The γ-ray spectra were calculated by summing the yields obtained for each α-particle energy, $Y_\alpha(E_\alpha)$, using a logarithmic interpolation for each energy range given by

$$\ln Y_\alpha(E_\alpha) = \ln Y_i + \frac{E_\alpha - E_i}{E_{i+1} - E_i} \ln\left(\frac{Y_{i+1}}{Y_i}\right) \tag{6.1}$$

where the i and $i+1$ subscripts indicate the tabulated yields Y at energies E bracketing the α-particle energy, E_α, for each element in the material. This logarithmic interpolation scheme is based on the observed exponential dependence of the thick-target yield on α-particle energy. In instances where the lower energy yield was zero, a linear interpolation was used. A number of the α-particles in both chains have energies below the lowest energy measurement at 5.6 MeV in this study. The contribution of these α-particles to the γ-ray spectrum was obtained through an extrapolation using equation (6.1) with data from the two lowest measured α-particle energies. The contribution of each elemental yield to the spectrum was obtained through a stopping power-weighted sum of the individual yields [He89].

For most elements, yield contributions due to α-particles with energies below our lowest measured energy were small. The contribution from α-particles with energies less than 5.6 MeV was largest for the lightest elements, and more important for the uranium chain due to a greater number of α-particles emitted with energies around 4 MeV. The extrapolated yields contributed less than 10% to γ-ray yields above 5 MeV in each element in both the uranium and thorium chains. Below this γ-ray energy, the yields for Be from the uranium chain were most sensitive to the extrapolation, with as much of 60% of the uranium chain yield and 20% of the thorium chain yield coming from α-particles with energies less than 5.6 MeV. A comparison of this yield calculation to a calculation supplemented by Be yields between $E_\alpha = 4$ and 5.6 MeV derived from the cross sections of Geiger and Van der Zwan [Ge75, Ge76] agreed within 10% for the uranium chain, and within 4% for the thorium chain. The B yields below $E_\gamma = 4$ MeV contained up to a 50% contribution for the uranium chain and 20% for the thorium chain from α-particles below 5.6 MeV. The γ-ray yields for F below 3 MeV also contained a contribution from low energy α-particles, with 25% and 6% of the uranium and thorium yield, respectively, attributed to α-particles with energies less than 5.6 MeV. All other targets at low γ-ray energies contained no more

Table 6.2: Composition of Materials for γ-Ray Spectrum Calculations

Element	Material Composition by Mass			
	Granite	Norite	Photomultiplier Tube Glass	Dolomite Concrete
H	—	0.15%	—	0.80%
B	—	—	7.00%	—
C	—	0.04%	—	10.30%
O	44.32%	46.00%	53.50%	52.30%
Na	2.86%	2.23%	3.20%	—
Mg	0.67%	3.29%	—	10.50%
Al	9.09%	8.95%	2.10%	0.40%
Si	30.08%	26.20%	30.70%	1.50%
P	—	0.12%	—	—
S	—	0.20%	—	0.10%
K	4.69%	1.15%	2.80%	—
Ca	2.59%	5.22%	—	23.40%
Ti	—	0.50%	—	—
Mn	0.25%	0.13%	—	0.10%
Fe	5.40%	6.21%	—	0.40%

than a 20% yield contribution in the uranium chain and 5% in the thorium chain at γ-ray energies above 2 MeV. In most applications, γ-rays from the (α, p) and (α, n) reactions below 4 MeV are a minor component of the total γ-ray spectrum, and so uncertainties introduced by this extrapolation can be largely ignored.

The calculated γ-ray spectrum for granite, a common host rock for several low-background laboratories, with a composition given in table 6.2 is shown in figure 6.1 for a thorium mass fraction which is five times that of the uranium mass fraction. The theoretical spectrum of Pomansky [Po86] for the direct production of γ-rays through the $(\alpha, n\gamma)$ and $(\alpha, p\gamma)$ reactions in granite is also shown in this figure, along with our own theoretical calculations. Both our experimental and theoretical yields fall considerably below those reported by Pomansky using the calculations of Glotov

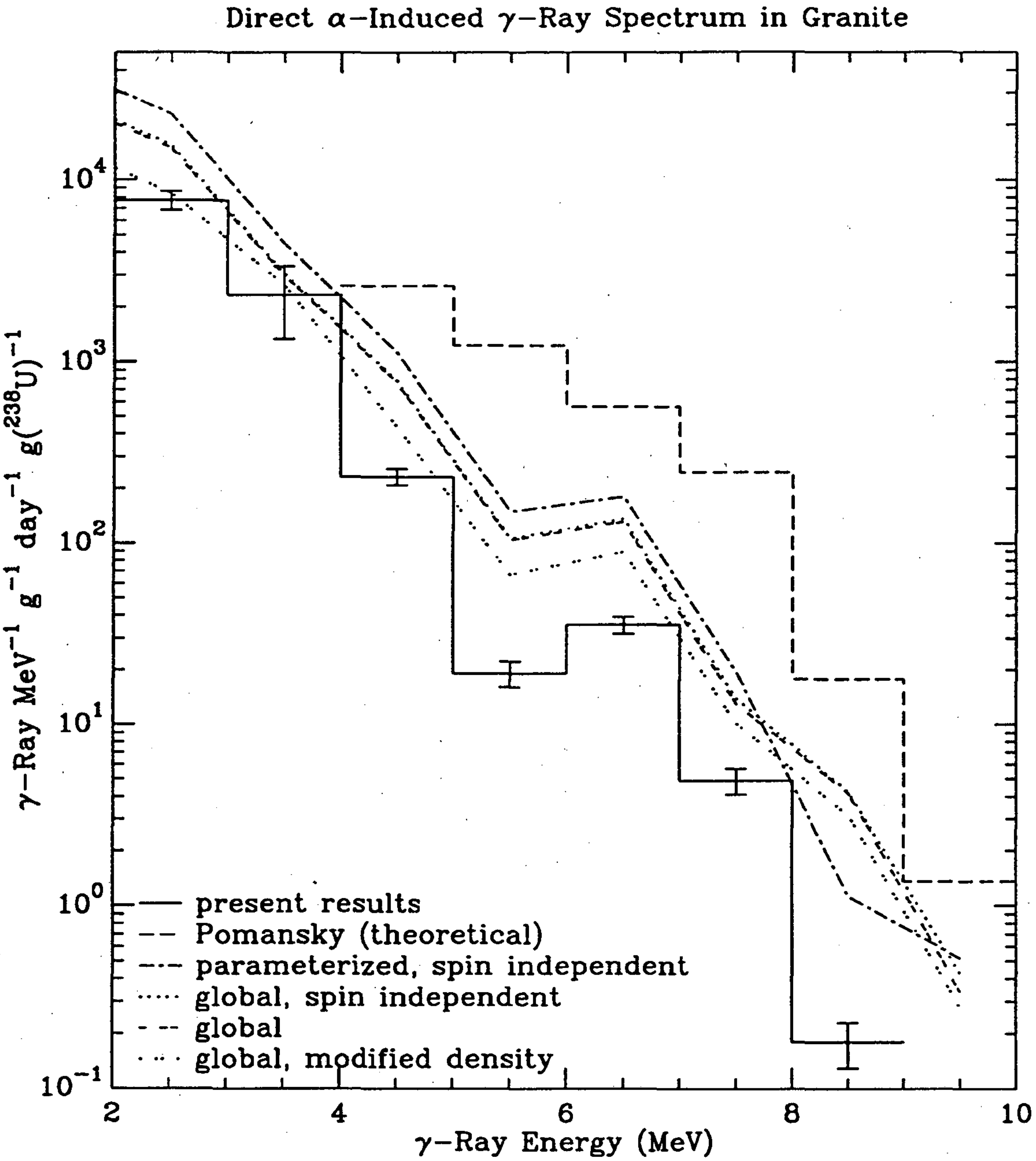

Figure 6.1: The direct α-induced γ-ray spectrum in granite has been constructed from our measurements of the γ-ray yield from Na, Mg and $A\ell$. The yields are reported in terms of the mass fraction of ^{238}U, under the assumption that there is five times as much ^{232}Th in the granite. The solid histogram shows the spectrum derived from experimental measurements, while the other lines show the results of theoretical calculations. The broken-line histogram shows the theoretical calculations of Pomansky for granite with the same radioactive content.

[Po86, Gl78, Gl71].

The spectrum in figure 6.1 labelled "present results" was derived from our measured Na, Mg and Aℓ elemental γ-ray yields. These elements constituted 13% by weight of the granite and were exceeded in composition only by oxygen and silicon. Only the rare ^{17}O and ^{18}O oxygen isotopes have a favourable Q-value for producing γ-rays, and only through the (α, n) reaction. The total neutron yield from the (α, n) reaction in oxygen for α-particles up to 10 MeV has been reported, and is known to be a factor of 50 smaller than the total neutron yield from aluminum [He89]. Since more than half the aluminum γ-ray come from the (α, p) reaction, it is expected that the element γ-ray yield from oxygen would be only 1% that of aluminum, and hence contribute no more than 5% to the granite γ-ray spectrum. Similarly for silicon, which has been shown by our measurements at $E_\alpha = 10$ MeV to have a much smaller yield than those for other targets, the published neutron yield is an order of magnitude below that of aluminum, and can be neglected in most calculations of the high energy γ-ray spectrum. This is supported by our own theoretical calculations, which indicate that Si reactions do not significantly contribute the γ-ray yield above $E_\gamma = 5$ MeV, and account for no more than 10% of the theoretical spectrum between 3 and 4 MeV in granite.

Carbon, although not present in granite, does occur in significant concentrations in some rocks. Available energy considerations indicate that the γ-rays from this element would primarily result from the (α, n) reaction on the rarer ^{13}C isotope. This situation parallels that for oxygen, with the known neutron yield for carbon occurring at a rate approximately two orders of magnitude below that for $A\ell$ and Mg. Since carbon typically occurs in concentrations on the same order as that of $A\ell$ and Mg, the γ-ray contribution from this element is assumed to be at most on the 1% level in most materials and can be neglected in most calculations.

Our own theoretical calculations for granite are shown in figure 6.1 by a number of continuous lines. In these calculations, we have adopted the same contamination of ^{238}U and ^{232}Th as Pomansky and Glotov, and have calculated the γ-ray yield using the parameterized cross section data set of Chatterjee *et al* [Ch81] and the global optical potential S-matrix cross section data set. Both spin-independent and fully spin-coupled calculations were used to produce a population distribution for each residual nucleus, with the two fully spin-coupled calculations using statistical and modified level densities, respectively. These spectra were constructed from sets of theoretical Na, Mg, $A\ell$ and Si element thick-target γ-ray yield tables, analogous to the binned tables 5.2 through 5.8. These tables were used in the same manner as our experimental results to create the theoretical γ-ray spectra for granite.

In constructing the theoretical yield tables, only (α, p) and (α, n) reactions were assumed to contribute to the high energy γ-ray yield. The excitation population distribution from our statistical model calculations for each residual nucleus was converted into a γ-ray spectrum by convolving these populations distributions with the average γ-ray cascade from the known decay schemes of all the levels within each 1 MeV excitation bin. In cases where no measured level decay schemes within an excitation bin were available, the excitation population of the bin was assumed to decay directly to the ground state. The spectrum for an element was constructed by adding together the individual γ-ray spectra from each residual nucleus, weighted by the target nucleus isotopic abundance.

Our theoretical γ-ray spectra calculations reproduced the gross structure of the measurement-based spectrum. All our calculated spectra share similar overall features, with satisfactory agreement over most of the measured range, except within 2 MeV of the maximum spectrum energy. The gross structure of each spectrum is largely determined by the excitation of the residual nuclei, while localized features such as the difference between adjoining bins, are largely determined by the de-excitation γ-ray cascade of the residual nuclei. In figure 6.1, we see that our theoretical spectra are no more than a factor of four larger than the measurement-based spectrum, with our most detailed calculation agreeing within a factor of two over most of the range. Our calculations produce spectra which are in better agreement with experiment than that of Pomansky and Glotov. This difference may result from their derivation of the $^{27}\mathrm{A}\ell(\alpha,p)$ and $^{23}\mathrm{Na}(\alpha,p)$ reaction rates from the experimental $^{25}\mathrm{Mg}(\alpha,n)$ yield measurements [Gl78]. This assumption was adopted because of a lack of experimental measurements of the (α,p) reaction for these nuclei, and was justified on the basis of the similarity of the reaction Q-values and the charge independence of the nuclear force.

Our different theoretical calculations show the effects of different levels of calculational complexity. The simplest calculation, the "parameterized, spin-independent" calculation utilizing the parameterized optical cross sections of Chatterjee *et al* and the statistical level densities of Gilbert and Cameron [Gi65b, Gi65c] and Von Egidy *et al* [Vo86, Vo88], predicted yields which are typically a factor of four greater than those observed experimentally. These calculations used the total absorption cross sections, and did not consider the effects of particle spin and angular momentum beyond accounting for an increase in momentum phase space for incident particles due to magnetic substates. A 25% reduction over this calculated γ-ray spectrum and an agreement with experimental results typically within a factor of three were obtained by replacing the parameterized cross sections with the total absorption cross sections obtained from DWBA calculations using global optical potentials. A much smaller improvement was obtained by increasing the complexity of these calculations through a detailed accounting of the angular momentum coupling of the particles involved in the reaction. This calculation, labelled "global" in figure 6.1, used cross sections from the same optical model calculation as the "global, spin independent" calculation, and resulted in no more than a 10% decrease in the γ-ray spectrum, compared to the spin independent calculation, over most of the energy range. The increased complexity introduced a factor of 40 increase in the time required to complete a calculation.

A much larger change in the calculated γ-ray spectrum was obtained by using a modified level density which more closely mirrored the observed level structure of the residual nuclei. This calculation, labelled "global, modified density" was performed using full spin-coupling. Agreement to within a factor of two with experimental results over most of the γ-ray energy range was obtained from these calculations, at the expense of a factor of three increase in computation time over the "global" calculation, primarily due to discontinuities in the level density necessitating a smaller step size in the numerical integrations.

Similar features are seen in the measurement-based and theoretically calculated γ-ray spectra for materials used in the SNO detector, shown in figures 6.2 through 6.4. These spectra are important in determining the energy threshold and detection limits which can be attained in the measurement of the neutrino flux from astrophysical sources. Prior to the present study, the theoretical spectrum of Glotov provided the only information available on α-induced γ-rays, and had been extensively used in early design calculations.

In the SNO detector, α-induced γ-rays can arise from any material containing light elements. Most notable among these are the norite host rock, the shielding concrete, and the glass used in the construction of the photomultiplier tubes. The spectra resulting from uranium and thorium decay chains in each of these materials are discussed below.

The measurement-based and theoretical γ-ray spectra from norite are shown in figure 6.2 in units of γ-ray quanta per MeV per gram per year. The measured concentrations of 1.13 ppm ^{238}U and 5.35 ppm ^{232}Th [Ha94] in the cavity rock were used in these calculations. The spectrum for norite is very similar to that for granite, and is largely dominated by the (α, p) reaction on Aℓ. The same agreement between experimental and theoretical calculations as for granite is observed.

The γ-ray spectra for the concrete used in the construction of the SNO detector

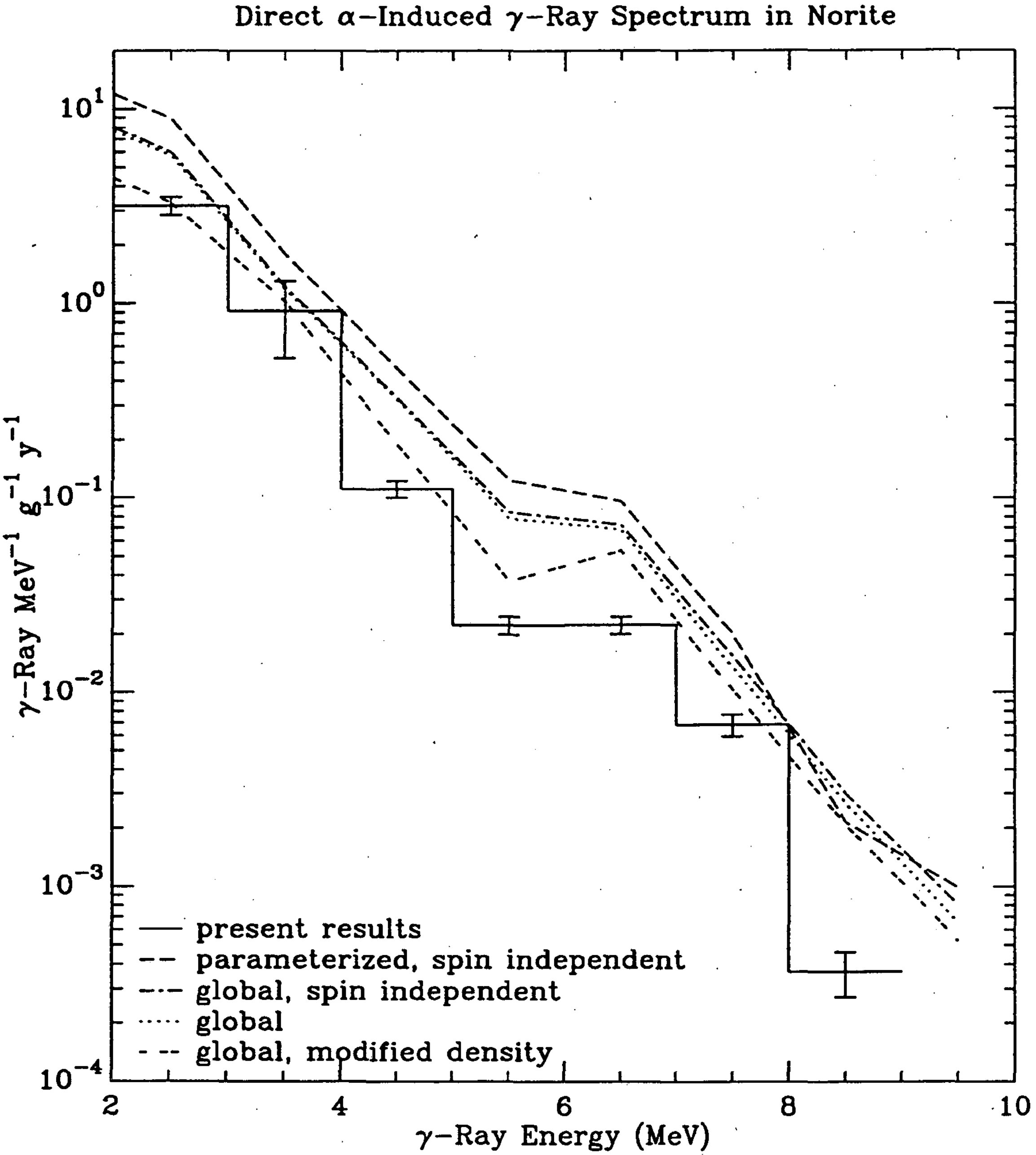

Figure 6.2: The direct α-induced γ-ray spectrum in norite has been constructed from our measurements of the γ-ray yield from Na, Mg and Aℓ. The yields is reported for 1.13 ppm ^{238}U and 5.35 ppm ^{232}Th. The solid histogram shows the measurement-based spectrum. The other lines show the theoretical spectra construct from calculations of γ-rays from Na, Mg, Aℓ and Si.

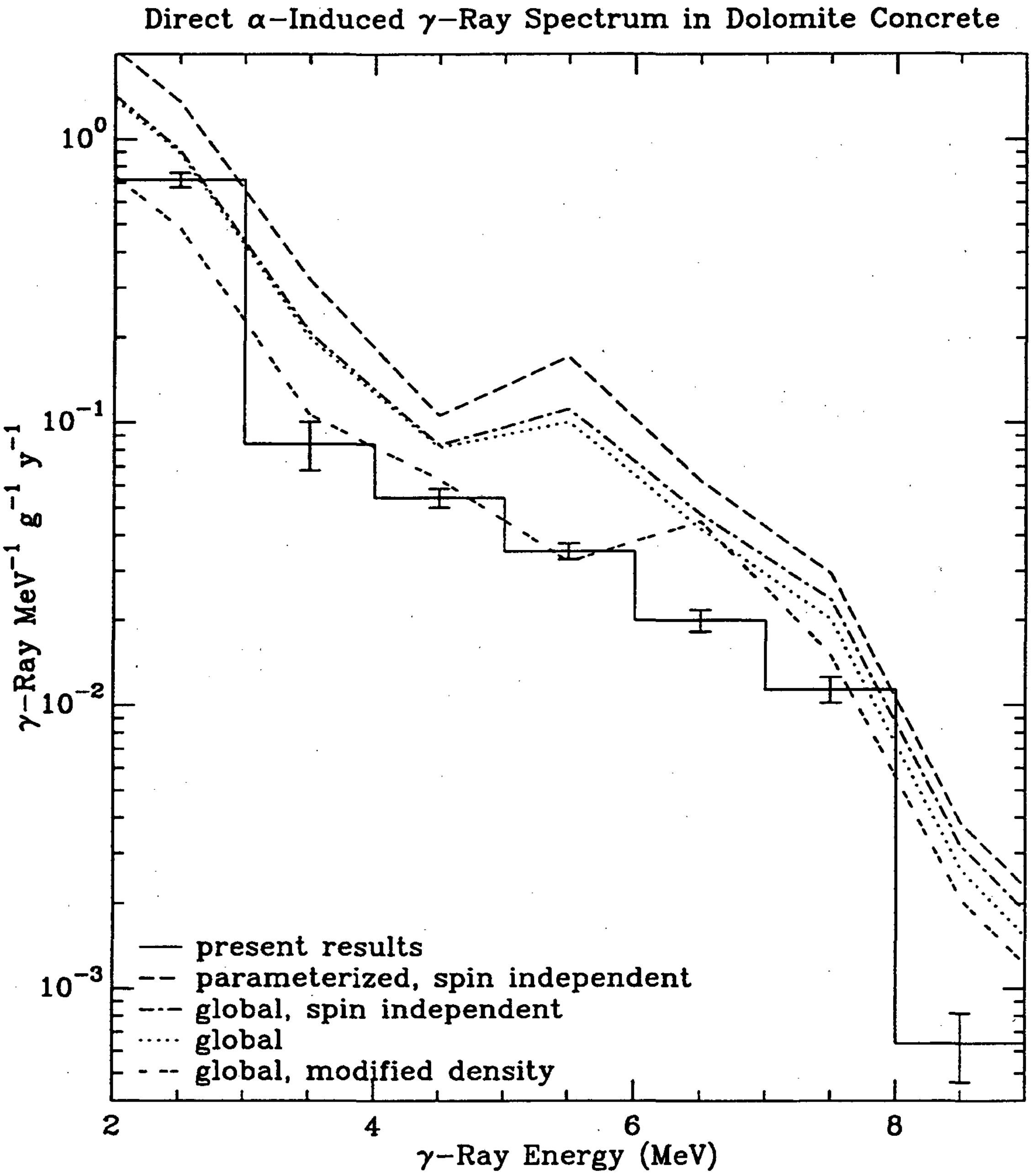

Figure 6.3: The direct α-induced γ-ray spectrum in dolomite concrete has been constructed from our measurements of the γ-ray yield from Na, Mg and Aℓ. The yields are reported for contamination levels of 1.19 ppm ^{238}U and 2.39 ppm ^{232}Th. The solid histogram shows the measurement based spectrum. The other lines show the theoretical spectra from calculations for α-induced γ-rays on Na, Mg, Aℓ and Si.

is shown in figure 6.3. The measured levels of ^{238}U and ^{232}Th at 1.19 and 2.39 ppm, respectively [Ha94], were used in this calculation. The γ-ray spectrum in concrete is largely determined by the Mg γ-ray yield, and in particular by the yield from the ^{25}Mg(α, n) reaction. Theoretical calculations produce a γ-ray spectrum in better agreement than that for norite, with the parameterized cross section calculation agreeing within a factor of three over most of the range, and the fully spin-coupled calculations with a modified level density agreeing with the measurement-based spectrum to within 50% over most of the range. The large yield in the theoretical calculations between 5 and 6 MeV is an artifact of the continuous level density used in this calculation, coupled with approximations used to convert the residual nucleus excitation into a γ-ray spectrum. The ^{28}Si residual nucleus from the ^{25}Mg(α, n) reaction contains no levels between 5 and 6 MeV, while our calculations using a statistical level density predict an excitation due to the non-zero level density in this region. Our calculation assumed that the population of a region in the residual nucleus for which no experimental decay schemes are known decays directly to the ground state, and so produced this high γ-ray yield between 5 and 6 MeV. The magnitude of this effect can be seen by comparing the theoretical calculations using the statistical level density to the calculation using a modified level density in which this region of the level density has been set to zero.

The γ-ray spectra for the photomultiplier tube glass used in the SNO detector is presented in figure 6.4. Spectra from both the ^{238}U and ^{232}Th chains are shown in this figure for contamination levels of 1 ppm each. These spectra are dominated by

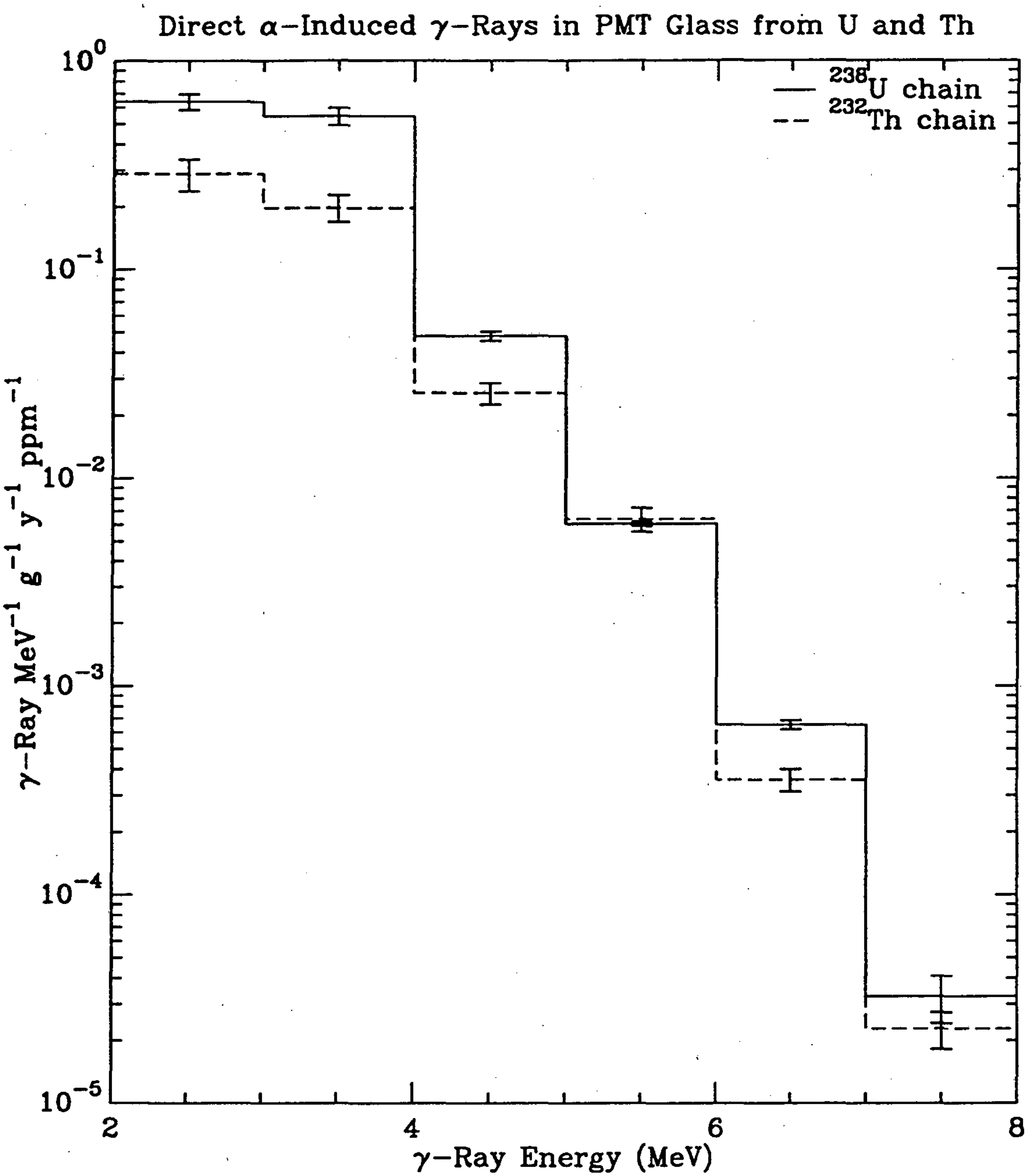

Figure 6.4: The direct α-induced γ-ray spectrum in photomultiplier glass has been constructed from our measurements of the γ-ray yield from B, Na, and Aℓ. The yields are reported for 1 ppm concentrations of both ^{238}U and ^{232}Th. The solid histogram shows the measurement derived spectrum from ^{238}U, while the broken histogram shows the measurement derived spectrum from ^{232}Th. Theoretical calculations for boron, the dominant γ-ray emitter, have not been performed, and so no theoretical spectrum has been provided.

γ-rays from α-particle reactions on boron. These nuclei contain so few nucleons and so few levels that statistical level densities and parameterizations of cross section and optical potential are not reliable, and so no theoretical spectra have been provided.

6.3 Excitation of the Residual Nucleus

The theoretical γ-ray spectra presented in the previous section are in agreement with experimental results to within a factor of two, a result which is typical of such calculations for higher mass nuclei [Mo91]. However, these γ-ray spectra are a sum of a number of calculations for different nuclei and reactions convolved with the respective average γ-ray cascade schemes. As such, the detailed structure of the different statistical model calculations has been obscured by these manipulations. In the following sections, we avoid these complications and provide a more detailed assessment of our statistical model calculations by using our experimental data to determine the excitation population distribution of several residual nuclei. Through this assessment we investigated the applicability and limitations of our theoretical models to these light nuclei.

Our theoretical calculations assumed that the detailed structure of the nuclei involved in the reactions could be neglected. The primary basis for this assumption is the existence of a continuum of overlapping states in the compound nucleus which results in a mixing of the configurations describing the nuclear level. Although this condition is met at our highest α-particle energy for some of the reactions investigated, it is somewhat ambiguous whether this overlap of states is sufficient at lower energies to justify a simple statistical treatment of the reaction process. In addition, our calculations apply to the average behaviour of the residual nucleus; as such, the experimental results to which we compare these calculations should sample a number of levels to reflect an average behaviour for the nucleus. At low excitation energies, this average behaviour is generally difficult to establish because of the low level density near the ground state of the residual nuclei. This low level density in some cases causes the behaviour of an energy interval to be determined by one or two levels rather than by a proper statistical ensemble. In the following sections, we investigate the ^{28}Si, ^{29}Si and ^{30}Si residual nuclei for signs of these effects.

In the first section, we compare the high energy experimental excitation distribution from 10 MeV α-particles with our range of calculations for the ^{28}Si, ^{29}Si and ^{30}Si residual nuclei. At these energies, the majority of the reaction intensity results from the interaction of α-particles in the 9 to 10 MeV range, and hence reflects the level of agreement obtained when a large overlap of compound nuclear states exists. Large differences between experimental and theoretical results reflect difficulties in the statistical characterization of experimental results rather than a breakdown in the theoretical model. In the section following this, we compare the theoretical and experimental population distribution dependence on α-particle energy and search for features which may signal the breakdown of statistical behaviour and indicate a limitation to our calculations.

6.3.1 Excitation Population Distribution

The excitation population distribution was obtained by using our measured yields from section 5.2.2 with the published decay schemes to deduce the population of as many levels in the residual nucleus as possible. The population of levels by cascade γ-ray decay was subtracted to allow a direct comparison of theoretical and experimental results. The population distribution of the ^{28}Si, ^{29}Si and ^{30}Si residual nuclei above a low energy cut-off were obtained using equation (3.101). We first discuss the general features of the excitation population distribution measured in the $E_\alpha = 10$ MeV runs below, and afterward discuss the features of the various theoretical calculations.

Figures 6.5 through 6.7 show the thick-target residual nucleus excited state population distribution for three residual nuclei extracted from the appropriate 10 MeV α-particle runs. Each distribution shows the deduced population from one reaction with a target isotope, displayed in 1 MeV wide bins. The population of several kinematically allowed but not observed levels was neglected in determining the population distribution shown in these figures. The majority of these levels decayed through a low energy γ-ray cascade, and so were not observed in this study. Most of these missing levels would not significantly change the observed distributions unless otherwise noted below. Uncertainties in the population distributions due to missing levels have not been factored into the uncertainties shown on these figures.

The $E_\alpha = 10$ MeV population distribution for the ^{28}Si nucleus is shown in figure 6.5. The ^{25}Mg(α, n) reaction populating this nucleus has one of the largest Q-

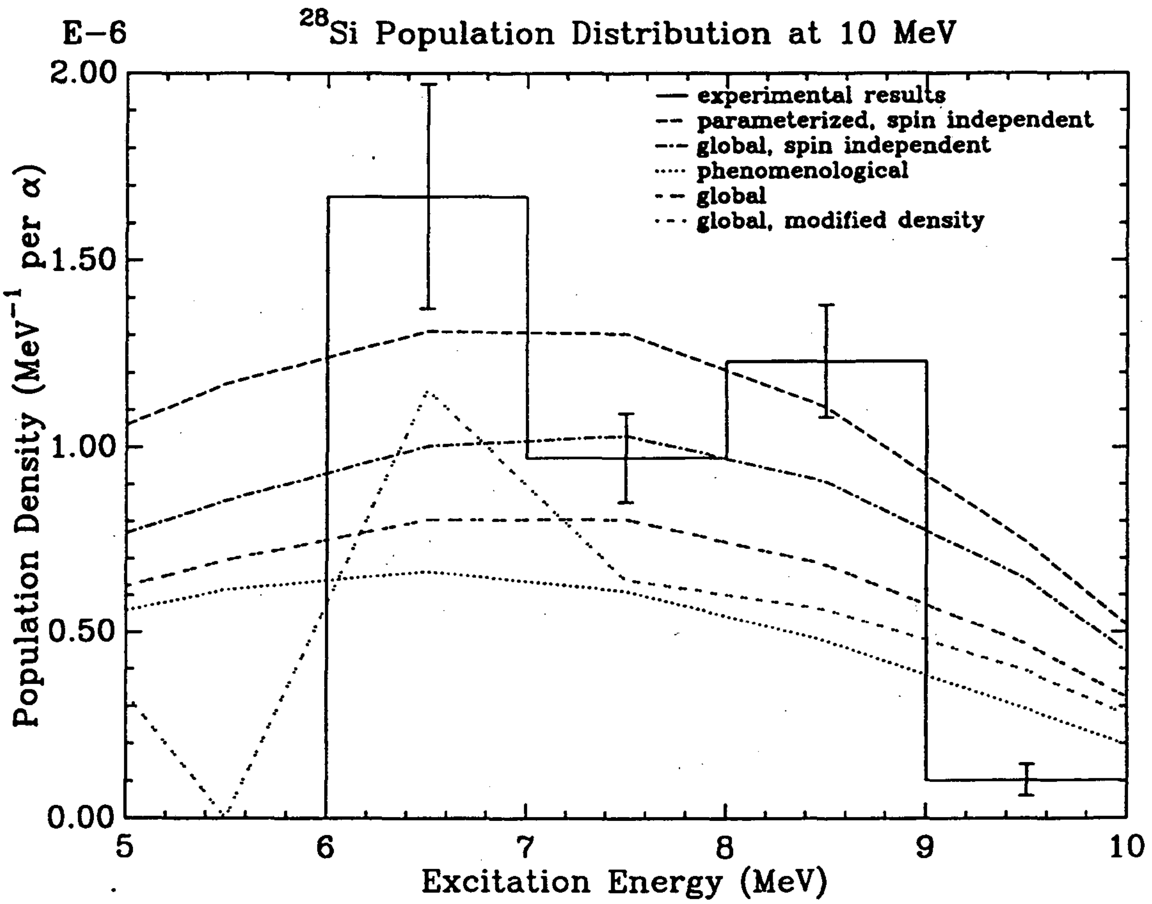

Figure 6.5: The excitation population distribution of ^{28}Si from the ^{25}Mg(α,n) reaction at E_α = 10 MeV. The deduced population distribution is shown by the histogram, with the error bars reflecting experimental uncertainties. The broken lines show the predicted populations of ^{28}Si from the statistical model, using the spin independent and spin-coupled calculations. The latter calculations were limited to a maximum compound nuclear spin of $13/2\hbar$. Theoretical populations were adjusted to reflect the 10% isotopic abundance of the target nucleus in Mg.

values of the reactions studied here, and correspondingly produced the highest energy excitation observed in a residual nucleus. This nucleus has only three excited states below an excitation of 5 MeV. The empty bin between 5 and 6 MeV is due to the absence of nuclear levels over this energy range. The population of each bin in the distribution was determined by three to six levels each. The validity of the statistical average is marginal with only three levels in some energy bins. The largest number of unobserved levels occurred in the highest energy bin, and could conceivably increase the 9 to 10 MeV bin population by as much as a factor of two.

The measured population distribution for the ^{29}Si nucleus resulting from the (α, n) reaction on ^{26}Mg is shown in figure 6.6. This nucleus contains five excited states below 4 MeV, two of which between 3 and 4 MeV decay through a γ-ray cascade which produced no characteristic γ-rays observable by this study. As a result, no determination of the population distribution below 4 MeV could be made, and we have restricted our characterization to energies above this. The population distribution was determined from a sample of five levels in each of the 4 to 5 MeV and 6 to 7 MeV range, and two levels in each of the remaining bins. The majority of undetermined level populations falls between 6 and 8 MeV, where with average populations could account for a factor of two increase in the 6 to 7 MeV population and a factor of 3 to 4 in the 7 to 8 MeV bin.

The population distribution for ^{30}Si from the ^{27}A$\ell(\alpha, p)$ reaction is shown in figure 6.7. This nucleus has a level structure containing six levels below an excitation energy of 5 MeV, five of which decay primarily through the emission of γ-rays with

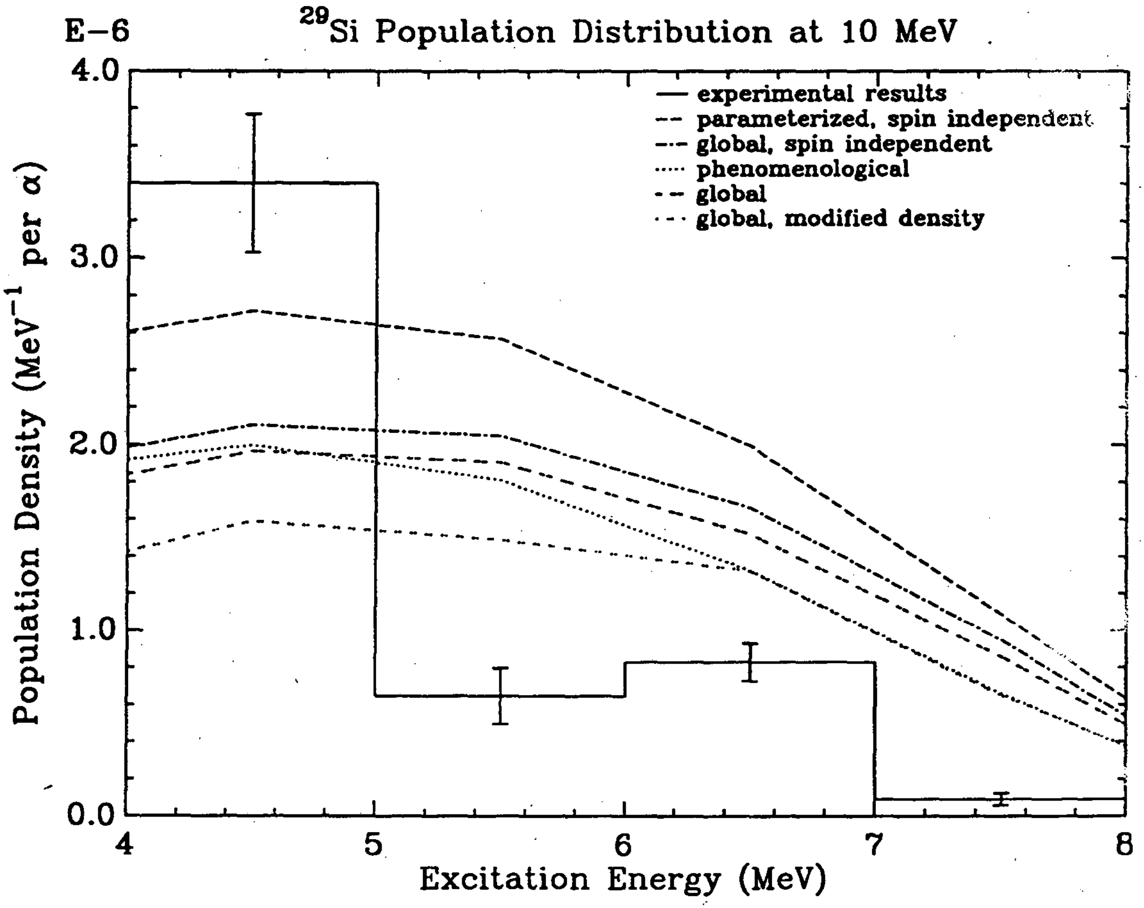

Figure 6.6: The excitation population distribution of ^{29}Si from the ^{26}Mg(α,n) reaction at E_α = 10 MeV. The deduced population distribution is shown by the histogram, with the error bars reflecting experimental uncertainties. The broken lines show the predicted excitation of the ^{29}Si from the statistical model, using the spin independent and spin-coupled calculations. The latter calculations were limited to a maximum compound nuclear spin of $5\hbar$. The theoretical populations were adjusted to reflect the 11% isotopic abundance of the target nucleus in Mg.

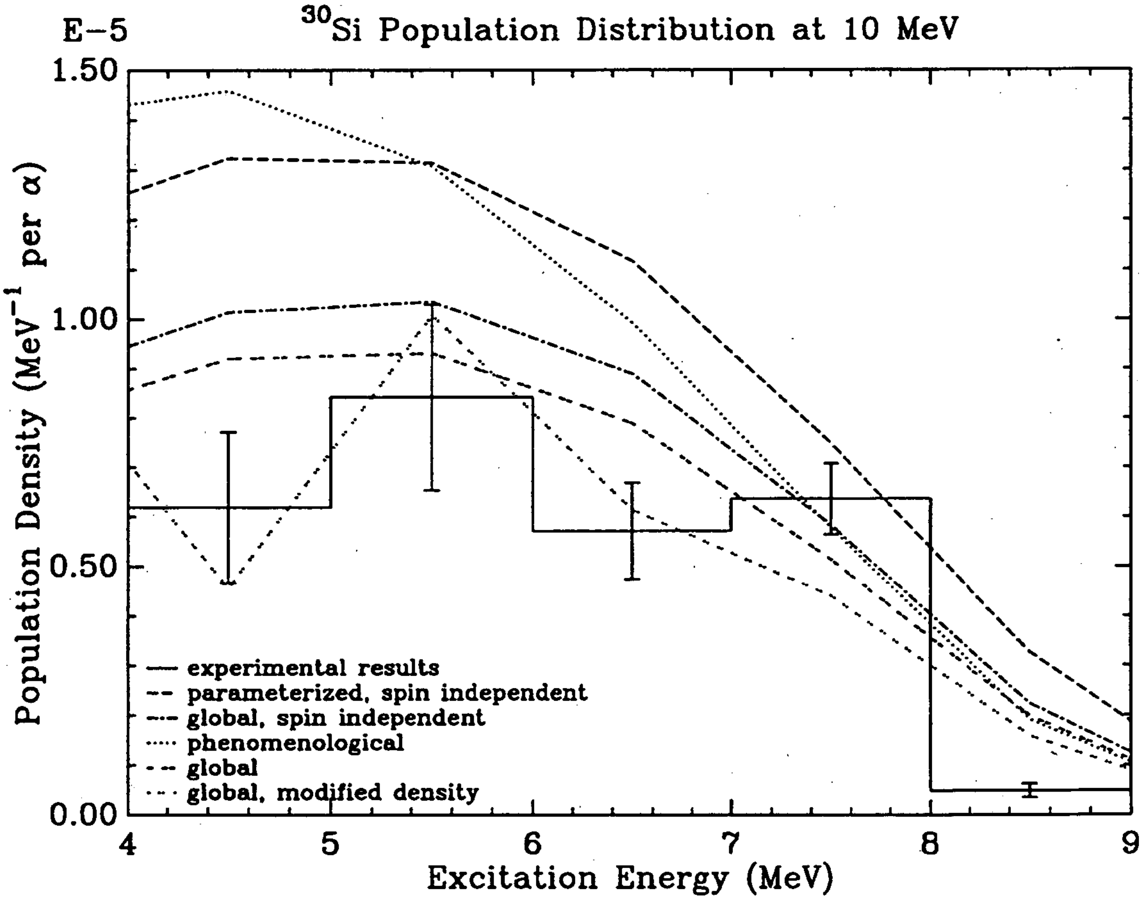

Figure 6.7: The excitation population distribution of ^{30}Si from the $^{27}\mathrm{A}\ell(\alpha,p)$ reaction at $E_\alpha = 10$ MeV. The experimentally deduced distribution is shown by the histogram, with the error bars reflecting experimental uncertainties. The broken lines show the predicted excitation of the ^{30}Si from the statistical model, using the spin independent and spin-coupled calculations. The latter calculations were limited to a maximum compound nuclear spin of $11/2\hbar$.

energies of 2 MeV or greater. This nucleus contained the smallest number of undetermined level populations of those studied, and provided our most complete determination of the population distribution. Above an excitation of 5 MeV, the population in each bin was determined by at least 5 levels. The population of the 4 to 5 MeV bin was determined by only 2 levels. Levels with an undetermined population would provide only a minor population contribution, increasing no bin by more than 20% for an average estimated population.

In addition to the experimentally deduced population distribution, a set of statistical model calculations of the population distribution are shown in each figure. The various statistical model calculations of the population distribution were summed into 1 MeV wide bins, and multiplied by the isotopic abundance of the particular isotope in each element. These are the same theoretical population distributions which were used in the calculation of the γ-ray spectra presented in figures 6.1 through 6.3. The various theoretical calculations are labelled in the same manner.

Each population distribution calculation, except for those using a modified level density, follows a smooth curve with excitation energy. In the γ-ray spectra shown in the previous section, this smooth behaviour was modified by the different cascade decay modes attributed to each excitation. Each theoretical calculation shows a somewhat better gross agreement with measurements than was observed in the γ-ray spectra calculations. Most calculations are well within a factor of two of the experimental measurements for these high energy excitations. In most cases, the parameterized, spin independent calculation predicts the largest populations over the energy range of this investigation, with a 30 to 40% reduction in population and a somewhat better agreement with experiment obtained by using cross sections from our global potential DWBA calculations. A further reduction in the theoretical population, although only on the order of 15%, was obtained from properly spin-coupled calculations using these cross sections. The modified level density calculation which employed the same cross sections was able to reproduce some of the measured structure seen in these nuclei, and generally achieved the best agreement with experimental results.

The results using the phenomenological potential DWBA calculations, labelled "phenomenological", are somewhat disappointing. It was hoped that in this mass regime, experimentally determined phenomenological potentials would provide an improved agreement with measurements over calculations using global optical potentials. The importance of non-systematic nuclear structure effects in light nuclei cause the optical potential parameters [Be69a, Va87] to exhibit a larger variation than those of heavier nuclei, and so makes these nuclei more difficult to parameterize by a global potential. The phenomenological potentials were used in an attempt to avoid these variations. However, for the nuclei studied here, the phenomenological potential calculations provided no improvement over the global potential calculations, and in some cases were in considerably poorer agreement. In part this disagreement may have arisen from the need to extrapolate some of the required optical potential parameters to unstable nuclei and different particle energies using the general trends established by the global potential, as well from inconsistencies between the optical parameters of different research groups.

The theoretical population distributions all show the same over-estimate within 2 MeV of the maximum possible excitation of the residual nucleus, corresponding to similar features observed in the theoretical γ-ray spectra in figures 6.1 through 6.3. This over-estimate of the high energy population is likely due to the compound-elastic component of the neutron and proton absorption cross sections from which the compound nucleus decay branches were calculated. The compound-elastic component of the cross section can be ignored at incident energy where a large number of decay channels are available [Ho71], but at low incident energies where only a few exit channels exist, this channel can account for a large fraction of the reaction cross section. In calculating the inverse reaction, these low incident energies correspond to the emission of low energy particles and consequently high energy excitations of the residual nucleus. This could result in the over-estimate of the population observed in these calculations.

At low excitation energies, not shown in these figures, the statistical model calculations fall considerably below the measured excitation population. In part this under-estimate was corrected by the use of the modified level density in the calculation, which moved some strength to these lower energy regions. In most cases these low excitation energy populations were dominated by one or two levels, and as such were sensitive to non-statistical effects. As a result of this, we believe that these levels are not accurately described by the theoretical calculations presented here, and we do not consider them further.

From this behaviour and that of the γ-ray spectra, we conclude that a simple calculation using the parameterized cross sections of Chatterjee *et al* can predict the gross excitation population distribution of the residual nucleus to within a factor of two in this mass region. A 50% improvement in the calculation can be obtained using cross sections derived from DWBA cross sections. Only a slight improvement is obtained by the proper treatment of spin-coupling, and no improvement in agreement with measured populations is obtained from using phenomenological potentials. A much better improvement is obtained from calculations using a level density which more accurately reflects the low energy level structure of the residual nucleus. Such a treatment is most similar to Hauser-Feshbach calculations which have been used by a number of researchers to determine reaction rates in heavier nuclei than considered here. From comparisons of our calculations to such calculations by Woosley *et al* (see figure 4.7), we find the same level agreement from both types of calculations, and so believe that little additional improvement in agreement would be gained from a full Hauser-Feshbach calculation. Any improvement from such a calculation would arise from a proper handling of level parities, and would be expected have a larger effect on the low energy populations, which tend to exhibit a parity bias, than at high energies. More significant improvements may be possible through a careful treatment of the compound-elastic component of the cross section. Such a calculation would be expected to significantly improve the agreement within 2 MeV of the maximum excitation energy.

6.3.2 Mean Excitation

Our application of a statistical model of nuclear reactions relies on the existence of a continuum of states in the compound nuclear system at excitation energies corresponding to our incident particle energies. This overlap of nuclear states ensures that the decay of the compound nucleus does not depend on any detailed structure, but rather on a large mixture of configurations whose decay can then be treated in a statistical manner. At excitation energies where a large overlap of states is not observed, structure dependent features can be expected in the measured behaviour, and differences in the behaviour predicted by statistical model calculations may appear. In this section, we search for such features by considering the α-particle energy dependence of the mean excitation of the residual nucleus.

The existence of a continuum of states can be quantified by a figure of merit obtained from the product of the level density and the average level width. This dimensionless number can be thought of as the average number of quantum states contributing to a particular excitation of the compound nucleus. A value greater than 10 is usually sufficient for most statistical calculations [Ma70, Ho71] of the type considered here, and a value of close to unity indicates that the conditions necessary for this type of statistical treatment are marginal and that observed nuclear structure features may not be reproduced by such a theoretical calculation.

The reactions considered in this study span a range of validity for the statistical nuclear reaction model. For zero energy α-particles on fluorine, sodium, magnesium and aluminum nuclei, excitation energies around 10 MeV are reached, with level densities for a particular spin and parity of around 10 MeV^{-1}. The level widths in this regime are only on the order of 10 keV [En90], giving a figure of merit around 0.1, and indicating that the requisite continuum of levels is not achieved in low energy α-particle reactions. At the lowest α-particle energy measured in this study, the compound nuclei for these elements reach an excitation of close to 15 MeV, with single spin and parity level densities between 50 and 200 MeV^{-1}. Level widths at this excitation are on the order of 10 to 100 keV [Ho71], indicating that between 0.5 and 20 quantum configurations participate in the excitation of an individual level in the compound nucleus at this energy, and suggesting that calculations for these low energy α-particle reactions may encounter deviations due to the breakdown of the statistical model. At $E_\alpha = 8.8$ MeV, an energy corresponding to the maximum α-particle energy of the natural radioactive decay chains, a compound nuclear excitation on the order of 17 MeV is achieved for these nuclei, with level widths generally on the order of 100 keV. At these energies, a level density of 400 MeV^{-1} is typical and the average number of configurations participating in the a single level excitation of the compound nucleus approaches 10 to 50 for particular spin and parity quantum numbers. Lighter nuclei such as beryllium and boron are usually not treated in a statistical manner. At excitations in the compound nuclei of ^{13}C, ^{14}N and ^{15}N close to 17 MeV, corresponding to the reaction of $\sim$8 MeV α-particles, a discrete level structure is observed, with same spin and parity level widths smaller than level separations [Aj81]. This suggests a figure of merit much less than 1, and precludes a statistical model treatment of reactions for these nuclei.

Even for the heavier nuclei in this study, some non-statistical nuclear structure effects are anticipated due to the single-particle nature of nuclei close to the closed shell of ^{16}O. Such structure may change the smooth dependence of the optical potential on atomic mass [Va87, Be69a], and may lead to larger uncertainties in the calculated cross sections.

From this discussion, we see that our calculations cover a range of validity for statistical model calculations, and so we may expect some change in the behaviour of the three nuclei considered in detail. This change would be expected to occur at low α-particle energies where relatively few configurations participate in the excitation of the compound nucleus. Such a change in behaviour was investigated through the dependence of the mean excitation of the residual nucleus of α-particle energy.

A mean excitation energy of the ^{28}Si, ^{29}Si and ^{30}Si residual nuclei was calculated from both our theoretical and experimental results. The experimentally determined mean excitation curves, shown in figures 6.8 through 6.10, were calculated using the same γ-ray cascade corrected data as the excitation population distributions presented in the previous section. The mean excitation energy was calculated from a population-weighted sum of the level energies. The theoretical mean excitation was calculated by treating the population of the individual bins as occurring at the central value of the bin. In each figure the different theoretical calculations are shown using the same line types as in the population distributions of figures 6.5 through 6.7.

In the calculation of the mean from experimental data, some additional adjustments were required. Due to different run time conditions, the populations of levels at one α-particle energy were occasionally not determined at others. Since the inclusion of any of these missing levels at different α-particle energies could introduce distortions into these calculations, we removed the population of levels which were found to be missing due to spectrum interference. As a result these level exclusions, our experimental mean should not be considered a true mean, but rather a sampling of the excitation which reflects the behaviour of the true mean. In addition to this, we have excluded the populations of some of the lowest energy levels. As mentioned previously, these populations typically fall into bins containing very few levels. This low level density makes an interpretation of their behaviour in terms of our theoretical calculations difficult, as an "average" behaviour is not sampled. These levels, when included in a calculation, tended to dominate the mean and masked the behaviour of the high energy excitation we are most interested in. The exclusion of these levels is indicated by a low energy cut-off, discussed below. The effect of levels with unknown populations is also discussed, as the population of some of these levels may be responsible for some of the observed behaviour. Because of these adjustments to the experimental calculations, our comparison of theory to experiment focuses more on the slope rather than the absolute magnitude of the calculated mean.

The calculation of the mean excitation for ^{28}Si, shown in figure 6.8, utilized the measured excitations of levels above 5 MeV. The same level energy cut was used for the evaluation of the theoretical mean excitations. By selecting this energy cut, we

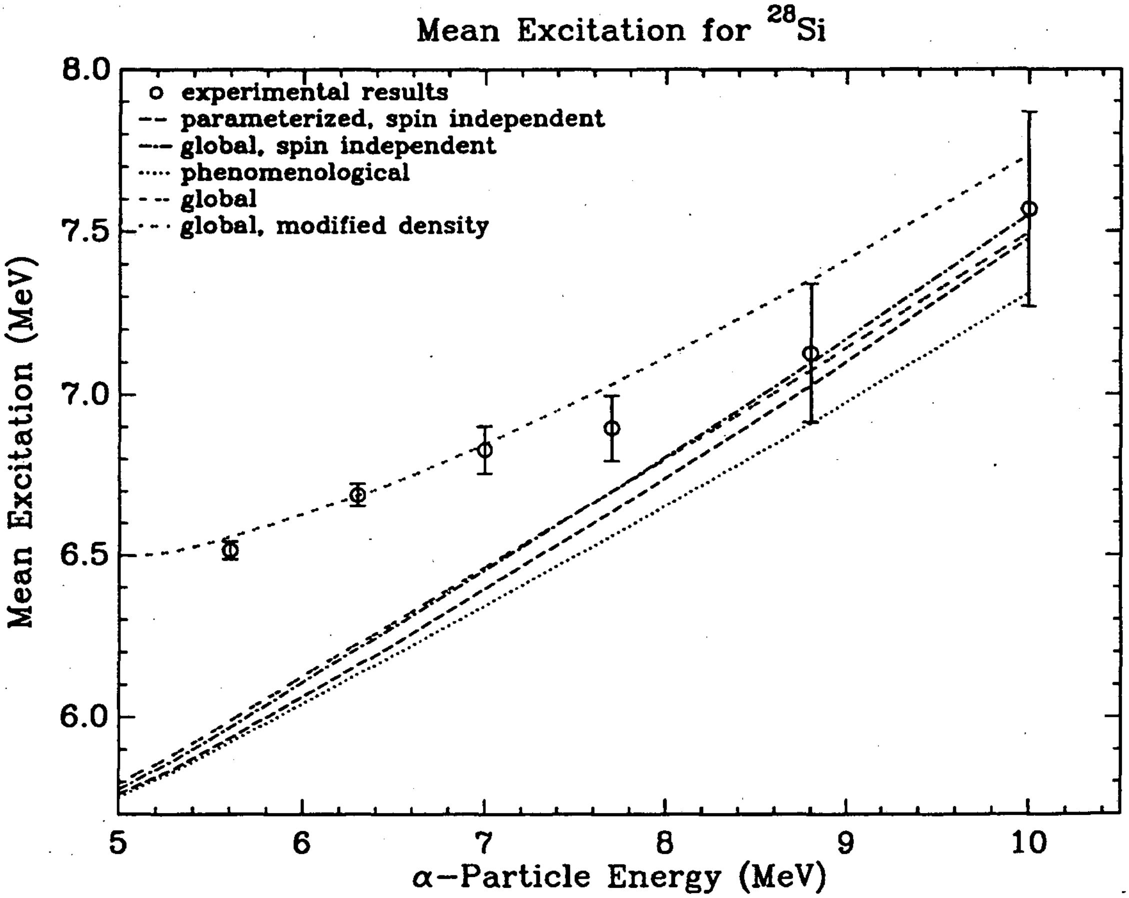

Figure 6.8: Mean excitation of ^{28}Si from the ^{25}Mg(α, n) reaction. The mean excitation energy has been calculated from observed and calculated excitations attributed to levels above an energy of 5 MeV.

have accentuated the effect of the discrete level structure by including a bin in which no excitations are possible. The resulting experimental points show a monotonically increasing excitation with α-particle energy. The calculation using the modified density shows a significantly higher mean energy due to the absence of an excitation in the 5 to 6 MeV bin, and is in somewhat better agreement with experiment than the other calculations, although all calculations reflect roughly the same energy dependence at high energies. Levels with unknown populations would only significantly affect the $E_\alpha = 10$ and 8.8 MeV mean excitations, increasing the mean excitation energy by no more than 150 keV and 50 keV, respectively, based on an estimate assuming an average population of each level. Such an effect would not significantly change figure 6.8.

The behaviour of the high energy mean excitations is fairly well reproduced by the theoretical calculations. The poorer agreement at lower α-particle energies for theoretical calculations using a purely statistical level density illustrates the importance of using realistic level densities in these calculations. Between $E_\alpha = 7$ and 7.7 MeV, there is a suggestion of a change in the behaviour of the mean excitation energy corresponding to a slight increase in the mean energy by roughly 100 keV. This behaviour appears to be more likely caused by an uneven distribution of levels within the lowest energy bin than by a deviation from statistical nuclear model behaviour. Only three level populations were determined between 5 and 6 MeV, with two strongly populated levels near 6.9 MeV, and one near 6.3 MeV. At low α-particle energies, where this bin accounts for most of the observed excitation, this distribution of levels could easily

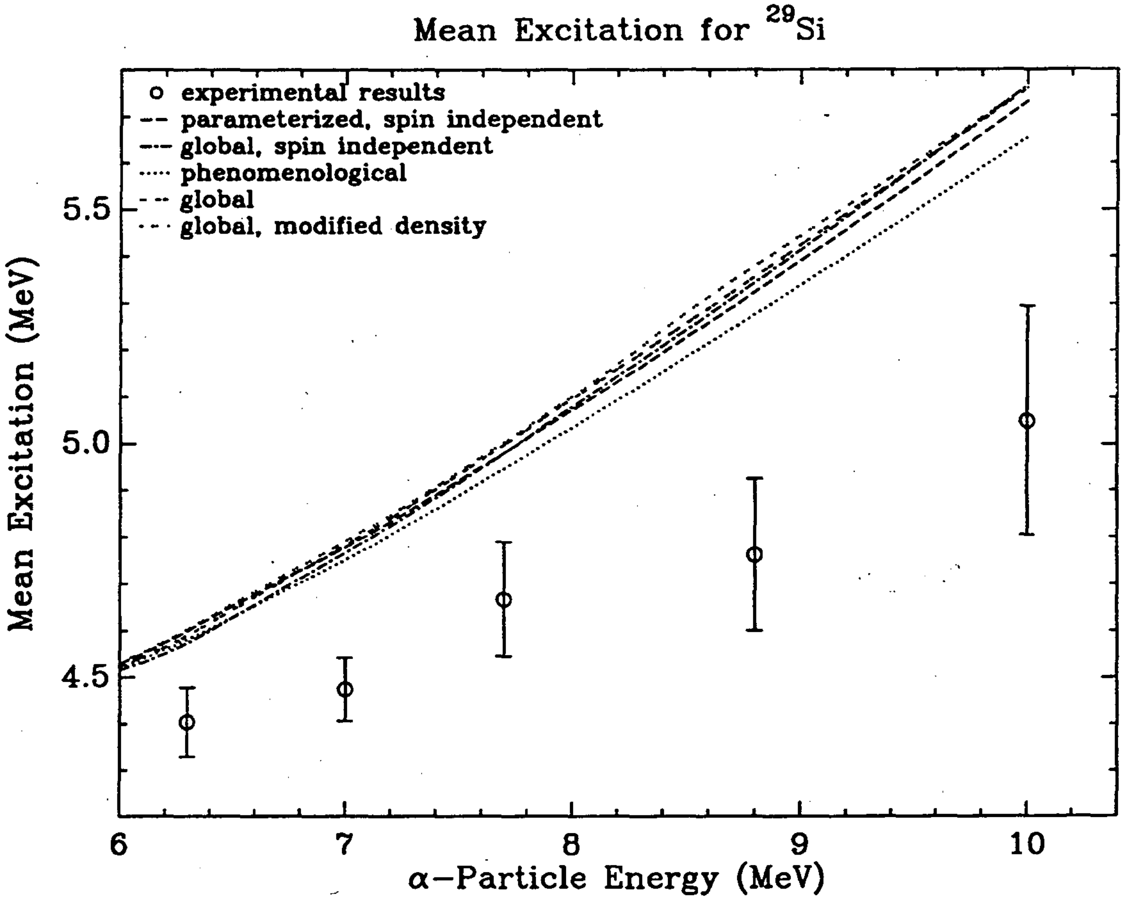

Figure 6.9: Mean excitation of ^{29}Si from the ^{26}Mg(α, n) reaction. The mean excitation energy has been calculated from experimentally and theoretically calculated excitations above 4 MeV.

account for the observed behaviour.

The mean excitation of the ^{29}Si nucleus is shown in figure 6.9. In this calculation of the mean, an energy cut of 4 MeV was used in order to avoid regions dominated by a few excitations. A mean excitation for $E_\alpha = 5.6$ MeV was not calculated because only one level population determined this point. All other experimental calculations utilized at least 5 level populations to determine the mean.

The experimental mean excitation exhibits less of a dependence on E_α than theoretical calculations. This behaviour could be caused by the population of unobserved levels. In the $E_\alpha = 10$ MeV measurement, the ^{29}Si nucleus contains 14 levels between 6 and 8 MeV whose populations have not been determined. If all these levels are assigned an average excitation, the mean excitation at 10 MeV is increased by 300 keV. Similarly, some population of the levels close to the highest determined excitation in the 8.8 MeV run would significantly increase the mean excitation energy. These considerations indicate that the difference between the theoretical and experimental energy dependence cannot be attributed with any certainty to a breakdown of our statistical model, and suggest that a comprehensive excitation measurement for this nucleus may be consistent with theory. In addition, there is a suggestion of a small change in the energy behaviour near 7.7 MeV, but such a change is well within uncertainty, and may be attributed to statistical fluctuations.

The mean excitation of the ^{30}Si nucleus, shown in figure 6.10, used an energy cut of 5 MeV. This excluded the 4 to 5 MeV bin which contained only the two levels at 4831 and 4809 keV. These levels were found to significantly distort the mean excitation curve compared to theoretical curves with a 4 MeV cut due their large population and high energy within the bin. Each theoretical calculation resulted in roughly the same slope and behaviour, with the shallowest slope produced by the spin-coupled calculations. For the experimental mean, a level measured at $E_\alpha = 10$ MeV was excluded from the calculation. This level at 6505 keV decayed through a cascade of low energy γ-rays below the lower threshold settings in the 5.6 through 8.8 MeV runs. The population of the 5231 keV level which is known only below $E_\alpha = 7.7$ MeV was also excluded from the calculation of the mean excitation, to allow an appropriate

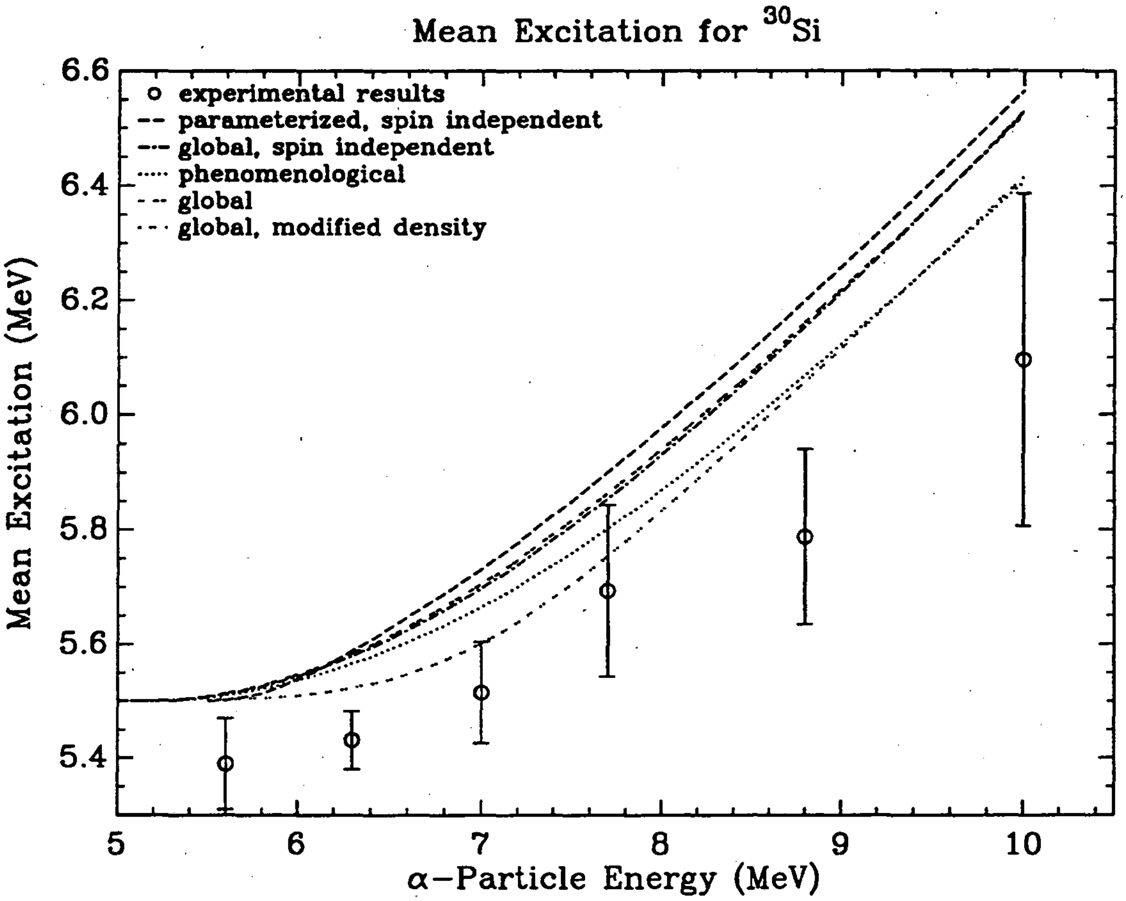

Figure 6.10: Mean excitation of ^{30}Si from the ^{27}A$\ell(\alpha, p)$ reaction. The mean excitation energy has been calculated from observed and calculated excitations attributed to levels above an energy of 5 MeV.

comparison of run results.

A total of 8 levels, including the two discussed above, were missing from the mean excitation energy determination at 10 MeV. Each of these levels decayed primarily to the second excited state in ^{30}Si, and as such had only a small chance of being observed. At 7.7 and 8.8 MeV there were only 6 undetermined levels and below this energy only 3 levels had unknown excitations. In all cases the measured excitations comprised the majority of all known levels, and so provided a reasonable sample of the excitation of the ^{30}Si nucleus. Estimating the effect of these missing levels by the same method as before suggests that the excitation of these levels would increase the measured results by less than 40 keV at all α-particle energies.

The theoretical calculations for ^{30}Si all predicted a mean excitation α-particle energy dependence which was observed by experiment. The experimental data show some deviation again near $E_\alpha = 7.7$ MeV, but such behaviour is well within uncertainty, and so could be a result of statistical variation.

Thus this comparison has not found any conclusive evidence that our measurements experienced a departure from the behaviour predicted by the statistical model of nuclear reactions. All statistical model calculations produced similar mean excitation energy curves for each nucleus which was largely followed by our experimental measurements. Thus, for the purposes of our investigations, we conclude that these optical model calculations provide a sufficient description of the high-energy excitation over the range of α-particle energies of interest. At low α-particle energies, we encountered difficulties in obtaining sufficient statistics to accurately parameterize the excitation of the residual nucleus. In this type of comparison, a Hauser-Feshbach calculation of the type performed by Woosley *et al* [Wo76] may be able to provide additional information on the applicability of these calculations to the low-energy regime. Such calculations would permit a one to one level correspondence and avoid the sensitivity to averaging which restricted our investigation to high-energy excitations of the residual nucleus.

Chapter 7

Conclusions

In this study we have measured the α-particle induced γ-ray yields above $E_\gamma = 2$ MeV for a number of light elements, and have used these yields to predict the high energy γ-ray spectrum from direct production (excluding (n,γ) reactions) for a number of materials in the SNO detector. These measurements and calculations constitute the first experimental determination of the direct production high-energy γ-ray background resulting from natural radioactivity in materials. We have found that previous estimates of this high-energy γ-ray background by Pomansky and Glotov [Po86, Gl78] are several orders of magnitude larger than our present measurements, and that our measurements significantly reduce the importance of direct production γ-rays in the intrinsic background spectrum for normal materials.

Further experimental investigations should be aimed at improving the characterization of the excitation of residual nuclei to permit an extension of our comparison of experimental results to theoretical predictions. Such studies would benefit from conditions which would improve on peak transition identification. This could be accomplished in a number of ways. One of the simplest approaches would be to reduce the low energy threshold on the data acquisition system to enable a complete measurement of the decay schemes from individual levels. These decay schemes would increase the number of known level populations and hence permit improved characterizations of the residual nucleus excitation. However, reducing this threshold alone would only be of limited value as background effects from neutron scattering in the detector materials become more severe, and γ-rays accompanying the β-decay of some residual nuclei provide an addition source of background below 2 MeV. In addition, many of the weak, low energy transitions from the cascade decay of high energy excited states would be overwhelmed by the large background continuum in this region. The background may be reduced by incorporating neutron shielding between the target and detector system and by moving the low energy γ-ray filters (1 cm of lead) closer to the target in order to reduce the number of scattered γ-rays entering the detectors.

More extensive refinements of our experimental techniques may be required to obtain a significant improvement in results. The use of single isotope targets would simplify some of the spectra by reducing the number of reactions studied. Similarly, when investigating a reaction using a compound target, less complicated spectra could be obtained by studying only one target nucleus and selecting inert, high atomic number elements for the other components in the compound. Such a study would require greater care in extracting element yields from the compound target as stopping powers exhibit greater differences in α-particle energy dependence as the difference between atomic numbers increases.

Finally, some improvement in spectrum peak separations may be obtained by employing thin targets. Spectra resulting from thin targets would contain some narrower peaks due to a reduction in the energy spread of α-particles reacting with target nuclei. However, such an experiment would require additional measures to monitor target thickness and surface contamination, and as well would significantly increase the amount of data required to obtain thick-target yields. The results from such extensions of our investigations would not be expected to significantly affect our direct production high-energy γ-ray background determinations for the SNO detector.

We have also studied the predictive value of the statistical model of nuclear reactions, and have investigated a number of the approximations and data sources available for these calculations. We have determined that detailed statistical model calculations reproduce the excitation population distribution of the residual nucleus to within a factor of two of the experimental distribution over most of the excitation energy range for reactions on moderately heavy nuclei (Mg and above). Within 2 MeV of the highest excitation, these statistical calculations predict an intensity larger than experimentally observed, possibly due to the increasing importance of the compound-elastic component of the absorption cross section used in determining the decay probabilities of the compound nuclear system. Extensions of this theoretical work should more fully investigate the role of the compound-elastic channel. At low excitation energies, theoretical calculations predict population distributions significantly smaller than experimentally observed. Further studies using Hauser-Feshbach calculations may indicate whether this effect is attributable to an increased sensitivity of reaction cross sections to the low energy nuclear structure of the residual nucleus.

In principle, nuclei lighter than Mg could also be modelled by statistical model calculations. The primary limiting factor for these calculations is not a breakdown of conditions necessary for a statistical treatment of the reaction, but rather a sensitivity of optical potential parameters to shell effects. Our calculations using published phenomenological potentials derived from scattering experiments suggest that no improvement over calculations using global potentials is gained, and hence the accuracy of such reaction calculations for nuclei near the ^{16}O closed shell is questionable. The application of these calculations to beryllium and boron, the lightest nuclei in this study, can be ruled out due to the absence of a continuum of levels in the compound nuclear system at excitation energies corresponding to α-particle energies in our range of interest.

Among the different levels of approximation in the statistical calculations, we have seen that the results in closest agreement with experimental observations were obtained using cross sections derived from distorted wave, Born approximation calculations with a global optical potential. The proper treatment of angular momentum coupling was shown to improve slightly the agreement with experiment compared to calculations which neglected spin coupling, while modifying the level density to more closely match the observed level spacing reproduced some of the features of the population distribution. Overall, these calculations were able to produce γ-ray spectra from moderately heavy nuclei in agreement with experimental measurements at a level similar to that obtained for the excitation population distributions. Some additional uncertainties were introduced from the association of the cascade decay scheme with the population distribution of each residual nucleus. The improvement observed from using a modified level density indicates the importance of accounting for the discrete level structure of these nuclei in reaction calculations. The use of full Hauser-Feshbach calculations in this energy regime can best accomplish this improvement. Such calculations would be expected to obtain a similar level of agreement with experiment, with some improvement anticipated at low excitation energies. However, such an improvement would primarily affect the low-energy γ-ray region of a background spectrum, which is typically dominated components other than the direct production.

The α-particle energy dependence of the mean excitation of the residual nucleus was generally reproduced in the three systems studied. Some differences between observed and predicted behaviour were attributed to difficulties in characterizing the excitation of the residual nuclei rather than to a breakdown of the statistical model. Further explorations of the validity of the statistical model for these nuclei would benefit from a full Hauser-Feshbach calculation using a discrete level structure. Such calculations would allow for a more direct determination of the excitation dependence on α-particle energy, and permit an extension of the investigation to lower energy levels.

Bibliography

[Aj80] F. Ajzenberg-Selove and C. L. Busch, *"Energy levels of light nuclei* $A = 11$–12*"*, Nuclear Physics **A336** (1980) 1.

[Aj81] F. Ajzenberg-Selove, *"Energy levels of light nuclei* $A = 13$–15*"*, Nuclear Physics **A360** (1981) 1.

[Aj87] F. Ajzenberg-Selove, *"Energy levels of light nuclei* $A = 18$–20*"*, Nuclear Physics **A475** (1987) 1.

[Al78] T. K. Alexander and J. S. Forster, *"Lifetime measurements of excited nuclear levels by Doppler-shift methods"*, Advances in Nuclear Physics **10** (1978) 197.

[Al90] J. M. Alexander and M. T. Magda, *"Inverse reactions and the statistical evaporation model: Ingoing-wave boundary-conditions and optical models"*, Physical Review C **42** (1990) 1092.

[Au62] E. H. Auerbach and F. G. J. Perey, *"Optical model neutron transmission coefficients,* 0.1 *to* 5.0 *MeV"*, Brookhaven National Laboratory Report BNL-765 (T-286) (1962).

[Ba79] J. K. Bair and J. Gomez del Campo, *"Neutron yields from alpha-particle bombardment"*, Nuclear Science and Engineering <u>71</u> (1979) 18.

[Ba89] J. N. Bahcall, **Neutrino Astrophysics**, Cambridge University Press: New York (1989).

[Be69a] F. D. Becchetti and G. W. Greenlees, *"Nucleon-nucleus optical-model parameters* $A > 40$*,* $E < 50$ *MeV"*, Physical Review <u>**182**</u> (1969) 1190.

[Be69b] P. R. Bevington, **Data Reduction and Error Analysis for the Physical Sciences**, McGraw Hill: New York (1969).

[Be92] A. N. Behkami and Z. Kargar, *"Nuclear level densities and spin cut-off factors deduced from microscopic theory for nuclei from* ^{20}F *to* ^{244}Am*"*, Journal of Physics G <u>18</u> (1992) 1023.

[Bl52] J. M. Blatt and V. F. Weisskoff, **Theoretical Nuclear Physics**, John Wiley and Sons: New York (1952).

[Ca91] C. Cai, Q. Shen and Y. Zhuo, *"Comparisons of global phenomenological and microscopic optical potentials for nuclear data predictions"* Nuclear Science and Engineering <u>**109**</u> (1991) 142.

[Cs83] J. Cseh, Á. Z. Kiss, E. Kolatay, B. Nyakó, and É. Pintye, *"Levels of* ^{14}N *near 13.7 MeV excitation from the analysis of doppler-broadened* γ*-line shapes in the* $^{10}B(\alpha, p\gamma)^{13}C$ *reaction"*, Nuclear Physics <u>**A410**</u> (1983) 147.

[Ch65] C. Chasman, K. W. Jones and R. A. Ristinen, *"Fast neutron bombardment of a lithium-drifted germanium gamma-ray detector"*, Nuclear Instruments and Methods **37** (1965) 1.

[Ch81] A. Chatterjee, K. H. N. Murthy, and S. K. Gupta, *"Optical reaction cross-sections for light projectiles"*, Pramāna **16** (1981) 391.

[Da76] R. A. Dayras, Z. E. Switkowski and T. A. Tombrello, *"^{14}C production by the reaction $^{11}B(\alpha,p)^{14}C$"*, Nuclear Phyusics **A261** (1976) 365.

[De77] W. del Bianco, S. Kundu, and J. Kim, *"The $^{11}B(\alpha,\gamma_0)^{15}N$ reaction in the giant dipole resonance region"*, Canadian Journal of Physics **55** (1977) 302.

[De78] A. Degré, M. Schaeffer, G. Bonneaud and I. Linck, *"Experimental study of the radiative capture $^{11}B(\alpha,\gamma_0)^{15}N$ for $15.5 \leq E_x \leq 19.5$ MeV"*, Nuclear Physics **A306** (1978) 77.

[De88] K. Debertin and R. G. Helmer, **Gamma- and X-Ray Spectrometry with Semiconductor Detectors**, Elsevier Science Publishers: Amsterdam (1988).

[Dy85] P. Dyer, D. Bodansky, D. D. Leach, E. B. Norman, and A. G. Seamster, *"Cross sections relevant to gamma-ray astronomy: Alpha-particle-induced reactions on ^{12}C, ^{14}N, and ^{16}O nuclei"*, Physical Review **32** (1985) 1873.

[En78] P. M. Endt *"Energy Levels of $A = 21$–44 Nuclei (VI)"*, Nuclear Physics **A310** (1978) 1.

[En90] P. M. Endt *"Energy Levels of $A = 21$–44 Nuclei (VII)"*, Nuclear Physics **A521** (1990) 1.

[Ew87] G. T. Ewan, H. C. Evans, H. W. Lee, J. R. Leslie, H.-B. Mack, W. McLatchie, B. C. Robertson, P. Skensved, R. C. Allen, G. Bühler, H. H. Chen, P. J. Doe, D. Sinclair, N. W. Tanner, J. D. Anglin, M. Bercovitch, W. F. Davidson, C. K. Hargrove, H. Mes, R. S. Storey, E. D. Earle, G. M. Milton, P. Jagam, J. J. Simpson, A. B. BcDonald, E. D. Hallman, A. L. Carter, D. Kessler, **"Sudbury Neutrino Observatory Proposal"**, SNO Collaboration Report SNO-87-12 (1987).

[Ew92] G. T. Ewan, W. F. Davidson, and C. G. Hargrove, *"The Sudbury Neutrino Observatory – An introduction"*, Physics in Canada **48**, (March 1992) 112.

[Ga69] A. Gallman, F. Hibou and P. Fintz, *"Résonances dans la réaction $^{10}B+\alpha$ par l'étude des rayonnements γ détectés avec un semi-conducteur Ge(Li)"*, Nuclear Physics **A123** (1969) 27.

[Ge75] K. W. Geiger and L. Van der Zwan, *"Radioactive neutron source spectra from $^{9}Be(\alpha,n)$ cross section data"*, Nuclear Instruments and Methods **131** (1975) 315.

[Ge76] K. W. Geiger and L. Van der Zwan, *"An evaluation of the $^{9}Be(\alpha,n)$ cross section"*, National Research Council of Canada Report 15303, PXNR #2404 (1976).

[Gi65a] J. H. Gibbons and R. L. Macklin, *"Total cross section for $^9Be(\alpha, n)$"*, Physical Review **137** (1965) B1508.

[Gi65b] A. Gilbert, F. S. Chen and A. G. W. Cameron, *"Level densities in lighter nuclei"*, Canadian Journal of Physics **43** (1965) 1248.

[Gi65c] A. Gilbert and A. G. W. Cameron, *"A composite nuclear-level density formula with shell corrections"*, Canadian Journal of Physics **43** (1965) 1446.

[Gl71] V. I. Glotov, *"γ-Radiation from the earth and neutrino experiments"*, translated from Atomnaya Énergiya **30** (1971) 384.

[Gl78] V. I. Glotov, *"Radiation background of the external environment and methods of reduction for solar neutrino experiments"* Ph.D. Dissertation (in Russian), Soviet Academy of Sciences, Institute of Nuclear Research, USSR, (1978) Unpublished.

[Gr83] P. J. Grant, E. B. Norman, G. L. Woodruff, D. L. Johnson, F. E. Chupp, and K. T. Lesko, *"Neutron yields from alpha particle-induced reactions of importance to reactors"*, unpublished report (1985).

[Ha69] W. D. Hay and S. M. Perez, *"Two subroutines for the calculation of distorted waves"*, Nuclear Physics Theoretical Group Report # 42, Atlas Program Library Report # 15, Oxford University, (1969) Unpublished.

[Ha94] D. Hallman, *"Summary of measurements of radioactive components of norite and shotcrete"*, private communication (1994).

[He88] R. Heaton, *"Neutron Shielding Calculations for the* SNO *Detector"*, Master's Thesis, Queen's University (1988) Unpublished.

[He89] R. Heaton, H. Lee, P. Skensved and B. C. Robertson, *"Neutron production from thick-target (α, n) reactions"*, Nuclear Instruments and Methods in Physics Research <u>**A276**</u> (1989) 529.

[He90] R. Heaton, H. Lee, P. Skensved and B. C. Robertson, *"Alpha-induced neutron activity in materials"*, Nuclear Geophysics <u>4</u> (1990) 499.

[Ho63] P. E. Hodgson, **The Optical Model of Elastic Scattering**, Clarendon Press: Oxford (1963).

[Ho71] P. E. Hodgson, **Nuclear Reactions and Nuclear Structure**, Clarendon Press: Oxford (1971).

[Ho78] W.-S. Hou, C.-S. Lin, M. Wen, H.-H. Hsu, and J.-C. Chou, *"Cross sections for the $^{11}B(\alpha,p)^{14}C$ reaction in the alpha-particle energy range from* 4.4 *to* 6.7 *MeV"*, Nuclear Science and Engineering <u>66</u> (1978) 188.

[Hu61] J. R. Huizenga and G. J. Igo, *"Theoretical reaction cross sections for alpha particles with an optical model"*, Argonne National Laboratory Report ANL-6373 (1961) Unpublished.

[Kj62a] J. Kjellman, T. Dazai, J. H. Neiler, *"Angular correlation study of the $^{9}Be(\alpha,n)^{12*}C\ (\gamma_{4.43})^{12}C$ Reaction"*, Nuclear Physics <u>30</u> (1962) 131.

[Kj62b] J. Kjellman and A. Nilsson, *"Neutron angular distributions from the $^9Be(\alpha,n)^{12}C$ reaction at* 12.7, 11.3 *and* 9.8 *MeV"*, Arkiv fŏr Fysik 22 (1962) 277.

[Kn76] G. F. Knoll, **Radiation Detection and Measurment**, John Wiley and Sons: New York (1979).

[Il92] A. S. Iljinov, M. V. Mebel, N. Bianchi, E. De Sanctis, C. Guaraldo, V. Lucherini, V. Muccifora, E. Polli, A. R. Reolon and P. Rossi, *"Phenomenological statistical analysis of level densities, decay widths and lifetimes of excited nuclei"*, Nuclear Physics **A543** (1992) 517.

[La83] R. Lappalainen, A. Anttila, and J. Räisänen, *"Absolute α-induced thick-target gamma-ray yields for elemental analysis of light elements"*, Nuclear Instruments and Methods **212** (1983) 441.

[Le78] C. M. Lederer and V. S. Shirley, **Tables of Isotopes, 7th ed.**, John Wiley and Sons: New York (1978).

[Ly86] L. Lyons, **Statistics for Nuclear and Particle Physicists**, Cambridge University Press: New York (1986).

[Lo81] M. A. Lone, R. A. Leavitt and D. A. Harrison, *"Prompt γ-rays from thermal-neutron capture"*, Atomic Data and Nuclear Data Tables 26 (1981) 511.

[Ma86] C. Mahaux, H. Ngô, G. R. Satchler, *"Causality and the threshold anomaly of the nucleus-nucleus potential"*, Nuclear Physics **A449** (1986) 354.

[Ma63] G. S. Mani., M. Melkanoff, I. Iore, *"Proton penetrabilities using an optical model potential"*, CEA-2379 Report (1963) Unpublished.

[Ma70] P. Marmier and E. Sheldon, **Physics of Nuclei and Particles, Vol. I and II**, Academic Press: New York (1970).

[Mc66] L. McFadden and G. R. Satchler, *"Optical-model analysis of the scattering of* 24.7 *MeV alpha particles"*, Nuclear Physics 84 (1966) 177.

[Mi70] G. Michaud and W. A. Fowler, *"Thermonuclear-reaction rates at high temperature"*, Physical Review C 2 (1970) 2041.

[Mo91] A. J. Morton, S. G. Tims, A. F. Scott, V. Y. Hansper, C. I. W. Tingwell and D. G. Sargood, *"The* $^{48}Ti(\alpha,n)^{51}Cr$ *and* $^{48}Ti(\alpha,p)^{51}V$ *cross sections"*, Nuclear Physics **A537** (1992) 167.

[No86] E. B. Norman, K. T. Lesko, T. E. Chupp, P. Schwalbach and M. A. Faccio, *"Gamma-ray production cross sections for* α*-particle induced reactions on* ^{19}F *and* ^{23}Na*"*, Radiation Effects 94 (1986) 307.

[Pe63] F. G. Perey, *"Optical-model analysis of proton elastic scattering in the range of* 9 *to* 22 *MeV"*, Physical Review **131**, (1963) 745.

[Pe76] C. M. Perey and F. G. Perey, *"Compilation of phenomenological optical-model parameters 1954–1975"*, Atomic Data and Nuclear Data Tables 17 (1976) 1.

[Po86] A. A. Pomansky, *"Underground low background laboratories of the Baksan Neutrino Observatory"*, Nuclear Instruments and Methods in Physics Research **B17** (1986) 406.

[Ra90] E. M. Rastopchin, M. I. Svirin, and G. N. Smirenkin, *"Tests of the basic phenomenological models of the nuclear level density"*, Soviet Journal Nuclear Physics **52** (1990) 799.

[Ro67] R. R. Roy and B. P. Nigam, **Nuclear Physics: Theory and Experiment**, John Wiley and Sons: New York (1967).

[Ro93] B. C. Robertson, SNO*: A multifunction spectrometer for solar neutrinos"*, in **Perspectives in Neutrinos, Atomic Physics and Gravitation**, J. Trân Thanh Vân, T. Damour, E. Hinds and J. Wilkerson (eds.), XIII Moriod Workshop: Editions Frontieres (1993) 119.

[Se63] J. B. Seaborn, G. E. Mitchell, N. R. Fletcher, and R. H. Davis, *"Gamma rays from the* $^9Be(\alpha, n_1)^{12}C$ *reaction"*, Physical Review **129** (1963) 2217.

[Se84] A. G. Seamster, E. B. Norman, D. D. Leach, P. Dyer, and D. Bodansky, *"Cross sections relevant to gamma-ray astronomy: Alpha-particle-induced reactions"*, Physical Review C **29**, (1984) 394.

[Sk91] P. Skensved and B. C. Robertson, *"Background estimates for the PMT region"*, SNO Collaboration Report SNO-STR-91-07 (1991).

[Sk94] P. Skensved and B. C. Robertson, *"Summary of backgrounds in* SNO*"*, SNO Collaboration Report SNO-STR-94-13 (1994).

[So73] H. W. Sobel, A. A. Hruschka, W. R. Kropp, J. Lathrop, R. Reines, M. F. Crouch, B. S. Meyer and J. P. F. Sellschop, *"High energy gamma rays from spontaneous fission of* ^{238}U*"*, Physical Review C 7 (1973) 1564.

[Ul64] I. Úlehla, L. Gomolčák, and Z. Pluhař, **Optical Model of the Atomic Nucleus**, Academic Press: New York (1964).

[Va70] L. Van der Zwan and K. W. Geiger, *"The* $^{9}Be(\alpha,n)^{12}C$ *cross section between* 1.5 *and* 7.8 *MeV"*, Nuclear Physics **A152** (1970) 481.

[Va73] L. Van der Zwan and K. W. Geiger, *"The* $^{10}B(\alpha,n)^{13}N$, $^{13}N^{*}$ *cross section for* α*-energies from* 1.0 *to* 5 *MeV"*, Nuclear Physics **A216** (1973) 189.

[Va87] R. L. Varner, T. B. Clegg, T. L. McAbee, and W. J. Thompson, *"Global parameterization of the nucleon-nucleus scattering potential"*, Physics Letters B **185** (1987) 6.

[Ve68] V. V. Verbinski, F. G. Perey, J. K. Dickens, and W. R. Burrus, *"Neutrons from the* $^{9}Be(\alpha,n)$ *Reaction for* E_α *between* 6 *and* 10 *MeV"*, Physical Review **170** (1968) 916.

[Vo86] T. Von Egidy, A. N. Behkami and H. H. Schmidt, *"Nuclear level densities and level spacing distributions from* ^{20}F *to* ^{244}Am*"*, Nuclear Physics **A454** (1986) 109.

[Vo88] T. Von Egidy, H. H. Schmidt and A. N. Behkami, *"Nuclear level densities and level spacing distributions: Part II"*, Nuclear Physics **A481** (1988) 189.

[Wa88] A. H. Wapstra, G. Audi and R. Hoekstra, *"The 1986-1987 Atomic Mass Predictions"*, Atomic Data and Nuclear Data Tables **39** (1988) 281.

[Wa92] C. E. Waltham, E. D. Hallman, P. Doe, R. G. H. Robertson, W. Frati, R. Van Berg, K. T. Lesko, B. C. Robertson, J. J. Simpson, *"Research and development for the Sudbury Neutrino Observatory"*, Physics in Canada **48** (March 1992) 135.

[We82] D. West and A. C. Sherwood, *"Measurements of thick-target (α, n) yields from light elements"*, Annals of Nuclear Energy **9** (1982) 551.

[Wi75] S. J. Wilson, *"$^{10}B(\alpha, n_0)^{13}N$ and $^{10}B(\alpha, p_i)^{13}C$ for $2 < E_\alpha < 8$ MeV"*, Physical Review **11** (1975) 1071.

[Wo76] S. E. Woosley, W. A. Fowler, J. A. Holmes and B. Z. Zimmerman, *"Tables of thermonuclear reaction rate data for intermediate mass nuclei"*, Orange Aid Preprint OAP-422, California Institute of Technology (1975).

[Zi85] J. F. Ziegler, J. P. Biersack, U. Littmack, *"The Stopping and Range of Ions in Solids"* in **The Stopping and Ranges of Ions in Matter**, Pergamon Press: New York (1985).

Appendix A

Optical Cross Section Calculations

The cross sections for the formation of the compound nucleus system are obtained from a general reaction theory, known as scattering matrix, or S-matrix theory and the optical model of the nucleus which is used to calculate elements of the S-matrix.

A.1 The Scattering Matrix

In general, we are interested in the effects of an interaction well beyond the spatial range of the interacting potential. The effect of the interaction is seen as a change, or transformation of the asymptotic wave function describing a free particle travelling through space. This transformation of the wave function can be described by a matrix, known as the S-matrix. For an asymptotic stationary solution of the wave function of the form

$$\psi = \psi_{in} + \psi_{out} \tag{A.1}$$

the out-going wave ψ_{out} is described by the transformation of the incoming wave ψ_{in} by the scattering matrix operator, $\boldsymbol{S}$, according to

$$\psi_{out} = \boldsymbol{S}\psi_{in}. \tag{A.2}$$

The elements of the S-matrix, S_{fi}, given by

$$S_{fi} \equiv \langle f\,|\boldsymbol{S}|\,i\rangle = \int \psi^{*}_{out}\boldsymbol{S}\psi_{in}\,d\Omega \tag{A.3}$$

are the transition amplitudes from an initial state $|i\rangle$ to a particular final state $|f\rangle$ [Ma70]. These final states include different particle types in the out-going wave as well different internal states of the interaction potential source.

The elements of the S-matrix are complex quantities which must possess certain basic properties. Since the S-matrix describes all possible final states of the system for any particular initial state, conservation of probability dictates that the S-matrix is a unitary matrix, so that

$$\sum_{f} |S_{fi}|^2 = 1. \tag{A.4}$$

In the special case of an elastic scattering reaction, the transformation depends only on the diagonal elements of the S-matrix. The non-elastic reaction, or absorption, probability given by the off-diagonal matrix elements, can be be found in terms of the diagonal elements using the unitarity of the S-matrix,

$$P_{abs} = 1 - |S_{ii}|^2. \tag{A.5}$$

In the application of scattering matrix theory presented here, only the diagonal elements of the matrix are obtained from solutions of the optical potential and so in what follows, the index indicating the final state is dropped in the understanding that the entrance and exit channels are the same. The particular channel i for a given particle is identified by the orbital and total angular momentum quantum numbers l and j, and the diagonal S-matrix element is written $S(lj)$.

A.2 The Optical Model Cross Section

The diagonal elements of the S-matrix are readily obtained by solving the wave equation for the average potential experienced by a particle incident on a nucleus. This model, commonly known as the optical model, assumes that the short range nucleon-nucleon interaction from each nucleon in the nucleus contributes to a long range average nuclear potential in which the constituent nucleons move independently. The potential contains both real and imaginary components, and so may absorb as well as scatter incident particles. The derivation of the reaction cross section from the optical model which follows is largely derived from the reviews of Úlehla, Gomolčák and Pluhař [Ul64], Hodgson [Ho63] and Marmier and Sheldon [Ma70].

The Schrödinger wave equation is solved by separating the equation into the usual angular and radial components. The potential is assumed to be independent of angle, and so the angular solution can be expressed as a sum of spherical harmonics. The radial equation is solved by separating the solution into two regions: an interior region dominated by the nuclear potential, and an exterior region where the incident particle can be treated as a free particle moving in a Coulomb field. The solution is obtained by numerically integrating the radial wave function out from the interior region and smoothly joining it to the asymptotic form of the wave function derived below.

A.3 The Asymptotic Wave Function

The Schrödinger wave equation for an incident particle in the centre-of-mass frame is given by

$$\left[-\frac{\hbar^2}{2\mu}\nabla^2 + V(r)\right]\psi(r) = E\psi(r) \tag{A.6}$$

where μ is the reduced mass of the incident particle, $V(r)$ is the central potential of the target nucleus, and E is the kinetic energy of the system outside the range of the potential. The asymptotic solution to this equation in the region where V can be neglected must describe an incident plane wave plus a scattered spherical wave. In the absence of a Coulomb field, and for an incident particle traveling in the positive z direction, the asymptotic solution can be written in the form of

$$\psi(r) = \frac{1}{v^{1/2}}\left[e^{ikz} + \frac{e^{ikr}}{r}f(\theta)\right]\chi_s, \tag{A.7}$$

where k is defined as

$$k^2 = \frac{2\mu E}{\hbar^2} \tag{A.8}$$

χ_s designates the intrinsic spin of the incident particle, and the normalization by $v \equiv \dfrac{\hbar k}{m}$ serves to set the incident particle flux to unity. From the axial symmetry of the incident wave about the z-axis, the amplitude of the scattered wave, f, can depend only on the azimuthal angle θ measured from this axis. Using the z-axis defined by the incident particle velocity vector as the quantization axis, an angular expansion of the wave in terms of spherical harmonics contains no projection of the angular momentum along this axis. Thus, on separating the wave function into angular and radial functions and introducing the quantum numbers l, s and j ($\vec{j} = \vec{l} + \vec{s}$) for the orbital, intrinsic and total angular momentum, the wave function can be written as

$$\psi = \frac{1}{v^{1/2}} \sum \frac{u_{lj}(r)}{r} Y_{l,0}(\Omega)\chi_s, \tag{A.9}$$

where $Y_{l,0}$ is the spherical harmonic normalized to unity over the angular coördinates Ω with angular momentum l and zero spin projection along the quantization axis, and χ_s is the appropriate spinor for the particle. The function $u_{lj}(r)$ is described by the equation

$$-\frac{\hbar^2}{2\mu}\frac{d^2u_{lj}(r)}{dr^2} + [V_{lj}(r) - E]\, u_{lj}(r) = 0. \tag{A.10}$$

The potential $V_{lj}(r)$ consists of the general potential discussed in section 4.2.1 for particular values of $\vec{l}$, $\vec{s}$ and $\vec{j}$:

$$V_{lj} = V(r, l, s, j) + \frac{\hbar^2}{2\mu}\frac{l(l+1)}{r^2} \tag{A.11}$$

where $V(r, l, s, j)$ is given in its general form by equation (4.1).

The asymptotic form of the wave function can be expressed in terms of the same variables by expanding ψ in terms of partial waves using the spherical Bessel functions $j_l(kr)$. These functions are related to the ordinary Bessel functions $J_{l+1/2}(kr)$ according to the equation,

$$j_l(kr) = \left(\frac{\pi}{2kr}\right)^{1/2} J_{l+1/2}(kr) \tag{A.12}$$

and can be generated according to

$$j_l(kr) = (-kr)^l \left[\frac{1}{kr}\frac{d}{d(kr)}\right]^l \left(\frac{\sin(kr)}{kr}\right). \tag{A.13}$$

For $kr \gg l$, these functions have an asymptotic form of

$$j_l(kr) = \frac{\sin\left(kr - \frac{l\pi}{2}\right)}{kr} \tag{A.14}$$

$$= \frac{1}{2ikr}\left\{\exp\left[i\left(kr - \frac{l\pi}{2}\right)\right] - \exp\left[-i\left(kr - \frac{l\pi}{2}\right)\right]\right\}. \tag{A.15}$$

The incident plane wave is expressed in terms of these functions as

$$\frac{1}{v^{1/2}}e^{ikz} = \frac{1}{v^{1/2}}\sum_l [4\pi(2l+1)]^{1/2} i^l j_l(kr) Y_{l,0}(\Omega) \tag{A.16}$$

$$= \left(\frac{4\pi}{v}\right)^{1/2}\frac{1}{kr}\sum_{l=0}(2l+1)^{1/2}\frac{i^{l+1}}{2}\left\{\exp\left[-i\left(kr - \frac{l\pi}{2}\right)\right]\right. \tag{A.17}$$

$$\left. - \exp\left[i\left(kr - \frac{l\pi}{2}\right)\right]\right\} Y_{l,0}(\Omega).$$

This form of the plane wave consists of two spherical waves centred about the interaction site at $z = 0$. These waves are an incoming spherical wave ψ_{in},

$$\psi_{in} \sim \frac{1}{kr}\exp\left[-i\left(kr - \frac{l\pi}{2}\right)\right] \tag{A.18}$$

and an out-going spherical wave ψ_{out},

$$\psi_{out} \sim \frac{1}{kr}\exp\left[i\left(kr - \frac{l\pi}{2}\right)\right]. \tag{A.19}$$

The presence of the potential disturbs the out-going wave, and changes the amplitude and phase of the out-going wave. This disturbance is quantified by the diagonal elements of the S-matrix, $S(lj)$, and so the asymptotic solution is written

$$u_{lj}(r) = (4\pi)^{1/2}\frac{(2l+1)^{1/2} i^l}{2ik}\left\{S(lj)\exp\left[i\left(kr - \frac{l\pi}{2}\right)\right]\right.$$

$$\left. - \exp\left[-i\left(kr - \frac{l\pi}{2}\right)\right]\right\} \tag{A.20}$$

and the components of the wave function can then be written

$$\psi_{lj} = \left(\frac{4\pi}{v}\right)^{1/2} \frac{1}{kr} (2l+1)^{1/2} \frac{i^{l+1}}{2} \left\{ \exp\left[-i\left(kr - \frac{l\pi}{2}\right)\right] \right.$$
$$\left. - S(lj) \exp\left[i\left(kr - \frac{l\pi}{2}\right)\right] \right\} Y_{l,0}(\Omega)\chi_s. \qquad \text{(A.21)}$$

The scattered partial wave is then

$$\psi_{lj}^{scat} = \psi_{lj} - \frac{1}{v^{1/2}} e^{ikz} \chi_s \qquad \text{(A.22)}$$
$$= \left(\frac{4\pi}{v}\right)^{1/2} \frac{1}{kr} (2l+1)^{1/2} \left(\frac{S(lj)-1}{2i}\right) Y_{l,0}(\Omega)\chi_s \qquad \text{(A.23)}$$

and the scattering amplitude from equation (A.7) is just

$$f_{lj}(\theta) = (4\pi)^{1/2} (2l+1)^{1/2} \left(\frac{S(lj)-1}{2ik}\right) Y_{l,0}(\Omega) \qquad \text{(A.24)}$$
$$= (2l+1) \left(\frac{S(lj)-1}{2ik}\right) P_l(\cos\theta) \qquad \text{(A.25)}$$

where the spherical harmonic $Y_{l,0}(\Omega)$ has been integrated over the cylindrical coördinate ϕ and expressed in terms of the Legendre polynomial $P_l(\theta)$.

The complex matrix elements $S(lj)$ are the only unknowns in the wave function, and are solved for by matching the logarithmic derivative of u_{lj} for the asymptotic solution of the wave function with the numerical solution of the internal wave equation (A.10) for the potential V_{lj} at a point where the V_{lj} can be ignored.

The scattering and absorption cross sections are easily obtained once the diagonal $S(lj)$ matrix elements have been determined. The elastic scattering cross section is given by the ratio of the out-going scattered flux to the incident flux, which we have normalized to unity, so for an uncharged particle

$$\sigma_{lj}^{scat} = \int vr^2 \left|\psi_{lj}^{scat}\right|^2 d\Omega \qquad \text{(A.26)}$$

$$= \int |f_{lj}(\theta)|^2 \, d\Omega \tag{A.27}$$

$$= \int \frac{\pi}{k^2} \left|(2l+1)^{1/2}(S(lj)-1)Y_{l,0}(\Omega)\right|^2 d\Omega \tag{A.28}$$

$$= \frac{\pi}{k^2}(2l+1)\,|S(lj)-1|^2 . \tag{A.29}$$

The absorption cross section is obtained from a consideration of the particle loss by taking the difference between the incoming and outgoing particle flux,

$$\sigma_{lj}^{abs} = \int vr^2 \left(|\psi_{in}|^2 - |\psi_{out}|^2\right) d\Omega \tag{A.30}$$

$$= \frac{\pi}{k^2}\,(2l+1)\left(1 - |S(lj)|^2\right) \tag{A.31}$$

which also follows directly from the unitarity of the S-matrix.

The effect of a Coulomb potential is obtained by adding the scattering solution for a charged particle from a point source to the asymptotic solution in the external region of the potential. The radial wave function for Coulomb scattering satisfies the wave equation

$$\frac{d^2u_l}{d\rho^2} + \left(1 - \frac{2\gamma}{\rho} - \frac{l(l+1)}{\rho^2}\right) u_l = 0 \tag{A.32}$$

where $\rho = kr$ and γ is defined in terms of the projectile charge z and target charge Z by

$$\gamma = \frac{\mu z Z e^2}{k\hbar^2}. \tag{A.33}$$

The asymptotic solution to this equation is given by [Ho71]

$$u_{lj} = F_l(r) + iG_l(r) + S(lj)\,(F_l(r) - iG_l(r)) \tag{A.34}$$

where $F_l(r)$ and $G_l(r)$ are the regular and irregular Coulomb functions. The scattering amplitude then takes the form of

$$f_{lj}(\theta) = f_C(lj)(\theta) + \frac{1}{2ik}(2l+1)(S(lj)-1)e^{2i\delta_l}Y_{l,0}(\Omega) \tag{A.35}$$

where $f_C(lj)$ is the Coulomb scattering amplitude and δ_l is the Coulomb phase shift. The real Coulomb potential provides no additional absorption, and the absorption cross section is still determined by equation A.31.

An added complication in the calculation of the wave function and cross sections arises from the presence of a potential which depends on the spin of the incident particle. In the case of a nucleon with spin s, the wave function separates into solutions for j, $|l-s| \leq j \leq l+s$. The weight for each of these solutions is determined by their Clebsch-Gordon coupling coefficients, and the wave equation then becomes

$$\psi_l = \frac{1}{r}\sum_{j,m_s,m_j} \langle l,0,s,m_s|j,m_j\rangle u_{lj} Y_{l,0}(\Omega)\chi_s \tag{A.36}$$

and the absorption cross section, σ_l, for a particular l is then

$$\begin{aligned}
\sigma_l &= \frac{2l+1}{2s+1}\frac{\pi}{k^2}\sum_{j,m_s,m_j} |\langle l,0,s,m_s|j,m_j\rangle|^2 \left(1-|S(lj)|^2\right) && \text{(A.37)}\\
&= \frac{2l+1}{2s+1}\frac{\pi}{k^2}\sum_j \frac{2j+1}{2l+1}\left(1-|S(lj)|^2\right) && \text{(A.38)}\\
&= \frac{\pi}{k^2}\sum_{j=|l-s|}^{l+s} \frac{2j+1}{2s+1}\left(1-|S(lj)|^2\right) && \text{(A.39)}\\
&= \sum_{j=|l-s|}^{l+s} \sigma(lj) && \text{(A.40)}
\end{aligned}$$

where the factor of $2s+1$ averages over the initial spin projections of the incident particle, and where we have defined the cross section $\sigma(lj)$ as

$$\sigma(lj) \equiv \frac{\pi}{k^2}\frac{2j+1}{2s+1}\left(1-|S(lj)|^2\right). \tag{A.41}$$

Appendix B

Live Time Determinations

The live times of each detector were determined from a pulser peak inserted into each spectrum. In all runs except for $E_\alpha = 10$ MeV, the pulser peaks were placed in the high energy region of each spectrum. In the $E_\alpha = 10$ MeV runs, the pulser in detector #1 was placed in a low energy region which was free of peaks.

In some runs, detector #1 experienced gain instabilities which necessitated the energy recalibrations described in section 3.2.2, and caused a broadening of all spectrum peaks, including the pulser peak. In two corroborating runs at 7.7 MeV, in one of which detector #1 experienced the worst gain instabilities, variations on the order of 10% in the calculated yield were observed, and this value was adopted as an additional systematic uncertainty for the run. In all other runs the gain instability affected no more than 4% of the counts in detector #1 with the additional systematic uncertainty taken from the ratio of the secondary pulser peak to total pulser peak area ratio.

B.1 10 MeV Live Times

A preliminary analysis of all target data indicated a systematic deviation of the γ-ray yield curves from smooth behaviour between energies of $E_\alpha = 10.0$ and 8.8 MeV. A comparison of the live time monitors for all energy runs revealed a discrepancy in those for the 10 MeV runs.

The anomalous behaviour of the $E_\alpha = 10$ MeV runs was indicated by a comparison between the live times calculated from the pulser peaks and from the MCA internal live time monitor. Two effects diminish the number of counts in the spectrum peaks: the first is the fraction of time the system requires to digitize signals, known as the "dead time", and the fraction of time two signals are superimposed on one another, resulting in "pile-up". Under normal operating conditions, the pulser peak measured both the dead time and pile-up contributions to the live time, while the MCA measured the dead time alone, and hence typically reported a larger live time. In the 10 MeV runs the difference between these two monitors was abnormally small, and in a few instances the MCA live time was smaller than the pulser peak live time. This behaviour indicated a failure of the live time monitoring system, and necessitated the estimate of the $E_\alpha = 10$ MeV live times from their dependence on the counting rate.

Both the dead time and pile-up in the detectors are a function of the counting rate in the detector, and so with a knowledge of this dependence, the live time can be calculated for any given counting rate. In order to minimized effects in the counting rate caused by spectral differences due to different low energy threshold settings among the α-particle energy runs, the counting rate was taken as the total number of counts in the spectrum above a particular energy divided by the real time over which the spectrum was accumulated. This definition of the detector counting rate, referred to as the "reduced" counting rate, was target specific, requiring different determinations for each target. An example of the deduced dependence for the Aℓ target is shown in figure B.1. This target required the largest live time adjustment of all targets in this study. As was typical for all the targets studied here, the required live times for the 10 MeV run corresponded to a relatively low counting rate and were well determined from the behaviour of lower energy runs.

The live time in each detector was found to be a smooth function of the reduced counting rate; however spectrum shape differences in the different targets caused the live time function to be target specific. For all targets, except Si, the 10 MeV live time was interpolated from the lower energy run behaviour. As has been noted, the counting electronics for these two runs differ by the inclusion of the linear gate and stretcher used to set the lower energy threshold in the 8.8 to 5.6 MeV runs. The effect of this modification was a reduction of pile-up at the expense of an increased dead time. Thus, to first order, the pile-up rejection circuit did not significantly alter the interpolation of the live time from the reduced counting rate.

The live time monitors reported a live time which was typically lower than the reduced counting rate based live time. Since the exact nature of the monitor failure is unknown, the actual live time may fall anywhere between the reported and adopted value. To reflect this, a systematic uncertainty equal to the difference between the

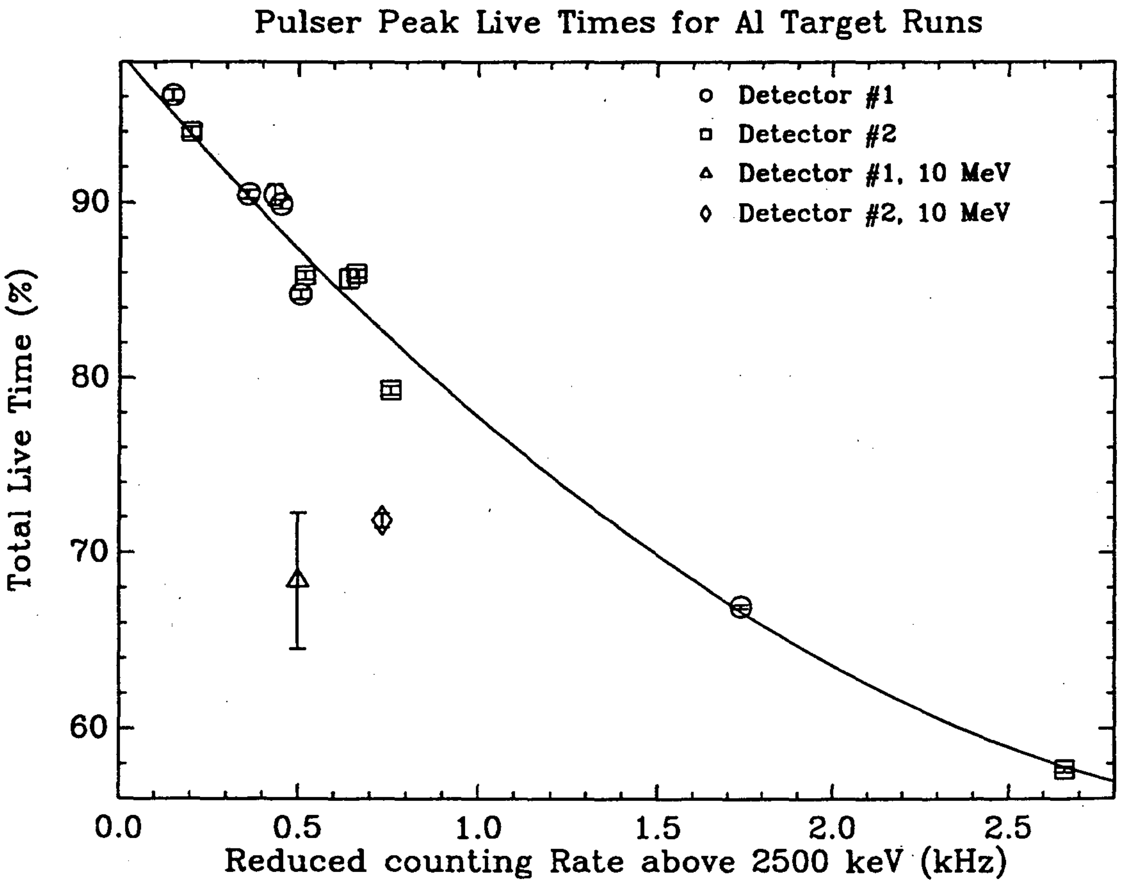

Figure B.1: The $A\ell$ target live times at α-particle energies other than 10 MeV can be seen to follow a smooth dependence on the reduced counting rate. The live time for both detectors in the 10 MeV target run fall below the average fit shown by the solid line.

two determinations has been adopted for the 10 MeV α-particle runs. This effect of this adjustment ranged from a small 3% change in the NaF target yields to close to a 20% decrease in the the Aℓ target yields.

In the Si target, no measurements other than the 10 MeV run were taken, and so a live time adjustment of this type was not possible. Instead, a live time adjustment was obtained by considering the average anisotropy from the a_2 terms of all measured transitions. This term was typically quite small in most cases, and for most targets averaged to zero for a transition. A small adjustment of the detector #1 live time was used to obtain a zero average in the single Si run, along with an additional uncertainty equal to the difference between the pulser and adopted live time values.

B.2 Live Time Pile-Up

The presence of the live time monitor pulser in the detector #2 spectrum added a small pile-up uncertainty to some of the low energy α-particle runs. This uncertainty was a result of γ-ray peaks being superimposed on the tail of the pulser signal, which created a shadow peak approximately 23 keV higher in the spectrum than the primary energy peak. The fraction of the time this type of pile-up occurred was proportional to the fraction of time a pulser peak occupies a given time interval, and so was proportional to the rate at which pulses were injected into the detector. Since the insertion of pulser signals was tied directly to the beam current, the pulser tail pile-up was directly proportional to the α-particle flux on each target.

This additional pile-up was found to be insignificant below α-particle fluxes of

10^{11} s^{-1}. Measurements taken at flux rates greater than this exhibited this shadow peak behaviour. Since many of the peaks possessed a width on the order of 23 keV due to Doppler effects, most of the strength of the shadow peak was included into the area of the primary peak by simply extending the peak area region. By treating the pulser tail pile-up in this manner, no correction to the live time was required; however an additional uncertainty equal to half the maximum estimated pile-up fraction was added to the live time systematic uncertainty, based on the particle flux for the run. This additional uncertainty ranged from 2% for most of the 7.7 MeV runs with 1.5×10^{11} s^{-1} on target to a maximum of 6% for several 7.0 MeV runs with 7×10^{11} s^{-1} on target.

Vita

Name: Robert Keith Heaton

Place and Year of birth: Leamington, Ontario, 1961

Education: Queen's University 1980-1984, B.Sc. (Eng), engineering physics 1984;

School of Graduate Studies and Research, Queen's University 1984-1988, M.Sc., Physics 1988

Experience: Summer Research Assistant, Chalk River Nuclear Laboratories, 1983, 1984; Research Assistant/Laboratory Demonstrator, Queen's University 1984–1988;

Research Assistant, Queen's University 1989;

Research Assistant/Laboratory Demonstrator, Queen's university 1989–1994;

Publications and Presentations:

1. R. Heaton, *"γ-Ray Transport using the EGS4 Monte Carlo Code"*, seminar and workshop at University of Guelph, November 1992.
2. R. Heaton, H. Lee, P. Skensved and B. C. Robertson, *"Alpha-induced Neutron Activity in Materials"*, Nuclear Geophysics 4 (1990) 499.
3. R.K. Heaton, H. Lee, P. Skensved and B.C. Robertson , *"Neutron Production from Thick-Target (α,n) Reactions"*, Nuclear Instruments and Methods in Physics Research, A276 (1989) 529.

4. P. Skensved, A. McDougall, R. Heaton, H. Lee and B. C. Robertson, *"Shield Uncertainties"*, Sudbury Neutrino Observatory Technical Report SNO-STR-88-102 (1988).

5. R. Heaton, H. Lee and B. C. Robertson, *"Neutron Yields in norite based on mineral composition"*, Sudbury Neutrino Observatory Technical Report SNO-STR-88-101 (1988).

6. R.K. Heaton, B.C. Robertson, P. Skensved, H.W. Lee, and SNO Collaboration *"Neutron Yields and Energy Spectra from the (α,n) Reaction on Light Elements"*, CAP Conference, Toronto, Ontario (June 1988) Physics in Canada 43, No. 3, Paper PM19

7. R. Heaton, H. Lee and B. C. Robertson, *"Evaluated (α,n) Data and Comparison"*, Sudbury Neutrino Observatory Technical Report SNO-87-102 (1987).

LAWRENCE BERKELEY LABORATORY
UNIVERSITY OF CALIFORNIA
TECHNICAL AND ELECTRONIC
INFORMATION DEPARTMENT
BERKELEY, CALIFORNIA 94720